Strain Rate, Temperature, and Their Coupled Effects on the Deformation Process of Four Polycarbonates and a Short Glass Fibre Reinforced Polycarbonate Composite

Student: Peihao Song (Linacre College)

Supervisor: Prof. Clive R. Siviour (Pembroke College)

Solid Mechanics and Materials Engineering Group

Department of Engineering Science

University of Oxford

A thesis submitted for the degree of Doctor of Philosophy

Trinity Term 2023

Abstract

Polycarbonate is a typical glassy thermoplastic polymer, which has been widely used in engineering applications because of its ductility, transparency and impact resistance. This research presents the thermomechanical responses of four polycarbonate resins: three are homo-polycarbonate with different melt flow rates, one is co-polycarbonate with impact-modified co-monomer; another one is polycarbonate-based short glass fibre composite. Specifically, the interplay between the effects of temperature and strain rate is investigated during the large strain deformation process.

The starting place for this research is to use low-temperature data to simulate the high-rate behaviour of polymer materials, which is inspired by the time-temperature equivalence theory in polymers. In high rate experiments, the strength of polymers increases; however, at the same time, the adiabatic environment-induced self-heating can cause thermal softening during the large strain deformation process. This study considers this trade-off and the combined effects of strain rate and temperature changes when describing the constitutive behaviour of polymer materials. Phenomenological finite element models are used to understand the experimental observations. In order to provide a full set of characterization data, experimental techniques were developed or improved for thermomechanical characterization in tension at low strain rates, combining full-field imaging and in-situ temperature measurements; measurements of temperature rise in polycarbonate during rapid deformation to large strains; application of time-temperature equivalence at large strains; characterization of polymer composites including thermal imaging and phase contrast X-ray imaging.

Experimental results show that the thermomechanical behaviour is consistent with time-temperature equivalence theory at small strains: both an increase in strain rate and a decrease in temperature increase the yield stress. At very low temperatures or high strain rates this is enhanced by the secondary molecular transition of polycarbonates. In large strain tensile tests, it was shown that using only a global force-displacement curve

to validate the constitutive parameters of the numerical model is insufficient because the test describes not only the material constitutive behaviour but also the structural response. For large strain compressive deformation, the temperature rise measurement results allow us to calculate the ratio of plastic work to heat generated, the Taylor-Quinney coefficient, in adiabatic experimental conditions. The value of this coefficient is dependent on both temperature and strain rate, and is affected by both the glass and secondary transitions. For the composite, data show the effect of localised heating on large strain behaviour, in particular causing significant strain localisation and hence weakening of the material. As well as giving a deeper understanding of the material response, the data generated in this study can be used to develop constitutive models over a wide range of temperatures and strain rates.

Acknowledgements

I would like to thank my supervisor Prof. Clive Siviour for offering me this opportunity to be involved in the *Impact Modelling of Polymers: high-Rate Experiments for Solid-state Simulations (IMPRESS)* project. In particular, this joint project also gives me a special chance to work with my bachelor university, the University of Nottingham. The patient guidance and consistent weekly discussions during the past four years make me not only understand the tasks of this project but also strengthen my scientific research capability. I also like to thank my colleague in this project, Dr. Akash Trivedi, for his selfless help during my first two years in Oxford. I would also like to thank Dr. David Chapman for his help in synchronising the high-speed optical images and for hosting me at the European Synchrotron Radiation Facility.

I would like to express my gratitude to the staff and my colleagues in the Department of Engineering Science. I would like to thank Dr Igor Dyson for his guidance in mechanical tests; Nicholas Hawkins for introducing the DMA, DSC and rheology device. I also thank the technicians of the Solid Mechanics Group workshop, in particular Andy Bateman and Neil Warland, for their help with the manufacture of specimens and fixtures for this project, and Dr. Davide De Focatiis and Grace Owen in the Nottingham team for their monthly discussion. I also thank my colleagues, Jimmy, Tom and Aaron in high-rate group, for their suggestions and discussion. I cannot thank Prof. Shuxin Li and his group enough for their suggestions about my academic career.

I would not be here without the love and support of my family, my parents, thank you for being with me every step of my life.

Finally, a further thanks to our industrial partner Sabic® for supplying materials and the DPI for funding under the Performance Polymers Programme, project 827t19.

Contents

Abstract I

Acknowledgements III

Contents IV

List of Figures X

1 Introduction 1

1.1 Motivation 1

1.2 Objective 2

1.3 Thesis Scope 3

1.4 Context of the Broad Research Project 5

2 Background and literature review 8

2.1 Polymers and their composites 8

2.2 Rate and temperature-dependent on PC 14

2.3 Experimental techniques 17

2.4 Time-temperature superposition 32

2.5 Additional measurement techniques and analysis 36

2.6 Bibliography 45

3 Large Strain Tension Experiments and Analysis 54

3.1 Introduction 54

3.2 Paper A: Tensile testing of polymers: Integration of digital image correlation, infrared

thermography and finite element modelling 55

Abstract 55

Introduction 56

Material information and sample preparation 59

Experimental procedure 61

Post-processing of experiments 63

Experimental results 65

Numerical model 70

Discussion 81

Conclusions 83

CRediT authorship contribution statement 84

Declaration of competing Interest 84

Acknowledgements 84

Data Availability 84

Appendix A. DIC and IR setup 85

Appendix B. Constitutive model [29] 86

Appendix C. FE model 88

Appendix D. Dynamic mechanical analysis (DMA) results 89

Appendix E. Modulated Differential Scanning Calorimetry (MDSC) result 90

References 94

4 Rate and Temperature Dependence 97

4.1 Introduction 97

4.2 Paper B: Mechanical response of four polycarbonates at a wide range of strain rates and temperatures 98

Abstract 98

Introduction 99

Material information and sample preparation 102

Experimental procedure 104

Experimental results 108

Varying rate and temperature compression tests 114

Discussion 116

Conclusions 121

CRediT authorship contribution statement 122

Declaration of competing Interest 122

Acknowledgements 122

Data Availability 122

Appendix A: Heat-cool-reheat DSC data 123

Appendix B: DIC setup 124

Appendix C: Single cantilever beam DMA results 125

Appendix D: Storage modulus versus log rate of PC2 using three-point bend configuration 126

Appendix E: Temperature-dependent compression data for PC8, PC3 and PC4 127

Appendix F: Rate-dependent compression data for PC8, PC3 and PC4 128

Appendix G: Frequency sweep DMA results for PC8, PC3 and PC4 129

Appendix H: Shift of yield stresses from temperature-dependent to rate-dependent 130

Appendix I: Low-temperature and high-rate compression data comparisons 131

References 132

5 Thermomechanical Effects in Large Strain Compression 135

5.1 Introduction 135

5.2 Paper C: Understanding the temperature, strain rate and their coupled effects on the plastic deformation of polycarbonate. Part I: Experimental study 136

Abstract 136

Introduction 137

Material information and sample preparation 141

Experimental procedure 142

Evaluation of thermal conditions 145

Experimental results 150

Discussion 158

Conclusions 164

CRediT authorship contribution statement 165

Declaration of Competing Interest 165

Acknowledgements 165

Data Availability 165

Appendix A. Calibration of an infrared camera 166

Appendix B. Calibration of emissivity of PC and IR camera settings for all experiments 167

Appendix C. Three network viscoplastic (TNV) model 168

Appendix D. Calculation of TQC using a constant C_p 170

References 172

6 Thermomechanical Properties of Short Glass Fibre Reinforced PC 175

6.1 Introduction 175

6.2 Paper D: Thermomechanical characterisation of thermoplastic polymer and its short glass fibre reinforced composite: Influence of fibre, fibre orientation, strain rates and temperatures 176

Abstract 176

Introduction 177

Material information and sample preparation 180

Experimental procedures 182

Experimental results 186

Conclusions 201

CrediT authorship contribution statement 203

Declaration of competing interesting 203

Acknowledgements 203

Data Availability 204

Appendix 205

References 206

7 Conclusions 209

7.1 Thesis objectives 209

7.2 Summary of accomplishments 211

7.3 Limitations and recommendations for future work 214

7.4 Closing remarks 216

List of Figures

Chapter 2

Figure 2-1 Prediction of the global plastic market from 2022 to 2023 [6]. 8

Figure 2-2 (a) LEXAN^{TM} bisphenol A-PC (BPA-PC): PC2, PC3 and PC8 (b) LEXAN^{TM} HFD copolymer, bisphenol A-sebacic acid (BPA-SA): PC4. Graphs are reproduced from [8]; (c) 3D Micro-CT scanning of cylindrical glass fibre reinforced PC (PC9) sample cut in the through-thickness direction 11

Figure 2-3 (a) Varying rate compression tests at 21 °C (b) Rate-dependent yield stresses at 21 °C (c) Varying rate compression tests at 5500 ± 500 s^{-1} (d) Temperature-dependent yield stresses at 5500 ± 500 s^{-1}. Reproduced from [43]. 15

Figure 2-4 A comparison of the simulated constitutive behaviour of PC in tension and compression [51]. 16

Figure 2-5 The strain rate regimes and their corresponding experimental techniques [56, 57] 17

Figure 2-6 Custom-built hydraulic machine for medium rate compression experiments. 20

Figure 2-7 (a) Schematic of split Hopkinson pressure bar (SHPB) system (b) Voltage-time curves in SHPB test. Reproduced from [56]. 21

Figure 2-8 (a) Forces, displacements and velocities at the bar-specimen interfaces (b) Comparison of forces calculated from the output signal (one wave) and the difference between the incident and reflected signal (two wave) analyses [56]. 22

Figure 2-9 Cross section of a TA Instrument heat flux DSC machine [93]. 25

Figure 2-10 A typical diagram of the DSC curve [94] 26

Figure 2-11 Modulation of the temperature around an average heating rate for a modulation [93] 27

Figure 2-12 The total heat flow, reversing and non-reversing heat flow for quenched PET measuring from MDSC [93]. 28

Figure 2-13 (a) Perspective view of TA Q800 DMA machine (b) Single/Dual cantilever beam fixture (c) Three-point bend fixture. Reproduced from [106]. 29

Figure 2-14 Example of oscillating stress applied to a polymeric sample [100]. 30

Figure 2-15 Idealised dependence of polymer modulus on temperature [100]. 30

Figure 2-16 Frequency sweep DMA test PC using single cantilever beam configuration (a) Storage modulus and loss modulus versus temperature (b) Isotherms showing the dependence of modulus on frequency and temperature (c) Master curve constructed at a reference temperature of 20 °C (d) Shift factor versus temperature curve. Data from [122]. 34

Figure 2-17 (a) Detail of β-transition (b) Detail of α-transition (c) Arrhenius plot for β- and α-transitions. Reproduced from [122]. 35

Figure 2-18 Typical 2D-DIC image acquisition setup [126]. 36

Figure 2-19 Schematic of tracking the reference subset in the deformed image using DIC [140]. 37

Figure 2-20 Schematic of ESRF ID-19 hutch for SHPB tests, the dimensions of this system are appropriate for hutch room (b) SHPB setup mounted perpendicular to the X-ray axis in ID-19 in ESRF. Reproduced from [165]. 42

Chapter 3

Figure 1. Geometry of the specimens used in uniaxial tension tests. Points A to I indicate the locations at which local strain measurements were later obtained. 59

Figure 2. (a) Annealing temperature profile (b) DSC data showing glass transition temperature. 60

Figure 3. Comparison of IR and thermocouple temperature readings. 61

Figure 4. Illustration of stress calculations (a) Method 1 and 2 (b) Method 3. 63

Figure 5. Force-displacement curves for tensile experiments at crosshead displacement speeds of 50 and 5 mm/min (In all tests, the specimens are tested to failure). 65

Figure 6. True (Hencky) strain maps obtained using DIC (a) Shear band initiation at 8.4 s (crosshead displacement = 7 mm) (b) unstable neck propagation at 12 s (10 mm) (c) stable neck propagation at 30 s (25 mm) (d) propagation towards the ends of specimen at 50 s (41.7 mm) (e) further propagation at 70 s (58.3 mm). 66

Figure 7. Data extracted from ten points in the gauge area, nine points evenly spaced as shown in Figure 1, plus an additional point at the location at which the neck formed (a) axial true strain vs time (b) axial true strain rate vs time. In this case, Point E was very close to Point Neck formation..... 67

Figure 8. Transverse true strain against time (a) Point B (b) Point E (c) Point Neck. 67

Figure 9. Uniaxial true stress-true strain curves, (a) Point B (b) Point E (c) Point Neck 68

Figure 10. Transverse true strain against position for seven points in the line of the Point Neck 68

Figure 11. Uniaxial true stress vs true strain curves, (a) Method 1, (b) Method 2, (c) Method 3 69

Figure 12. Schematic of three-network model, and illustration of where the model parameters (Table 1) affect the stress-strain response. 70

Figure 13. (a) Mechanical and thermal boundary conditions on the tensile specimen (b) Load-displacement curves comparison between experiment and model with different assumptions: with and without defects and with and without heat effects (thermal radiation and heat conduction). 72

Figure 14. Constitutive model using parameter Set 1 compared to (a) rate-dependent compression tests, (b) temperature-dependent compression tests; experimental and simulation results showing (c) load-displacement curve (d) axial true strain - time curve..... 72

Figure 15. Compression and tension yield stress against strain rate. 73

Figure 16. Constitutive model using parameter Set Final compared to (a) rate-dependent compression tests (b) temperature-dependent compression tests; experimental and simulation results showing (c) load-displacement curves (d) axial true strain-time curve. 75

Figure 17. Comparison of model and experimental axial strain data at 8.4, 12, 30, 50, 70 s: (a) to (e) axial strain obtained from DIC; (a') to (e') axial strain obtained from FE model. 75

Figure 18. Comparison of model and experimental data at 8.4, 12, 30, 50, 70 s, (a) to (e) Experimental temperature change obtained from IR camera; (a') to (e') Numerical temperature change extracted from FE model. 76

Figure 19. Experimental (IR) and numerical (surface, inside) temperature profile down the centre of the gauge area at (a) shear band first occurring at 8.4 s (b) unstable neck propagation at 12 s (c) stable neck propagation at 30 s (d) neck extension to both ends at 50 s (e) 70 s. 77

Figure 20. Effects of λ_L (a), (a'); μ_{Bf} (b), (b'); and β (c), (c') on the load-displacement and strain-time curves. 79

Figure 21. Experimental ((a) to (d)) and numerical ((a') to (d')) thermal behaviours of Point F. 81

Chapter 4

Figure 1. Injection moulded ISO 527 1A dogbone sample (all dimensions in mm) 102

Figure 2. (a) Heal-cool-reheat DSC measurement on PC2, heating and cooling rates of 2 °C/min (b) Temperature profile during annealing. 103

Figure 3. Experimental setup (a) Quasi-static compression, (b) Hydraulic compression, (c) Split Hopkinson pressure bar. 106

Figure 4. Temperature sweep DMA results using different modes (a) Storage modulus versus temperature (b) Loss modulus versus temperature. 108

Figure 5. Results from three-point bend frequency sweep experiments: (a) Original data for storage modulus (b) Detail of β-transition region; (c) Time-temperature superposition master curves, converted to strain rate (d) Shift factor versus temperature. Note that the experiments were performed as isothermal frequency sweeps. 109

Figure 6. Frequency sweep results using single cantilever beam modes (a) Detail of β-transition for PC2 (b) Arrhenius plot for β-transition for all PCs (c) Detail of α-transition temperature for Tan delta for PC2 (d) Arrhenius plot for α-transition for all PCs. 111

Figure 7. Example of virtual extensometer used for Engineering strain extraction via DIC. 112

Figure 8. Engineering stress-strain curves. 113

Figure 9. Data from experiments on PC2 at a constant true strain rate of 0.01 s^{-1} and different temperatures (a) True stress-true strain curves (b) Yield stresses. 115

Figure 10. (a) Comparison of the four polycarbonates at 20 and 120 °C, showing the difference in post-yield softening of PCs 8 and 3 compared to 2 and 4. (b) Fracture in PC3 specimens tested in compression at 120 °C. 115

Figure 11. Data from experiments on PC2 at room temperature and different strain rates (a) true stress-true strain curves (b) yield stress vs log strain rate. 115

Figure 12. Comparing the three point bend and single cantilever beam mode frequency DMA results of PC2 (a) frequency sweep results (the dash line is obtained from temperature sweep (b) Time-temperature superposition curves (c) Shift factor versus temperature curves. 116

Figure 13. Comparison of (a) Temperature-dependence of yield stress in compression (b) Rate-dependence of yield stress in compression and tension 117

Figure 14. (a) Result of shifting temperature-dependent yield stress onto the yield stress-log rate curve, for PC2 (b) Comparison of shift factors obtained from three-point bend DMA data and from yield stress data (c) Result of shifting temperature-dependent yield stress onto rate-dependent yield stress using DMA shift factors. 118

Figure 15. Comparison of stress-strain curves at low temperatures and high strain rates (PC2). The colours indicate which temperature/rate combinations are equivalent (e.g. 3100 s^{-1}, 20 °C and 0.01 s^{-1}, -60 °C). 118

Chapter 5

Figure 1. (a) Comparison of stress-strain curves at high strain rates and low temperatures. The colours indicate the equivalent temperature/rate combinations (e.g. 3100 s^{-1}, 20 °C and 0.01 s^{-1}, -60 °C), reproduced from [6], (b) Previously published results for temperature rise measurements in high rate deformation of PC [12, 17, 21, 25-27], (c) Comparison of stress-strain curves at 2600 s^{-1} and 20 s^{-1} with two equivalent quasi-static experiments (which have similar yield stresses) with and without temperature profiling, reproduced from [22]. 139

Figure 2. Mechanical test machines (a) Quasi-static compression, (b) Hydraulic compression, (c) Long Split Hopkinson pressure bar. 143

Figure 3. (a) Numerical model setup (here, true strain is 0.8) (b) Simulated temperature rise under different experimental conditions representing the extremes likely condition (c) Simulation of temperature rises using TQC = 0.55, and conductance 150 W m^{-2} K^{-1}. 147

Figure 4. (a) Experimental (IR camera) and numerical temperature profiles along the length of the specimen at (a) 0.2 true strain (b) 0.4 true strain (c) 0.6 true strain (d) 0.8 true strain 148

Figure 5. (a) True stress-true strain curve at 0.1 and 0.5 s^{-1} using two different sample sizes; (b) Temperature rise-true strain curve at 0.1 and 0.5 s^{-1} using two different sample sizes, measured using an IR camera only, averaged over the window indicated in (d); (c) Effects of thermocouple on true stress-true strain curve, and comparison of temperature rise measured by different methods at 0.5 s^{-1}; (d) IR temperature maps obtained on a sample embedded with a thermocouple at 0.5 s^{-1}. 149

Figure 6. Temperature-dependent reverse specific heat capacity measured by MDSC..... 150

Figure 7. DMA data using three-point bend configuration, reproduced from [6] 151

Figure 8. Data from quasi-static tests: (a) True stress - True strain curves; (b) Temperature rise - True strain curves obtained from IR camera using window shown in (d); (c) Total work and Heat work against true strain

at 0.5 s^{-1}; (d) Thermal images from experiment at 0.1 s^{-1} (e) Thermal images from experiment at 0.5 s^{-1}.... 152

Figure 9. (a) Comparison of true stress - true strain between 0.1 and 0.5 s^{-1} at different temperature tests (all samples are pristine) (b) Comparison of yield stresses between 0.1 and 0.5 s^{-1} at different temperatures.... 153

Figure 10. (a) True stress - True strain curves at low-temperature tests with and without embedded thermocouple (b) Temperature rise in low temperature experiments measured by an embedded thermocouple (c) Thermal energy (calculated using the simultaneous temperature-dependent C_p) versus true strain. 153

Figure 11. Data from medium rate tests (a) True stress-True strain curves (b) Temperature rise-true strain curves (c) Total mechanical energy and thermal energy (using the temperature-dependent simultaneous C_p)-true strain curves (d) Thermal images in experiment at 1.5 s^{-1} (e)Thermal images in experiment at 13.5 s^{-1}. 154

Figure 12. Data from high strain rate experiments: (a) True stress-true strain curves for seven Hopkinson bar tests; (b) Time-shifted output bar signal and IR monitor output from two tests; (c) Mean temperature rise-true strain for all the images obtained (d) Selected thermal images from low to high strain, montage produced from seven tests. 155

Figure 13. Comparison of true-stress-true strain curves at different test conditions (pristine samples) and corresponding temperature rise measurements..... 156

Figure 14. An example of TQC calculation (a) True stress against three different strains (b) Three mechanical work calculations obtained by integrating the curves in Fig. 14(a), with thermal energies calculated using simultaneous and constant C_p (c) TQC based on three different mechanical works, and simultaneous C_p. . 159

Figure 15. Temperature-dependent TQCs calculated based on three different mechanical works and the simultaneous C_p (here, all temperature rise data are obtained using a thermocouple). 159

Figure 16. (a) Comparison of TQC calculated from the temperature rise measured using both an IR camera and a thermocouple at 0.5 s^{-1}; (b) Comparison of temperature rise measurements from IR and thermocouple; (c) Temperature rise measurements performed using an IR camera only on a pristine sample..... 160

Figure 17. Rate-dependent TQCs calculated based on three different mechanical works calculated using a temperature-dependent specific heat capacity. All temperature rise data are measured using an IR camera. The blue circles indicate the stitched high strain rate data in different tests, and the solid blue line is generated using polynomial curve fitting. 160

Figure 18. Temperature-dependent TQC calculated using (a) Total work (b) Plastic work (c) Shifted plastic work, and simultaneous specific capacities. 161

Figure 19. Temperature-dependent TQC calculated using total work, plastic work, shifted plastic work, and simultaneous C_p. 161

Figure 20. (a) Undeformed sample (b) Tested sample at 150 °C and 0.5 s^{-1} strain rate to 0.8 true strain. 162

Figure 21. Non-reversed specific heat capacity against temperature. 163

Chapter 6

Figure 1. (a) Schematic of sample cutting, (b) Dimensions of tension sample. 181

Figure 2. (a) Screw-driven tests, (b) Hydraulic machine, (c) Split Hopkinson pressure bar. 183

Figure 3. (a) Storage modulus against temperature, (b) Time-temperature superposition master curves at 20 °C, (c) Shift factor versus temperature. 186

Figure 4. Engineering stress-strain curves at three different loading rates for the composite cut in three orientations relative to the injection flow direction and PC matrix (representative specimens shown here, raw data provided online for all specimens tested). 187

Figure 5. (a) Temperature dependent stress-strain curves for PC matrix, (b) Temperature dependent stress-strain curves for PC composite (TT), (c) Yield stress versus temperature for PC matrix and composite 188

Figure 6. (a) Rate dependent stress-strain curves for PC matrix, (b) Rate dependent stress-strain curves for PC composite (TT), (c) Yield stress versus logarithm strain rate for PC matrix and composite. 188

Figure 7. Comparison of stress-strain curves at low temperatures and high strain rates; the colours indicate

which temperature and rate combinations are equivalent. (a) PC matrix, (b) PC composite (TT). 189

Figure 8. (a) stress-strain data for three quasi-static experiments on PC; (b) mean temperature rise data obtained from thermal images of these experiments; (c) selected thermal images from experiment at $0.1s^{-1}$, (d) selected thermal images from experiment at 0.5 s^{-1}. 190

Figure 9. (a) True stress versus true strain curves in two medium rate tests on PC; (b) true strain versus time data for the same experiments; (c) mean temperature-true strain; (d) selected thermal images from experiment at 1.5 s^{-1}, (e) selected thermal images from experiment at 11 s^{-1}. Markers on the stress-strain and strain-time curves indicate when the thermal images were taken. 191

Figure 10. (a) True stress versus true strain curves for eight Hopkinson bar experiments on PC; (b) Time-shifted IR monitor out signal and LSHPB output bar signal from two experiments; (c) Mean temperature rise versus true strain for all the images obtained, the numbers S1-S8 indicate the eight different specimens tested; (d) Selected thermal images from low to high strain, montage produced from a number of experiments, again the numbers S1-S6 indicate from which specimen the image was obtained. 192

Figure 11. (a) stress-strain data for three quasi-static experiments on PC composite; (b) maximum and mean temperature rise data obtained from thermal images of these experiments; Temperature against true strain at different rates; (c) selected thermal images from experiment 0.1 s^{-1}; (d) selected thermal images from experiment at 0.5 s^{-1} 193

Figure 12. (a) True stress versus true strain curves in two medium rate tests on PC composite; (b) true strain versus time data for the same experiments; (c) maximum and mean temperature vs true strain; (d) selected thermal images from experiment at 1.4 s^{-1}, (e) selected thermal images from experiment at 11.4 s^{-1}. Markers on the stress-strain and strain-time curves indicate when the thermal images were taken. 194

Figure 13. Temperature rise measurements in high rate experiments on PC composite (a) True stress-true strain curves for fibre flow parallel to the IR camera (P), markers indicate when the IR images were taken; (b) True

stress-true strain curves for fibre flow towards the IR camera (T), note that the stress-strain behaviour for P and T is the same, but the data are shown separately for easier comparison to the thermal images; (c) Temperature rise measurements for the eight experiments; (d) Thermal images for fibre flow parallel to the IR camera, (e) Thermal images for fibre flow towards the IR camera (note that green colour indicates that the temperature has exceeded 150 °C..... 196

Figure 14. True stress versus true strain curves: (a) In-plane specimens (2 × 2 mm), loaded in the injection flow direction (b) Through thickness specimens (2 × 2 mm) with the injection flow direction parallel (P) and perpendicular (T) to the image plane..... 197

Figure 15. X-ray images and DIC mapping for 2 × 2 mm samples: (a) and (a') loaded in the injection flow direction, (b) and (b') injection flow direction parallel to the image plane (P), (c) and (c') injection flow direction perpendicular to the image plane (T). Zoomable images will be made available online. 198

Figure 16 (a) Temperature vs strain for PC matrix and maximum temperature vs strain for PC composite, (b) Temperature change inferred using global strain in ESRF data compared to temperature change inferred using local maximum strain in ESRF data. 199

Figure 17. Temperature rise comparison for PC and its composite at different strain rates: (a) 0.5 s^{-1}, (b) ~1.5 s^{-1}, (c) ~12 s^{-1}, (d) ~2500 s^{-1}..... 200

1 Introduction

1.1 Motivation

Polycarbonate and its composites are widely used for lightweight design in industrial applications. For many products, such as helmets and car bumpers, impact events are one of the most common causes of failure or damage. However, the impact performances of polycarbonate materials are not well understood, which prevents us from taking the best advantage of them during the design process. Therefore, the final products are possibly heavier or less effective than they could be.

It is well known that the mechanical properties of polymers and polymeric materials are highly temperature- and rate-dependent, therefore, data obtained from quasi-static tests are not suitable for analysing or simulating dynamic performance. Moreover, with the changing temperature or loading rate, a single polymer can undergo a variety of states such as glassy, rubbery and viscous. Considerable changes in mechanical properties, caused by the state transition, pose a significant challenge to the accuracy of the experimental measurement. Furthermore, because the natural frequencies of polymer samples in high-rate experiments are similar to the loading pulse frequency, and with existing experimental techniques, it is challenging to monitor the temperature change during the experiments.

With the increasing improvement of experimental techniques, research on polycarbonate has been constantly evolving over the past few decades. However, several studies have described the strain rate and temperature-coupled effects during large strain deformation, especially at high-rate. As a result, no well-established physical model can accurately address the change in constitutive behaviours caused by temperature rise during the high-rate tests. Thus, it is necessary to calibrate the constitutive behaviours of polycarbonate materials, and some accompanying observations during the tests must be measured and interpreted.

1.2 Objective

The main task of this joint project (Impact Modelling of Polymers: High-Rate Experiments for Solid-state Simulations ((IMPRESS), with the University of Nottingham) is to predict the high-rate performances of polymeric materials based on low-rate data obtained from the quasi-static experiments. These high-rate behaviours are expected to include but are not limited to dynamic deformation, yield, strain softening and hardening. Specifically, the current project focuses on four polycarbonate resins (three of them are homo-polycarbonate with different melt flow rates, and one of them is co-polycarbonate with the impact modifier) and one 20 wt% short glass fibre reinforced polycarbonate provided by our industrial partners. The mechanical responses of these materials under varying loading rates and temperatures will be investigated. Within this project, my research will focus on the experimental study, and the ultimate aim is to provide a sufficient dataset and build a deep understanding of the deformation mechanism for these polycarbonate materials to be used in future industry and scientific research.

1.3 Thesis Scope

A summary of the contents of this thesis is as follows:

Chapter 1 Introduces the motivation, objective, scope and work outline of this research.

Chapter 2 Provides a background of this thesis, such as the material information and selection, the aims and goals of this project. Moreover, it critically reviews the related experimental techniques and results, especially in high-rate characterisation for polymeric materials.

Chapter 3 conducts tensile tests for polycarbonate accompanied by digital image correlation and infrared thermography techniques. Moreover, a viscoplastic finite element model with calibrated parameters (using the low-rate compression test results in **Chapter 4**) is used to understand the experimental observations. It illustrates that the traditional tensile test is not only a material constitutive behaviour but also a structural response, thus, it is insufficient to use force-displacement information (global behaviour) from tensile experiments to calibrate, or validate, constitutive models of polymers. This chapter has been published as a journal paper: http://dx.doi.org/10.1016/j.jmps.2022.105161.

Chapter 4 extensively characterises the three different melt flow rate homo-polycarbonate resins and one co-polycarbonate resin at a wide temperature and strain-rate range. It can provide a more comprehensive dataset for polycarbonate and allows an understanding of the melt flow rate effects and co-monomer effects on the thermomechanical performance of polycarbonates. This chapter has been published as a journal paper: http://dx.doi.org/10.1016/j.polymertesting.2023.107986.

Chapter 5 is motivated by the research question given in **Chapter 4**: Why can apparent thermal softening be observed in medium-rate tests rather than high-rate tests at the large strain deformation region for polycarbonate? To address this question, this chapter measures the temperature rise at different loading conditions: low to high strain rate and low to high temperature. Furthermore, the Taylor-Quinney coefficient at different loading conditions is calculated to understand how plastic work can be converted to heat. The

results imply that the molecular transition plays a significant role in energy distribution during the large strain deformation process. This chapter has been submitted for publication.

Chapter 6 extends the developed methodologies (in **Chapter 5**) into the polycarbonate composite, and high-rate compression tests are performed with in-situ X-ray imaging in the European Synchrotron Radiation Facility. The thermal images under different strain-rate (especially in high-rate) and digital image correlated high-rate X-ray images show how adiabatic shear band formation can lead to very high-temperature rises and lead to significant softening in the polycarbonate composite. These data will enhance the use of polycarbonate composite in different engineering applications and facilitate the development of micromechanical models. This chapter has been submitted for publication.

Chapter 7 concludes the innovativeness and achievements of this work, as well as highlights some scientific questions identified in this project that have not yet been addressed. Furthermore, some recommendations for future investigations are given.

1.4 Context of the Broad Research Project

This Dutch Polymer Institute (DPI) funded joint project has involved seven researchers. Five researchers are in the Oxford team: Prof. Clive R Siviour, Dr. Akash R Trivedi, Dr. David J Chapman, Aaron G Graham and a PhD student---Peihao Song (me), who mainly takes charge of experimental characterisation; two researchers are in the Nottingham team: Dr. Davide De Focatiis and a PhD student---Grace Owen, who mainly develops the constitutive model. This project starts with one-dimensional (1D) experimental characterisation under different loading conditions; then the results obtained from these 1D tests are used to develop the constitutive model; following that, some two-dimensional (2D) and three-dimensional (3D) tests are performed to validate the developed constitutive model. Two types of materials, polycarbonate (PC) and PC composite and polyamide 6 (PA6) and PA6 composites, are investigated in this project. In this project, my research mainly focuses on PCs and a polycarbonate composite, and everyone plays their respective roles and assists each other, resulting in many scientific achievements and publications.

1.4.1 Publications

First-authored publications

1. **P Song**, AR Trivedi, CR Siviour*, Tensile testing of polymers: Integration of digital image correlation, infrared thermography and finite element modelling, 2022, Journal of the Mechanics and Physics of Solids, 105161, **Published journal paper – this paper forms Chapter 3**
2. **P Song**, AR Trivedi, CR Siviour*, Mechanical response of four polycarbonates at a wide range of strain rates and temperatures, 2023, Polymer Testing, 107986, **Published journal paper – this paper forms Chapter 4**
3. **P Song,** DJ Chapman, A Graham, AR Trivedi, CR Siviour*, Understanding the temperature, strain rate and their coupled effects on the plastic deformation of polycarbonate. Part I: Experimental study, **Submitted journal paper – this paper forms Chapter 5**

4. **P Song,** DJ Chapman, A Graham, Bratislav Lukić, Alexander Rack, CR Siviour*, Thermomechanical characterisation of thermoplastic polymer and its short glass fibre reinforced composite: Influence of fibre, fibre orientation, strain rates and temperatures, **Submitted journal paper – this paper forms Chapter 6**
5. **P Song***, DJ Chapman, A Graham, CR Siviour, Compression behaviour of short glass fibre reinforced polycarbonate composite at varying rates during large strain deformation, 2023, 17th Internation Conference on Advances in Experimental Mechanics, **Published conference paper; Awarded as Runner-up in *Young Stress Analyst Competition***
6. **P Song*,** AR Trivedi, CR Siviour, Mechanical response of two different molecular weight polycarbonates at varying rates and temperatures, 2021 EPJ Web of Conferences 250, 06013, **Published conference paper**
7. **P Song*,** AR Trivedi, CR Siviour, Thermomechanical properties of three different molecular weight polycarbonates and one co-polycarbonate, 2022, 18th International Conference on Deformation, Yield and Fracture of Polymers, **Published conference paper & poster**
8. **P Song***, AR Trivedi, CR Siviour, The temperature rise in polycarbonate at varying temperature and rate compression tests during large strain deformation, 2022, 18th International Conference on Deformation, Yield and Fracture of Polymers, **Published conference paper & poster**
9. **P Song***, AR Trivedi, CR Siviour, Investigating the large strain tensile behaviour of a glassy amorphous polymer using the virtual fields method, 2022, 18th European Mechanics of Materials, **Published conference abstract**
10. **P Song**, AR Trivedi, N Hawkins, DJ Chapman A Graham, CR Siviour*, Thermomechanical characterisation of polyamide 6 over a wide range of rates and temperatures, **Submitted journal paper**

11. **P Song**, AR Trivedi, N Hawkins, DJ Chapman A Graham, CR Siviour*, Thermomechanical characterisation of short glass fibre reinforced polyamide 6 composites using advanced optical imaging techniques, **Journal paper in preparation**

Publications led by collaborators

12. AR Trivedi*, **P Song**, CR Siviour, Experimentally simulating adiabatic behaviour: Capturing the high strain rate compression response of polymers using low strain rate experiments switch programmed temperature profiles, 2022, Polymer Testing, 107773, **Published journal paper**
13. H Chen, **P Song**, T Commins, A Graham, AR Trivedi, CR Siviour*, Characterisation and modelling of bisphenol-a type epoxy polymer over a wide range of rates and temperatures, 2022, Polymer, 124860, **Published journal paper**
14. AR Trivedi*, **P Song**, CR Siviour, Experimentally simulating the adiabatic self-heating observed in polymers under high-rate loading, 2022, 18th International Conference on Deformation, Yield and Fracture of Polymers, **Published conference paper & poster**
15. AR Trivedi*, **P Song**, CR Siviour, Characterising the varying rate bending response of short glass fibre filled polycarbonate, 2022, 18th European Mechanics of Materials Conference, **Published conference abstract**
16. S. Salimi, AM. Graham, Y. Wu, **P Song**, LR. Hart, DJ. Irvine, RD. Wildman, CR. Siviour, and W. Hayes, An effective route to the additive manufacturing of a mechanically gradient supramolecular polymer nanocomposite structure, **Submitted journal paper**
17. AM. Graham, **P Song**, CR Siviour, Application of the T-test and virtual fields method to the constitutive response of materials, **Submitted journal paper**
18. DJ Chapman*, **P Song**, CR Siviour, Mechanics of Taylor Impact test of polycarbonate and short glass fibre reinforced polycarbonate, **Journal paper in preparation**

2 Background and literature review

2.1 Polymers and their composites

2.1.1 History of polymers and composites

Polymers and polymer matrix composites have played a significant role in daily life for many years, and no other material can replace them in terms of cost, processability and weight. Unlike metal materials, which have been used for millennia, it was only in 1862 that the first synthetic plastic, a type of cellulose nitrate, came into public view at the Great International in London [1]. Over the subsequent decades, the plastic and rubber industries ushered in considerable development, but the molecular structure of polymers was not well understood until the work of Staudinger, who proposed that the chemical essence of rubber, celluloid and protein was formed by the chemically bonded repeating units in 1920 [2]. Staudinger's revolutionary idea was widely accepted by the 1930s, after which plastics and rubbers were categorised as polymers. He was awarded the Nobel Prize in 1953 for this discovery. In this period, a lot of well-known polymers, such as nylon [3], polyethylene [4], and polyvinyl chloride (PVC) [5] began to be synthesised.

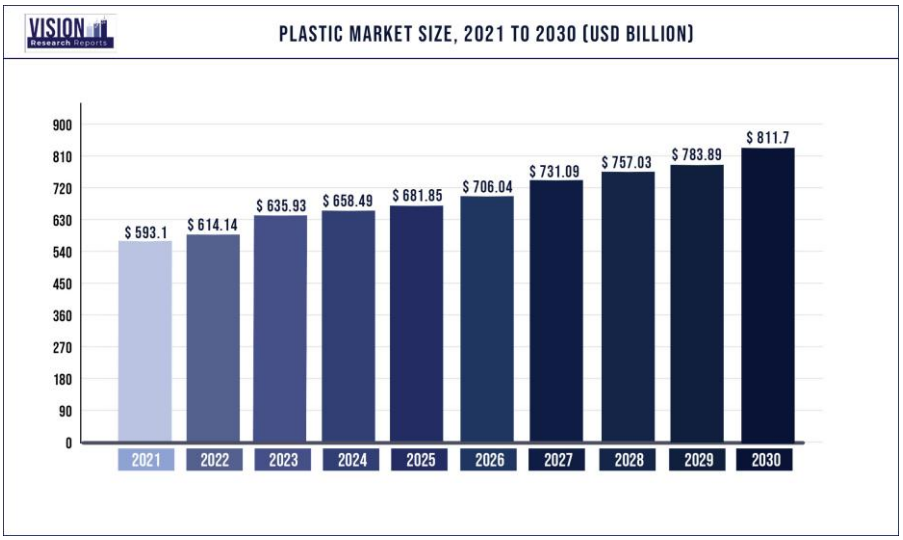

Figure 2-1 Prediction of the global plastic market from 2022 to 2023 [6].

Today, the output of plastic production is experiencing explosive growth [1], and this growth trend is expected to continue, as shown in Fig. 2-1 [6]. This can be attributed to the high specific strength, relatively

low cost, and availability of polymers with superior physical and chemical resistance [6]. Moreover, plastics can be fabricated with modified properties to suit different requirements, such as fibre reinforced plastics (FRPs) and nanocomposites or shaped into various forms.

2.1.2 Material information and selection in this project

Knowledge of the mechanical properties of polymers over a wide range of temperatures and strain rates is increasingly vital as they are used in specific fields such as automotive and aerospace [7]. These properties are dominated by the microstructure (amorphous or semi-crystalline), which plays a significant role in the constitutive model development. Although significant experimental data are required to construct a reliable model, once the material is characterised, this work is beneficial to predict the mechanical behaviours in engineering use, and the model may be expanded to other similar polymers. This thesis will investigate a typical amorphous polycarbonate (PC) experimentally and numerically, although the techniques developed are also being used on the semi-crystalline polymer, PA6.

Sabic® kindly provided all PC and PC-based materials, including different melt flow rates (MFR) homo-PCs, impact modified co-PCs, and a 20 wt% short glass fibre reinforced PC, listed in Table 2-1.

Table 2-1 Product descriptions (from datasheets and industrial partner)

Product (LEXAN™)	PC101	PC103R	HF1110	HFD1014	HFD1711	EXL1414T-NA	EXL1414T-BK	MC 500R Resin	20 wt% short glass fibre reinforced PC8
Code	PC1	**PC2**	**PC3**	**PC4**	PC5	PC6	PC7	**PC8**	**PC9**
Melt flow rate (300 °C/1.2kgf)	6	6	25	6	25	10	10	12	
D/B transition temperature (°C)	-30	-30	0	-40	-10	-40	-40		

- All materials are made by injection flow moulding.
- Melt flow rate (MFR) indicates the molecular weight; high MFR means low molecular weight.

- PC1, PC2, PC3, and PC8 are homo-polycarbonate with different MFRs and ductile/brittle (D/B) transition temperatures.
- PC4, PC5, PC6 and PC7 are impact-modified homo-polymer.
- PC9 is 20 wt% short glass fibre reinforced PC8.
- The **bold font** labelled materials in Table 2-1 are used in this research.

PC2, PC3, PC4, PC8 and PC9 were selected for investigation in this research:

- PC2, PC3 and PC8 are homo-PCs with different molecular weights and ductile/brittle transition temperatures. The time-temperature equivalence theory [7] (reviewed in the next section), indicates that low temperatures have similar effects as the high strain rates on the mechanical response of polymer materials. For these materials, lower MFR (higher molecular weight) PC has a lower ductile/brittle transition temperature; thus, comparing the mechanical properties of these three materials may allow us to understand the molecular weight effects at high-rate or low-temperature.
- PC2 and PC4 have the same MFR (molecular weight) but different D/B transition temperatures; comparing these two materials enables us to understand the co-monomer effects on the mechanical properties, especially in high-rate tests.
- PC9 allows us to investigate the role of fibre in different loading conditions.

The chemical structures of the selected resin materials are shown in Fig. 2-2.

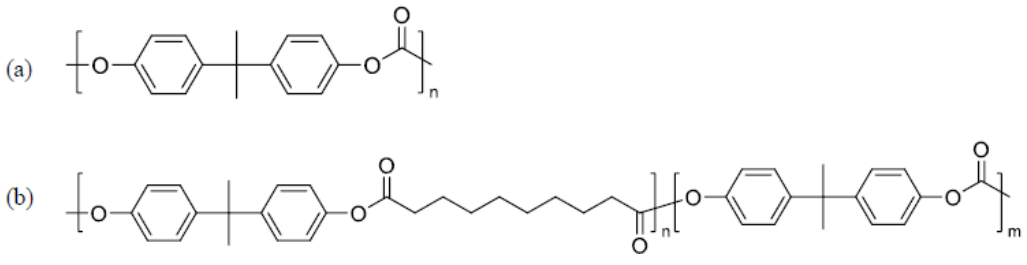

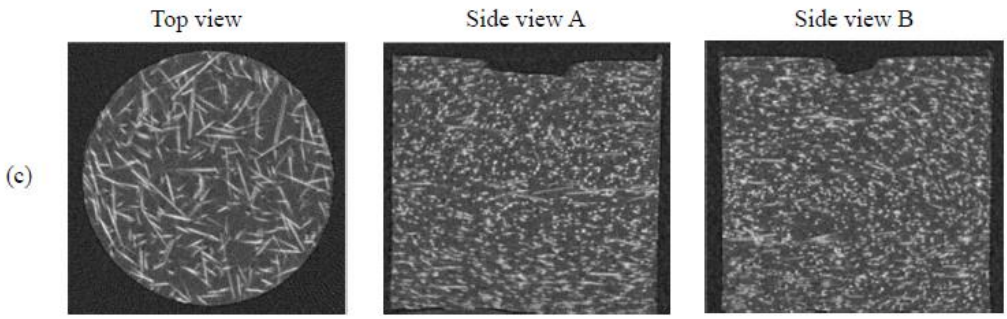

Figure 2-2 (a) LEXAN™ bisphenol A-PC (BPA-PC): PC2, PC3 and PC8 (b) LEXAN™ HFD copolymer, bisphenol A-sebacic acid (BPA-SA): PC4. Graphs are reproduced from [8]; (c) 3D Micro-CT scanning of cylindrical glass fibre reinforced PC (PC9) sample cut in the through-thickness direction

2.1.3 Polycarbonate and polycarbonate composite

Bisphenol A polycarbonate (BPA-PC) products were commercialised in the 1960s in Germany and the United States [9]. Currently, LEXAN, produced by Sabic®, and MAKROLON, produced by Bayer®, are major products in the PC market [9]. Global PC consumption increased from 3.3 x 10^6 tons in 2008 to 4.6 x 10^6 tons in 2013, and the demand for PCs and their composites grew about 10% each year from 1995 to 2010 [10].

PC is an amorphous engineering thermoplastic polymer that is described as having outstanding thermomechanical properties. The advantages of PC products include but are not limited to transparency, high toughness, good electrical insulation characteristics and dimensional stability [9]. The injection moulded commercial PCs usually have a number average molar mass of 22 to 32 kg/mol, and PCs manufactured by extrusion are slightly higher. An increase in molar mass can sharply increase the mechanical properties, such as tensile, flexural and impact, up to a molar mass of around 22 kg/mol, above which they increase more slowly. At the same time, values below 20 kg/mol can lead to brittle fracture and stress cracking, but improve the optical properties [9]. Table 2-2 lists the range of molar masses measured using gel permeation chromatography (GPC) and melt flow rate (MFR) of some commercial PCs.

PC resins do have some shortcomings, such as being brittle under sharp impact loading [10] and sensitive

to scratches [11]. Adding additives, such as fillers, chemical modifiers or polymer blends, is a typical way to improve PC properties.

Table 2-2 Molar mass data for PCs (reproduced from [9])

BPA-PC	Melt flow rate	Number average M_N (kg/mol)	Weight average M_w (kg/mol)
Ultrahigh viscosity	3.1	28.1	72.6
Very high viscosity	4.9	25.4	66.1
High viscosity	6.5	25.4	62.0
Medium high viscosity	7.4	24.4	60.6
Medium viscosity	9.2	23.9	57.0
Medium low viscosity	11.2	22.7	54.5
Low viscosity	16.2	20.4	49.8
High flow	20.9	18.4	46.9
Optical quality	78	13.90	35.8

For blended PC, PC/acrylonitrile/butadiene/styrene (ABS) is one of the most common commercial products. This can inherit the toughness and colourfastness of PC and improve the chemical resistance, processability and notched impact resistance, which are provided by ABS [12-14]. Blends of PC and poly(methyl methacrylate) (PMMA) have received significant attention in recent years [15] because of their application prospects as separation membranes [16], thermal insulations [17] and packaging material [18]. PC/polyethylene (PE) blends are opaque and can be colour-matched in a wide range [10], and this blend can have increased impact toughness compared with PC [19]; the applications of these blends are usually in headgear, sports goods and automotive components [10]. There are many other blended PC, such as PC/poly(vinyl chloride) [20], PC/polyurethane [21], and PC/poly(ethylene terephthalate) [22], and due to their different mechanical performances, they are applied in various engineering applications.

Besides mixing with blended polymers, adding reinforcement material is another way to improve resin performance. Introducing nanofillers, such as carbon nanotubes (CNTs) [23] and graphene [24], can improve the mechanical, electrical and thermal properties of the PC matrix. Some metal powders, like silver powder

[25] and aluminium power [26], enable PC to become electrical conductors. Furthermore, nanoclay-PC composite can increase the wear resistance and reduce the friction of PC resin [27]. Adding carbon fibre is also a common way to improve the mechanical properties, such as stiffness, strength and creep resistance of PC resin [28, 29]. With the development of production technology, the industry can combine different blends, reinforcements and nanofillers according to different engineering applications.

Table 2-3 Effects of glass content on PC composite properties, reproduced from [10]

Properties	Units	0% glass	10% glass	20% glass	40% glass
Density	g/cm^3	1.2	1.27	1.35	1.52
Tensile strength	MPa	62	66	103	138
Tensile modulus	GPa	2.3	3.4	5.5	11.0
Elongation to break	%	130	6.0	3.7	2.3
Izod-notched impact	J/m	850	134	144	218

Glass fibre (GF) reinforced PC is the most relevant material to this research. Adding glass fibres can increase stiffness, strength [30] and wear resistance [31, 32] but adversely affect impact resistance compared with PC resin [9]. The preferred and typically used glass fibres are E-glass fibres, which are alkali-free aluminium borosilicate; the length and diameter of fibres used in the product are usually from 100 to 300 μm and 8 to 14 μm, respectively; the weight percentage (wt%) of glass fibre can be up to 40% [9, 10]. Table 2-3 lists some mechanical properties relevant to this project, and these data are reproduced from the review literature [10]. The PC composites with 5 to 30 wt% GF are often used for structural applications manufactured by injection flow moulding [10], allowing high-quality products to be moulded with very complex shapes quickly [33]. In this research, PC composite is manufactured by injection flow moulding and reinforced by 20 wt% E-glass fibre with a length from 100 to 200 μm and fibre diameter from 10 to 20 μm.

2.2 Rate and temperature-dependent of PC

The main aim of this project is to understand the thermomechanical behaviours of polycarbonates and their composite, thus, the mechanical performances of PC and this type of amorphous polymer, such as PMMA [34] and PVC [35], will be emphasised. Characterisation of the mechanical response of PC has been performed for many decades. In 1972, Bauwens *et al*. [36] revealed the stress-strain relationship of PC through different low-rate uniaxial compression and tensile tests from low to high temperature. The experimental results initially demonstrated the temperature and rate sensitivity of such materials, but this research stayed in the quasi-static stage because of the experiment apparatus limitations. Walley *et al*. [37] used the direct impact Kolsky bar to test the high rate response of polymers, such as PC and PA 6, at the compressive rate of 20,000 s^{-1}. Moreover, further development of the Split Hopkinson Bar, focusing on improving experimental techniques for brittle and soft materials, has enabled the measurement of dynamic responses of low-impedance materials science in the 1990s and early 2000s [38-40].

Investigation of the dynamic compressive response of PC was carried out by Bauwens *et al*. [41], Mulliken *et al*. [42], Siviour *et al*. [43] and Richeton *et al*. [44, 45]. They summarised previous work and studied the integrated compression response of the PC. Kendall and Siviour [46] and Safari *et al*. [47] increased the strain rate to 6400 and 10,000 s^{-1}. In dynamic and quasi-static experiments, PC presents viscoelastic properties at small deformation until the stress-strain curve reaches the first peak (yield point). After yielding, strain-softening is observed; strain-hardening is seen as the strain increases further. When the PC is characterised at varying temperatures, the stress-strain behaviours observed are similar to those under different loading rates [42, 43]. Furthermore, PC shows rate and temperature sensitivity like many other polymeric materials, this is reflected in (1) the modulus and yield stress of PC will increase with the increasing strain rate or decreasing temperature, (2) with the decreasing rate or increasing temperature, the softening process is more significant [34, 43]. It is worth mentioning that in these two early studies [42, 43] on the dynamic compression behaviours

of PC, the researchers all believe that the bilinear increase in yield stress as a function of logarithm strain rate is attributed to the secondary (β) molecular transition of PC; and similar observations are found in rate-dependent tests on PMMA [34, 42] and PVC [35, 48]. At the same time, Siviour *et al.* [43] applied time-temperature equivalence, which indicates that the yield stress increase with an increase in strain rate or decrease in temperature can be related through a simple mapping (Fig. 2-3 (b) and (d)). The basic principle of this theory is similar to time-temperature superposition (TTS), and allows the high-rate behaviour to be linked with quasi-static low-temperature data. The effects of molecular transition on high-rate behaviours and time-temperature equivalence will be discussed later in this research.

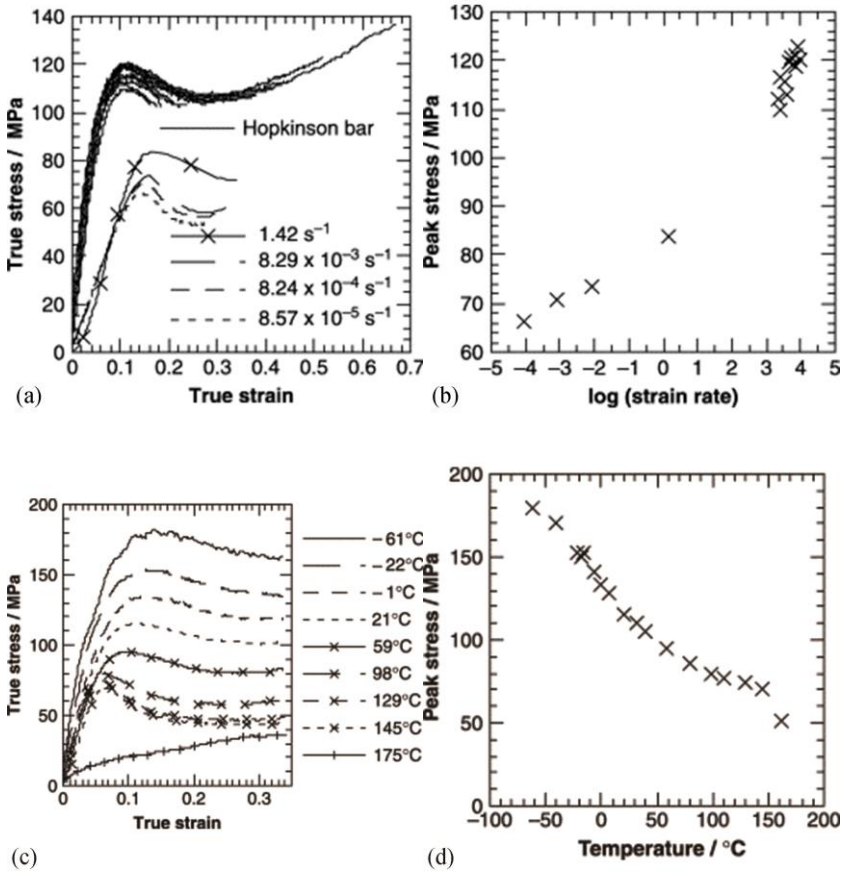

Figure 2-3 (a) Varying rate compression tests at 21 °C (b) Rate-dependent yield stresses at 21 °C (c) Varying rate compression tests at 5500 ± 500 s^{-1} (d) Temperature-dependent yield stresses at 5500 ± 500 s^{-1}. Reproduced from [43].

Boyce *et al.* [49, 50] conducted tensile and compressive tests on PC at room temperature. These

demonstrated that the strain hardening process for the compressive test was induced by in-plane molecular movement. However, in the tensile experiment, the axial molecular motion in the necking area initiated the hardening process. Based on this research, Sarva [51] experimentally and numerically conducted high-rate tensile tests for polycarbonate at room temperature and made the comparison with the high-rate compression tests [42]. This study indicated that the shape of the stress-strain curves of PC obtained from dynamic compressive and tensile tests was similar at low strain but diverged as strain increased, as shown in Fig. 2-4. At the same strain rate, the tensile yield stress is lower than the compressive yield stress, which indicates that the PC is sensitive to pressure. Secondly, the strain hardening in the tensile test occurred earlier than in the compressive test and increased more rapidly. This is due to the different movement and distribution of the internal molecular chain of the polymer under different loading orientations. This explanation was consistent with the theory in [49, 50]. The results showed that the modulus and yield stress of the PC would increase with the hydrostatic pressure growth [52]. However, unlike compression tests, strain localisation always occurs in tensile tests [53-55]; thus, extracting the constitutive behaviour (true stress-true strain) curve in tension tests is difficult.

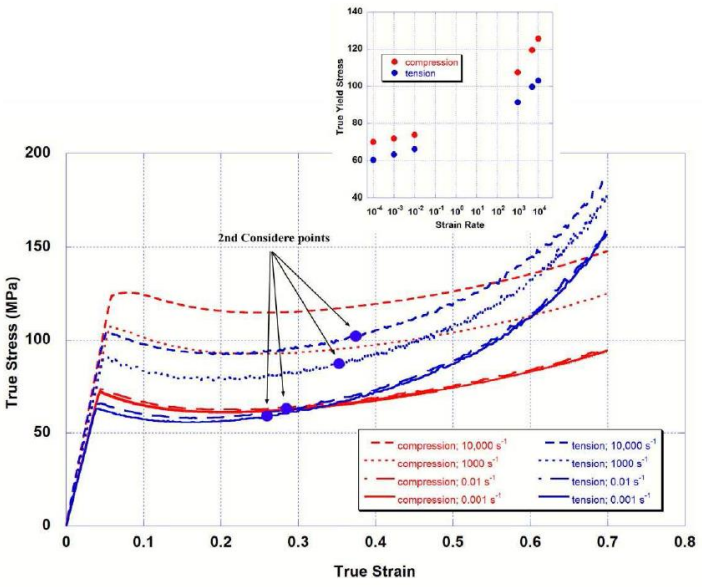

Figure 2-4 A comparison of the simulated constitutive behaviour of PC in tension and compression [51].

2.3 Experimental techniques

It is well known that the mechanical properties of polymeric materials are highly rate-dependent. Many studies have been conducted for PC to understand the temperature-dependent constitutive behaviours at a low rate, and the test techniques at low-rate are already very mature. Therefore, it is essential to characterise the responses of these materials loaded at different strain rates. Fig. 2-5. presents techniques which can be used to test the behaviours of polymers when deformed at a wide range of rates. However, it is a challenge to distinguish whether the captured responses are natural properties of a material or artifacts from the specific loading used [56, 57]

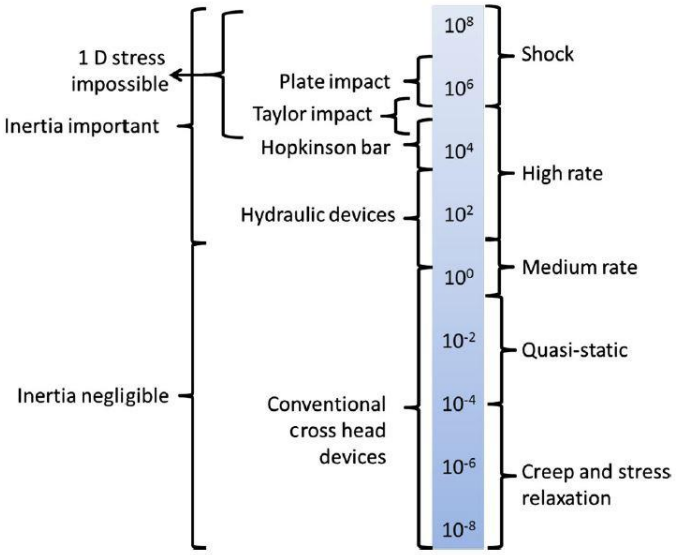

Figure 2-5 The strain rate regimes and their corresponding experimental techniques [56, 57]

In this project (IMPRESS), we will start with 1-dimensional (1D) characterisations from low to high strain rates using conventional crosshead devices, hydraulic devices and Hopkinson bar; then move to the 2D and 3D issues, which are more industrial-relevant scenarios to validate the constitutive model. The research in this thesis aims to understand the large deformation constitutive behaviour (mechanisms) of PCs and PC composite under different 1D loading conditions using new experimental methodologies; thus, three apparatuses are reviewed in detail in terms of uniaxial response: crosshead devices at low rates; hydraulic device at intermediate strain rates and Hopkinson bar at high rates.

2.3.1 Low strain rate tests

Nowadays, for quasi-static (QS) tests, commercial test machines and test standards have been developed to a mature level. The electromechanical and servo-hydraulic systems, such as the Instron Universal Test Machine, can conduct tensile or compressive experiments at rates from 0.0001 to 0.5 s^{-1} with varying temperatures provided by appropriate heating and cooling systems. Because many polymers can be deformed to large strains, true strain and true stress are usually used to understand their constitutive behaviours. In this research, an extensometer was attached to the loading anvils to obtain the strain and reduce rig compliance effects when the higher loads were applied. In addition, an appropriate pre-load was applied to the specimens before the start of each test to improve two aspects of the data: (1) minimise the effects of apparatus expansion or shrinkage when performing temperature-dependent compression tests; (2) remove the 'toe-in' region, which helps to ensure accurate strain measurements under true strain control. The temperature is maintained using an environmental chamber equipped with a heating element or liquid nitrogen for the true strain rate-controlled temperature-dependent characterisation. A digital thermometer with two thermocouples was used to measure the temperature: one connected with the platen to monitor the specimen temperature and another attached to the outer metal part of the load cell to monitor heat exchange into the load cell. Lubricants were applied at different temperature tests to avoid friction and inertia effects for PC based on [58].

The outputs generated from the conventional crosshead machine are typically the displacement, L, and load, F. Moreover, the camera, laser, or extensometer will be equipped in tests to visualise or obtain more actual results. The nominal (engineering) strain, ε_e, and nominal (engineering) stress, σ_e, can be written as:

$$\varepsilon_e = \frac{\Delta L}{L_0} \tag{2-1}$$

$$\sigma_e = \frac{F}{A_0} \tag{2-2}$$

Where L_0 is the original length of the specimen, $\Delta L = L - L_0$; L is the current length of the specimen. F is the

force that can be obtained directly from the universal test machine, and A_0 is the original specimen cross-section area. Assuming the specimen is incompressible, true strain, ε_t, and true stress, σ_t, are defined as:

$$\varepsilon_t = \int_{L_0}^{L} \frac{dL}{L} = \ln\left(\frac{L}{L_0}\right) = \ln(1 + \varepsilon_e) \tag{2-3}$$

$$\sigma_t = \frac{F}{A} = \frac{FL}{A_0 L_0} = \sigma_e(1 + \varepsilon_e) \tag{2-4}$$

In equation (2-3), ε_e is positive in the tension test and negative in the compression test. In equation (2-4), the volume of the specimen is assumed to be constant ($A_0L_0 = AL$), F and A are the current force and current cross-section area; again, tension and compression tests give the positive and negative values in ε_e, respectively. Indeed, volume conservation is an assumption which is not valid when the sample experiences damage and large plastic strain deformation. However, the volume change of polymer under its glass-transition temperature will not significantly affect the true stress calculation, and the true stress-true strain curves are more representative of further analyses in this research.

2.3.2 Medium strain rate tests

It is a considerable challenge to carry out the medium strain rate tests, i.e. in the range from 1 to 500 s^{-1} for all materials, the inertia effect of the loading system should be minimised; thus, the acceleration of the apparatus is required to take place over a short period [56].

The often-used systems are hydraulic machine [59], drop weight [60], or modified Hopkinson bar [61]. These experimental techniques fill the important rate range from 1 to 1000 s^{-1}, in which the molecular mobility is restricted for many polymers [56, 62]. In this research, two machines are used to perform the medium strain rate tests; a self-built hydraulic machine characterises PCs from 1 to 50 s^{-1}, and a long split-Hopkinson bar (LSHPB) can characterise PCs at about 500 s^{-1}. In this section, only hydraulic machine is discussed, and in the next section, SHPB and LSHPB will be discussed because their basic working principle is the same.

Fig. 2-6 shows the custom-built hydraulic compression machine used in this research. The movement of

loading anvils is measured using linear variable differential transformers (LVDTs), and the averaged value of these two LVDTs is used as displacement, which can be used to calculate true strains using the equations in Section 2.3.1. The force is measured using the calibrated force transducer, which is screw-fixed. Before starting the tests, the force transducer should be carefully positioned (tightened) to put a light pre-force on the specimen. If the pre-force is too high, the collected force will be lower than the actual value; however, if the pre-force is too low, it can cause poor contact between the sample and the force transducer.

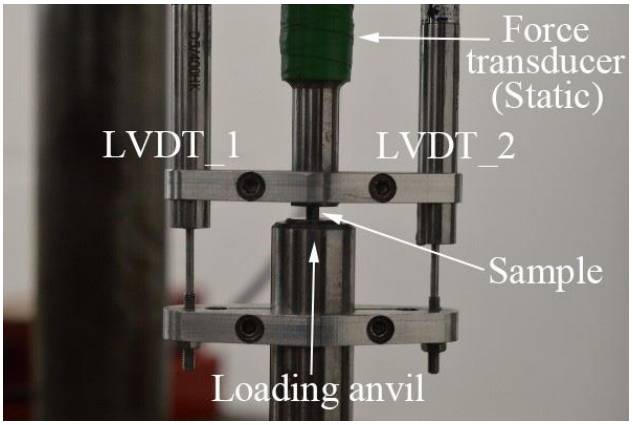

Figure 2-6 Custom-built hydraulic machine for medium rate compression experiments.

2.3.3 High strain-rate test and Hopkinson bar techniques

The Split Hopkinson Bar (SHB) system has been widely used to characterise the uni-axial mechanical properties of materials for the strain rate from 1000 to 10,000 s^{-1}. Hopkinson [63] pioneered using a long metal rod as a pressure bar to character elastic wave propagation in 1914, and this experimental technique was developed by Kolsky [64] in 1949 to investigate the dynamic behaviours of materials. Although there is no standard for dynamic property measurement at loading rates between 100 to 10,000 s^{-1}, the Hopkinson bar experimental technique has been widely used in dynamic tests in tension [65-67], compression [68-71], shear [72], torsion [73], tension-torsion [74, 75], bending [76, 77] and fracture [78, 79].

Fig 2-7 (a) shows a typical split-Hopkinson pressure bar (SPHB) system [56]. During the compressive test, the specimen is placed between the input (incident) bar and output (transmitted) bar, which are

instrumented with strain gauges to measure the propagating stress waves. The input bar is loaded by a strike bar, which is propelled by a gas gun and generates a stress wave. The changes in impedance at the interface between bars and specimen cause part of the wave to be reflected in the input bar (reflected signal) and part to be transmitted to the output bar (transmitted signal), as shown in Fig. 2-7 (a). All three signals are usually measured using strain gauges mounted on the incident bar (incident and reflected signal) and output bar (transmitted signal), and representative voltage-time curves for an SHPB test are demonstrated in Fig. 2-7 (b). The duration of the loading pulse, which indicates the maximum effective strain, is mainly determined by the length of the striker. Thus, the striker length is usually less than half the length of the incident bar to avoid stress wave overlap at the strain gauge on the incident bar. Typically, two strain gauges are located diametrically opposed to each other to cancel out the effects of bending waves. In this research, the gauge on the incident bar is placed in the middle of the bar to isolate the incident and reflected signals better. The gauge on the transmitted bar is placed close to the loaded end edge to achieve a longer transmitted signal (large effective strain). Moreover, gauge signals can be converted into force when the gauges are calibrated.

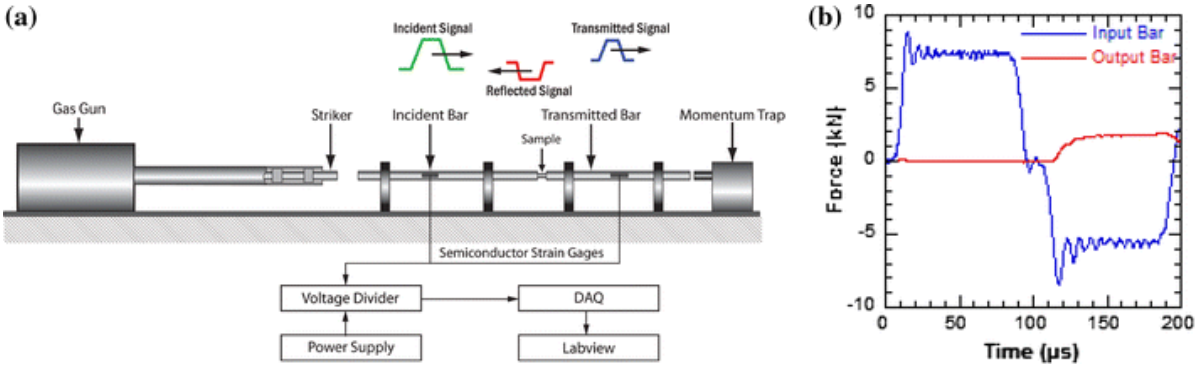

Figure 2-7 (a) Schematic of split Hopkinson pressure bar (SHPB) system (b) Voltage-time curves in SHPB test. Reproduced from [56].

First, the voltage signals are converted force:

$$F = \textit{gauge signal/amplification factor/calibration factor} \tag{2-5}$$

Then, the force equilibrium at the two bar-specimen interfaces, F_1 and F_2 (Fig. 2-8 (a)), should be checked.

$$F_1 = F_I + F_R \tag{2-6}$$

$$F_2 = F_T \tag{2-7}$$

F_I, F_R, and F_T are the incident, reflected and transmitted forces. Usually, the engineering plastic (i.e. PC, PMMA) should show the force equilibrium ($F_1 \sim F_2$) in SHPB tests, as Fig. 2-8 (b). Some soft matter, such as elastomers, it is difficult to achieve equilibrium because of the very low impedance. At the same time, the velocities at the end of the incident and transmitted bar, v_1 and v_2, can be calculated based on the density (ρ), wave speed (c), and cross-section area (A_b) of the bar.

$$v_1 = \frac{F_I - F_R}{\rho c A_b} \tag{2-8}$$

$$v_2 = \frac{F_T}{\rho c A_b} \tag{2-9}$$

$$c = \sqrt{\frac{E}{\rho}} \tag{2-10}$$

where E is Young's modulus of the bar. Typically, incident and transmitted bars will use the same material; however, equation (2-10) can be modified if different bar material is selected.

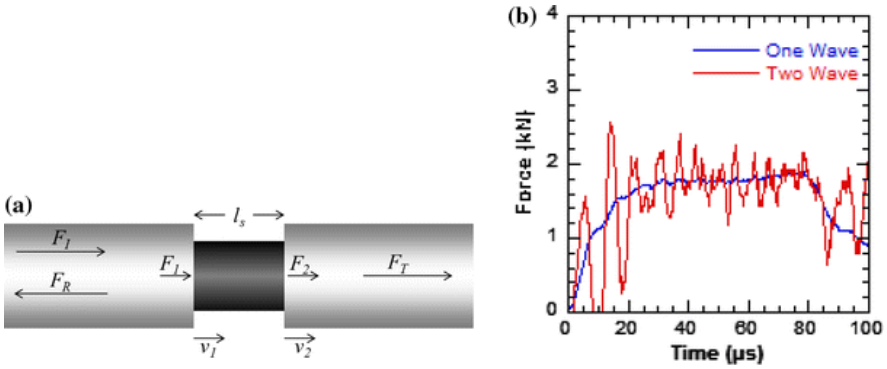

Figure 2-8 (a) Forces, displacements and velocities at the bar-specimen interfaces (b) Comparison of forces calculated from the output signal (one wave) and the difference between the incident and reflected signal (two wave) analyses [56].

Being based on the stress (force) equilibrium, as Fig. 2-8 (b), the one and two wave stress can be calculated:

$$\sigma = \frac{F_T}{A_s} \tag{2-11}$$

$$\sigma = \frac{F_I + F_R}{A_s} \tag{2-12}$$

where the stresses are engineering stress, and A_s is the constant initial specimen area, it is usual to use the first of these expressions, as calculation of F_I involves finding the difference of two similar numbers: the output can be noisy.

The engineering strain and strain rate can be calculated by integrating the bar speeds, given by:

$$\dot{\varepsilon} = \frac{v_1 - v_2}{l_s} \tag{2-13}$$

$$\varepsilon = \frac{\Delta l}{l_s} \tag{2-14}$$

For polymeric materials, the semiconductor strain gauge is often recommended [56] because it has a large gauge factor of about 140, which enables accurate measurement of the small input signal [80]. Only using a foil gauge with a gauge factor of about 2, which is usually used for metallic specimens, can cause the transmitted signals that cannot be distinguished from noise. Furthermore, piezoelectric gauges can be used to enhance the sensitivity of the input force for soft materials [81].

Modifying the bar itself, such as changing its material, length and shape, also improves the signals obtained from low strength specimens. Chen *et al.* [82] used hollow, aluminium transmitted bars to reduce the cross-section area and impedance of the bar to increase the transmitted signal. Moreover, light metal, such as titanium alloy [83], magnesium alloy[84] and aluminium alloy [82], or polymeric bars, such as PMMA and PC [85-87], are possible selections as low impedance bar materials to characterise polymers. To achieve the large strain, the length of the SHPB system can be increased, called long split Hopkinson bar (LSHPB), allowing a longer pulse duration [88].

SHPB sample design is challenging because there is no standard, and it should obey the assumptions made for SHPB tests: (a) the specimen deforms uniformly (no friction or inertia effects); (b) static stress equilibrium, indicated by force equilibrium at the specimen-bar interfaces; (c) specimen is loaded in a uniaxial stress

condition [89]. Gray III [90] suggested that minimizing the area difference between specimen and bars can reduce the impact of radial and longitudinal inertia and friction, and the ratio between specimen length and diameter is recommended to be from 0.5 to 1. Gray III [90] pointed out that static stress equilibrium cannot be achieved until 1% plastic strain, thus, it is impossible to measure the dynamic compressive modulus using SHPB. However, the thinner specimen (specimen length-diameter ratio less than 0.5) can be used to reduce the stress nonequilibrium in the specimen [89]. Siviour and Jordan [56] suggested that the maximum length of specimen for glassy polymer is about 5 mm and less for rubbery polymers to shorten the stress equilibrium time. Thus, the design of SHPB samples needs to be adjusted appropriately based on different testing materials, different SHPB systems, and testing requirements while meeting the basic guidelines.

Some other components can be used to provide positive effects on SHPB tests. A suitable pulse shaper (usually a thin layer metal) can reduce strain rate rise time in the specimen and provide a ramp-shaped incident pulse, which can theoretically generate a constant reflected pulse to achieve the constant strain rate [89, 90]. At the same time, the pulse shaper can reduce the oscillations due to wave dispersion in the bar [56]. Lubrication is important in all compression tests, especially in polymer high-rate tests. The thin polymer specimen is often required because of the low sound speeds, and the large diameter might also be needed because of the low strength. Therefore, the ratio between the length and diameter of the polymer specimen is small, which can result in frictional effects during high-rate tests. Moreover, the friction between specimen-bar interfaces can lead to barreling, which can cause stress inhomogeneity and overmeasure the strength of the material [56, 91]. Thus, depending on different samples, adequate lubrication should be used in high-rate tests, such as petroleum jelly [58, 92] and molybdenum disulphide grease [93]. Again, the pulse shaper and lubrication selection should be according to the characterised material and test facility on the premise of achieving the basic SHPB test criteria.

2.3.4 Differential scanning calorimetry

Differential scanning calorimetry (DSC) is a widely used thermal analysis technique that can measure how thermal properties of a sample change, along with time and temperature. This is achieved by measuring the difference in heat flow rate to a small pan containing the sample and an empty reference pan while they experience the same, controlled temperature profile [92]. Fig. 2-9 shows a schematic of a typical heat flux DSC machine; the heating block contains the heater, sensors and the holders where the sample and reference pan are placed. During the test, the furnace supplies the linear heating or cooling rate, and the purge gas flows through the cell [93]. The heat flow rate ($\dot{Q}$) can be determined by:

$$\dot{Q} = \frac{\Delta T}{R} \tag{2-15}$$

where ΔT is the temperature difference between the sample and the reference sensors, and R is the thermal resistance of the heat leak disk.

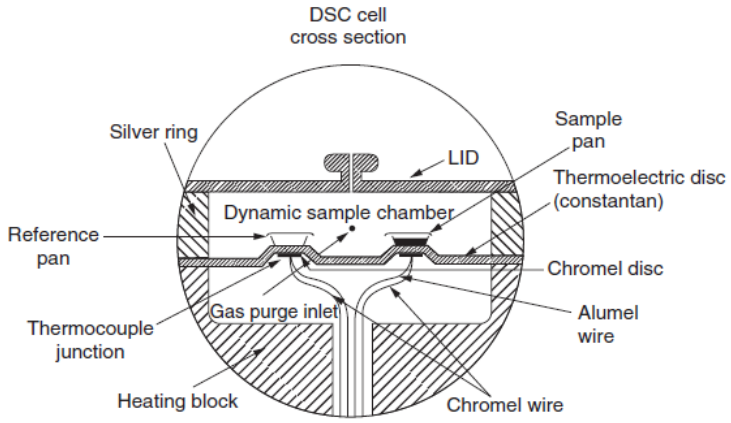

Figure 2-9 Cross section of a TA Instrument heat flux DSC machine [93].

Fig. 2-10 shows an example of a DSC curve, which plots heat flow as a function of temperature or time.

The enthalpy change is the most important part of the DSC measurements. The change in enthalpy is measured based on the heat flow rate ($\dot{Q}$) from a baseline which indicates no transition or reaction is occurring. The enthalpy-increasing (endothermic) processes are glass transition, melting and evaporation, and the enthalpy-decreasing (exothermic) processes are crystallization, curing and degradation (decomposition) [94].

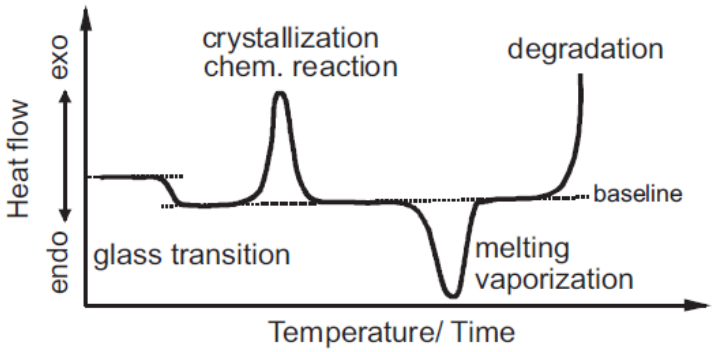

Figure 2-10 A typical diagram of the DSC curve [94].

In literature [95], the applications of DSC machine are summarised as follows:

- Detect melting, crystallisation, and transition temperatures;
- Measure the crystallinity of semi-crystalline polymers;
- Characterise decomposition temperature or thermal stability;
- Measure specific heat;
- Test degree of curing in resin.

Based on the traditional DSC, some methods have been developed according to different experimental requests. Heat-cool-reheat DSC is developed to understand or erase the effects of thermal history by heating the sample above its glass-transition temperature, where relaxation or molecular rearrangement can occur, then cooling at a known rate before heating again [96]. Thus, the difference between similar materials in the reheat curves is real internal differences, such as molecular weight, rather than the thermal history effects. Hasan and Boyce [97] and Lin et al. [98] performed DSC tests for large compression-strained PC samples to investigate the energy distribution. More recently, Flash-DSC has been developed to measure heat flux with a much faster heating or cooling rate than traditional DSC. Shamim *et al.* [97] measured the heat flow rate of polycarbonate using the heating rate from 1 to 1000 K s^{-1}, and the results indicated that a higher heating rate can increase the glass-transition temperature of PC.

Modulated different scanning calorimetry (MDSC) is a family of DSC in which the temperature is

modulated on a linear heating and cooling rate [98]. MDSC usually heats the sample using sinusoidal temperature modulation, as shown in Fig. 2-11. It can generate total heat flow as traditional DSC and separate the heat flow into reversing and non-reversing signals [93]. The reversing curve represents changes in heat capacity, C_p, relevant to the glass transition: the α-transitions can be detected easily in this curve. The non-reversing signal gives information about events with kinetic dependence, such as enthalpy relaxation, crystallisation, decomposition and cure [93].

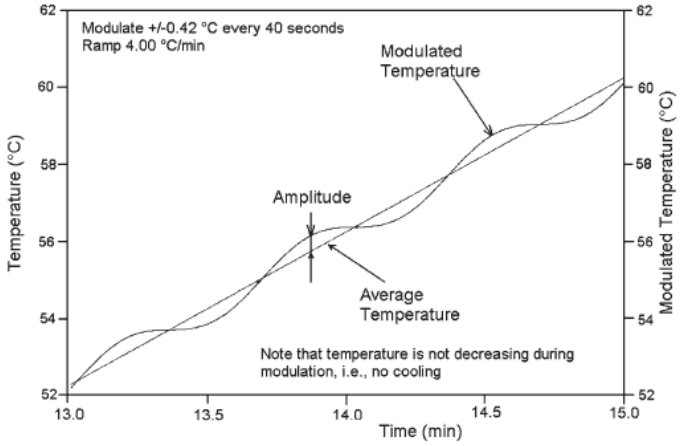

Figure 2-11 Modulation of the temperature around an average heating rate for a modulation [93].

The heat flow rate $\dot{Q}$ can be written as:

$$\dot{Q} = C_p \frac{\mathrm{d}T}{\mathrm{d}t} + f(t,T) \tag{2-16}$$

The sample's heat capacity mainly determines the reversing heat flow, and some transitions also contribute to the reversing heat flow, which responds directly to changes in the ramp rate, and the events are reversing at the time and temperature. At the same time, the thermal events that do not respond to changes in the ramp rate are observed in the non-reversing heat flow [93]. The reversing C_p can be calculated as:

$$C_{p,rev} = K \times heat\ flow\ amplitude/heating\ rate\ amplitude \tag{2-17}$$

where K is the calibration constant for reversing heat capacity, and the amplitude of the heat flow signal can be obtained using the Fourier transform. Thus, the reversing heat flow is:

$$Reversing\ heat\ flow = C_{p,rev} \times underlying\ heating\ rate \tag{2-18}$$

Following that, the non-reversing heat flow can be calculated from the difference between the total heat flow and the reversing heat flow:

$$Nonreversing\ heat\ flow = Total\ heat\ flow - reversing\ heat\ flow \quad (2\text{-}19)$$

Fig. 2-12 shows the total, reversing and non-reversing heat flow curve of quenched poly (ethylene terephthalate) (PET) measured by MDSC. More recently, Trivedi and Siviour [99] used the reversing C_p obtained from MDSC to successfully predict the temperature rise of plasticised PVC in the SHPB test.

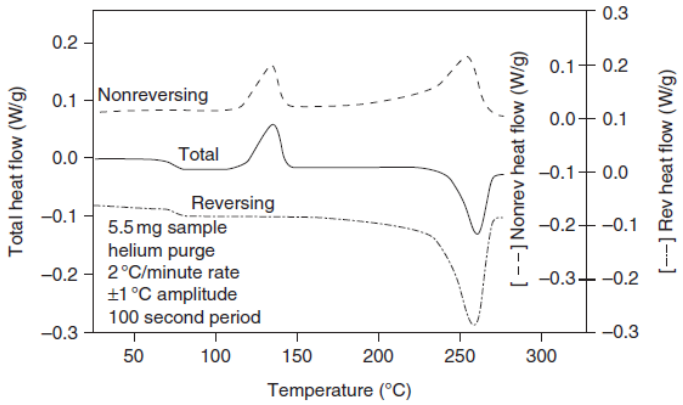

Figure 2-12 The total heat flow, reversing and non-reversing heat flow for quenched PET measuring from MDSC [93].

2.3.5 Dynamic mechanical analysis

Dynamic mechanical analysis (DMA) is a technique that is more sensitive to glass transition than DSC and can provide other localised transitions (secondary- or tertiary-transition) that cannot be detected in DSC [100]. Moreover, DMA can measure the modulus and viscosity of polymeric materials as a function of temperature, strain and frequency [101]. Fig 2-13(a) shows a schematic of the most popular type of DMA machine, forced frequency, where the signal is applied at a set frequency. Commercial DMA systems can use different loading modes, such as tension, compression, dual/single cantilever beam, three-point bend and shear [101, 102], whilst single cantilever beam mode (Fig. 2-13((b)) is suggested to be used for thermoplastics [102]; the three-point bend mode (Fig. 2-13(c)) is suitable for composites [102] and PC [103-105].

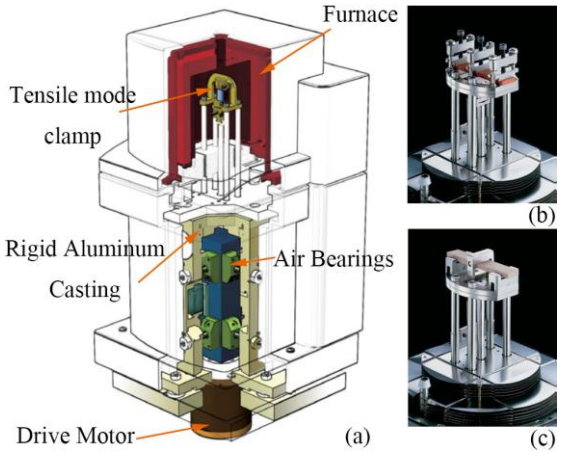

Figure 2-13 (a) Perspective view of TA Q800 DMA machine (b) Single/Dual cantilever beam fixture (c) Three-point bend fixture. Reproduced from [106].

Fig. 2-14 illustrates the theory of forced frequency derived DMA. The oscillating force is applied to the sample sinusoidally; correspondingly, the sample will be deformed sinusoidally. For viscoelastic materials, the strain wave shape will be determined by the viscous and elastic components presented as in-phase and out-of-phase, respectively. The main results of the DMA tests are the temperature (T), storage modulus (E', elastic component), loss modulus (E'', viscous component) and frequency (f). Together, they can be written as dynamic moduli or complex moduli:

$$E^*(T,f) = E'(T,f) + iE''(T,f) \tag{2-20}$$

Another important parameter is loss tangent, which indicates the ratio between dissipated energy to stored energy per deformation cycle, and it is defined as:

$$\tan\delta\,(T,f) = \frac{E''(T,f)}{E'(T,f)} \tag{2-21}$$

It is the phase angle as shown in Fig. 2-14, and its value is from zero (pure elastic solid) to infinity (pure liquid).

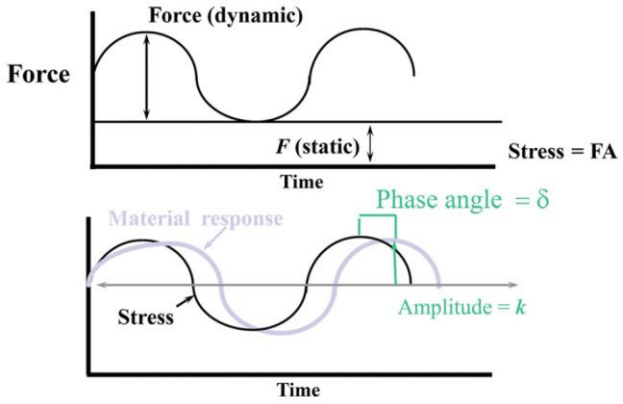

Figure 2-14 Example of oscillating stress applied to a polymeric sample [100].

As an example, the dependence of storage modulus on temperature for typical polymers is shown in Fig. 2-15. At low-temperature regions, the molecule is tightly compressed; with an increase in temperature, the 'free volume' increases giving whole side chains and localised groups enough space to move, causing a decrease in modulus. This phenomenon is typically called the β-transition [107] (other lower temperature transitions may also occur). This transition, below the temperature of use, gives polymers toughness. On further heating, the glass (α)- transition occurs, as the large motion assigned to main chains in the amorphous region is allowed, this leads to a significant reduction in modulus and the onset of rubbery behaviour.

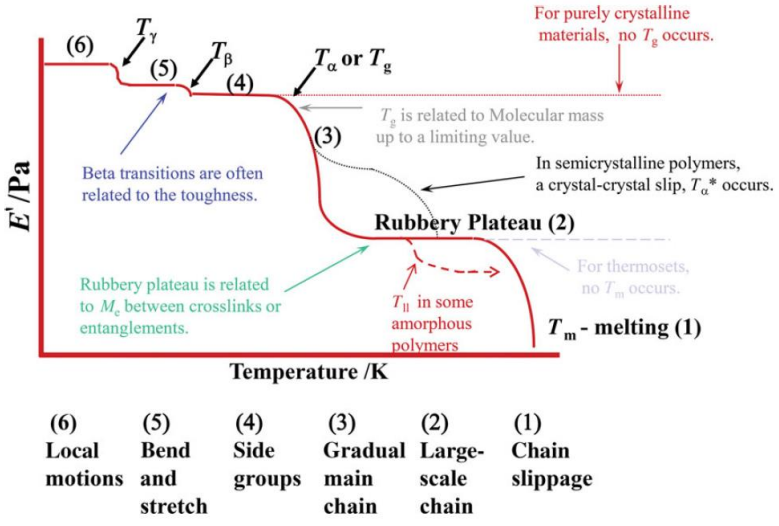

Figure 2-15 Idealised dependence of polymer modulus on temperature [100].

For comparison to other mechanical properties, especially rate-dependent properties, the frequencies in DMA experiments can be converted to strain rates using the following equations:

$$\dot{\varepsilon} = 2\pi f \tag{2-22}$$

$$\dot{\varepsilon} = \frac{\Delta\varepsilon}{\Delta t} = \frac{\varepsilon_0}{1/4f} = 4f\varepsilon_0 \tag{2-23}$$

Equation (2-22) is obtained using the Cox-Merz rule [108]; Equation (2-23) is provided in [56] and proposed by Mulliken and Boyce [42], where ε_0 is the applied strain. It should be noted that these are approximate strain rates depending on the different sample geometries. However, the change in mechanical performance of a polymer a function of the logarithm of frequency or strain rate, and being based on this log-scale dependence, the effect on the anticipated mechanical response of an error in the approximation of strain rate will be small. The following section will give more detailed information on the frequency sweep DMA, and the data analysis approaches will also be discussed.

2.4 Time-temperature superposition

2.4.1 Theory of time-temperature superposition

Time-temperature superposition (TTS) was first noticed in a study of the viscoelastic behaviours of polymers [109] in the late 1930s. Afterwards, further studies indicated that the TTS could be implemented using molecular relaxations or transitions [110]. The basic concept of TTS is that the elastic moduli increase with the increase in loading rate but decrease with an increase in temperature, which means that the increase in strain rate and the temperature have a reverse effect on the mechanical performance of polymers [111]. Bauwens-Crowet and co-workers investigated the rate- and temperature-dependent properties of PVC [112], PC [36, 112-114] and PMMA [115]; these studies first provided an insight into two molecular processes (α- and β-transitions), which were represented at the rate- and temperature-dependent yield stress in glassy polymers. These observations allow us to plot a master curve to predict the mechanical responses beyond the experimental test regime (this part will be discussed later). Afterwards, Walley and Field [116] performed rate-dependent tests for seventeen engineering plastics, which include semi-crystalline and amorphous polymers, up to 10, 000 s^{-1}, and the tests with strain rate above 1000 s^{-1} were conducted using a direct impact Hopkinson bar. Most plastics exhibited that the yield stress increases more rapidly at the high rate region compared with yield stresses at a low-rate regime, which enhanced the two molecular processes theory.

Based on the TTS, Siviour *et al.* [43] proposed an approach to find the equivalence between temperature and strain rate, thus, the high-rate performance can be represented using low-temperature data. In this work, a linear relationship between temperature and rate was proposed as follow:

$$T = T_0 + A(\log\dot{\varepsilon}_0 - \log\dot{\varepsilon}) \tag{2-24}$$

where A is a temperature-strain rate equivalence parameter that can be obtained by fitting temperature- and rate-dependent yield stress; at the same time, it can also be obtained or validated using shift factors from the DMA experiment [35]. T_0 and $\dot{\varepsilon}_0$ are referenced temperature and strain rate, and T and $\dot{\varepsilon}$ are target temperature

and strain rate. This approach has been applied to PVDF [43], PTFE [117] and particulate composites [118].

Another time-temperature equivalence approach was pioneered by Mulliken and Boyce [42], a method named 'Decompose/shift/reconstruct' (DSR), which was used to predict the storage modulus of PC and PMMA at temperature and strain rates well beyond the DMA device regime. The innovation of the DSR method was to separate the effects of the α- and β-transitions on the modulus into two components, then shift them individually with frequency, and finally add them together.

Both Siviour's mapping [43] and the DSR method [42] are related to the DMA experiments, and they can predict the rate-dependent viscoelastic behaviour (i.e. yield stress) far beyond the DMA frequency regime for many polymeric materials in the past two decades. However, these two methods are limited in their ability to predict large strain deformation at high-rate. At high-rate tests, the conversion of plastic work to heat occurs much faster than the heat dissipating speed, which will result in thermal softening, and it is not truly representative of the constitutive behaviour of materials [56]. The following section will discuss the use of DMA data to predict the high-rate behaviour, and the effects of adiabatic heating on material behaviour and heat measurement techniques will be addressed later in this research.

2.4.2 DMA frequency sweep and data processing

Fig. 2-16(a) shows a temperature-dependent storage and loss modulus for polycarbonate obtained from the frequency sweep DMA test (0.2, 1, 2, 5, 10 Hz) with a single cantilever beam configuration. As discussed previously, the secondary (β)- and glass (α)-transition of PC can be distinguished in these curves, and the storage moduli exhibit more rate-dependent in the transition region. Instead of plotting the storage modulus against temperature, Fig. 2-16(b) presents the moduli versus the log frequency, and then, these curves can be used to construct a master curve. Although there are many methods to construct a master curve, such as Matlab code developed by McGill University [119], BSI standard [120] and the manual shifting method [83, 121], the basic principle of TTS curve shifting is similar. The isotherms above the reference temperature are shifted to

the left-hand side (lower frequency), and the isotherms below the reference temperature are shifted to the right-hand side (higher frequency), and the constructed master curve is shown in Fig. 2-16(c). Each segment must overlap with the previous, and it can be seen that the scope of rate-dependent modulus in Fig. 2-16(c) is far beyond the DMA tests. The numerical amount of shifting required is called the shift factor, log (a_T), in Fig. 2-16(d). The total shifted factor is accumulated by the sum of each local shift factor that overlaps the isotherms with its neighbour, and it can be presented as:

$$\log(a_T) = \log(f_{ref}) - \log(f_n) \tag{2-25}$$

where f_{ref} is the reference frequency, in this case, 20 °C is defined as a reference temperature, and log (f_{ref}) at 20 °C should be zero. f_n is the shifted frequency needed to shift the isotherms to adjacent lines based on the reference curve. No matter the distance between the isotherm and the reference line, the same procedures can be used incrementally to overlap the reference curve.

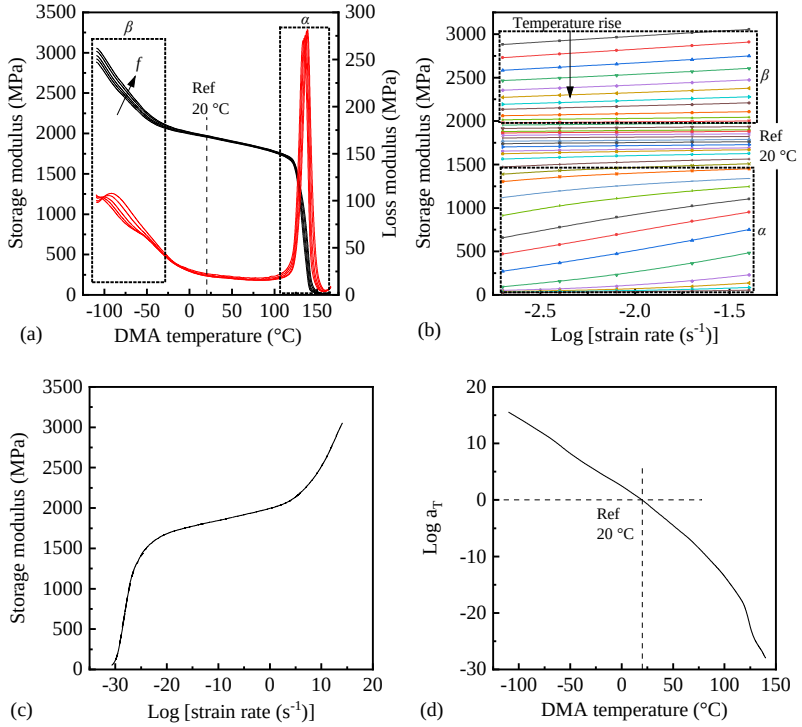

Figure 2-16 Frequency sweep DMA test PC using single cantilever beam configuration (a) Storage modulus and loss modulus versus temperature (b) Isotherms showing the dependence of modulus on frequency and temperature (c) Master curve constructed at a reference temperature of 20 °C (d) Shift factor

versus temperature curve. Data from [122].

There are two well-known methods to fit the shift factor-temperature curve: the Williams, Landel and Ferry (WLF) equation [123] and the Arrhenius equation [124]. The WLF equation is more suitable for describing behaviours above the glass transition (T_g), and the Arrhenius plot is appropriate to fit the shift factor-temperature curve below T_g for amorphous glassy polymers [125]. In addition to constructing the master curve, the DMA data can be used to calculate the frequency-dependent molecular relaxation energies. In this case, Tan delta obtained from frequency sweep DMA is used as an example to show the calculation processes of β- and α-transition energies. Here, the modified Arrhenius equation was employed to calculate the activation energy of both relaxations,

$$\ln(f) = \ln A - \frac{E_a}{RK} \tag{2-26}$$

where f is frequency, A is the preexponential factor, E_a is the activation energy, R is the gas constant, and K is the absolute temperature. If the logarithms are taken to the base 10, the gradient of the log(f) vs $1/K$ is:

$$k = -\frac{E_a}{2.303K} \tag{2-27}$$

k is the slope in Fig. 2-17(c), and the activation energies of two transitions of PC can be calculated.

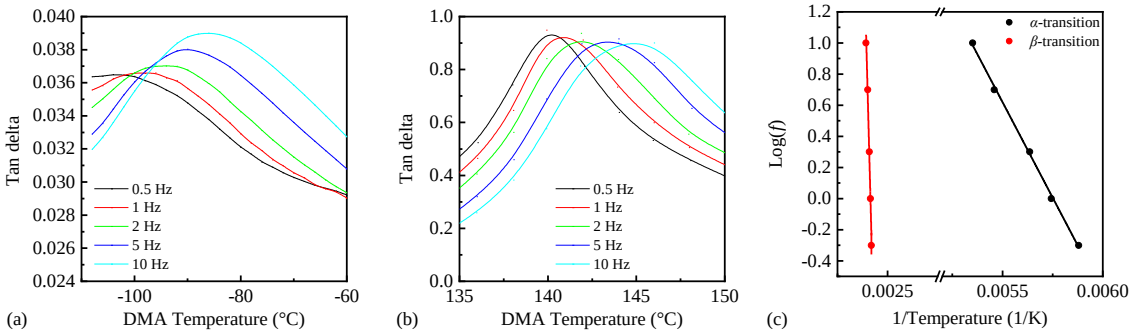

Figure 2-17 (a) Detail of β-transition (b) Detail of α-transition (c) Arrhenius plot for β- and α-transitions. Reproduced from [122].

2.5 Additional measurement techniques and analysis

Besides the above-mentioned experimental techniques and processing approaches, more measurement techniques can be added to provide more useful experimental information. This section will review the digital image correlation system, the approaches to *in-situ* temperature measurement and synchrotron X-ray imaging.

2.5.1 Digital image correlation system

Digital Image Correlation (DIC) is a non-contact optical measurement technique used to analyze the full-field surface deformation and motion of objects [126]. This technique has been developed for about four decades since 1980s [127-129], and the use of DIC techniques experienced explosive growth from 2000 to 2009; to date, this technique has been widely commercialised and applied to metals [130], polymers [54, 131, 132], composites [133] and biological materials [134], from microscopic [135] to macroscopic, from local to global [54, 131], from static to dynamic [53, 136]. If the deformation is not planar (i.e. three-dimensional (3D) deformation), 2D-DIC might not be appropriate, and a 3D or stereo-DIC is required [126]. Because this research aims to understand the uniaxial deformation mechanisms, only 2D-DIC will be reviewed here.

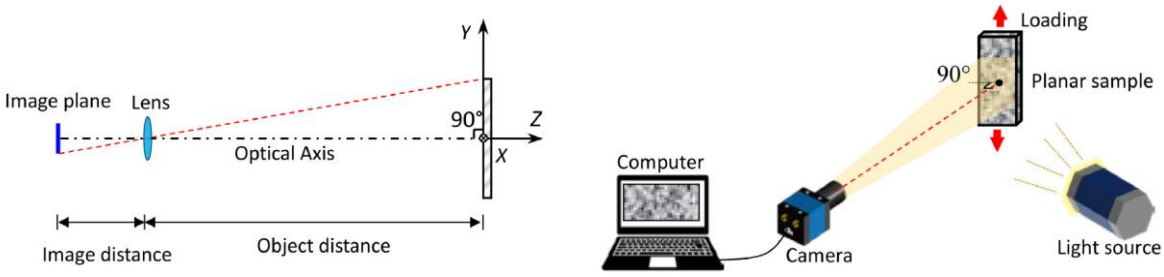

Figure 2-18 Typical 2D-DIC image acquisition setup [126].

Fig. 2-18 presents a typical 2D-DIC setup for image acquisition of planar deformation, and the processes of this system generally have the following three steps:

1. ***Speckle pattern on the sample surface for tracking.*** A good speckle pattern should meet (a) **High contrast:** varying grayscale intensities, and relatively large intensity levels [137]; (b) **Randomness:** to guarantee the presence of recognisable patterns in various areas [138]; (c) **Suitable size:** having an average size of 3-7

pixels to avoid aliased effects [139]; (d) **Stability:** pattern can be stretched during the sample deformation process without cracking; pattern should not affect the properties of the sample; pattern should adhere very well with the sample surface. For engineering plastics, water-based ink can satisfy these requests.

2. ***Capture images of the sample during deformation.*** The accurate timing (triggering) control is very important for image acquisition, especially in high-rate tests. For low-rate tests, the commercial universal test machine can be programmed to control the triggering of the camera. For high-rate tests, the oscilloscope can be used to trigger the camera with an external loading configuration.
3. ***Displacement and strain field calculation.*** The basic calculation principle of 2D-DIC is tracking the same acquisition point or pixels between the reference image and deformed images [126], illustrated in Fig. 2-19 [140]. Here, u and v are the displacements between a point, $P(x_0, y_0)$, at the centre of an undeformed subset (a portion of the pattern) to the same point, $P(x'_0, y'_0)$, at a deformed subset. The position of the target subset centre is obtained by searching the peak position of the distribution of the correlation coefficient [140]. Thus, the displacement field-related results, such as displacement, strain, velocity and strain rate, can be mapped.

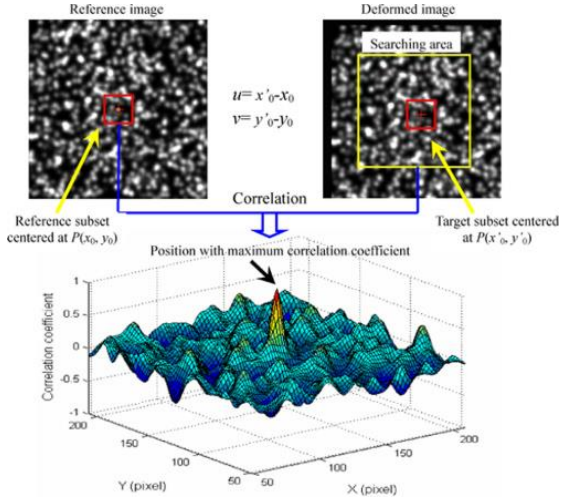

Figure 2-19 Schematic of tracking the reference subset in the deformed image using DIC [140].

Before processing the acquired images, the following components should be defined:

1. ***Correlation criterion.*** Correlation criteria must be defined in advance to evaluate the difference

degree between the reference and deformed subset [140]. The correlation criteria can be divided into two main groups: cross-correlation (CC) and sum-squared difference (SSD) correlation, and the CC criteria are related to the SSD criteria [141]. MatchID [142] summarised the application scenarios for the four most used criteria: (a) Normalized SSD (NSSD): accounts for scaling in intensity and can compensate for an offset in the image contrast; (b) Approximated NSSD (ANSSD): similar to NSSD, more faster and more robust to intensity scaling variations; (c) Zero-Normalized SSD (ZNSSD): Accounts for offset and scaling in intensity variations. Slower but performs much better on image contrast variations; (d) Zero-Normalized CC (ZNCC, equivalent to ZNSSD): CC alternative that accounts for offset and scaling in intensity variation.

2. ***Interpolation scheme.*** It is a method for creating a continuous signal from discrete pixel positions. There are two main categories: splines and polynomial interpolation. Bilinear interpolation is a fast method but lacks accuracy. Local splines use a small kernel to solve the interpolation, while global splines take into account the entire image [142]. Local splines are generally faster and require less computational cost, however, polynomial interpolation is recommended because they can provide higher accuracy and better convergence character.[143, 144].

3. Subset and step size. The subset size is the width and height of the subset square in the reference (undeformed) image, and the step size is the distance between subset centres, which are measured using pixels. The most important rule of subset size determination is that each subset should have at least three speckles [145]. A larger subset has a large area with more unique features, and a smaller subset has a better spatial resolution; moreover, the large subset size needs more computation time. The step size significantly affects spatial resolution more than the subset size. Smaller step sizes can generate more data points, resulting in higher spatial resolution [145], but need more computation time. At the same time, the large steps are faster than the smaller steps, but have poor sampling, and

it is difficult to get accurate DIC results at the edge or hole area [142].

4. ***Shape function.*** The different shape functions should be selected carefully depending on the different displacement fields. (a) The zero-shape function is selected for the rigid body, which indicates that the displacements of each data point in the subset are the same [141]. An affine (first order) subset can describe a linear varying displacement field, such as translation, rotation and shearing [141, 142]. The second-order shape function was introduced in [146] to describe more complex deformation fields (i.e. bend).

Nowadays, the DIC technique has been highly integrated, and various commercial software options are available on the market. Researchers should select appropriate material preparation methods, image acquisition setup, and post-processing parameters based on their test requirements.

2.5.2 Temperature measurement using infrared techniques and thermocouple

It is well known that plastic work can be converted to heat, which can significantly affect the mechanical responses of polymeric materials because their constitutive behaviours are highly temperature-dependent. In particular, in high-rate tests, the heat cannot be dissipated into the environment because of the adiabatic experimental environment, it can cause very apparent thermal softening at large strain regions for several polymers, such as PMMA [34, 42], PVC [35, 48]. Thus, it is important to understand the transformation mechanisms between plastic work and heat and then quantify the effects of the heat on the mechanical responses.

Based on the works of Farren and Taylor [147], Taylor and Quinney [148] proposed a parameter to describe the conversion between plastic work to heat, namely, Taylor-Quinney coefficient (TQC). This value is considered to be about 0.9 for many metallic materials [149-152], however, there is no definite conclusion for polymeric materials. More recently, Rittel [153] developed a differential TQC to describe the rate of change in this conversion for polycarbonate. The formulas of integration and differential TQC are as follows:

$$TQC_{int} = \frac{\rho C_p \Delta T}{\int_{\varepsilon}^{\varepsilon_p} \sigma d\varepsilon_p} \quad (2\text{-}28)$$

$$TQC_{diff} = \frac{\rho C_p \Delta \dot{T}}{\int_{\varepsilon}^{\varepsilon_p} \sigma d\dot{\varepsilon_p}} \quad (2\text{-}29)$$

where ρ is the material density, C_p is the specific heat capacity, and $\rho C_p \Delta T$ is the heat work. $\int_{\varepsilon}^{\varepsilon_p} \sigma d\varepsilon_p$ is the integration of the true stress-true strain curve after yield. Moreover, equation (2-29) represents the increment rate of TQC from each data point.

The temperature change (ΔT) must be measured to quantify the temperature-dependent effects on the plastic deformation region and calculate TQC. Three methods are usually used for the in-situ temperature rise measurements: thermocouple, infrared (IR) detector and infrared camera. Rittel and colleagues compared the thermal measurements under dynamic loading using IR detector and IR camera [154] as well as IR detector and thermocouple [155]; Walley *et al.* [156] compared the use of thermocouple and IR camera during the Hopkinson bar tests. All these papers [154-156] summarized previous research, and combined with the results of their experiments, a new evaluation of the advantages and disadvantages of the applied techniques has been provided, shown in Table 2-4.

Table 2-4 Comparison of thermocouple, IR detector and IR camera. Summarised from [154-156].

	Thermocouple	IR detector	IR camera
Sampling rate	$t = \frac{V\rho C_p}{KA}$ (2-30) [157]	Up to 1.5 MHz data acquisition, but 5-10 μs sampling time.	Depending on the type, up to 10 kHz (Telops M3K) or 100 kHz at a lower resolution
Device calibration	Needed, but easy	Needed, complex	Not needed
Ease of use	Easy	Complex	Variable
Measurement field	Data point	Narrow area	Full-field
Sample integrity	Damaged	Non-destructive	
Emissivity calibration	No needed	Needed	Needed

In Equation 2-30, t is the response time of the thermocouple, V is the volume of the thermocouple, ρ is the density, C_p is the specific heat capacity, and A is the surface area; K is the thermal conductivity of the tested sample. However, the authors did not use this equation to evaluate the response time of the thermocouple; instead, they validated the thermocouple-measured results by observing the time lag. The IR detector can

acquire thermal data very quickly, although care needs to be taken to consider the true sampling rate rather than the data acquisition rate. However, the calibration process of this technique is more complex than the other two, and the narrow measurement field (cone of radiation) can possibly be blocked by the loading device during compression tests [155, 158]. IR camera, especially high-speed IR camera, is a relatively new device and less tested than thermocouples and IR detectors. It is very challenging to do the thermal measurements using the IR camera during high-rate tests because the time duration of these tests is usually in hundred μs; only recently, sufficient thermal image acquisition has become available with the development of the high-speed thermal camera [156]. The most important advantage of an IR camera is that it can visibly show the full-field thermal image, which means this technique can provide the thermal gradient when the strain or stress localisation (i.e. adiabatic shear band [133], damage [159]) occurs. As a contact measurement method, the thermocouple cannot avoid damaging the sample, and it might introduce strain localisation in the tests; at the same time, this method can only measure one data point, which will cause variation in the test results. IR-based approaches can avoid this issue, however, more effort is needed to calibrate not only the device but also the emissivity of tested materials. A more detailed literature review is given in **Chapter 5** for the temperature rise measurement of polycarbonate, and in this chapter, a new approach is developed to measure the temperature rise under dynamic loading using a high-speed IR camera.

2.5.3 Synchrotron X-ray imaging applied to high-strain rate experiments

Advances in multi-scale modelling for understanding material behaviour have prompted a need for more comprehensive information on deformation within a specimen rather than relying on average strain across its length [160]. To address this, digital image correlation has been effectively combined with Hopkinson bar experiments to capture the dynamic progression of strain across the entire surface of the specimen [161]. In the case of transparent materials, a high-speed camera can also be used to document the history of internal damage [162]. However, when the specimen is optically opaque or its transparency is compromised by damage,

it becomes impossible to observe the detailed distribution of deformation or the progression of damage inside using optical imaging [163]. In such cases, X-rays offer a natural solution for imaging through the thickness of the specimen, enabling the recording and exploration of internal damage histories [164].

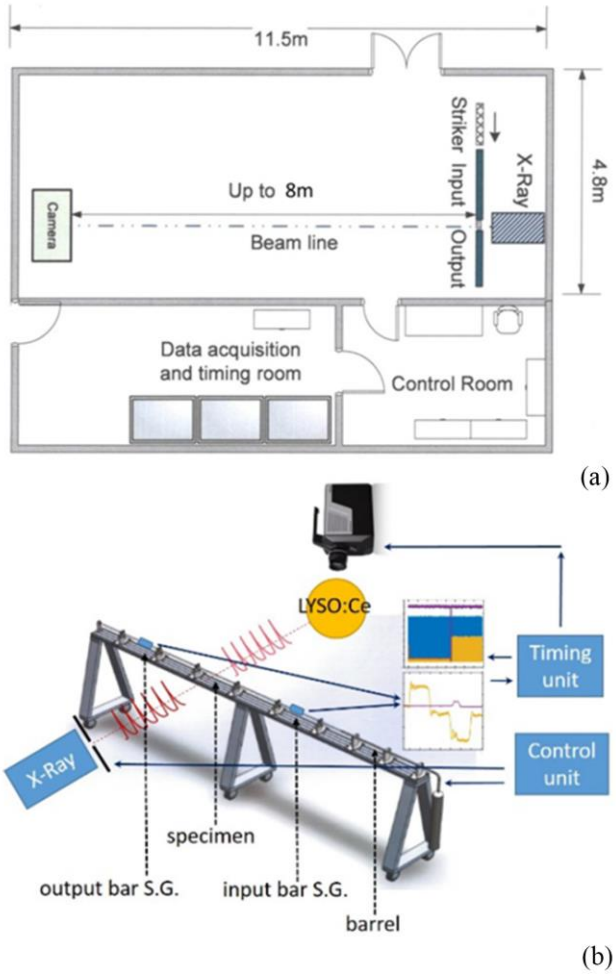

Figure 2-20 Schematic of ESRF ID-19 hutch for SHPB tests, the dimensions of this system are appropriate for hutch room (b) SHPB setup mounted perpendicular to the X-ray axis in ID-19 in ESRF. Reproduced from [165].

Researchers have built a gas gun system, which can be accompanied by Hopkinson bar and shock experiments, at beamline ID-19 of the European Synchrotron Radiation Facility (ESRF) [165] and beamline 32-ID of the Argonne National Laboratory (APS) [166]. Fig. 2-20(a) shows the schematic of the Hopkinson bar experiments in the ESRF ID-19 hutch. The length of the Hopkinson input and output bar fits the space of the hutch room, and the striker's and bars' material and diameter can be changed to meet the different test

requirements. The experiments are remotely controlled from the control room, and the SHPB system and fast shutter of the X-ray are triggered together. A delay generator controls the necessary time interval between an input trigger signal, the camera exposure time, and the X-ray pulse train. The specific delay is calculated to ensure that the camera is triggered at the desired time relative to the duration of the sample loading and the X-ray pulse train. When the incident signal is received, two separate DAC scopes are triggered: one measures the SHPB data, including projectile velocity and strains on the bars, while the second generates the bunch clock signal (X-ray pulse train), camera trigger-in, and camera trigger out (as shown in Fig. 2-20(b)). This sequential process establishes a reliable control system and aligns all signals on two synchronized time axes, enabling dependable data analysis [165].

X-rays have been extensively used in medical and security fields for visualizing objects concealed by various materials. However, when studying dynamic fracture phenomena, which occur on microscopic scales and at faster time scales compared to medical imaging, the X-ray imaging system used for such experiments must possess adequate temporal and spatial resolutions. Two criteria become imperative: achieving high intensity and enhancing contrast, and synchrotron X-ray radiation is the most logical way to fit these imaging requests in microseconds [166].

In traditional radiography, there is usually a substantial difference in density between the tested object and the background, and these pronounced density variations contribute to clear and distinct images in the X-rays. However, engineering systems do not always possess such extreme density differences. To improve the image quality and enhance the distinguishability of high-speed X-ray images, the unique characteristics of synchrotron radiation are utilized for X-ray phase contrast imaging (XPCI). The complex index of refraction, n, of material for X-rays can be described as follows [160, 164, 166]:

$$n = （1 - \delta） + i\beta \tag{2-31}$$

where δ and β are phase shift and absorption. If the distance between the sample and detector is *zero* or very

small, the image contrast is derived from the X-ray absorption by different phases of the specimen material. If the distance between the sample and detector is *finite* or very large (i.e., 8 m in Fig. 2-20(a)), it allows the spatial variations in the X-ray phases induced by heterogeneous phase objects with small absorption, β; during the free space propagation from *zero* to *finite*, the intensity of X-ray can be modulated due to overlapping and interference of the wavefront.

In order to convert the X-rays to high speed oprical images, an indirect detector (i.e., LYSO:CE in Fig. 2-20(b)) based on a single-crystal scintillator is used [165]. The specific design of the experiment needs to be adjusted based on the material properties, the test requirements, the X-ray intensity, and the hutch space. Gao and colleagues [163, 167-169] have characterised polymeric composites using the high-speed synchrotron X-ray phase contrast imaging technique and successfully observed the micro-crack in SHPB tests. More details about the synchrotron X-ray experiments and results for short glass reinforced PC under dynamic loading are provided in **Chapter 6**.

2.6 Bibliography

1. McCrum, N.G., et al., *Principles of polymer engineering*. 1997: Oxford University Press, USA.
2. Staudinger, H., *On Polymerization*, in *A Source Book in Chemistry, 1900-1950*. 2013, Harvard University Press. p. 259-264.
3. Flory, P.J., *Preparation of polyamides*. 1941, Google Patents.
4. Demirors, M., *The history of polyethylene*, in *100+ Years of Plastics. Leo Baekeland and Beyond*. 2011, ACS Publications. p. 115-145.
5. Mulder, K. and M. Knot, *PVC plastic: a history of systems development and entrenchment.* Technology in Society, 2001. **23**(2): p. 265-286.
6. *Plastic Market (By Product: PE, PP, PU, PVC, PET, Polystyrene, ABS, PBT, PPO, Epoxy Polymers, LCP, PC, Polyamide; By Application; By End Use) - Global Industry Analysis, Size, Share, Growth, Trends, Revenue, Regional Outlook and Forecast 2022-2030*. 2022, Vision Research Reports.
7. Siviour, C.R. and J.L. Jordan, *High strain rate mechanics of polymers: a review.* Journal of Dynamic Behavior of Materials, 2016. **2**: p. 15-32.
8. Micciche, F., V. Ramakrishnan, and T.L. Hoeks, *The effect of molecular structure on the secondary transitions and their influence on the decoloration kinetics of photochromic dyes in co-polycarbonates.* Journal of Polymer Science Part B: Polymer Physics, 2016. **54**(16): p. 1593-1601.
9. Kyriacos, D., *Polycarbonates*, in *Brydson's Plastics Materials*. 2017, Elsevier. p. 457-485.
10. Pisanova, E., *Polycarbonate composites.* Wiley Encyclopedia of Composites, 2011: p. 1-9.
11. Raj, P. and R. Kumar, *A Brief Review: Study on Mechanical Properties of Polycarbonate with Different Nanofiller Materials.* Advances in Materials and Manufacturing Engineering: Select Proceedings of ICMME 2019, 2021: p. 285-291.
12. Greco, R. and A. Sorrentino, *Polycarbonate/ABS blends: A literature review.* Advances in Polymer Technology: Journal of the Polymer Processing Institute, 1994. **13**(4): p. 249-258.
13. Suarez, H., J.W. Barlow, and D.R. Paul, *Mechanical properties of ABS/polycarbonate blends.* Journal of applied polymer science, 1984. **29**(11): p. 3253-3259.
14. Kausar, A., *A review of filled and pristine polycarbonate blends and their applications.* Journal of Plastic Film & Sheeting, 2018. **34**(1): p. 60-97.
15. Sinha Ray, S. and M. Bousmina, *Compatibilization efficiency of organoclay in an immiscible polycarbonate/poly (methyl methacrylate) blend.* Macromolecular rapid communications, 2005. **26**(6): p. 450-455.
16. Kim, M., et al., *Control of phase separation behavior of PC/PMMA blends and their application to the gas separation membranes.* Journal of Polymer Science Part B: Polymer Physics, 1999. **37**(21): p. 2950-2959.
17. Estaji, S., et al., *Polycarbonate/poly (methyl methacrylate)/silica aerogel blend composites for advanced transparent thermal insulations: Mechanical, thermal, and optical studies.* Polymer Composites, 2021. **42**(10): p. 5323-5334.
18. Magida, M.M., *Study of structural and thermal properties of electron beam irradiated polymethylmethacrylate/bisphenol-A-polycarbonate blends.* Journal of applied polymer science, 2012. **125**(4): p. 3184-3190.
19. Li, Z.-M., et al., *Anisotropic microstructure-impact fracture behavior relationship of polycarbonate/polyethylene blends injection-molded at different temperatures.* Polymer, 2005. **46**(23): p. 10466-10477.
20. Braun, D., B. Boehringer, and J. Herth. *Properties of poly (vinyl chloride) blends with polycarbonates*

and chlorinated polyethylene. Wiley Online Library.

21. Nazemidashtarjandi, S., S.A. Mousavi, and D. Bastani, *Preparation and characterization of polycarbonate/thermoplastic polyurethane blend membranes for wastewater filtration.* Journal of water process engineering, 2017. **16**: p. 170-182.
22. Kong, Y. and J.N. Hay, *Miscibility and crystallisation behaviour of poly (ethylene terephthalate)/polycarbonate blends.* Polymer, 2002. **43**(6): p. 1805-1811.
23. Pötschke, P., T.D. Fornes, and D.R. Paul, *Rheological behavior of multiwalled carbon nanotube/polycarbonate composites.* Polymer, 2002. **43**(11): p. 3247-3255.
24. Kim, H. and C.W. Macosko, *Processing-property relationships of polycarbonate/graphene composites.* Polymer, 2009. **50**(15): p. 3797-3809.
25. Patole, A. and G. Lubineau, *Carbon nanotubes with silver nanoparticle decoration and conductive polymer coating for improving the electrical conductivity of polycarbonate composites.* Carbon, 2015. **81**: p. 720-730.
26. Derazkola, H.A. and F. Khodabakhshi, *Development of fed friction-stir (FFS) process for dissimilar nanocomposite welding between AA2024 aluminum alloy and polycarbonate (PC).* Journal of Manufacturing Processes, 2020. **54**: p. 262-273.
27. Carrión, F.J., et al., *Physical and tribological properties of a new polycarbonate-organoclay nanocomposite.* European Polymer Journal, 2008. **44**(4): p. 968-977.
28. Andriss, C., et al., *Characterization and modeling of continuous carbon fiber-reinforced polycarbonate under multiaxial loads.* Composites Part B: Engineering, 2022. **235**: p. 109740.
29. Carneiro, O.S., et al., *Production and assessment of polycarbonate composites reinforced with vapour-grown carbon fibres.* Composites Science and Technology, 1998. **58**(3-4): p. 401-407.
30. Law, T.T., et al., *Experimental analysis and theoretical modeling of the mechanical behavior of short glass fiber and short carbon fiber reinforced polycarbonate hybrid composites.* Polymer Composites, 2016. **37**(4): p. 1238-1248.
31. Bergstrom, J., et al., *Wear of die materials in full scale plastic injection moulding of glass fibre reinforced polycarbonate.* Wear, 2001. **251**(1-12): p. 1511-1521.
32. Ho, K.-C. and M.-C. Jeng, *Tribological characteristics of short glass fibre reinforced polycarbonate composites.* Wear, 1997. **206**(1-2): p. 60-68.
33. Gohil, M. and G. Joshi, *Perspective of polycarbonate composites and blends properties, applications, and future development: A review.* Green Sustainable Process for Chemical and Environmental Engineering and Science, 2022: p. 393-424.
34. Kendall, M.J. and C.R. Siviour, *Experimentally simulating high-rate behaviour: rate and temperature effects in polycarbonate and PMMA.* Philosophical Transactions of the Royal Society A: Mathematical, Physical and Engineering Sciences, 2014. **372**(2015): p. 20130202.
35. Kendall, M.J. and C.R. Siviour, *Rate dependence of poly (vinyl chloride), the effects of plasticizer and time–temperature superposition.* Proceedings of the Royal Society A: Mathematical, Physical and Engineering Sciences, 2014. **470**(2167): p. 20140012.
36. Bauwens-Crowet, C., J.C. Bauwens, and G. Homes, *The temperature dependence of yield of polycarbonate in uniaxial compression and tensile tests.* Journal of Materials Science, 1972. **7**: p. 176-183.
37. Walley, S.M., et al., *The response of various polymers to uniaxial compressive loading at very high rates of strain.* Le Journal de Physique Colloques, 1985. **46**(C5): p. C5-607.
38. Chen, W., F. Lu, and B. Zhou, *A quartz-crystal-embedded split Hopkinson pressure bar for soft materials.* Experimental mechanics, 2000. **40**: p. 1-6.
39. Song, B. and W. Chen, *Dynamic stress equilibration in split Hopkinson pressure bar tests on soft*

materials. Experimental mechanics, 2004. **44**: p. 300-312.

40. Gray III, G.T. and W.R. Blumenthal, *Split-Hopkinson pressure bar testing of soft materials.* ASM handbook, 2000. **8**: p. 488-496.
41. Bauwens-Crowet, C., J.C. Bauwens, and G. Homes, *The temperature dependence of yield of polycarbonate in uniaxial compression and tensile tests.* Journal of Materials Science, 1972. **7**(2): p. 176-183.
42. Mulliken, A.D. and M.C. Boyce, *Mechanics of the rate-dependent elastic–plastic deformation of glassy polymers from low to high strain rates.* International Journal of Solids and Structures, 2006. **43**(5): p. 1331-1356.
43. Siviour, C.R., et al., *The high strain rate compressive behaviour of polycarbonate and polyvinylidene difluoride.* Polymer, 2005. **46**(26): p. 12546-12555.
44. Richeton, J., et al., *Influence of temperature and strain rate on the mechanical behavior of three amorphous polymers: Characterization and modeling of the compressive yield stress.* International Journal of Solids and Structures, 2006. **43**(7-8): p. 2318-2335.
45. Richeton, J., et al., *Modeling and validation of the large deformation inelastic response of amorphous polymers over a wide range of temperatures and strain rates.* International journal of solids and structures, 2007. **44**(24): p. 7938-7954.
46. Kendall, M.J. and C.R. Siviour, *Experimentally simulating high-rate behaviour: rate and temperature effects in polycarbonate and PMMA.* Philos Trans A Math Phys Eng Sci, 2014. **372**(2015): p. 20130202.
47. Safari, K.H., et al., *Constitutive modeling of polycarbonate during high strain rate deformation.* Polymer Engineering & Science, 2013. **53**(4): p. 752-761.
48. Mulliken, A.D., *Mechanics of amorphous polymers and polymer nanocomposites during high rate deformation.* PhD Thesis, Massachusetts Institute of Technology, 2006.
49. Boyce, M.C., E.M. Arruda, and R. Jayachandran, *The large strain compression, tension, and simple shear of polycarbonate.* Polymer Engineering & Science, 1994. **34**(9): p. 716-725.
50. Boyce, M.C. and E.M. Arruda, *An experimental and anaiytical investigation of the large strain compressive and tensile response of glassy polymers.* Polymer Engineering & Science, 1990. **30**(20): p. 1288-1298.
51. Sarva, S. and M. Boyce, *Mechanics of polycarbonate during high-rate tension.* Journal of Mechanics of Materials and Structures, 2007. **2**(10): p. 1853-1880.
52. Spitzig, W.A. and O. Richmond, *Effect of hydrostatic pressure on the deformation behavior of polyethylene and polycarbonate in tension and in compression.* Polymer Engineering & Science, 1979. **19**(16): p. 1129-1139.
53. Zhang, L., et al., *Temperature Dependent Dynamic Strain Localization and Failure of Ductile Polymeric Rods under Large Deformation.* International Journal of Mechanical Sciences, 2021. **204**: p. 106563.
54. Parsons, E., M.C. Boyce, and D.M. Parks, *An experimental investigation of the large-strain tensile behavior of neat and rubber-toughened polycarbonate.* Polymer, 2004. **45**(8): p. 2665-2684.
55. Cao, K., et al., *Tensile behavior of polycarbonate over a wide range of strain rates.* Materials Science and Engineering: A, 2010. **527**(16): p. 4056-4061.
56. Siviour, C.R. and J.L. Jordan, *High Strain Rate Mechanics of Polymers: A Review.* Journal of Dynamic Behavior of Materials, 2016. **2**(1): p. 15-32.
57. Field, J.E., et al., *Review of experimental techniques for high rate deformation and shock studies.* International Journal of Impact Engineering, 2004. **30**(7): p. 725-775.
58. Trautmann, A., et al., *Lubrication of polycarbonate at cryogenic temperatures in the split Hopkinson*

pressure bar. International Journal of Impact Engineering, 2005. **31**(5): p. 523-544.
59. Gerlach, R., et al., *Experimental characterisation and constitutive modelling of RTM-6 resin under impact loading.* Polymer, 2008. **49**(11): p. 2728-2737.
60. Yoon, S.-h., I. Giannakopoulos, and C.R. Siviour, *Application of the Virtual Fields Method to the uniaxial behavior of rubbers at medium strain rates.* International Journal of Solids and Structures, 2015. **69**: p. 553-568.
61. Chen, W.W. and B. Song, *Split Hopkinson (Kolsky) bar: design, testing and applications*. 2010: Springer Science & Business Media.
62. Okereke, M.I., C.P. Buckley, and C.R. Siviour, *Compression of polypropylene across a wide range of strain rates.* Mechanics of Time-Dependent Materials, 2012. **16**(4): p. 361-379.
63. Hopkinson, B., *X. A method of measuring the pressure produced in the detonation of high, explosives or by the impact of bullets.* Philosophical Transactions of the Royal Society of London. Series A, Containing Papers of a Mathematical or Physical Character, 1914. **213**(497-508): p. 437-456.
64. Kolsky, H., *An investigation of the mechanical properties of materials at very high rates of loading.* Proceedings of the physical society. Section B, 1949. **62**(11): p. 676.
65. Clausen, A.H., *Tensile Testing Using the Kolsky-Hopkinson Bar Machine*, in *The Kolsky-Hopkinson Bar Machine*. 2018. p. 27-74.
66. Gerlach, R., C. Kettenbeil, and N. Petrinic, *A new split Hopkinson tensile bar design.* International Journal of Impact Engineering, 2012. **50**: p. 63-67.
67. Owens, A.T. and H.V. Tippur, *A Tensile Split Hopkinson Bar for Testing Particulate Polymer Composites Under Elevated Rates of Loading.* Experimental Mechanics, 2008. **49**(6): p. 799-811.
68. Kara, A., A. Tasdemirci, and M. Guden, *Modeling quasi-static and high strain rate deformation and failure behavior of a (±45) symmetric E-glass/polyester composite under compressive loading.* Materials & Design, 2013. **49**: p. 566-574.
69. Koerber, H. and P.P. Camanho, *High strain rate characterisation of unidirectional carbon–epoxy IM7-8552 in longitudinal compression.* Composites Part A: Applied Science and Manufacturing, 2011. **42**(5): p. 462-470.
70. Kuhn, P., et al., *Fracture toughness and crack resistance curves for fiber compressive failure mode in polymer composites under high rate loading.* Composite Structures, 2017. **182**: p. 164-175.
71. Leite, B.M., et al., *Strain rate effects on the intralaminar fracture toughness of composite laminates subjected to compressive load.* Composite Structures, 2018. **186**: p. 94-105.
72. Koerber, H., J. Xavier, and P.P. Camanho, *High strain rate characterisation of unidirectional carbon-epoxy IM7-8552 in transverse compression and in-plane shear using digital image correlation.* Mechanics of Materials, 2010. **42**(11): p. 1004-1019.
73. Omar, M.F., et al., *Dynamic properties of pultruded natural fibre reinforced composites using Split Hopkinson Pressure Bar technique.* Materials & Design, 2010. **31**(9): p. 4209-4218.
74. Zhou, J., et al., *The mechanical response of commercially pure copper under multiaxial loading at low and high strain rates.* International Journal of Mechanical Sciences, 2022. **224**: p. 107340.
75. Xu, Y., et al., *Optimal Design, Development and Experimental Analysis of a Tension–Torsion Hopkinson Bar for the Understanding of Complex Impact Loading Scenarios.* Experimental Mechanics, 2023. **63**(4): p. 773-789.
76. Chen, R., et al., *Determination of dynamic fracture parameters using a semi-circular bend technique in split Hopkinson pressure bar testing.* Engineering Fracture Mechanics, 2009. **76**(9): p. 1268-1276.
77. Pierron, F., M. Sutton, and V. Tiwari, *Ultra high speed DIC and virtual fields method analysis of a three point bending impact test on an aluminium bar.* Experimental Mechanics, 2011. **51**(4): p. 537-563.

78. Hoffmann, J., H. Cui, and N. Petrinic, *Determination of the strain-energy release rate of a composite laminate under high-rate tensile deformation in fibre direction.* Composites Science and Technology, 2018. **164**: p. 110-119.
79. Chen, Y., et al., *A comprehensive experimental investigation of the rate-dependent interlaminar delamination behaviour of CFRP composites.* Composites Part B: Engineering, 2023. **261**: p. 110788.
80. Jordan, J.L., J.R. Foley, and C.R. Siviour, *Mechanical properties of Epon 826/DEA epoxy.* Mechanics of Time-Dependent Materials, 2008. **12**: p. 249-272.
81. Nie, X., et al., *Dynamic tensile testing of soft materials.* Experimental mechanics, 2009. **49**: p. 451-458.
82. Chen, W., B. Zhang, and M.J. Forrestal, *A split Hopkinson bar technique for low-impedance materials.* Experimental mechanics, 1999. **39**: p. 81-85.
83. Trivedi, A.R. and C.R. Siviour, *A Simple Rate–Temperature Dependent Hyperelastic Model Applied to Neoprene Rubber.* Journal of Dynamic Behavior of Materials, 2020. **6**: p. 336-347.
84. Hughes, F., A. Prudom, and G. Swallowe, *The high strain-rate behaviour of three molecular weights of polyethylene examined with a magnesium alloy split-Hopkinson pressure bar.* Polymer testing, 2013. **32**(5): p. 827-834.
85. Casem, D.T., W. Fourney, and P. Chang, *Wave separation in viscoelastic pressure bars using single-point measurements of strain and velocity.* Polymer testing, 2003. **22**(2): p. 155-164.
86. Zhao, H. and G. Gary, *A three dimensional analytical solution of the longitudinal wave propagation in an infinite linear viscoelastic cylindrical bar. Application to experimental techniques.* Journal of the Mechanics and Physics of Solids, 1995. **43**(8): p. 1335-1348.
87. Butt, H.S.U., et al., *Parametric identification for material of viscoelastic SHPB from wave propagation data incorporating geometrical effects.* International Journal of Mechanical Sciences, 2015. **91**: p. 46-54.
88. Song, B., et al., *A long split Hopkinson pressure bar (LSHPB) for intermediate-rate characterization of soft materials.* Experimental mechanics, 2008. **48**: p. 809-815.
89. Gama, B.A., S.L. Lopatnikov, and J.W. Gillespie Jr, *Hopkinson bar experimental technique: a critical review.* Appl. Mech. Rev., 2004. **57**(4): p. 223-250.
90. Gray, G.T., III, *Classic split Hopkinson pressure bar testing.* ASM handbook, 2000. **8**: p. 462-476.
91. Siviour, C.R. and S.M. Walley, *Inertial and frictional effects in dynamic compression testing.* The Kolsky-Hopkinson bar machine: selected topics, 2018: p. 205-247.
92. Höhne, G.W.H., W. Hemminger, and H.-J. Flammersheim, *Differential scanning calorimetry*. Vol. 2. 2003: Springer.
93. Menczel, J.D. and R.B. Prime, *Thermal analysis of polymers: fundamentals and applications*. 2009: John Wiley & Sons.
94. Ehrenstein, G.W., G. Riedel, and P. Trawiel, *Thermal analysis of plastics: theory and practice*. 2012: Carl Hanser Verlag GmbH Co KG.
95. Abd-Elghany, M. and T.M. Klapötke, *A review on differential scanning calorimetry technique and its importance in the field of energetic materials.* Physical Sciences Reviews, 2018. **3**(4).
96. Instruments, TA. *Different Scanning Calorimetry (DSC)*. 2022; Available from: chrome-extension://oemmndcbldboiebfnladdacbdfmadadm/https://www.tainstruments.com/wp-content/uploads/San-Jose-Thermal-DSC.pdf.
97. Shamim, N., et al., *Glass transition temperature of thin polycarbonate films measured by flash differential scanning calorimetry.* Journal of Polymer Science Part B: Polymer Physics, 2014. **52**(22): p. 1462-1468.
98. Reading, M. and D.J. Hourston, *Modulated temperature differential scanning calorimetry: theoretical*

and practical applications in polymer characterisation. Vol. 6. 2006: Springer Science & Business Media.

99. Trivedi, A.R. and C.R. Siviour, *A novel methodology for predicting the high rate mechanical response of polymers from low rate data: application to (plasticised) poly (vinyl chloride).* Mechanics of Time-Dependent Materials, 2021. **25**: p. 383-409.
100. Menard, K.P. and N.R. Menard, *Dynamic mechanical analysis in the analysis of polymers and rubbers.* Encyclopedia of polymer science and technology, 2002: p. 1-33.
101. Menard, K.P. and N. Menard, *Dynamic mechanical analysis*. 2020: CRC press.
102. Instruments, TA. *Dynamic Mechanical Analysis Basic Theory & Applications Training*. 2018; Available from: chrome-extension://oemmndcbldboiebfnladdacbdfmadadm/http://docs.tainstruments.com/training/DMA_Training_2018-August.pdf.
103. Shao, Q. and P. Lee-Sullivan, *Guidelines for performing storage modulus measurements using the TA Instruments DMA 2980 three-point bend mode II. Contact stresses and machine compliance.* Polymer testing, 2000. **19**(3): p. 239-250.
104. Lee-Sullivan, P. and D. Dykeman, *Guidelines for performing storage modulus measurements using the TA Instruments DMA 2980 three-point bend mode: I. Amplitude effects.* Polymer testing, 2000. **19**(2): p. 155-164.
105. Deng, S., M. Hou, and L. Ye, *Temperature-dependent elastic moduli of epoxies measured by DMA and their correlations to mechanical testing data.* Polymer testing, 2007. **26**(6): p. 803-813.
106. Instruments, TA. 2007 Available from: http://www.tainstruments.com/pdf/DMA.pdf".
107. Lee, K., et al., *Experimental observation and numerical simulation of transient "stress fangs" within flowing molten polyethylene.* Journal of Rheology, 2001. **45**(6): p. 1261-1277.
108. Marrucci, G., *Dynamics of entanglements: A nonlinear model consistent with the Cox-Merz rule.* Journal of non-newtonian fluid mechanics, 1996. **62**(2-3): p. 279-289.
109. Vinogradov, G.V. and A.Y. Malkin, *Rheology of polymers: viscoelasticity and flow of polymers*. 1980: Springer.
110. Phan-Thien, N., *On the Time—Temperature Superposition Principle of Dilute Polymer Liquids.* Journal of Rheology, 1979. **23**(4): p. 451-456.
111. Li, R., *Time-temperature superposition method for glass transition temperature of plastic materials.* Materials Science and Engineering: A, 2000. **278**(1-2): p. 36-45.
112. Bauwens, J.C., C. Bauwens-Crowet, and G. Homes, *Tensile yield-stress behavior of poly (vinyl chloride) and polycarbonate in the glass transition region.* Journal of Polymer Science Part A-2: Polymer Physics, 1969. **7**(10): p. 1745-1754.
113. Bauwens-Crowet, C., J.C. Bauwens, and G. Homes, *Tensile yield-stress behavior of glassy polymers.* Journal of Polymer Science Part A-2: Polymer Physics, 1969. **7**(4): p. 735-742.
114. Bauwens, J.C., *Relation between the compression yield stress and the mechanical loss peak of bisphenol-A-polycarbonate in the β transition range.* Journal of Materials Science, 1972. **7**: p. 577-584.
115. Bauwens-Crowet, C., *The compression yield behaviour of polymethyl methacrylate over a wide range of temperatures and strain-rates.* Journal of Materials Science, 1973. **8**: p. 968-979.
116. Walley, S.M. and J.E. Field, *Strain rate sensitivity of polymers in compression from low to high rates.* DYMAT J, 1994. **1**(3): p. 211-227.
117. Jordan, J.L., et al., *Compressive properties of extruded polytetrafluoroethylene.* Polymer, 2007. **48**(14): p. 4184-4195.
118. Thompson, D.G., R. Deluca, and G.W. Brown, *Time–temperature analysis, tension and compression*

in PBXs. Journal of Energetic Materials, 2012. **30**(4): p. 299-323.
119. Jamarani, R., et al., *Rheology of Green Plasticizer/Poly(vinyl chloride) Blends via Time–Temperature Superposition.* Processes, 2017. **5**(4).
120. *Mechanical vibration and shock — Characterization of the dynamic mechanical properties of visco-elastic materials*, in *Part 6: Time-temperature superposition*. 2017, BSI Standards Publication.
121. Yoon, S.-h. and C.R. Siviour, *Application of the Virtual Fields Method to a relaxation behaviour of rubbers.* Journal of the Mechanics and Physics of Solids, 2018. **116**: p. 416-431.
122. Song, P., A.R. Trivedi, and C.R. Siviour, *Mechanical response of four polycarbonates at a wide range of strain rates and temperatures.* Polymer Testing, 2023. **121**: p. 107986.
123. Williams, M.L., R.F. Landel, and J.D. Ferry, *The temperature dependence of relaxation mechanisms in amorphous polymers and other glass-forming liquids.* Journal of the American Chemical society, 1955. **77**(14): p. 3701-3707.
124. Laidler, K.J., *The development of the Arrhenius equation.* Journal of chemical Education, 1984. **61**(6): p. 494.
125. Angell, C.A., et al., *Relaxation in glassforming liquids and amorphous solids.* Journal of applied physics, 2000. **88**(6): p. 3113-3157.
126. Pan, B., *Digital image correlation for surface deformation measurement: historical developments, recent advances and future goals.* Measurement Science and Technology, 2018. **29**(8): p. 082001.
127. Chu, T.C., W.F. Ranson, and M.A. Sutton, *Applications of digital-image-correlation techniques to experimental mechanics.* Experimental mechanics, 1985. **25**: p. 232-244.
128. Peters, W.H. and W.F. Ranson, *Digital imaging techniques in experimental stress analysis.* Optical engineering, 1982. **21**(3): p. 427-431.
129. Peters, W.H., et al., *Application of digital correlation methods to rigid body mechanics.* Optical Engineering, 1983. **22**(6): p. 738-742.
130. Tung, S.-H., M.-H. Shih, and J.-C. Kuo, *Application of digital image correlation for anisotropic plastic deformation during tension testing.* Optics and Lasers in Engineering, 2010. **48**(5): p. 636-641.
131. Parsons, E.M., et al., *Three-dimensional large-strain tensile deformation of neat and calcium carbonate-filled high-density polyethylene.* Polymer, 2005. **46**(7): p. 2257-2265.
132. Grytten, F., et al., *Use of digital image correlation to measure large-strain tensile properties of ductile thermoplastics.* Polymer Testing, 2009. **28**(6): p. 653-660.
133. Pournoori, N., et al., *Adiabatic heating and damage onset in a pultruded glass fiber reinforced composite under compressive loading at different strain rates.* International Journal of Impact Engineering, 2021. **147**: p. 103728.
134. Graham, A. and C. Siviour, *Characterising the frequency-response of ultra-soft polymers with the Virtual Fields Method.* Strain, 2021. **57**(5): p. e12386.
135. Teixeira Pinto, J.M., et al., *DIC strain measurements at the micro-scale in a semi-crystalline polymer.* Experimental Mechanics, 2013. **53**: p. 1311-1321.
136. Xu, Y., et al., *Experimental analysis of the multiaxial failure stress locus of commercially pure titanium at low and high rates of strain.* International Journal of Impact Engineering, 2022. **170**: p. 104341.
137. Dong, Y.L. and B. Pan, *A review of speckle pattern fabrication and assessment for digital image correlation.* Experimental Mechanics, 2017. **57**: p. 1161-1181.
138. Quino, G., et al., *Speckle patterns for DIC in challenging scenarios: rapid application and impact endurance.* Measurement Science and Technology, 2020. **32**(1): p. 015203.
139. Sutton, M.A., *Digital image correlation for shape and deformation measurement.* Springer handbook of experimental solid mechanics, 2008: p. 565-600.
140. Pan, B., H. Xie, and Z. Wang, *Equivalence of digital image correlation criteria for pattern matching.*

Applied Optics, 2010. **49**(28): p. 5501-5509.
141. Pan, B., et al., *Two-dimensional digital image correlation for in-plane displacement and strain measurement: a review.* Measurement Science and Technology, 2009. **20**(6): p. 062001.
142. MatchId, *MatchID Manual*. 2022, MatchID: Metrology Beyond Colors Gent, Belgium.
143. Knauss, W.G., I. Chasiotis, and Y. Huang, *Mechanical measurements at the micron and nanometer scales.* Mechanics of materials, 2003. **35**(3-6): p. 217-231.
144. Schreier, H.W., J.R. Braasch, and M.A. Sutton, *Systematic errors in digital image correlation caused by intensity interpolation.* Optical engineering, 2000. **39**(11): p. 2915-2921.
145. Sutton, M.A., J.J. Orteu, and H. Schreier, *Image correlation for shape, motion and deformation measurements: basic concepts, theory and applications*. 2009: Springer Science & Business Media.
146. Lu, H. and P.D. Cary, *Deformation measurements by digital image correlation: Implementation of a second-order displacement gradient.* Experimental mechanics, 2000. **40**: p. 393-400.
147. Farren, W.S. and G.I. Taylor, *The heat developed during plastic extension of metals.* Proceedings of the Royal Society of London. Series A, Containing Papers of a Mathematical and Physical Character, 1925. **107**(743): p. 422-451.
148. Taylor, G.I. and H. Quinney, *The latent energy remaining in a metal after cold working.* Proceedings of the Royal Society of London. Series A, Containing Papers of a Mathematical and Physical Character, 1934. **143**(849): p. 307-326.
149. Rittel, D., L.H. Zhang, and S. Osovski, *The dependence of the Taylor–Quinney coefficient on the dynamic loading mode.* Journal of the Mechanics and Physics of Solids, 2017. **107**: p. 96-114.
150. Soares, G.C. and M. Hokka, *The Taylor–Quinney coefficients and strain hardening of commercially pure titanium, iron, copper, and tin in high rate compression.* International Journal of Impact Engineering, 2021. **156**: p. 103940.
151. Mason, J.J., A.J. Rosakis, and G. Ravichandran, *On the strain and strain rate dependence of the fraction of plastic work converted to heat: an experimental study using high speed infrared detectors and the Kolsky bar.* Mechanics of Materials, 1994. **17**(2-3): p. 135-145.
152. Kapoor, R. and S. Nemat-Nasser, *Determination of temperature rise during high strain rate deformation.* Mechanics of materials, 1998. **27**(1): p. 1-12.
153. Rittel, D., *On the conversion of plastic work to heat during high strain rate deformation of glassy polymers.* Mechanics of Materials, 1999. **31**(2): p. 131-139.
154. Goviazin, G.G., A. Shirizly, and D. Rittel, *A Comparative Study of the Performance of IR Detectors vs. High-Speed Cameras Under Dynamic Loading Conditions.* Experimental Mechanics, 2023. **63**(1): p. 115-124.
155. Regev, A. and D. Rittel, *Simultaneous transient temperature sensing of impacted polymers using infrared detectors and thermocouples.* Experimental mechanics, 2008. **48**: p. 675-682.
156. Walley, S.M., et al., *Comparison of two methods of measuring the rapid temperature rises in split Hopkinson bar specimens.* Review of scientific instruments, 2000. **71**(4): p. 1766-1771.
157. Chou, S.C., K.D. Robertson, and J.H. Rainey, *The effect of strain rate and heat developed during deformation on the stress-strain curve of plastics: Temperature rise developed during deformation can have significant effects on the stress-strain relationship. Four hard plastics are tested at various strain rates, and temperature changes are measured during deformation of the specimen.* Experimental mechanics, 1973. **13**(10): p. 422-432.
158. Lerch, V., G. Gary, and P. Herve, *Thermomechanical properties of polycarbonate under dynamic loading.* Journal de Physique IV (Proceedings), 2003. **110**: p. 159-164.
159. Sassi, S., M. Tarfaoui, and H.B. Yahia, *In-situ heat dissipation monitoring in adhesively bonded composite joints under dynamic compression loading using SHPB.* Composites Part B: Engineering,

2018. **154**: p. 64-76.

160. Chen, W.W., et al., *In situ damage assessment using synchrotron X-rays in materials loaded by a Hopkinson bar.* Philosophical Transactions of the Royal Society A: Mathematical, Physical and Engineering Sciences, 2014. **372**(2015): p. 20130191.
161. Siviour, C.R., *High strain rate characterization of polymers.* AIP Publishing Conference Proceedings, 2016. **1793**: p. 060029.
162. Chen, P., B. Guo, and J. Chen, *Dynamic Brazilian Test Using the Kolsky-Hopkinson Bar Machine.* The Kolsky-Hopkinson Bar Machine: Selected Topics, 2018: p. 121-141.
163. Gao, J., et al., *Dynamic fracture of glass fiber-reinforced ductile polymer matrix composites and loading rate effect.* Composites Part B: Engineering, 2022. **235**: p. 109754.
164. Hudspeth, M., et al., *High speed synchrotron x-ray phase contrast imaging of dynamic material response to split Hopkinson bar loading.* Review of Scientific Instruments, 2013. **84**(2): p. 025102.
165. Cohen, A., et al., *In-situ radiography of a split-Hopkinson bar dynamically loaded materials.* Journal of Instrumentation, 2019. **14**(06): p. T06008.
166. Parab, N.D., *10 - Investigating fracture mechanisms in opaque materials under dynamic loading using high-speed synchrotron X-ray imaging*, in *Advances in Experimental Impact Mechanics*, B. Song, Editor. 2022, Elsevier. p. 285-314.
167. Gao, J., et al., *Real-time damage characterization for GFRCs using high-speed synchrotron X-ray phase contrast imaging.* Composites Part B: Engineering, 2021. **207**: p. 108565.
168. Gao, J., et al., *High-speed synchrotron X-ray phase-contrast imaging for evaluating microscale damage mechanisms and tracking cracking behaviors inside cross-ply GFRCs.* Composites Science and Technology, 2021. **210**: p. 108814.
169. Gao, J., K. Fezzaa, and W. Chen, *Multiscale dynamic experiments on fiber-reinforced composites with damage assessment using high-speed synchrotron X-ray phase-contrast imaging.* NDT & E International, 2022. **129**: p. 102636.

3 Large Strain Tension Experiments and Analysis

3.1 Introduction

The project started with transitional tensile tests, one of the most commonly used methods for material characterisation, to understand the baseline material properties, such as tensile yield stress and modulus. As a very ductile polymer, polycarbonate can be stretched to a very large strain, and, moreover, strain localisation makes it challenging to differentiate between the intrinsic material behaviour and structural (specimen geometry) response. To obtain more information during large tension deformation, a CCD camera and an infrared camera were utilized to collect the full-field displacement and temperature maps. A digital image correlation system was employed to capture local true strain, enabling us to understand the strain localisation effects and better estimate true stress using a number of different assumptions. A finite element model was created to interpret the experimental observations. Uniaxial compression test results from the same material were used to refine constitutive model parameters, which allowed the simulation to effectively represent the global deformation and temperature field and local true strain data during the whole deformation process.

The research highlights the inadequacy of relying only on global force-displacement data or engineering stress-strain curves from tensile tests for calibrating or validating polymer constitutive models. The local behaviour, such as true strain at different data points in the gauge area, should also be considered.

3.2 Paper A: Tensile testing of polymers: Integration of digital image correlation, infrared thermography and finite element modelling[1]

Abstract

Tensile tests are often used as part of material characterisation strategies; however, the observed deformation is often complex, and it can be difficult to distinguish the underlying material behaviour from the structural response of the specimen. The objective of the research in this paper was to investigate whether a more accurate calibration of a material model could be obtained by considering not just the global behaviour of the specimen, but also the local strain-time response calculated from full-field displacement information obtained using digital image correlation. Tensile experiments were performed using ISO standard, flat, dog bone specimens. Optical and infra-red imaging were used to calculate full field displacement and temperature maps, and a finite element model of the experiment was produced. These were combined with compression test data from the same material to calibrate a constitutive model, which was shown to describe well the deformation and temperature rise in the specimen. The research demonstrates that it is insufficient to use force-displacement information from tensile experiments to calibrate, or validate, constitutive models of polymers. Further, it demonstrates a more applicable method, which could be further automated in the future.

Keywords: Polycarbonate; Tensile test; Digital Image Correlation; Thermography; Strain localisation; Viscoplastic constitutive model

[1]**Song, P**., Trivedi, A., & Siviour, C. R. (2023). Tensile testing of polymers: Integration of digital image correlation, infrared thermography and finite element modelling. *Journal of the Mechanics and Physics of Solids*, *171*, 105161.

Introduction

Polycarbonate (PC) is a typical amorphous thermoplastic polymer, which is widely used in engineering applications because of its good mechanical properties. These properties have been extensively characterised in the past half-century. Of particular relevance are papers showing data from characterisation of the tensile and compressive response of PC at room temperature [1, 2]. Results on the pressure-dependent yield stress of polycarbonate indicate that the tensile yield stress is lower than the compressive at the same strain rate [3]. The deformation process in a uniaxial tension test is strongly unstable, and the instability first appears as a shear band followed by stabilized neck formation and propagation [4]. This is consistent with other studies on amorphous polymers [5-8].

Quasi-static tensile experiments are often performed on dog-bone specimens using contacting strain gauges or extensometers for strain measurement. However, the first of these only gives strain measurements at a point, and the second the average strain in a specimen, and both are unable to give information in experiments in which necking is observed; this also prevents the calculation of true stress [9].

If suitable images of the specimen can be obtained during deformation, digital image correlation (DIC), provides a solution to measure the full-field behaviour throughout the experiment [7-10]. Parsons *et al.* performed experiments on PC in which local strain (true strain) was extracted from DIC, and the true stress was estimated using the current cross-section area, assuming the stretch ratio in transverse and through-thickness directions were the same [7]. However, the formation of an inhomogeneous shear band and potential anisotropic deformation in the lateral and transverse directions at large strains can affect this calculation.

During the loading process, most mechanical energy is dissipated into thermal energy, while the rest of the energy is partially used for microstructural evolution [11], and hardening [12]. The heat generated from the plastic work can cause the temperature of the material to rise. It is well known that the mechanical behaviours of polymers are temperature- and rate-dependent, thus, a temperature rise during the tests can significantly

affect the mechanical response. Thermal cameras have been used to measure the temperature in uniaxial tension tests in several studies [13-15]. Moreover, the DIC and thermography techniques were combined to measure the temperature change and the onset of fatigue damage for a composite material [16]. Combining these contactless measuring techniques (DIC and thermal imaging) provides an opportunity to understand the interactions between thermal and mechanical behaviours, which can help build up a more accurate constitutive model.

In order to predict experiments with complex stress states (i.e. impact test), the intrinsic material properties, such as the stress-strain relationship during homogeneous deformation, should be first evaluated and described by a material model [17] because the deformation in a tensile test is inhomogeneous and much more difficult to interpret than tests with homogeneous deformation [18]. The investigation of constitutive models of polymeric materials started from the work of Haward and Thackray, who used models with two parallel springs to describe viscoelastic and post-yield behaviours [19]. Following that, many scholars developed time- and temperature-dependent thermomechanical constitutive models to interpret the constitutive behaviours of glassy polymers; commonly used models include the Boyce-Parks-Argon (BPA) model [20-22], the Oxford Glass Rubber (OGR) model [23-25], and the Eindhoven Glassy Polymer (EGP) model [26-28]. One method to incorporate these into commercial Finite Element (FE) code is to generate user-defined material behaviour as a subroutine using a material library, PolyUMod® [29], which has been used to simulate the tensile [30] and biaxial impact tests [17, 30]. In this material library [29], the three network model (TNM) has been explicitly developed for thermoplastic polymers and agrees well with experimental results for high density polyethylene (HDPE) [31] and Ultra-high molecular weight polyethylene (UHMWPE) [32].

The current paper presents a comprehensive study of the tensile response of polycarbonate, considering experimental data and analysis techniques. Tensile experiments were performed at speeds of 5 and 50 mm/min on flat dogbone specimens designed according to ISO 527 1A, with nominal gauge lengths of 80 mm. DIC

was employed to measure the deformation field on one of the specimen surfaces. At the same time, a thermal camera was used to image the other side of the specimen to monitor the temperature field. From the DIC outputs, axial strain data were extracted from different positions on the specimen, and the stress was estimated using three different methods. A time-temperature coupled viscoplastic constitutive model (TNM) [29, 32] was used to model the large strain tension deformation process. Firstly, stress-strain data from true strain rate controlled varying rate and temperature uniaxial compression experiments were used to find material parameters. Then, an FE model of the experiment was built and used to refine the parameters through comparison with the tensile data, including the local strains and temperature rises mentioned above. At the same time, the temperature change and Taylor Quinney Factor (TQC) obtained from the experimental and numerical study are compared. Following that, parametric studies were performed to build a further understanding of the large strain related parameters. The calibrated model was shown to describe the stress-strain curves and temperature evolution very well. This study demonstrates the more general need for this fully integrated approach to obtaining constitutive data from tensile experiments on polymers.

Material information and sample preparation

The Bisphenol A-Polycarbonate (PC) used in this study was LEXAM^{TM} RESIN 103R, provided by SABIC. Dogbone samples (ISO 527 1A) were injection moulded with gauge section dimensions 80 × 10 × 4 mm, as shown in Figure 1.

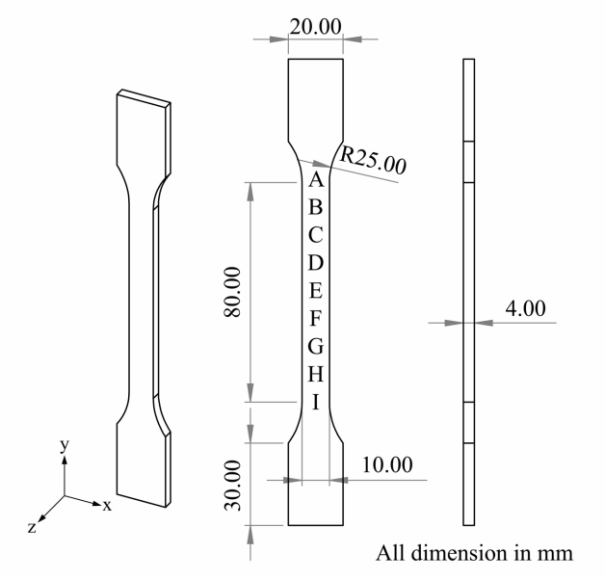

Figure 1. Geometry of the specimens used in uniaxial tension tests. Points A to I indicate the locations at which local strain measurements were later obtained.

To minimise the residual stress resulting from manufacturing, the specimens were annealed. The annealing profile consisted of a 25 °C/hour heat to 155 °C, which is 10 °C above the glass transition temperature (T_g ~ 145 °C). This temperature was held for six hours, following which it was decreased to room temperature at a 10 °C/hour cooling rate. During the annealing process, the specimens were sandwiched between two metal plates and a thermocouple was placed on one of the plates at a location 3 mm from the edge of the sample to confirm the temperature profile. The maximum dimension change of the samples was 1.5 %, and the removal of in-plane residual stress was confirmed using polarising films. The nominal heating profile, along with the thermocouple data for one of the specimens is shown in Figure 2(a). To inform the annealing process, a TA Q2000 differential scanning calorimeter (DSC) was used to measure the glass transition temperature (T_g). Starting with unannealed material, the specimen was heated to 180 °C, then cooled back to 100 °C and heated

again. The heating and cooling cycles were performed at 2 °C/min and data were recorded on both heating cycles. Data from these measurements, Figure 2(b), indicate a glass transition temperature of 145 °C.

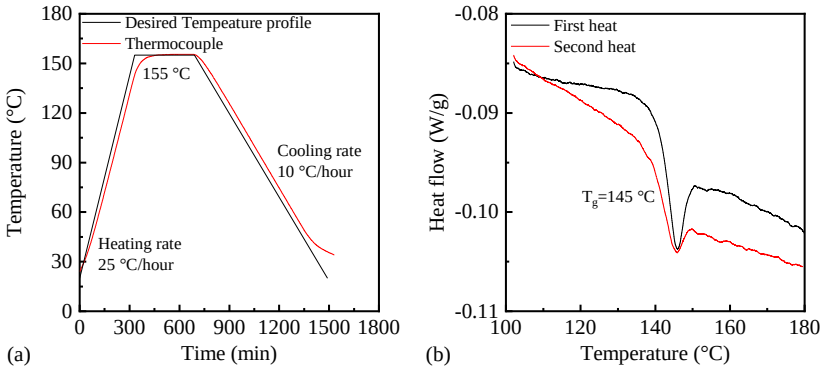

Figure 2. (a) Annealing temperature profile (b) DSC data showing glass transition temperature.

Experimental procedure

Calibration of thermal camera

PC is a transparent polymer with good infrared transmission, which is itself sensitive to thermal history and stress [33]. In these experiments, the emissivity was controlled by coating the specimen with black ink, which was found to deform with the specimen during loading. To confirm the value of the emissivity, a disk of material of diameter 5 mm and thickness of 3 mm was painted on one side and placed in contact with a hot plate whose temperature was measured using a thermocouple. The temperature of the hot plate was varied from room temperature to 60 °C, and the TELOPS FAST-IR M350 infrared camera used for the rest of the experiments presented in this paper was employed to read the temperature of the specimen. As shown in Figure 3, when using an emissivity of 1, the temperature of the specimen matches the thermocouple to within ± 0.5 °C.

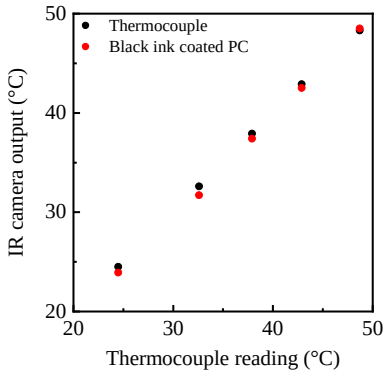

Figure 3. Comparison of IR and thermocouple temperature readings.

Testing procedure

Uniaxial tension experiments were performed on the annealed specimens using an Instron model 5582 screw-driven load frame with a 100 kN load cell at room temperature (around 24 C) and loading speeds of 50 and 5 mm/min. For the DIC measurements, a white background was produced on one face of the specimen using an airbrush, and the speckles are made by a black marker pen. Black ink was coated on the other face as described above. A Point Grey camera with a 60 mm Nikon lens was placed 960 mm from the sample surface

and used to obtain images for the DIC measurements. The thermographic images were acquired by an infrared (IR) camera with a resolution of 320 × 256 pixels^2; the frame rates were 100 and 10 Hz for 50 and 5 mm/min loading speeds, respectively. The adopted DIC and IR camera settings can be found in Table A1 in Appendix A.

Post-processing of experiments

Strain measurements

In order to obtain displacement, strain and strain rate information, the optical images were analysed using the commercial software MatchID® (www.matchid.eu, version 2022.2.1). In particular, to help understand the strain localization and deformation processes, nine data points were selected from the centreline of the specimen at 10 mm intervals along the gauge length, labelled as points A to point I in Figure 1. Strain data, in the form of Henkey (true) strain, were extracted at these points as functions of time, as well as from the first necking point, which occurred randomly in the gauge region.

Transverse true strain estimation and axial true stress calculation

The axial strains obtained above were then used to estimate the axial true stress at different points in the specimen. This requires an estimate of the transverse and through thickness strains, ε_{xx} and ε_{zz}. In this study, three approaches with different assumptions were used to estimate the strains and the axial stress (σ_{yy}) using each of the following methods:

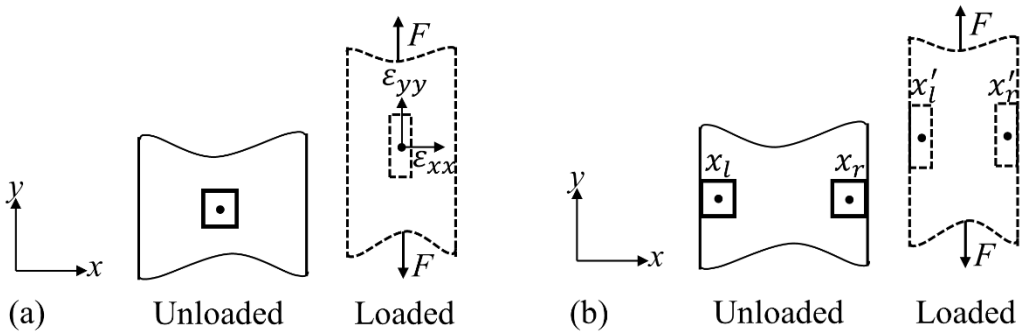

Figure 4. Illustration of stress calculations (a) Method 1 and 2 (b) Method 3.

In each case, it was assumed that the stretch ratio in transverse and through-thickness directions was the same: $\lambda_{xx} = \lambda_{zz}$ ($\varepsilon_{xx} = \varepsilon_{zz}$). The three approaches used for ε_{xx} and σ_{yy} were:

Method 1 (Figure 4(a)): to obtain ε_{xx} from the DIC at the same point as ε_{yy}, and calculate the stress as:

$$\sigma_{yy} = \frac{F}{A_0 \times \exp(2\,\varepsilon_{xx})} \tag{1}$$

Where A_0 is the initial cross-section area in the gauge area.

Method 2 (Figure 4(a)): to calculate ε_{xx} from ε_{yy} assuming constant volume, so that:

$$\varepsilon_{xx} = \varepsilon_{zz} = \frac{-\varepsilon_{yy}}{2} \tag{2}$$

$$\sigma_{yy} = \frac{F \times \exp(\,\varepsilon_{yy})}{A_0} \tag{3}$$

Method 3 (Figure 4(b)): to estimate ε_{xx} and σ_{yy} using data from the edge of the specimen as:

$$\varepsilon_{xx} = \ln\left(\frac{x_r^{'} - x_l^{'}}{x_r - x_l}\right) \tag{4}$$

$$\sigma_{yy} = \frac{F}{A_0 \times \exp(2\,\varepsilon_{xx})} \tag{5}$$

Experimental results

Force-displacement curves and optical Images

Several tests were conducted for each loading speed; the load-displacement curves obtained are shown in Figure 5. In this paper, one of the 50 mm/min tests is used as an example to illustrate the results and data analysis process; the numerical results presented in the next section are also based on this test.

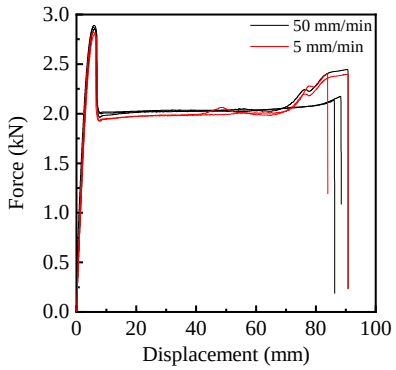

Figure 5. Force-displacement curves for tensile experiments at crosshead displacement speeds of 50 and 5 mm/min (In all tests, the specimens are tested to failure).

Figure 6 shows contours of axial true strain calculated using DIC for a 50 mm/min tension test at different times. The specimen experiences necking initiation, unstable neck propagation and steady necking propagation in succession, following which the neck extends to the whole specimen, the stress rises rapidly, and failure occurs.

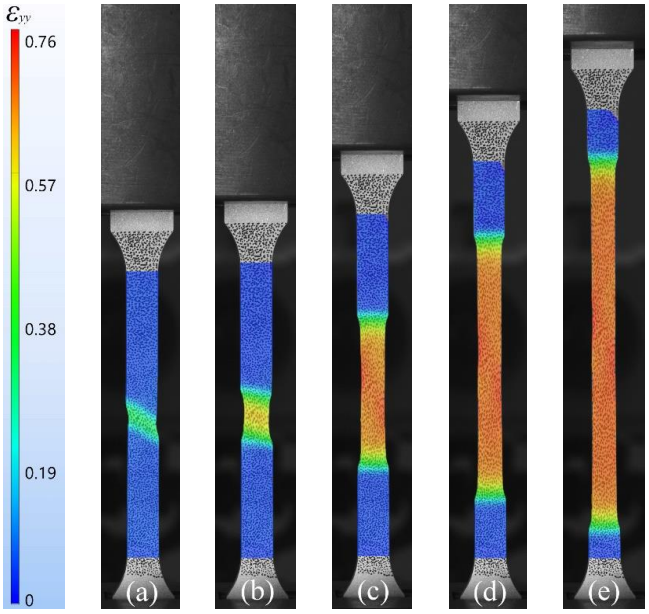

Figure 6. True (Hencky) strain maps obtained using DIC (a) Shear band initiation at 8.4 s (crosshead displacement = 7 mm) (b) unstable neck propagation at 12 s (10 mm) (c) stable neck propagation at 30 s (25 mm) (d) propagation towards the ends of specimen at 50 s (41.7 mm) (e) further propagation at 70 s (58.3 mm).

Axial strain and strain rate

Figure 7 shows strain and strain rate data extracted as functions of time for 10 locations on the specimen gauge length (Point A to I indicated in Figure 1, and Point Neck which occurred between Point E and F, this point was picked at the location of initial shear band formation, and in the centre of the specimen width). In Figure 7(a), the specimen is shown to deform homogeneously at axial true strain less than 0.06; however, once necking begins, the curves diverge. Close to the initial localisation, there is a very rapid increase in strain rate as the neck forms, whilst points distant from the neck experience a small drop in strain associated with the decrease in the force supported by the specimen, and resulting recovery of some of the elastic strain. As the neck progresses through the specimen, more distant points experience a rapid increase in the strain as they progress from elastic to plastic deformation, but the rates are not as high as at the Point Neck formation, where the speed of necking is greatly increased by the relaxation of elastic strain elsewhere in the specimen and load

chain. These data, combined with the displacement maps in the previous section, indicate why it is necessary to obtain full-field information rather than relying on overall force-displacement data to calibrate constitutive models.

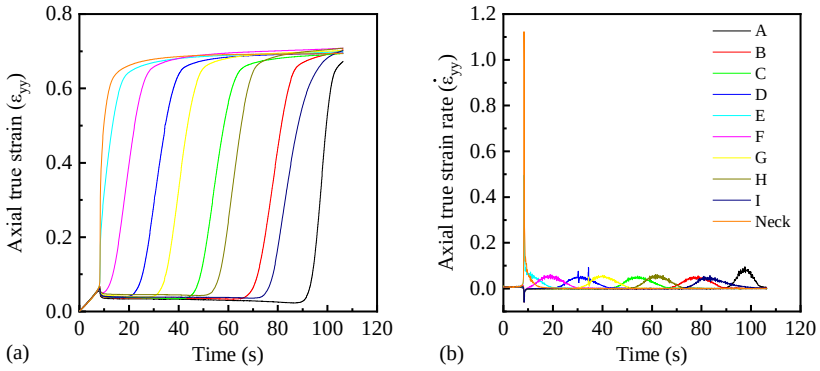

Figure 7. Data extracted from ten points in the gauge area, nine points evenly spaced as shown in Figure 1, plus an additional point at the location at which the neck formed (a) axial true strain vs time (b) axial true strain rate vs time. In this case, Point E was very close to Point Neck formation.

Transverse strain and uniaxial stress approximation

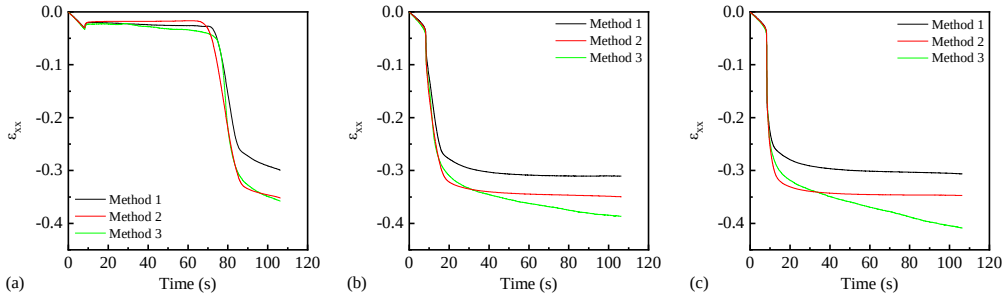

Figure 8. Transverse true strain against time (a) Point B (b) Point E (c) Point Neck.

Using the methods discussed in the previous section, transverse strain-time data were calculated. Data from three points, Point B (far from neck initiation area), Point E (near neck initiation area) and Initial neck, on the specimen are shown in Figure 8 as examples. It is observed that the transverse true strains are inconsistent with each other, explored further below. The true stress-strain curves for the same points are plotted in Figure 9, and the results obtained from these three methods are again shown not to agree at large

strains.

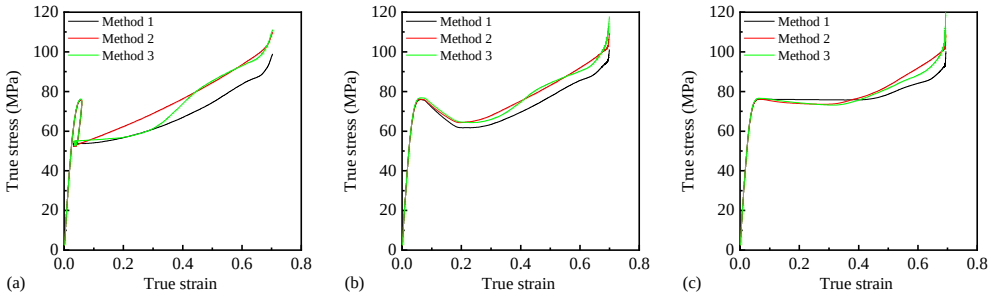

Figure 9. Uniaxial true stress-true strain curves, (a) Point B (b) Point E (c) Point Neck

To further understand the inconsistency of transverse true strain and true stress obtained using three different methods, the transverse true strain obtained directly from DIC is plotted against a horizontal position along a line through the centre of the initial neck, at a number of different times, Figure 10. Before necking, the value of ε_{xx} is the same at all points. Later on, however, the points closer to the edge experience larger transverse strains than those in the centre. This is consistent with the larger strains calculated using Method 3 above. It is noted that in this figure, the strains shown at $x = 0$ are equivalent to the 'Method 1' strains. The differences between Methods 1 and 2 may be errors owing to them being based on a single DIC location, or to the incompressibility assumption used in Method 2.

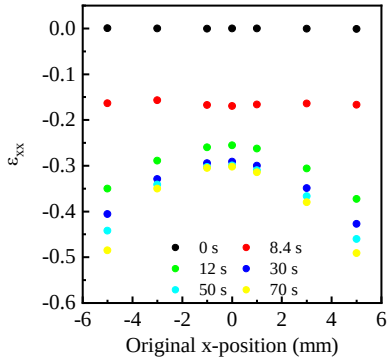

Figure 10. Transverse true strain against position for seven points in the line of the Point Neck

Using these three methods, true stress-strain curves were produced for the 10 axial locations considered above (Point A-I and Point Neck) in Figure 11. The curves obtained before yield are the same for the three different approaches; however, there are significant differences after yield. On the other hand, the stress-strain

curves for different points on the specimen are very similar, apart from the Point Neck and Point E nearby. At these two locations, the strain increases very rapidly after yield, and within a few seconds, re-joins the other stress-strain curves at a much larger strain. The other points tend to move more slowly along the curve, as expected from the lower strain rates observed in Figure 7. Figure 11 also shows the unloading of these points during the force drop that accompanies initial necking. Owing to the viscoelastic nature of the material, this does not exactly follow the initial loading path.

As well as the discrepancies from the different strain calculations, there is no way to accurately verify whether the strains in the transverse and through-thickness directions are the same. Thus, finite element (FE) simulations are required to better interpret the large strain data.

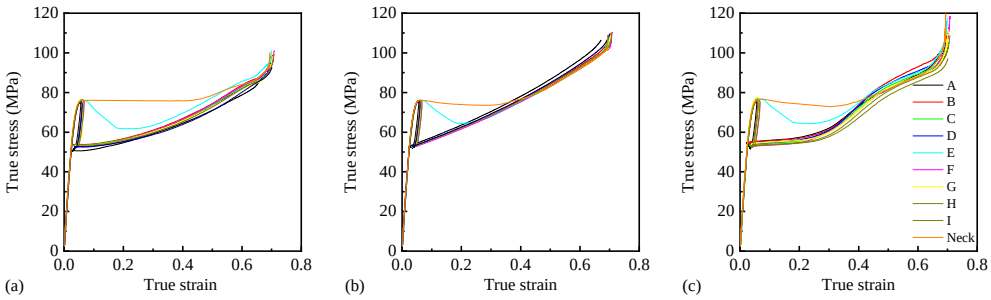

Figure 11. Uniaxial true stress vs true strain curves, (a) Method 1, (b) Method 2, (c) Method 3

Numerical model

Constitutive model summary

The three-network model (TNM) [29] was used to describe the tensile deformation behaviour of the polycarbonate. In this viscoplastic model, the stress is decomposed into three parallel networks: both network A and network B consist of an elastic and viscoplastic components, whilst network C is an elastic spring, as shown in Figure 12. The model behaviour is governed by a number of parameters, which affect the stress-strain behaviour as outlined in Figure 12 and Table 1. The implementation of this model is described in Appendix B, and the reader is referred to the literature for more detailed information [29, 34].

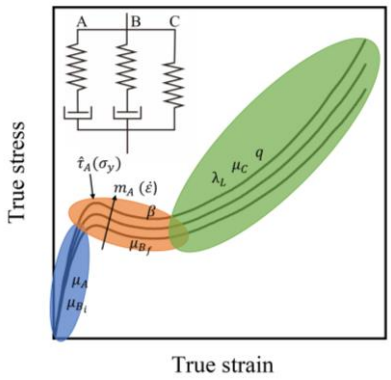

Figure 12. Schematic of three-network model, and illustration of where the model parameters (Table 1) affect the stress-strain response.

Table 1 Material parameters for three-network model used in Abaqus/Standard

Quantity	Fit to compression (Set 1)	Final to compression (Set Final)
Material parameters of PC		
Density, ρ	1.08 g/cm^3 [35]*	
Shear modulus of network A, μ_A	271.1 (MPa)	308.9 (MPa)
Locking stretch, λ_L	9.9	2.2
Bulk modulus, κ	4.4 (GPa) [36]	
Flow resistance of network A, $\hat{\tau}_A$	31.8 (24 °C)/ 27.5 (60 °C) (MPa)	38.5 (24 °C)/ 33.5 (60 °C) (MPa)
Pressure-dependence of flow, a	0.1	
Stress exponential of network A, m_A	40	
Initial shear modulus of network B, μ_{Bi}	271 (MPa)	233.2 (MPa)
Final shear modulus of network B, μ_{Bf}	7.7 (MPa)	13.5 (MPa)

Evolution rate of μ_{Bi}, β	14	18.2
Flow resistance of network B, $\hat{\tau}_B$	92.7 (MPa)	21.1 (MPa)
Shear modulus of network C, μ_C	2.5 (MPa)	5 (MPa)
Relative contribution of I_2 of network C, q	0	2
Thermal properties for PC		
Temperature factor, $\hat{\theta}$	0	
Temperature exponential, n	0	
Thermal expansion coefficient, α	0	
Thermal expansion reference temperature, θ_0	24 °C	
Specific heat capacity, C_p	1.065 J/ (g °C)	
Thermal conductivity, K	0.2 W/(m K) [35]	
Inelastic heat fraction, Taylor Quinney Factor (TQC)	0.9*	
Absolute zero temperature	-273 (°C)	
Stefan-Boltzmann constant	5.67 x 10^{-8} (kg s^{-3} K^{-4})	
Emissivity of black ink	0.99	

* In the product property report [35], the value of density (ρ) is 1.2 g/cm^3; at the same time, in this project all plastic work is assumed to be converted to heat during the large strain deformation, thus, the inelastic heat fraction (TQC) is 1.0. However, the default value of TQC in Abaqus/standard is 0.9, which cannot be changed using the current user-defined material model. According to the formula for simulating the temperature rise, $\Delta T = \frac{TQC}{\rho C_p}\int_0^{\varepsilon_{yy}} \sigma d\varepsilon_p$, lowering the density and using the default TQC of 0.9 provides the same effect as TQC = 1 with normal density when simulating the temperature rise.

Finite element model

A finite element (FE) model was built using a commercial FE software Abaqus/standard [37]. The Three Network Model model was incorporated in Abaqus as a user material subroutine (UMAT) using the PolyUMod® material library [29]. Eight-node thermally coupled brick, trilinear displacement elements (C3D8T) were used with a 1 mm global mesh size with 8256 elements. The final results obtained were found to be independent of mesh size for global mesh sizes of 0.8, 1, 1.3 and 2 mm (Appendix C). As Figure 13(a) shows, one end of the specimen is fixed, and a tensile displacement was applied on the other end. The temperature was set as 24 °C to match the experiment, and the thermal conduction and radiation are enabled to capture the heat dissipation during the large strain deformation process. In order to trigger the shear band in the FE model, small artificial material or geometric defects have been utilized in many previous numerical studies [5-7, 38-40] to form the shear band or strain localization, and the authors state that there is no significant effect on the post-localisation results. In our study, two 0.05 mm deep symmetric perturbations in the *x*-direction were created; these artificial defects are small enough to have no significant effect on the post-yield

behaviours: a comparison of force-displacement curves with and without defects are plotted in Figure 13(b).

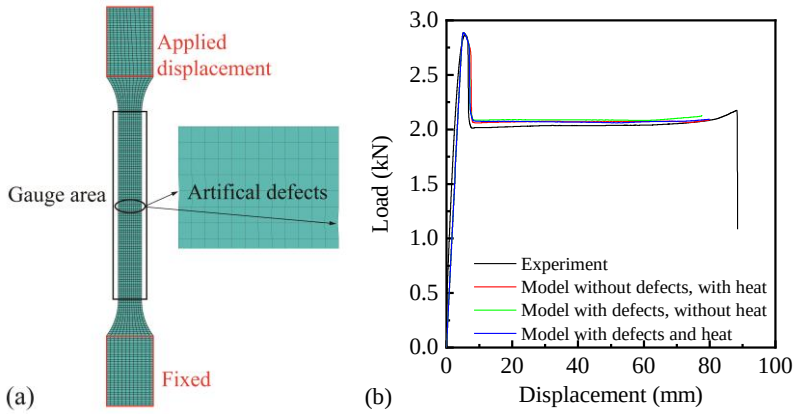

Figure 13. (a) Mechanical and thermal boundary conditions on the tensile specimen (b) Load-displacement curves comparison between experiment and model with different assumptions: with and without defects and with and without heat effects (thermal radiation and heat conduction).

Determination of constitutive parameters - Step 1: Compression experiments

It is challenging to obtain the material parameters directly during the tensile tests because of the necking instability. Therefore, true strain-rate controlled compression experiments were performed at varying rates and temperatures, and the data obtained were used to determine initial material parameters in the constitutive model.

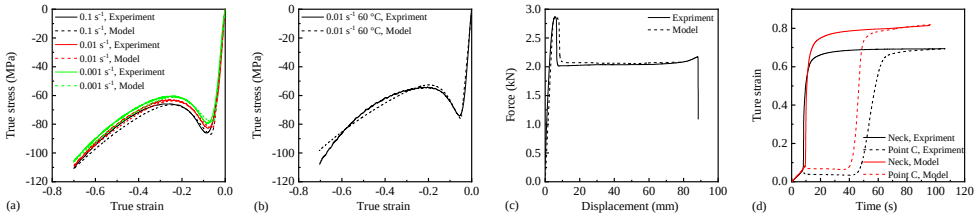

Figure 14. Constitutive model using parameter Set 1 compared to (a) rate-dependent compression tests, (b) temperature-dependent compression tests; experimental and simulation results showing (c) load-displacement curve (d) axial true strain - time curve.

The varying rate compression test data in Figure 14(a) were used to estimate the initial parameters. Firstly, the sum of μ_A and μ_{Bi} is used to fit the stress-strain curve before yield. Because elastic modulus at room temperature is not very sensitive to the strain rate, over the experimental range of rates and temperature

(Dynamic Mechanical Analysis (DMA) data demonstrating this are shown in Appendix D), a constant summed value of μ_A and μ_{Bi} were used to simulate the pseudo-linear-elastic behaviour. As a starting approximation, the individual values of μ_A and μ_{Bi} were made equal, as shown in Table 1 Set 1.

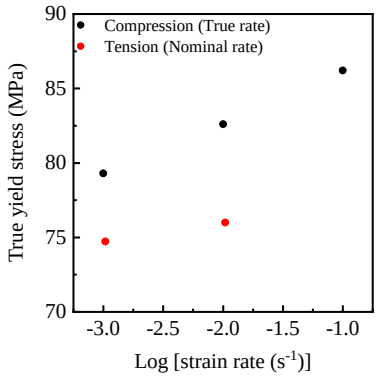

Figure 15. Compression and tension yield stress against strain rate.

The value of $\hat{\tau}_A$ was determined by fitting to the rate dependence of the yield stress, and the pressure-dependence parameter a can be determined from,

$$\frac{|\sigma_{cy}|}{\sigma_{ty}} = \frac{3+a}{3-a} \tag{6}$$

where, σ_{cy} and σ_{ty} are compression and tension yield stresses presented in Figure 15. The rate-dependent post-yield behaviour is determined by m_A. The strain-softening process is dominated by μ_{Bf} and β in network B, and the strain-hardening at large strains is defined using parameters λ_L, μ_C and q; these parameters were fitted to the compression curves using PolyUMod, which uses a minimization algorithm based on the Nelder-Mead simplex methods [29, 32].

In the TNM, temperature dependence is usually incorporated by multiplying the whole stress-strain relationship by $\left(\frac{\theta}{\theta_0}\right)^n$, however, this changes the whole curve, including the modulus. The modulus of polycarbonate between room temperature and 60 °C is approximately constant (Appendix D and Figure 14(a)). The $\hat{\tau}_A$ in compression tests at 60 °C is changed to fit the yield stress without modifying other parameters in this model, as shown in Figure 14(b). The specific heat capacity C_p was obtained from Modulated Differential

Scanning Calorimetry (MDSC) using the low mass T-zero pan (Appendix E).

These parameters were then used in the simulation of the tensile experiment. The results obtained show excellent agreement with the global load-displacement curve (Figure 14(c)); however, they do not correctly describe the local strain-time curves of different points, Figure 14(d). Hence, further parameter refinement was performed.

Determination of constitutive parameters - Final values

After the initial fit of the material parameters, the parameter set was updated manually to better fit the tensile experiments. Some of the values derived above were kept constant: the sum of the shear moduli (i.e. μ_A + μ_B, but not the moduli themselves), the bulk modulus κ, the pressure-dependence of flow (a), the stress exponential of network A (m_A) and the thermal properties. In addition, the stress reduction caused by temperature rise is simulated using reduced $\hat{\tau}_A$.

After some trials, the resulting material parameters, which are able to fit the global (Figure 16(c)) and local (Figure 16(d)) behaviours, are listed in Table 1, as Set Final. Figure 16 also shows the compression curves implied by these parameters. The key observation here is that modifying the parameters has made little difference to the overall force-displacement curve, but has significantly improved the local strain-time curves. This is expected because the force is determined by the stress required to propagate plastic displacement along with the specimen; at all times, this displacement moves into a region of the specimen in which the strain is the same and the temperature is equal to the initial, ambient temperature: the only material parameter affecting the propagation is the initial yield stress. Hence, the force-displacement curve is a poor validation of constitutive response. As shown in Figure 16(c), the models predicted using parameters Set 1 and Set Final give a very similar response in load-displacement, and they are consistent with the experimental results well. However, the local strain-time curves in Figure 16(d) present good agreement with experimental results, not like the simulation results shown in Figure 14(d). A parametric study of large-strain behaviour related

parameters are shown in the next section and Appendix F.

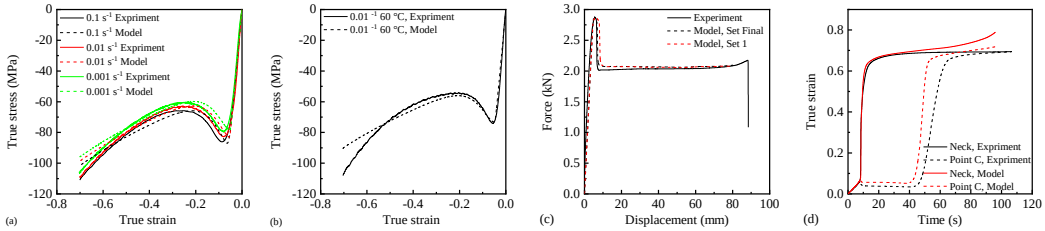

Figure 16. Constitutive model using parameter Set Final compared to (a) rate-dependent compression tests (b) temperature-dependent compression tests; experimental and simulation results showing (c) load-displacement curves (d) axial true strain-time curve.

Further comparison between experimental and simulation results (final parameters)

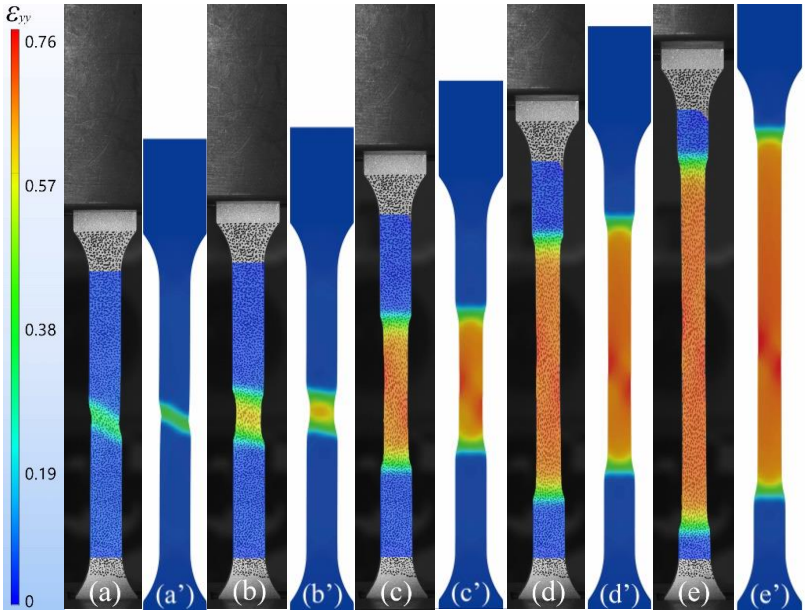

Figure 17. Comparison of model and experimental axial strain data at 8.4, 12, 30, 50, 70 s: (a) to (e) axial strain obtained from DIC; (a') to (e') axial strain obtained from FE model.

In the experiment, the shear band initiates at 8.4 s (Figure 17 (a)), and the strain quickly jumps to 0.35; the numerical model (Figure 17(a')) agrees well with the DIC results. Following the initiation of the strain localization, the specimen experiences an unsteady necking propagation, Figure 17(b), (b'). After that, the shear band propagates stably towards both ends of the specimen as it is further deformed; at 30 s, the unsymmetrical shear band has evolved into a steadily propagating symmetrical neck, Figure 17(c), (c'), which

continues to extend. In all cases, the FE simulation agrees well with the experimental measurements. Lu and Ravi-Chandar demonstrated the process of neck formation from micro shear bands in polycarbonate [4]. The macroscopic behaviour of their specimens was similar to that observed in the current study.

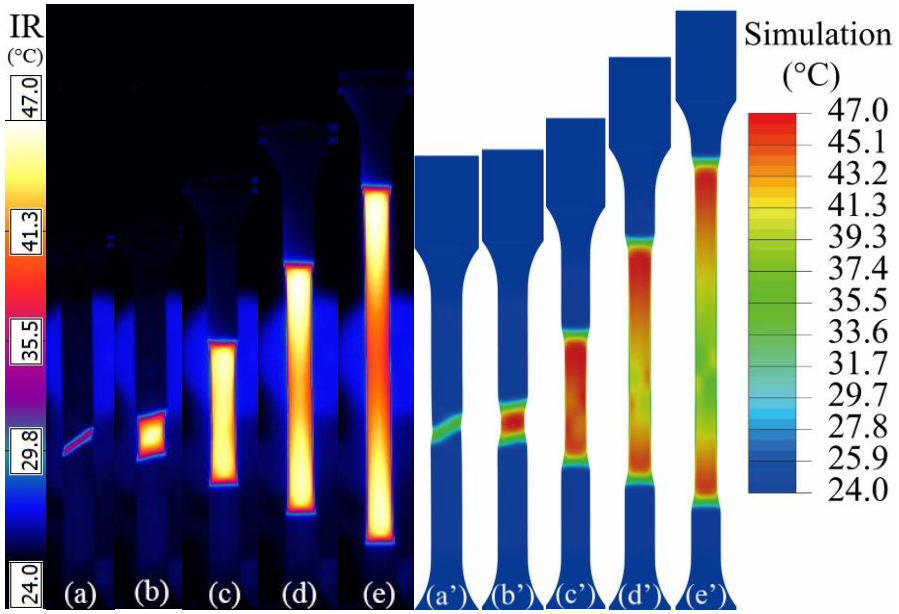

Figure 18. Comparison of model and experimental data at 8.4, 12, 30, 50, 70 s, (a) to (e) Experimental temperature change obtained from IR camera; (a') to (e') Numerical temperature change extracted from FE model.

Considering the temperature rises, a comparison of the experimental and numerical temperature profiles are plotted for different times in Figure 18. Images in Figure 18 indicate good agreement between the experiment and model, with a rapid rise in temperature just behind the plastic deformation front, but the centre of the specimen cooling radiatively as the experiment progresses.

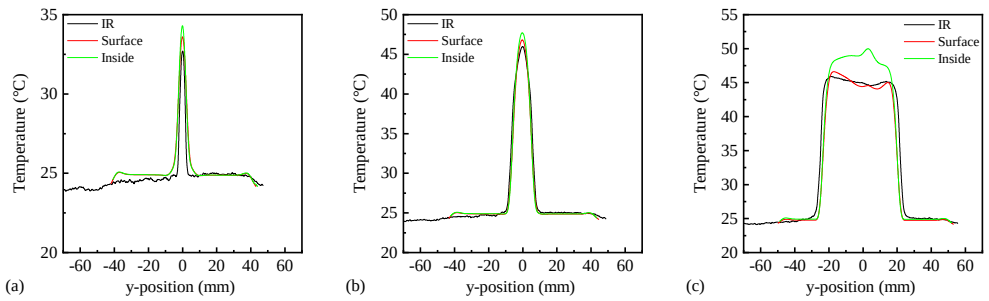

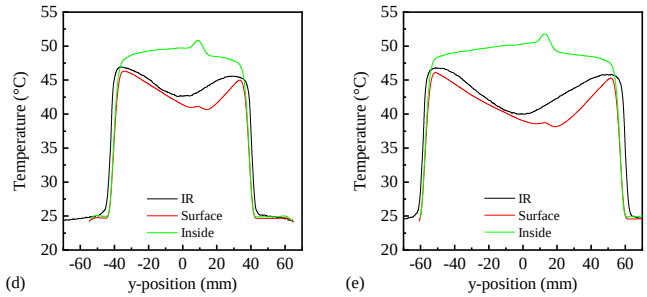

Figure 19. Experimental (IR) and numerical (surface, inside) temperature profile down the centre of the gauge area at (a) shear band first occurring at 8.4 s (b) unstable neck propagation at 12 s (c) stable neck propagation at 30 s (d) neck extension to both ends at 50 s (e) 70 s.

In order to perform more quantitative comparisons, temperature data were extracted from a line down the centre of the specimen and the model, Figure 19. For the model, the surface temperature is shown along with the internal temperature extracted from the middle of the specimen (i.e. between the second and third of the four elements). These are different because of the temperature gradient needed to support radiation from the specimen surface. The y-positions are given with reference to the position of the first necking point. In Figure 19 (a), the model outputs agree well with the experimental data when strain localization occurs at 8.4 s. The inelastic area becomes broader as the shear band propagates, and the 'hot area' extends correspondingly. At 12 s, all three sets of data show a small peak, corresponding approximately to the first necking area, but the effect of the radiation is already visible in the difference between the surface and internal temperatures from the simulation[1]. At 30 to 70 s, the surface temperature in the simulation shows similar behaviour to the experiment: the temperature at the first necking area drops due to radiation from the specimen surface. Even though the specimen continues to deform, the plastic deformation rate is minimal here, so there is almost no heat generation. The exact value of the surface temperature from the FE model is a very good match to the

[1] The temperature difference between the surface of the specimen and the centre may seem large, but is consistent with the gradient required to support radiation from the specimen surface. For a surface temperature of 40 °C and an emissivity of 1, the radiation is calculated from the Stefan-Boltzmann constant σ as $\sigma T^4 = 5.7 \times 10^{-8} \times 313^4 = 550$ W m^{-2}. At 60 s the temperaure difference at the centre is approximately 8 °C over a distance of 2 mm. This implies a heat flow of $k\,\Delta T/\Delta x = 0.2 \times 8 / 0.002 = 800$ W m^{-2}, which is reasonably consistent.

experiment. Discrepancies may be due to one of the thermal parameters, particularly the assumed conversion of plastic work to heat; it is also possible that the specific heat capacity or thermal conductivity changes with either temperature or strain.

Investigation of large-strain parameters

A parametric study was performed for the large strain behaviour of the three-network model since the elastic modulus and temperature-, rate-, and pressure-dependent yield stresses fit well with the experimental data. The parameters investigated were locking stretch (λ_L), final shear modulus of network B (μ_{Bf}), evolution rate of μ_B (β), shear modulus of network C (μ_C) and relative contribution of I_2 of network C (q). Their values were changed in turn by ±25% from those in Table 1 'Set Final', and the strain-time data for two points on the specimen was compared, in addition to the global force-displacement curves.

The effects of varying λ_L are shown in Figure 20 (a) and (a'). The load-displacement curves are very similar apart from the one produced at the largest value. As expected, the initial value of λ_L equaling 2.2 gives the best fit to the experimental results; the timing of the strain increase at point C does not perfectly match the experiment because the necking propagation is not symmetrical in the experiment. Furthermore, for large values of λ_L (which implies less strain hardening), a second necking instability can form at the location of the first neck, which is interesting but not observed in the experiment.

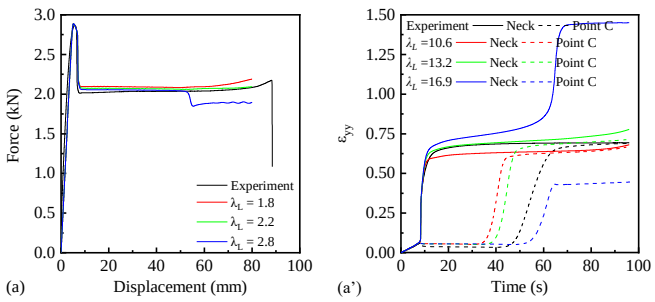

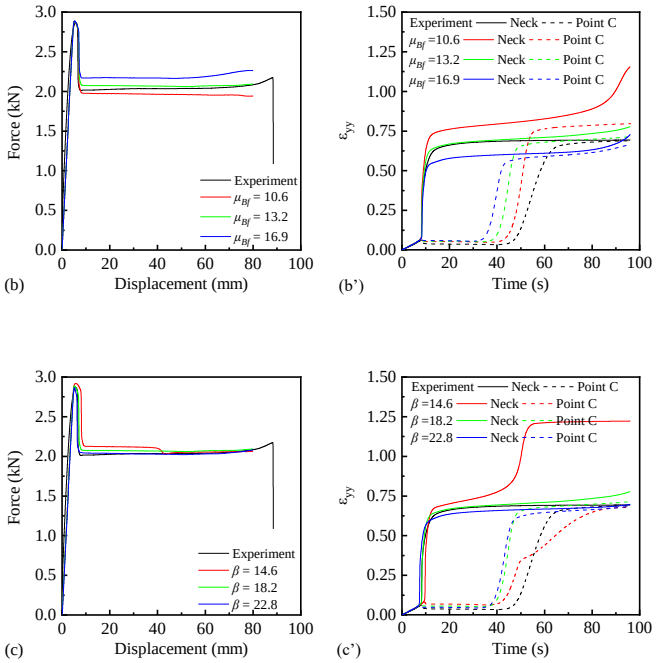

Figure 20. Effects of λ_L (a), (a'); μ_{Bf} (b), (b'); and β (c), (c') on the load-displacement and strain-time curves.

The residual shear modulus of network B, μ_{Bf} controls the strain-softening process. In Figures 20 (b) and (b'), the magnitude of the force drop increases with the lower μ_{Bf} Further, the inflection point of the strain-time curve occurs later, and the final strain is larger because it becomes more difficult for the plastic deformation to propagate (the force is lower), so the material deforms to a larger strain post-yield to achieve a high enough stress.

The evolution rate of shear strength of network B (β) controls the speed of stress decrease from yield stress to the lowest peak stress after yield. To understand the influence of β on large strain deformation, two values of 14.6 and 22.8 are added to compare with the initial value of 18.2 in parameter Set Final. Lowering β (14.6) can increase the peak force and delay the yield occurring, as presented in Figure 20(c) and (c'). In contrast, an increase of β can cause a lower peak force and bring the yield forwards because the softening area is narrowed. The forces obtained from three different values of β overlap when the model is stretched around 40 mm. This results from the value of residual strength of network B: μ_{Bf} is kept constant when investigating

the effects of β. Interestingly, for small values of β, a second necking instability can be observed at the location of neck initiation, which is not observed in the experiment.

The network C related parameters: the shear modulus of network C (μ_C), and relative contribution of I_2 of network C (q) are discussed in Appendix F.

Discussion

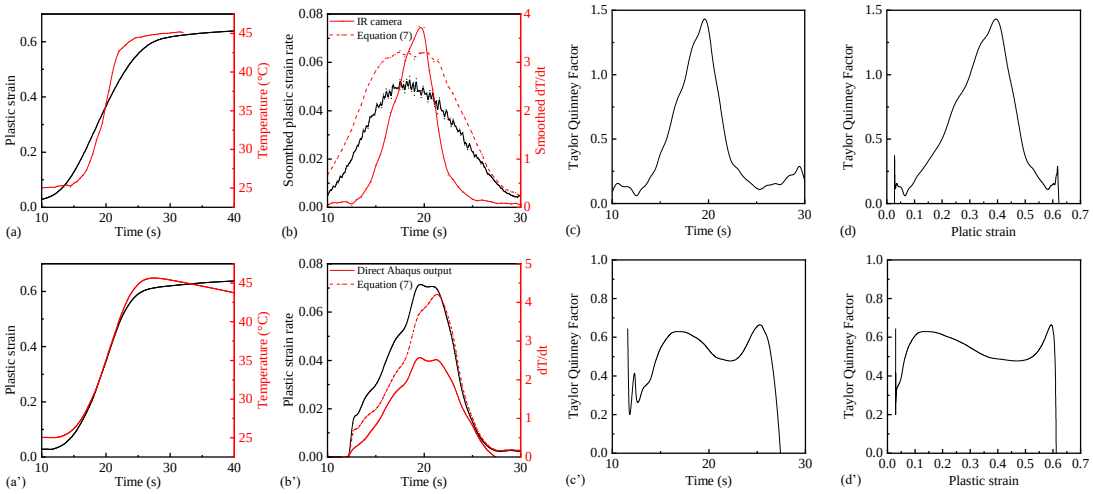

Figure 21. Experimental ((a) to (d)) and numerical ((a') to (d')) thermal behaviours of Point F.

The results above have presented an integrated method for fitting a constitutive model for polycarbonate to compressive and tensile experiments, and in particular, have shown that the global force-deformation behaviour is not sensitive to many of the model parameters, meaning that the fit is further enhanced by the use of local strain fields, in this case, obtained from DIC. Further, temperature maps have also been obtained. These temperature maps provide a further opportunity to examine the conversion of work to heat in the specimen. Whilst a full analysis [41] is beyond the scope of this research, it is instructive to make a simple comparison of the experimental and FE data.

Figure 21 shows the steps required to calculate the so-called Taylor-Quinney factor (TQC), the fraction of plastic work converted into heat using data from the experiment and the final Abaqus simulation. In this case, the so-called differential value is calculated. This represents the instantaneous conversion of work to heat. Firstly, in Figure 21 (a) and (a'), the plastic strain and temperature are obtained for a location on the specimen. In this case, it is point F in Figure 1. Whilst it is initially tempting to perform these calculations at the location of the initial neck, the very high instantaneous strain rate during neck formation makes this more challenging experimentally: imaging speeds of order 1000 frames per second would be required to obtain sufficient data, and the bandwidth of the load cell (and load chain) would probably be insufficient for the stress measurements.

Having obtained the plastic strain, the plastic strain rate is obtained. The experimental data are smoothed using a moving average. The expected rate of temperature rise can now be calculated from the stress and plastic strain rate using

$$\frac{\mathrm{d}T}{\mathrm{d}t} = TQC\frac{\sigma}{\rho C_p}\frac{\mathrm{d}\varepsilon_p}{\mathrm{d}t} \tag{7}$$

This can be compared to the value of dT/dt measured using the thermal camera (experiment), or output directly from Abaqus (simulation) The ratio of the measured value of dT/dt to calculated value of $\frac{\sigma}{\rho C_p}\frac{\mathrm{d}\varepsilon_p}{\mathrm{d}t}$ therefore gives the value of TQC. The variation of the TQC with time, or strain, is very interesting and because it peaks at a value greater than 1, indicates that energy is stored in the specimen before being released as heat. This analysis does not take into account heat transfer within the specimen (or indeed radiation from the specimen surface). Hence, it is instructive to compare the experimental data to equivalent calculations using the model outputs, in which these effects are implicitly considered. Here, it is remembered that the model used TQC = 0.9, with a modified density. Comparison of the data, particularly Figure 21(c) and (c') shows that whilst a more detailed analysis is required, the observed increase in the TQC above 1, in the experimental data, does appear to reflect a material response, and is not just an artefact of the experiment. Further work is required on this.

Conclusions

The large strain tensile response of polycarbonate has been investigated using tensile experiments instrumented with Digital Image Correlation (DIC) system and an infrared (IR) camera. In all experiments, a shear band was observed; combined with relaxation in the rest of the specimen and load chain, this causes a very high strain rate at the point of initial yielding. As the plastic deformation propagates from this initial shear band, a lower strain rate deformation is observed sequentially at points along with the specimen. A significant temperature rise (~24 °C in experiments at 50 mm/min) is observed during this plastic deformation. Using a combination of DIC and axial load measurements, it is possible to produce stress-strain curves for the material; however, these are highly dependent on the assumptions used to calculate the strains perpendicular to the loading axis.

Using one of the experiments at 50 mm/min as an example, a constitutive model was calibrated. The calibration was initially based on compression test data. When applied to a finite element (FE) simulation of the tensile experiment, there was an excellent agreement with the load-displacement behaviour, but not with local strain-time data obtained from different points on the specimen. This indicates that tensile force-displacement curves are not a good validation (or calibration) of constitutive models. Instead, the model parameters were updated to make it match the strain-time contours. A parametric study was then performed, which confirmed again that the force-displacement data are weakly dependent on the constitutive parameters, whilst the strain-time curves are highly dependent. The temperature rises predicted by the FE model thus obtained were shown to have very good agreement with those from the experiments. A preliminary study of heat generation in the specimen was performed.

Fundamentally, the tensile test is not only a test of constitutive behaviour, but also of structural (specimen geometry) response. Hence local and global behaviours must be considered in order to separate these responses if model parameters are to be obtained.

CRediT authorship contribution statement

Peihao Song: Conceptualisation, Methodology, Investigation, Formal analysis, Writing - original draft. **Akash R. Trivedi:** Methodology, Investigation, Writing – review & edit. **Clive R. Siviour:** Conceptualisation, Project administration, Supervision, Writing – review & edit, Funding acquisition.

Declaration of competing Interest

The authors declare that they have no known competing financial interests or personal relationships that could have appeared to influence the work reported in this paper.

Acknowledgements

This research forms part of the research programme of DPI, project 827t19, *Impact Modelling of Polymers: high-Rate Experiments for Solid-state Simulations* and the materials were kindly supported by Saudi Basic Industries Corporation (SABIC). The authors thank our colleagues on this project, Dr David Chapman in the Solid Mechanics Group at the University of Oxford, for useful suggestions on thermal analysis, and Dr Davide De Focatiis and Grace Owen at the University of Nottingham for helpful discussions. We are very grateful for the support of Nick Hawkins for DMA and DSC experiments, and to the technicians of the Solid Mechanics Group (especially Andy Bateman) for specimen preparation.

For the purpose of Open Access, the authors have applied a CC BY public *copyright license to* any Author Accepted Manuscript (AAM) version arising from this submission.

Data Availability

All data supporting this study will be made openly available from the Oxford University Research Archive at: DOI: 10.5287/bodleian:R8apaQJ9g

Appendix A. DIC and IR setup

Table A1 Digital Image Correlation and Infrared camera Setup

Loading speeds (mm/min)	50	5
Adopted Digital Image Correlation (DIC) Setup		
Camera (Point Grey)	GS3-U3-41C6M-C	GS3-U3-120S6M-C
Image resolution (pixel)	2048 x 2048, 10-bit	4240 x 2824, 14-bit
Frame rate (frame/s)	10	2
Lens	Nikon 60 mm Lens	
Field of view (pixels)	288 x 2048	380 x 2824
Pixel to mm conversion	0.01010	0.06135
Stand-off distance (mm)	960	
Speckle size (pixels)	≈ 7	≈ 10
DIC software	MatchID, version 2022.1.1	
Image filtering	Gaussian, 5 x 5 pixel kernel	
Subset size (pixel)	21	25
Step size (pixel)	5	3
Subset shape function	Quadratic	
Matching criterion	Zero-normalized sum of square differences (ZNSSD)	
Interpolant	Bicubic polynomial interpolation	
Strain tensor	Hencky (True) strain tensor	
Estimates progress history	Spatial and updated reference	
Strain window size	15 x 15 pixels^2, Quadratic Quadrilateral	
Adopted Infrared (IR) camera Setup		
Camera	Telops Fast-IR M350	
Exposure time	1000 μs	
Frame rate (frame/s)	100	10
Field of view (pixel)	180 x 512	
Resolution and bit depth	96 x 96 (dpi), 24-bit	
Pixel to mm conversion	0.4	
IR software	IR reveal, version 2022. 2. 1	

Appendix B. Constitutive model [29]

The deformation gradient for network A can be decomposed into elastic and viscoplastic components as,

$$F = F_A^e F_A^v \tag{B1}$$

The Cauchy (true) stress loading on network A is simulated using a temperature-dependent eight-chain model [21]:

$$\sigma_A = \frac{\mu_A}{J_A^e \overline{\lambda_A^{e*}}}\left[1 + \frac{\theta - \theta_0}{\hat{\theta}}\right]\frac{\mathcal{L}^{-1}\left(\overline{\lambda_A^{e*}}/\lambda_L\right)}{\mathcal{L}^{-1}(1/\lambda_L)}\mathrm{dev}[b_A^{e*}] + \kappa(J_A^e - 1)1 \tag{B2}$$

Here μ_A is the shear modulus of network A, $J_A^e = det[F_A^e]$, $\lambda_L$is the locking limitation of the chain, θ and θ_0 are the current temperature and reference temperature, respectively, $\hat{\theta}$ is a material property representing the relationship between temperature and stiffness, $b_A^{e*} = (J_A^e)^{-2/3} F_A^e (F_A^e)^T$ is the Cauchy-Green deformation tensor, $\overline{\lambda_A^{e*}} = (\mathrm{tr}[b_A^{e*}]/3)^{1/2}$ is the effective chain stretch length according to the eight-chain theory [21], $\mathcal{L}^{-1}(x) = \coth(x) - 1/x$ is the inverse Langevin function, κ is the bulk modulus.

Similarly, the stress acting on network B is also separated into elastic and viscoplastic components $F = F_B^e F_B^v$, and the Cauchy stress for network B is based on the same eight-chain assumptions used for network A:

$$\sigma_B = \frac{\mu_B}{J_B^e \overline{\lambda_B^{e*}}}\left[1 + \frac{\theta - \theta_0}{\hat{\theta}}\right]\frac{\mathcal{L}^{-1}\left(\overline{\lambda_B^{e*}}/\lambda_L\right)}{\mathcal{L}^{-1}(1/\lambda_L)}\mathrm{dev}[b_B^{e*}] + \kappa(J_B^e - 1)1 \tag{B3}$$

In this equation, the definition of the initial parameters is the same as network A. However, the effective shear modulus of network B is evaluated with plastic strain from an initial value of μ_{Bi} to the final value of μ_{Bf} as

$$\dot{\mu}_B = -\beta\left[\mu_B - \mu_{Bf}\right] \cdot \dot{\gamma}_A. \tag{B4}$$

The model can hence capture the evolution from yielding to large strain flow.

The stress loading on network C is calculated using the eight-chain model with first-order I_2 dependence, whose representation is similar to the Mooney-Rivlin model with non-Gaussian chain statistics [42],

$$\sigma_C = \frac{1}{1+q}\left\{\frac{\mu_C}{J\lambda_{chain}}\left[1+\frac{\theta-\theta_0}{\hat{\theta}}\right]\frac{\mathcal{L}^{-1}(\lambda_{chain}\backslash\lambda_L)}{\mathcal{L}^{-1}(1\backslash\lambda_L)}\,\mathrm{dev}[b^*] + \kappa(J-1)1 + q\frac{\mu_C}{J}\left[I_1^* b^* - \frac{2I_2^*}{3}I - (b^*)^2\right]\right\} \tag{B5}$$

where the definition of J, b^* and λ_{Chain} are the same as the network A and B, and the magnitude of the I_2 dependence is dominated by q.

The total Cauchy stress in this model is the sum of the stresses in these three networks,

$$\sigma = \sigma_A + \sigma_B + \sigma_C \tag{B6}$$

For the rate kinematics of this material model, the effective deviatoric flow rate of network A is estimated using the power-flow equation,

$$\dot{\gamma}_A = \dot{\gamma}_0 \cdot \left(\frac{\tau_A}{\hat{\tau}_A + aR(p_A)}\right)^{m_A} \cdot \left(\frac{\theta}{\theta_0}\right)^n \tag{B7}$$

where $\dot{\gamma}_0 \equiv 1/s$ is a constant introduced for dimensional consistency, $p_A = -[(\sigma_A)_{11} + (\sigma_A)_{22} + (\sigma_A)_{33}]/3$ is the hydrostatic pressure, $R(x) = (x + |x|)/2$ is the ramp function, and $\hat{\tau}_A$, a, m_A and n are material parameters. In addition, the velocity gradient of the viscoelastic flow of network A is presented as,

$$\dot{F}_A^v = \dot{\gamma}_A F_A^{e-1}\frac{\mathrm{dev}[\sigma_A]}{\tau_A}F \tag{B8}$$

The total velocity gradient of network B can be predicted as similar to the network A,

$$\dot{\gamma}_B = \dot{\gamma}_0 \cdot \left(\frac{\tau_B}{\hat{\tau}_B + aR(p_B)}\right)^{m_B} \cdot \left(\frac{\theta}{\theta_0}\right)^n \tag{B9}$$

and the definition of $\dot{\gamma}_0$, $\hat{\tau}_B$, p_B, a, m_A and n are similar to network A. Moreover, the velocity gradient of the viscoelastic flow of network B is,

$$\dot{F}_B^v = \dot{\gamma}_B F_B^{e-1}\frac{\mathrm{dev}[\sigma_B]}{\tau_B}F \tag{B10}$$

Appendix C. FE model

The mesh sensitivity is investigated using the global mesh size of 0.8, 1, 1.3 and 2 mm with the element type of C3D8T. The Point Neck, 10 and 20 mm from this neck point are extracted as an example to show that the simulation results are independent of the mesh size using this element type.

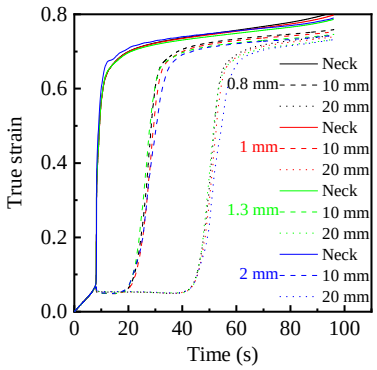

Figure C1. Mesh sensitivity using C3D8T elements of four different sizes.

Appendix D. Dynamic mechanical analysis (DMA) results

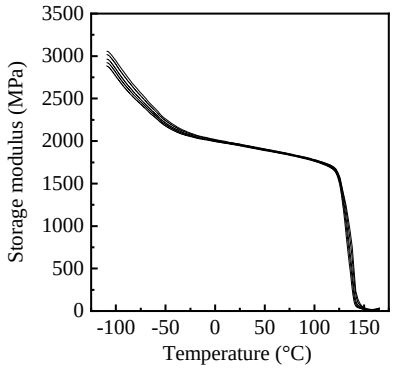

Figure D1. Data from DMA experiments performed using single cantilever beam specimens at frequencies from 0.5 to 10 Hz and temperatures from -110 to 180 °C.

Appendix E. Modulated Differential Scanning Calorimetry (MDSC) result

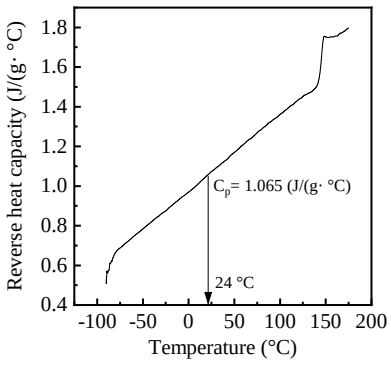

Figure E1. MDSC test for PC using T-zero pan with 2 °C/min temperature increment and ±0.6 °C amplitude.

Appendix F. The effects of network C related parameters on large strain deformation

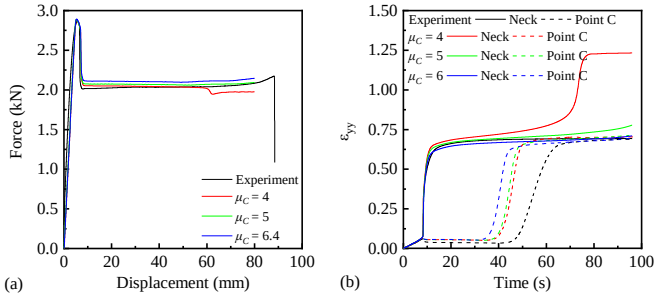

Figure F1. Effect of changing μ_C on the large strain deformation

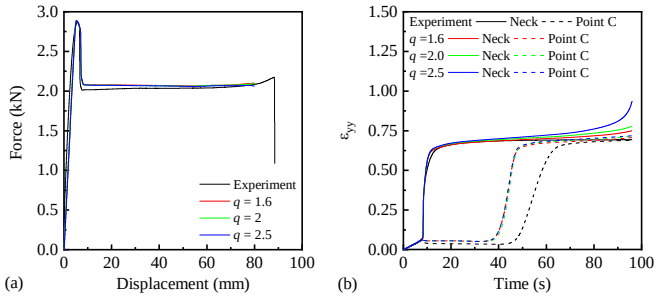

Figure F2. Effect of q on the large strain deformation.

Appendix G. Thermal images at different loading speeds

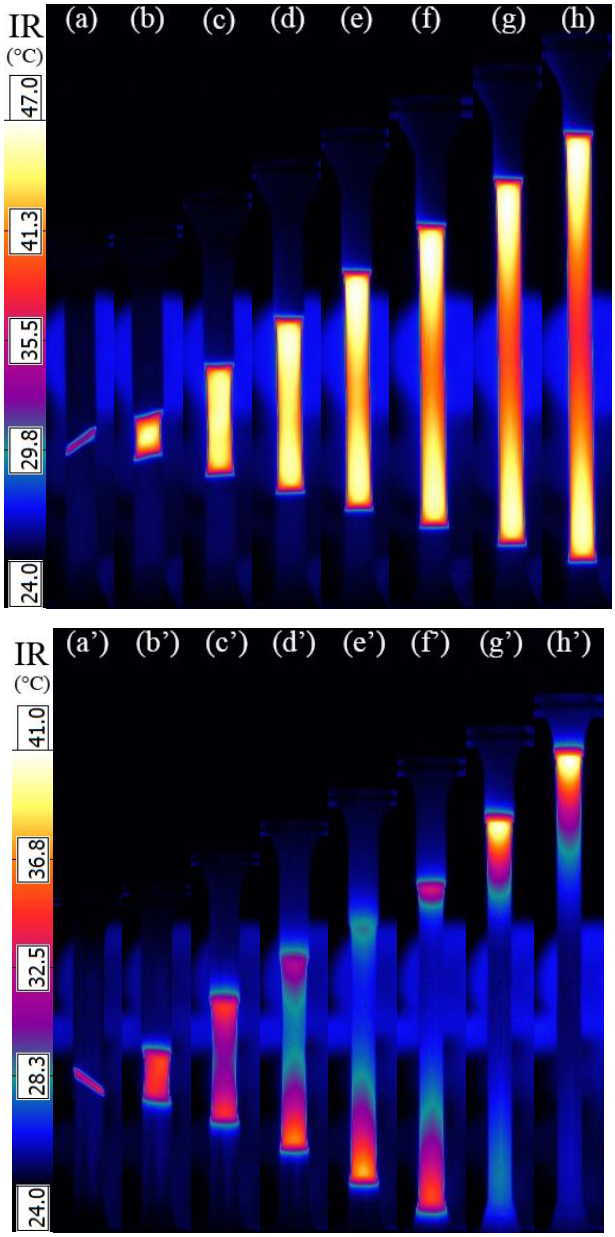

Figure G1. Thermal mapping obtained from the IR camera during tension tests at 50 mm/min (top) and 5 mm/min (bottom) at different cross-head displacements: (a) neck initiation (b) 10 mm (c) 20 mm (d) 30 mm (e) 40 mm (f) 50 mm (g) 60 mm (h) 70 mm.

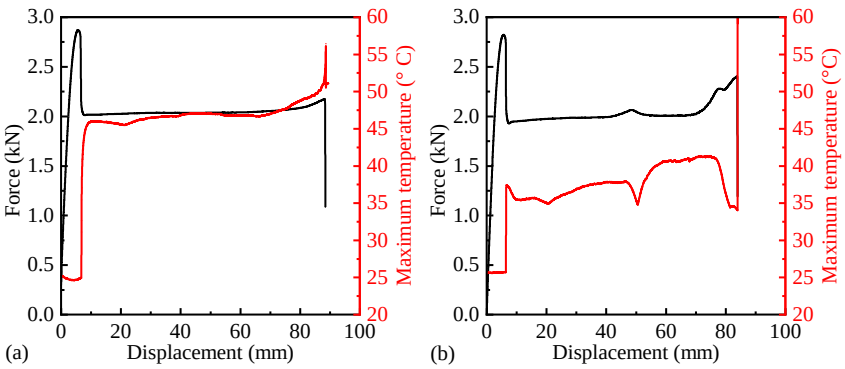

Figure G2. Force-displacement curves and maximum temperature-displacement curves for tension tests at (a) 50 mm/min and (b) 5 mm/min.

References

1. Boyce, M.C. and E.M. Arruda, *An experimental and anaiytical investigation of the large strain compressive and tensile response of glassy polymers.* Polymer Engineering & Science, 1990. **30**(20): p. 1288-1298.
2. Boyce, M.C., E.M. Arruda, and R. Jayachandran, *The large strain compression, tension, and simple shear of polycarbonate.* Polymer Engineering & Science, 1994. **34**(9): p. 716-725.
3. Siviour, C.R. and J.L. Jordan, *High Strain Rate Mechanics of Polymers: A Review.* Journal of Dynamic Behavior of Materials, 2016. **2**(1): p. 15-32.
4. Lu, J. and K. Ravi-Chandar, *Inelastic deformation and localization in polycarbonate under tension.* International Journal of solids and structures, 1999. **36**(3): p. 391-425.
5. Li, H.X. and C.P. Buckley, *Evolution of strain localization in glassy polymers: A numerical study.* International Journal of Solids and Structures, 2009. **46**(7-8): p. 1607-1623.
6. Li, H.X. and C.P. Buckley, *Necking in glassy polymers: Effects of intrinsic anisotropy and structural evolution kinetics in their viscoplastic flow.* International journal of plasticity, 2010. **26**(12): p. 1726-1745.
7. Parsons, E., M.C. Boyce, and D.M. Parks, *An experimental investigation of the large-strain tensile behavior of neat and rubber-toughened polycarbonate.* Polymer, 2004. **45**(8): p. 2665-2684.
8. Zhang, R., et al., *Aging-dependent strain localization in amorphous glassy polymers: From necking to shear banding.* International Journal of Solids and Structures, 2018. **146**: p. 203-213.
9. Grytten, F., et al., *Use of digital image correlation to measure large-strain tensile properties of ductile thermoplastics.* Polymer Testing, 2009. **28**(6): p. 653-660.
10. Lei, M., et al., *Thermomechanical behaviors of polyether ether ketone (PEEK) with stretch-induced anisotropy.* Journal of the Mechanics and Physics of Solids, 2021. **148**: p. 104271.
11. Haward, R.N., *Heating effects in the deformation of thermoplastics.* Thermochimica acta, 1994. **247**(1): p. 87-109.
12. Krairi, A. and I. Doghri, *A thermodynamically-based constitutive model for thermoplastic polymers coupling viscoelasticity, viscoplasticity and ductile damage.* International Journal of Plasticity, 2014. **60**: p. 163-181.
13. Jordan, B., M.B. Gorji, and D. Mohr, *Neural network model describing the temperature-and rate-dependent stress-strain response of polypropylene.* International Journal of Plasticity, 2020. **135**: p. 102811.
14. Lin, P., J. Liu, and S.-Q. Wang, *Delineating nature of stress responses during ductile uniaxial extension of polycarbonate glass.* Polymer, 2016. **89**: p. 143-153.
15. Shen, F., et al., *Thermo-elastic-viscoplastic-damage model for self-heating and mechanical behavior of thermoplastic polymers.* International Journal of Plasticity, 2019. **121**: p. 227-243.
16. Dattoma, V. and S. Giancane, *Evaluation of energy of fatigue damage into GFRC through digital image correlation and thermography.* Composites Part B: Engineering, 2013. **47**: p. 283-289.
17. Torres, J.P. and P.M. Frontini, *Mechanics of polycarbonate in biaxial impact loading.* International Journal of Solids and Structures, 2016. **85**: p. 125-133.
18. Meijer, H.E.H. and L.E. Govaert, *Mechanical performance of polymer systems: The relation between structure and properties.* Progress in polymer science, 2005. **30**(8-9): p. 915-938.
19. Haward, R.N. and G. Thackray, *The use of a mathematical model to describe isothermal stress-strain curves in glassy thermoplastics.* Proceedings of the Royal Society of London. Series A. Mathematical and Physical Sciences, 1968. **302**(1471): p. 453-472.

20. Boyce, M.C., D.M. Parks, and A.S. Argon, *Large inelastic deformation of glassy polymers. Part I: rate dependent constitutive model.* Mechanics of materials, 1988. **7**(1): p. 15-33.
21. Arruda, E.M. and M.C. Boyce, *A three-dimensional constitutive model for the large stretch behavior of rubber elastic materials.* Journal of the Mechanics and Physics of Solids, 1993. **41**(2): p. 389-412.
22. Hasan, O.A. and M.C. Boyce, *A constitutive model for the nonlinear viscoelastic viscoplastic behavior of glassy polymers.* Polymer Engineering & Science, 1995. **35**(4): p. 331-344.
23. Buckley, C.P., et al., *Deformation of thermosetting resins at impact rates of strain. Part 2: constitutive model with rejuvenation.* Journal of the Mechanics and Physics of Solids, 2004. **52**(10): p. 2355-2377.
24. Buckley, C.P. and D.C. Jones, *Glass-rubber constitutive model for amorphous polymers near the glass transition.* Polymer, 1995. **36**(17): p. 3301-3312.
25. De Focatiis, D.S.A., J. Embery, and C.P. Buckley, *Large deformations in oriented polymer glasses: Experimental study and a new glass-melt constitutive model.* Journal of Polymer Science Part B: Polymer Physics, 2010. **48**(13): p. 1449-1463.
26. Klompen, E.T.J., et al., *Modeling of the postyield response of glassy polymers: influence of thermomechanical history.* Macromolecules, 2005. **38**(16): p. 6997-7008.
27. Tervoort, T.A., et al., *A constitutive equation for the elasto-viscoplastic deformation of glassy polymers.* Mechanics of Time-Dependent Materials, 1997. **1**(3): p. 269-291.
28. Van Breemen, L.C.A., et al., *Extending the EGP constitutive model for polymer glasses to multiple relaxation times.* Journal of the Mechanics and Physics of Solids, 2011. **59**(10): p. 2191-2207.
29. Bergstrom, J.S., *PolyUMod–A library of advanced user materials.* Veryst Engineering, LLC, Needham, Mass, USA, 2012.
30. Torres, J.P., et al., *Deformation and failure of semicrystalline polymers under dynamic tensile and biaxial impact loading.* International Journal of Impact Engineering, 2016. **98**: p. 52-61.
31. Rueda, F., et al., *External pressure induced buckling collapse of high density polyethylene (HDPE) liners: FEM modeling and predictions.* Thin-Walled Structures, 2015. **96**: p. 56-63.
32. Bergstrom, J.S. and J.E. Bischoff, *An advanced thermomechanical constitutive model for UHMWPE.* The International Journal of Structural Changes in Solids, 2010. **2(1)**: p. 31-39.
33. Soloukhin, V.A., et al., *Physical aging of polycarbonate: elastic modulus, hardness, creep, endothermic peak, molecular weight distribution, and infrared data.* Macromolecules, 2003. **36**(20): p. 7585-7597.
34. Bergstrom, J.S., *Mechanics of solid polymers: theory and computational modeling*. 2015, Amsterdam, The Netherlands: Elsevier.
35. SABIC, *LEXAN™ Resin 103R Europe Technical Data Sheet*. 2021.
36. Knauss, W.G. and W. Zhu, *Nonlinearly viscoelastic behavior of polycarbonate. II. The role of volumetric strain.* Mechanics of time-dependent materials, 2002. **6**(4): p. 301-322.
37. Manual, A.U., *Abaqus user manual.* Abaqus, 2021.
38. Kweon, S. and A.A. Benzerga, *On the localization of plastic flow in glassy polymers.* European Journal of Mechanics-A/Solids, 2013. **39**: p. 251-267.
39. Tvergaard, V., A. Needleman, and K.K. Lo, *Flow localization in the plane strain tensile test.* Journal of the Mechanics and Physics of Solids, 1981. **29**(2): p. 115-142.
40. Wu, P.D. and E. van der Giessen, *On neck propagation in amorphous glassy polymers under plane strain tension.* International Journal of Plasticity, 1995. **11**(3): p. 211-235.
41. Maquin, F. and F. Pierron, *Heat dissipation measurements in low stress cyclic loading of metallic materials: From internal friction to micro-plasticity.* Mechanics of Materials, 2009. **41**(8): p. 928-942.
42. Boyce, M.C. and E.M. Arruda, *Constitutive models of rubber elasticity: a review.* Rubber chemistry and technology, 2000. **73**(3): p. 504-523.

4 Rate and Temperature Dependence

4.1 Introduction

This chapter continues the baseline characterisation of polycarbonate; in addition to the material in **Chapter 3,** two different molecular weight homo-polycarbonates and a co-monomer polycarbonate were also added. This chapter aims to provide a comprehensive dataset of characterised PCs based on consistent thermal histories.

Dynamic Mechanical Analysis was used to obtain the frequency and temperature-dependent modulus data, which were used to construct time-temperature superposition master curves. The same test strategy was used as in **Chapter 3** to perform quasi-static tensile tests. Furthermore, the compression properties within a range of strain rates from 0.001 to 3000 s^{-1} at 20 °C and from -60 to 120 °C at a constant true strain rate of 0.01 s^{-1} were measured. The mechanical behaviours of polycarbonates strongly depended on strain rate and temperature. Specifically, the yield stresses, across a wide spectrum of rates and temperatures, exhibited a time-temperature equivalence: as the strain rate increases or the temperature decreases, the yield stress rises. When plotting yield stresses against the logarithm strain rate, there is an increasing gradient with higher rates, which is attributed to the secondary molecular transition. The time-temperature superposition parameters derived from DMA measurements and those obtained from yield stress are compared; further, the comparisons between stress-strain curves acquired at various strain rates and temperatures are made. In the large strain region, the apparent thermal softening was observed in medium rate tests because the experimental condition was changing from isothermal in quasi-static to adiabatic. In contrast, the softening is not apparent in high rate tests, which is consistent with observations in the literature.

4.2 Paper B: Mechanical response of four polycarbonates at a wide range of strain rates and temperatures [1]

Abstract

Polycarbonate is widely used in engineering applications in which its mechanical properties need to be well understood over a wide range of strain rates and temperatures. These properties can be dependent on the molecular structure. In this research, the thermomechanical properties of three homo-polycarbonates with different melt flow rates, and a modified co-polycarbonate, were extensively characterized to produce a large dataset of mechanical properties based on consistent thermal histories. Dynamic Mechanical Analysis was performed to obtain modulus data from which time-temperature superposition master curves were constructed. Quasi-static tensile tests were conducted at two loading speeds, using a digital image correlation system to calculate strain fields. Compression properties were measured at strain rates from 0.001 to 3000 s^{-1} at 20 °C, and from -60 to 120 °C at a constant true strain rate of 0.01 s^{-1}. The mechanical response of the polycarbonates is highly rate- and temperature-dependent, and the yield stresses at a wide range of rates and temperatures show time-temperature equivalence: the yield stress increases with an increase in strain rate or a decrease in temperature. Curves of yield stresses versus logarithm strain rate present an increasing gradient with increasing rate, which results from the secondary transition. Comparisons are drawn between time-temperature superposition parameters obtained from modulus data and from yield stress data, and between stress-strain curves obtained at different strain rates and at different temperatures. In the large strain region, apparent thermal softening can be observed during the medium rate tests, consistent with the transition from adiabatic to isothermal loading, whilst softening is less than expected at the higher rates.

Keywords: Polycarbonates; Dynamic Mechanical Analysis; Tension; Compression; Rate- and

[1] Song, P., Trivedi, A. R., & Siviour, C. R. (2023). Mechanical response of four polycarbonates at a wide range of strain rates and temperatures. *Polymer Testing*, *121*, 107986.

temperature-dependence

Introduction

Polycarbonate (PC) is a typical glassy thermoplastic polymer with ductility, transparency and high impact resistance, and its mechanical properties have been investigated for many decades. These studies included, but were not limited to, investigation of molecular weight effects [1, 2], co-monomer effects [3], rate- and temperature-dependence [4-6], ageing [1, 2] and hydrostatic pressure dependence [7]. However, the thermal or manufacturing history of the material prior to testing can significantly affect the mechanical properties [8], and full mechanical characterisation data from consistently prepared specimens are not available in the literature.

It is well known that the mechanical properties of polymers are highly dependent on the temperature and strain rate, or frequency. Dynamic Mechanical Analysis (DMA) is a valuable tool for evaluating frequency- and temperature dependence of the complex modulus [9, 10]. Essential features that can be measured include storage modulus, loss modulus, tan delta, and the locations of glass (α)- and secondary (β)- transitions [11]. DMA tests for PC were reported in [12], using three-point bend and single cantilever beam configurations, where it was shown that modulus measurements from three-point bend DMA experiments are consistent with data from standard tension tests.

Large strain characterisation of polymers is typically performed in tension or compression, although shear configurations can also be used [13]. The quasi-static [10, 14, 15] and dynamic [16-19] tensile properties of PC have been investigated by a number of authors; however, it is challenging to extract constitutive model parameters from tensile experiments [15], and also difficult to perform high strain rate tension tests because of the time required for stress to equilibrate in the specimen

A number of authors have performed rate dependent characterisation of polymers in compression, using

the split Hopkinson pressure bar (SHPB) for high rate experiments. A key observation is that the yield stress shows an increase with increasing rate or decreasing temperature, with a higher rate of increase at high rates and low temperatures [7, 20]. This behaviour is attributed to the α- and β- relaxations in the material, with the β-transition particularly affecting the highest rates and lowest temperatures. This can be confirmed by using time-temperature equivalence to compare yield stresses at different rates and temperatures [6], an approach that has been successfully applied to understand the high rate behaviours of plasticized polyvinyl chloride (PVC) [21] and polytetrafluoroethylene (PTFE) [22]. Mulliken and Boyce [5] defined another approach to time-temperature equivalence, named 'decompose/shift/reconstruct' (DSR), which separated the temperature dependence of the modulus into two components, representing the α- and β- relaxations, shifted them individually with frequency, and finally added them together. This method offered an opportunity to predict the storage modulus of polymers at temperatures and strain rates well beyond the regime of the DMA.

The high-rate performance of PC, from 1000 s^{-1} to 10,000 s^{-1}, has been extensively investigated [4-6, 23, 24]. Typically, these data again show the effect of the β-transition on the high rate response; however Safari et al. [25] also saw evidence of the γ-relaxation. A key weakness of these compression studies is that they only present experimental data at rates lower than 0.1 s^{-1} and/or higher than 1000 s^{-1}, and do not include the range of 1 to 500 s^{-1}. This is a challenging range of rates, which requires either very high acceleration actuators and high bandwidth load cells or very long Hopkinson bars [26]. Successful techniques for achieving this include hydraulic machines [27], drop weights [28-30], and long split Hopkinson pressure bar (LSHPB) [31]. For polycarbonate, this range of rates is significant because it covers the region over which the β-transition becomes important, and therefore the inhibition of this transition leads to a more rapid increase in yield stress.

An additional complication when considering rate dependence in polymers is that above strain rates of about 0.1 s^{-1}, the constitutive stress-strain behaviours can be affected by adiabatic heating, particularly in the large strain regimes [32-34]. As the strain rate increases, the experimental conditions change from isothermal

to adiabatic because the experiment occurs over a shorter timescale than is required for heat to be dissipated to the environment [35], and the heat generated from plastic work leads to a temperature rise that can cause a qualitatively different constitutive response to that observed in quasi-static tests [4, 34].

The research presented in the current paper aims to provide a comprehensive data set on the rate dependence mechanical response of four grades of PC, allowing the development of constitutive models for these materials, and to advance our understanding of time-temperature equivalence at small and large strains. To achieve this, the PCs were subjected to consistent heat treatments to ensure comparability between data. DMA experiments were performed to measure viscoelastic properties under small-strain loading at varying frequencies and temperatures. For the large-strain responses, experiments at strain rates from 0.001 to 3000 s^{-1} were carried out using a conventional crosshead device, a hydraulic device, an LSHPB, and an SHPB. Further, experiments at a constant strain rate of 0.01 s^{-1} were performed at temperatures from -60 to 120 °C. The results are compared to understand the effects of temperature and rate on the small to large strain deformation process. Time-temperature equivalence of the mechanical properties is thereby investigated, and the influences of adiabatic heating on the large strain response under high rate deformation are discussed.

Material information and sample preparation

Table 1 shows the four injection moulded PCs characterised in this study. Three (PC2, PC8 and PC3) are homo-PCs with different melt flow rates (MFR); PC4 is a co-PC with sebacic acid [3]. The average molecular weight of each polycarbonate was measured using Gel Permeation Chromatography (GPC). The material was provided as 175 × 175 × 3 mm or 6 mm sheets, from which compression specimens were cut, and as dogbone tensile samples injection moulded according to ISO 527 type 1A with 80 mm gauge length and 4 mm thickness (Fig.1). All materials were provided directly by SABIC®.

Table 1. Grades of PCs used in the current investigation [3].

PC (LEXAN™ RESIN)	Code[1]	MFR at 300 °C/1.2 kg	Number average molecular weight (M_n) (g/mol)	T_g (°C)[2]
103R[3]	PC2	6 (Low MFR)	32400	145
500R Resin[4]	PC8	12 (Medium MFR)	30100	145
HF1110	PC3	25 (High MFR)	25600	145
HFD1014	PC4	6 (Co-polycarbonate)	37400	130

1. Nine materials were provided for this project, of which four were selected for characterisation, the codes here refer to the original material numbers.
2. Obtained in this study from DSC measurements.
3. Also contains a mould release agent and UV stabiliser.
4. This polycarbonate is the pure matrix material for the SABIC composite marketed as 500R.

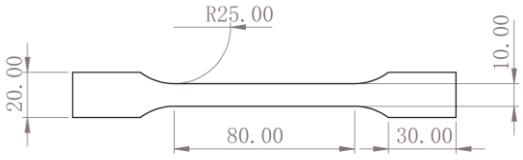

Figure 1. Injection moulded ISO 527 1A dogbone sample (all dimensions in mm)

To determine the glass (α)- transition temperature (T_g) of the materials, heat-cool-reheat differential scanning calorimetry (DSC) tests were performed using a commercial DSC system (TA Instruments Q2000). Each specimen was heated at 2 °C/min from 110 °C to 180 °C; subsequently, the temperature was reduced back to the initial temperature at 2 °C/min, finally, the temperature was increased to 180 °C at the same heating

rate. The glass transition temperature was determined from the second heating curve to minimize manufacturing history effects. An example of the DSC data is shown in Fig. 2; data for other materials are given in Appendix A.

For the mechanical test specimens, the PC sheets and dogbone tensile samples were annealed by heating at 25 °C/hour to 10 °C above their T_g (155 °C) where they were held for six hours to minimise the residual stress resulting from manufacturing. Then, the temperature was decreased to room temperature at a 10 °C/hour cooling rate. During this process, a thermocouple was placed very close to the samples to measure the real temperature change. A comparison between the desired temperature profile and the measured temperature change is presented in Fig.2. The maximum shrinkage of the sheets and dogbone samples was 1.5%, and it was confirmed that in-plane residual stress had been removed by observing the specimens through polarising film.

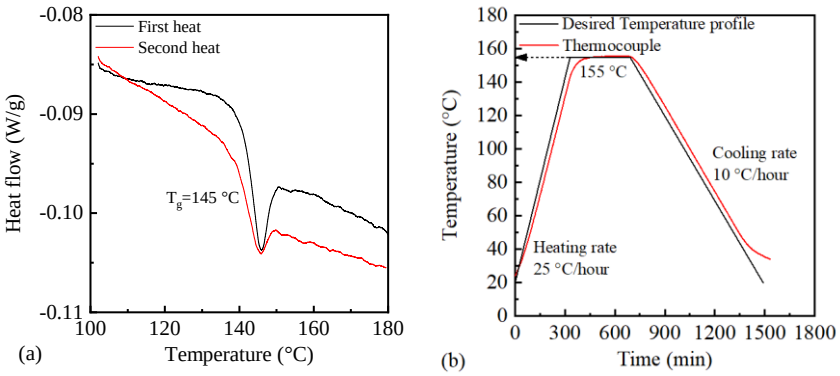

Figure 2. (a) Heal-cool-reheat DSC measurement on PC2, heating and cooling rates of 2 °C/min (b) Temperature profile during annealing.

The samples used for the temperature-dependent compression tests were cut from the centre (~ 100 x 100 mm) of the annealed sheets to produce discs of 5 mm diameter. For the varying rate compression tests, a 3 mm thick sample was used for rates from 0.001 to 50 s^{-1} and higher than 1000 s^{-1}. A 6 mm thick disc was used for rates of 100 to 1000 s^{-1} (LSHPB tests) as this makes it easier to achieve a constant strain rate during the experiment. All DMA specimens were cut from the centre of the annealed 3 mm sheets.

Experimental procedure

Dynamic Mechanical Analysis (DMA)

Two configurations were used for DMA experiments: three point bend and single cantilever beam. The former were used to obtain modulus measurements, and the latter to obtain the activation energy for glass transition. The sample dimensions used are listed in Table 2. The use of two specimen types is based on observations in the literature and from our own experiments.

The three point bend samples used were consistent with ASTM standard D4065 and literature studies [9, 10]. For example, in [9] it is reported that the most reproducible three-point bend DMA experiment uses a specimen with 50 mm span and 3 mm thickness and 100 μm displacement amplitude. However, TA Instruments documentation [36] reported that, for PC, sample sagging occurs in three point bend tests above T_g, and that therefore the loss modulus peak and Tan delta peak cannot be measured. The single cantilever configuration is suggested instead to show the entire viscous behaviour over a wider range of temperatures. On the other hand, a previous study [12] illustrated that the modulus obtained from three-point bend was close to that measured in tensile tests, whilst the value obtained from the single cantilever beam test was lower because of the clamping force. This is consistent with our own observations, presented below.

Hence, both configurations were used in the current study. The three point bend dimensions were chosen as above, and the single cantilever sample dimensions according to the operating range of the clamp [36]. A commercial DMA (Thermal Analysis Q800) was used for all the experiments. Firstly, temperature sweep DMA tests at a single frequency were performed. After that, isothermal frequency sweep experiments were performed, and the data obtained were used to construct time-temperature superposition (TTS) master curves and to plot α- and β-transition activation energies.

Table 2. DMA specimen dimensions

Configuration	Sample dimensions (mm)		
	Span	Width	Thickness
Three-point bend	50	10	3
Single cantilever beam	17.5	10	2

Tension tests

An Instron 5980 universal test machine with a 100 kN load cell was used to characterise the tensile properties of annealed PC dogbone samples at room temperature. As shown in Fig.1, the gauge length was 80 mm, and the thickness was 4 mm. Two loading speeds were used: 5 and 50 mm/min. A high resolution camera (Point Grey) mounted with a 60 mm Nikon lens was placed 960 mm from the sample to obtain images for subsequent digital image correlation (DIC) analysis. To produce a speckle pattern suitable for this analysis, the sample was first coloured white with water-based white ink, before a black marker pen was used to create a random pattern of dots on top of this background. The adopted DIC setup is detailed in Appendix B.

Compression tests

Because of the ductile nature of PC in compression, samples can be deformed to large strain. Therefore, true strains are used in this study, and constant true strain rate control was maintained for all quasi-static (QS) compression tests.

The Instron 5980 universal test machine with a 100 kN load cell was used to characterise the material responses at 0.001, 0.01 and 0.1 s^{-1}. An extensometer was attached to the loading anvils near the specimen to measure the strain and reduce the effect of rig compliance, Fig. 3a. This extensometer was also used for closed-loop control to achieve a constant true strain rate. In addition, an appropriate pre-load was applied to the specimens before the start of each test to remove the ‘toe-in’ region, which helps to ensure accurate strain measurements under true strain control. For the characterisation of the temperature-dependent mechanical properties, an environmental chamber equipped with a heating element or liquid nitrogen is employed, and a

digital thermometer was used to measure the temperature of the loading anvils close to the specimen. Lubricants were used to avoid friction effects [30]: petroleum jelly was used at room temperature and high temperatures, and AEROSPEC® 210 graphited grease was used in the low-temperature tests.

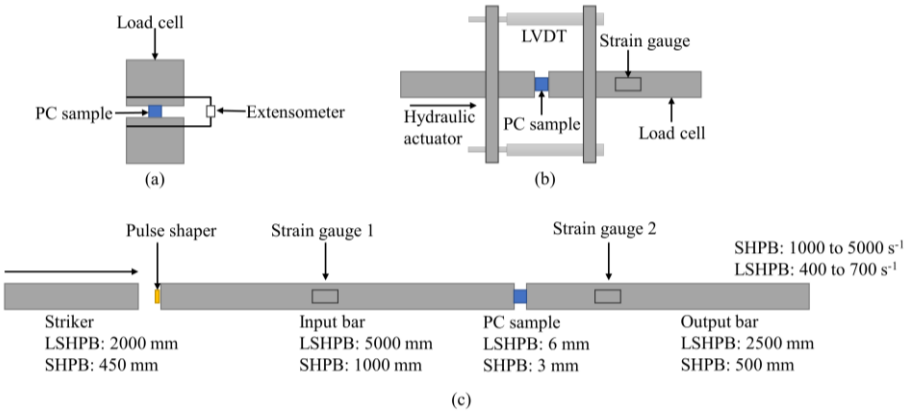

Figure 3. Experimental setup (a) Quasi-static compression, (b) Hydraulic compression, (c) Split Hopkinson pressure bar.

Medium rate experiments at rates between 1 and 50 s^{-1} were performed using a hydraulic machine (Fig. 3(b)). The force was measured by a strain gauge-based transducer, and the displacement was determined using the averaged value obtained from two linear variable differential transformers (LVDTs). The strain and stress were calculated from the LVDT signals and force transducer, respectively. A long split-Hopkinson pressure bar (LSHPB) was utilized to test the material properties at rates from 400 to 700 s^{-1}, and an SHPB was used to characterise the material properties from 1000 to 5000 $s^{-1.}$ A schematic of the split Hopkinson pressure bar system used is shown in Fig 3(c). Here, the cylindrical specimen was sandwiched between the input and output bar, which were made from Ti-6AL-4V. A gas gun is used to propel a Ti-6AL-4V striker to generate an input wave, which propagates down the bar to the specimen. The impedance change at the interface between bar and specimen causes some energy to be reflected back to input bar and some to be transmitted into the output bar, forming the reflected and transmitted signals. The input and reflected waves were measured using the gauges attached to the input bar, and the transmitted wave was similarly obtained from the output bar. For a more

detailed review of the use of split Hopkinson pressure bar (SHPB) systems on polymers, including data analysis, the reader is referred to the paper by Gray and Blumenthal [37]. The current study used a thin brass film as a pulse shaper to reduce the oscillations induced by wave dispersion in the input bar, as suggested in [38]. Petroleum jelly was used to lubricate the specimen ends for all samples, and no sample barrelling was observed.

Experimental results

DMA tests

Temperature sweep DMA tests

Two PC2 DMA specimens: a three-point bend and a single cantilever beam, were subjected to the oscillation at a frequency of 2 Hz and strain amplitude of 0.1%, or 137 μm. The specimens were then heated from -110 to 180 °C at a rate of 2 °C per minute. The storage modulus and loss modulus obtained from these experiments are presented in Fig. 4(a) and Fig 4(b). In Fig. 4(a), as expected from the discussion in section 3.1, the storage moduli do not agree well with each other; however, the modulus obtained from the three-point bend configuration at room temperature is, as expected, very close to the standard tension test results presented in the next section. In Fig. 4(b), the glass-transition peak can be observed from the single cantilever data, but only the secondary-transition peak around -90 °C can be measured in the three-point bend. Thus, the three-point bend configuration was used to obtain the temperature- and rate-dependent moduli of all materials, whilst the activation energies according to the Arrhenius relationship were calculated using loss modulus-temperature curves from the single cantilever beam experiments [39].

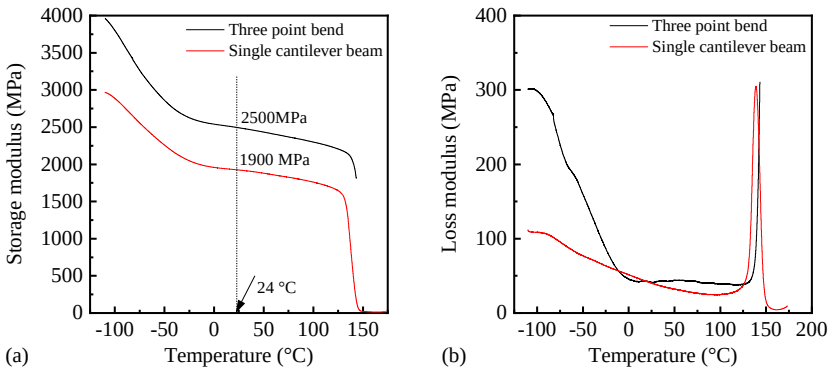

Figure 4. Temperature sweep DMA results using different modes (a) Storage modulus versus temperature (b) Loss modulus versus temperature.

Frequency sweep DMA tests

Full calibration of the apparatus and clamp were performed before the data acquisition. For the isothermal frequency sweeps, an oscillatory displacement of 0.1% strain amplitude was applied at a number of frequencies at 2 °C increments in temperature from -110 °C to 170 °C. At each temperature, a five-minute equilibrium time was allowed before the start of measurement. Frequencies of 0.5, 1, 2, 5, and 10 Hz were used for the single cantilever beam specimens, and 0.2, 0.5, 1, 2, and 5 Hz for the three-point bend configuration. It is worth noting that running tests at a frequency lower than 0.2 Hz is very time consuming, and 10 Hz (single cantilever) and 5 Hz (three-point bend) are the highest frequencies that can be tested in this machine for PC: at higher frequencies the data collection was affected by noise.

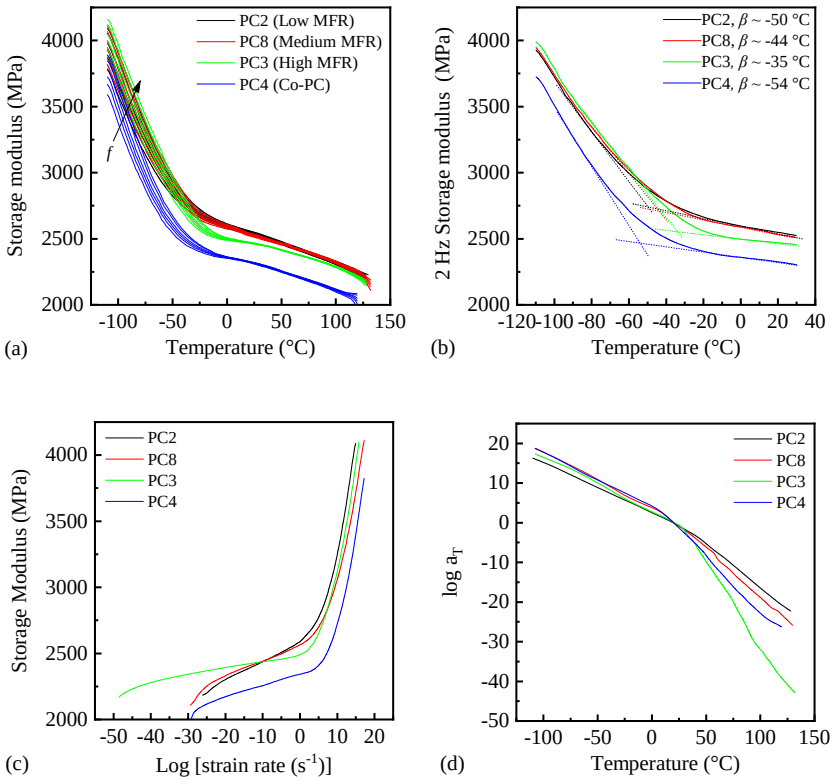

Figure 5. Results from three-point bend frequency sweep experiments: (a) Original data for storage modulus (b) Detail of β-transition region; (c) Time-temperature superposition master curves, converted to strain rate (d) Shift factor versus temperature. Note that the experiments were performed as isothermal frequency sweeps.

The three-point bend results are presented in Fig.5. As shown in Fig. 5(a), both temperature and frequency can affect the moduli, which decreases gradually with temperature increase until the temperature reaches the glass transition temperature (T_g), where all moduli show a very large drop. In particular, between -30 and 130 °C the modulus of low MFR (high molecular weight) polycarbonate (PC2) is slightly higher than that of the medium and high MFR polycarbonates. It is well known that the high-rate performance is governed by the β-transition: in this region (from -110 to -40 °C), the moduli of PC8 and PC3 show more frequency dependence than that of PC2. The rapid change of mechanical properties at a low temperature or high rate is reflected in the β-transition inflection point on the storage modulus versus temperature curve. The inflection point of the co-monomer PC (PC4) occurs at a lower temperature, and at higher rates than the other materials, as presented in Fig. 5(b) and Fig. 5(c). Similar results can be observed in the single cantilever data (Appendix C).

It is known that an increase of frequency can have a similar effect on the polymer response as reducing the temperature; this forms the basis of time-temperature superposition (TTS), which is here used to create the master curve shown in Fig. 5(c). The horizontal shifting algorithm moves the isotherms at temperatures above the reference temperature (20 °C) to the left-hand side (i.e. lower frequency), and the isotherms below 20 °C to the right-hand side (higher frequency) so that each segment overlaps with its neighbours; the shifts used are plotted in Fig. 5(d). The isotherms for PC2 obtained using the three-point bend configuration are shown in Appendix D. Many methods can be used to overlap the isotherms, which can cause slightly different final master curves. In this study, shifting is conducted manually; the details can be seen in previous literature [21, 40]. Here, to make comparisons to the later compression data, the frequencies in the DMA tests are converted to a strain rate using [26]:

$$\dot{\varepsilon} \approx \frac{\Delta\varepsilon}{\Delta t} = \frac{\varepsilon_0}{1/4f} = 4f\varepsilon_0 \qquad (1)$$

where f and ε_0 are applied frequency and strain in the DMA experiments.

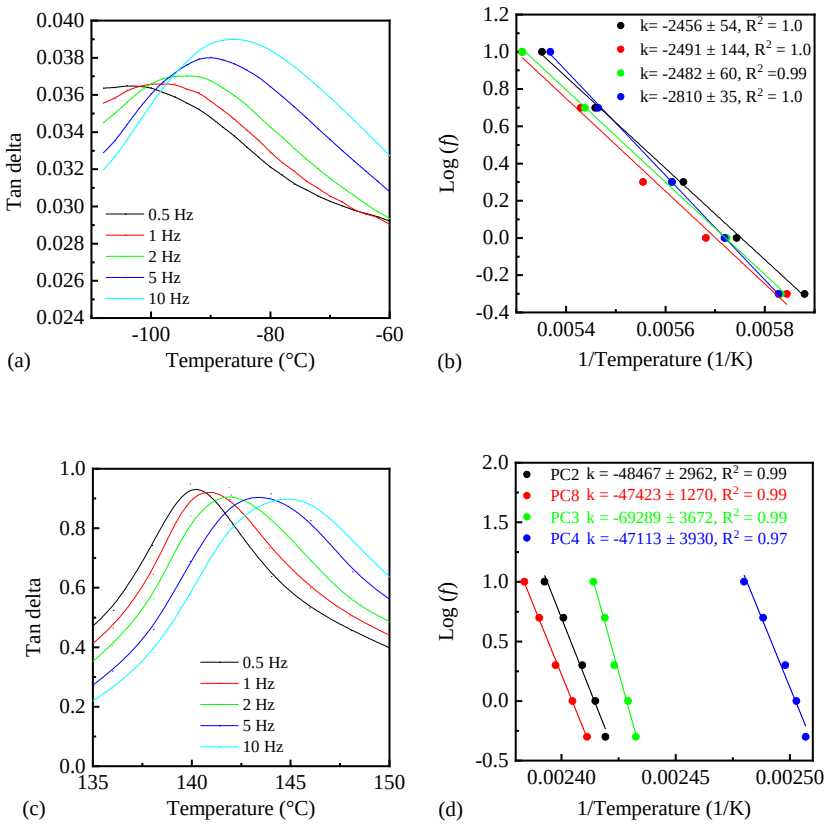

Figure 6. Frequency sweep results using single cantilever beam modes (a) Detail of β-transition for PC2 (b) Arrhenius plot for β-transition for all PCs (c) Detail of α-transition temperature for Tan delta for PC2 (d) Arrhenius plot for α-transition for all PCs.

The distinct peaks for α and β-relaxations can be observed in Tan delta-temperature curves for all PCs. Here, PC2 is presented as an example in Fig. 6(a) and Fig. 6(c); the experimental data for other PCs can be found in the supplementary data. These relaxations are frequency-dependent, and the activation energies for both transitions can be calculated using the Arrhenius equation:

$$\ln(f) = \ln(A) - \frac{E_a}{R}\frac{1}{T}, \qquad (2)$$

where f is frequency, A is the preexponential factor; E_a is the activation energy, R is the gas constant, and T is the absolute temperature. If the logarithms are taken to the base 10, the gradient of $\log(f)$ vs $1/T$ is given by:

$$k = -\frac{E_a}{2.303R} \quad (3)$$

The activation energies for β- and α- relaxations, which are often needed for modelling, can be calculated using the gradients in Fig 6(b) and Fig. 6(d), and the values are listed in Table 3. The co-PC (PC4) has higher β-transition activation energy, as shown in Fig. 5(c). For the activation energy of the glass transition, the value for PC2, PC8, and PC4 are similar and slightly lower than the value from [41]; however, PC3 has higher glass-transition activation energy.

Table 3 Activation energies of β- and α-relaxations of different grade PCs (kJ/mol).

	PC2	**PC8**	**PC3**	**PC4**
***β*-relaxation**	47 ± 1	48 ± 3	48 ± 1	54 ± 1
***α*- relaxation**	928 ± 57	904± 24	1327 ± 70	902 ± 75

Tension tests

In order to obtain tensile modulus, a virtual extensometer was placed in the gauge area of the tension specimens to extract the engineering strain using the commercial software MatchID® (www.matchid.eu, version 2022.2.1), Fig 7. At the same time, the engineering stress, shown in Fig. 8, can be calculated using the measured force and original cross-sectional area. In all tensile tests, yielding was accompanied by the formation of a shear band. A strong strain softening (around 20 MPa) is observed followed by deformation at constant engineering stress as the yield propagates along the specimen gauge length. The increase in stress observed at very large strains is associated with the yield reaching the transition between the gauge section and the shoulders; most of the specimens (PC2, PC8, PC4) failed shortly after this. This makes interpreting the high strain data more difficult; however, all strains reported here are the strains within the gauge section and represent the material response. Further discussion of the tensile experiments can be found in [15].

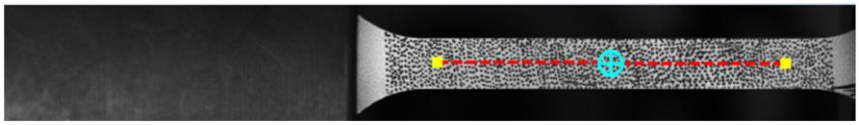

Figure 7. Example of virtual extensometer used for Engineering strain extraction via DIC.

The PC2, PC8 and PC4 samples exhibited ductile behaviour during the tension test, with a failure strain of approximately 100 % (nominal). However, the high MFR PC (PC3) is brittle and breaks at a smaller strain than other PCs. The yield stress and modulus both increase with an increase in loading speed or decrease in MFR, Table 4; the DMA results obtained at 20 °C with 2 Hz frequency are also listed in Table 4 as a reference. The co-PC (PC4), is somewhat more ductile than the others, however, the modulus and yield stress are lower. In these tests, the modulus presented is the secant modulus calculated between engineering strains of 0.0005 and 0.0025, as suggested in standard ISO 527. Tension tests were performed three times on each material in each configuration and mean values are listed in Table 4.

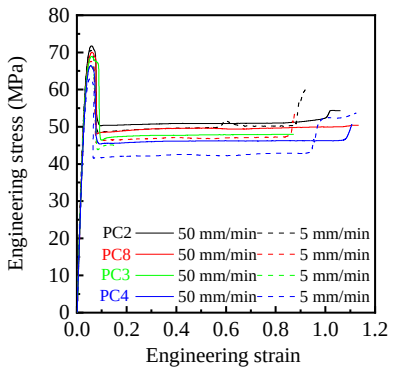

Figure 8. Engineering stress-strain curves.

Table 4. Summary of tension and DMA test results (all stiffnesses and strengths in MPa). Tensile modulus calculated from data presented in Fig. 8, yield stress and strain at break show values from three individual experiments, and the mean value of these experiments.

		PC2	**PC8**	**PC3**	**PC4**
DMA Modulus	**Three-point bend**	2550	2520	2470	2330
	Single cantilever beam	1960	1900	1920	1730
Tensile Modulus	**50 mm/min**	2430	2300	2350	2120
	5 mm/min	2390	2220	2230	2070
Yield	**50 mm/min**	71.7 71.1, 71.8, 72.2	70.1 69.5, 70.2, 70.7	68.2 67.2, 68.6, 68.8	65.0 63.1, 65.6, 66.3

stress	**5 mm/min**	69.7 68.5, 70.1, 70.5	69.4 67.3, 70.0, 71.0	68.7 66.6, 69.6, 70.0	65.0 63.0, 65.6, 66.3
Strain at break	**50 mm/min**	1.00 0.89, 0.98, 1.01	0.48 0.22, 0.33, 0.84	0.47 0.32, 0.29, 0.80	1.12 1.04, 1.12, 1.20
	5 mm/min	1.10 1.07, 1.10, 1.13	0.80 1.10, 1.13, 0.15	0.22 0.15, 0.15, 0.36	1.22 1.12, 1.27, 1.27

Varying rate and temperature compression tests

For each PC, compression tests were performed three times at rates up to 50 s^{-1}, whilst five LSHPB and five SHPB tests were conducted using different pressures to give a range of rates in each apparatus. It is common in the literature to compare rate and temperature dependence through the yield stress, here defined as the peak stress at yield, before strain softening begins. Fig. 9 presents the compressive response of PC2 at different temperatures from -60 °C to 120 °C and a constant true strain rate of 0.01 s^{-1}. Here, one true stress-strain curve and three yield stresses are plotted for each temperature. The deformation process shows yield, softening and hardening, and the yield stress increases with decreasing temperature, from 58 MPa at 120 °C to 120 MPa at -60 °C. Data for the other PCs can be found in Appendix E. A key observation is that at 120 °C, there is a fundamental difference in the behaviour of PC8, PC3 compared to PC2 and PC4, see Fig. 10(a). The post-yield strain softening takes a different form, occurring more slowly over a longer strain; further, samples of PC3 fragmented when the true strain exceeded 0.8 at this temperature, Fig. 10(b). This was not observed in any other tests and needed further investigation.

Compression data at different strain rates are shown in Fig. 11 for PC2, and Appendix F for the other polymers. Over seven decades of strain rate, the yield strength increased from 80 MPa to 120 MPa. It is noted that the final strain obtained in the Hopkinson bar experiments depends on the experimental duration and the strain rate, and therefore varies with rate. These data show clearly the effect of the beta transition, which causes an increase in the dependence of yield stress on log strain rate at high rates. More detailed analysis of the yield stress data will be presented in the discussion.

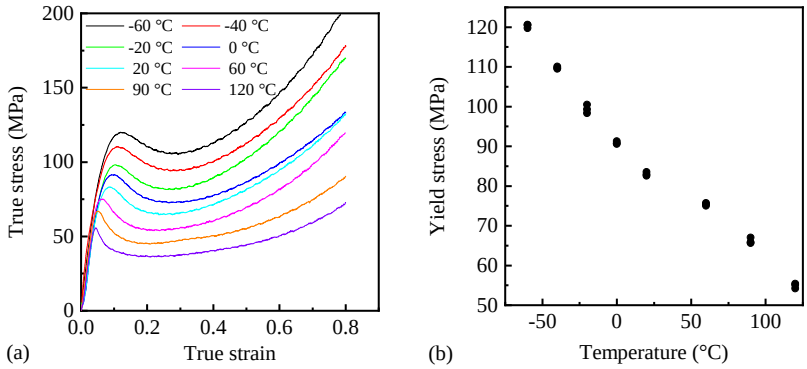

Figure 9. Data from experiments on PC2 at a constant true strain rate of 0.01 s^{-1} and different temperatures (a) True stress-true strain curves (b) Yield stresses.

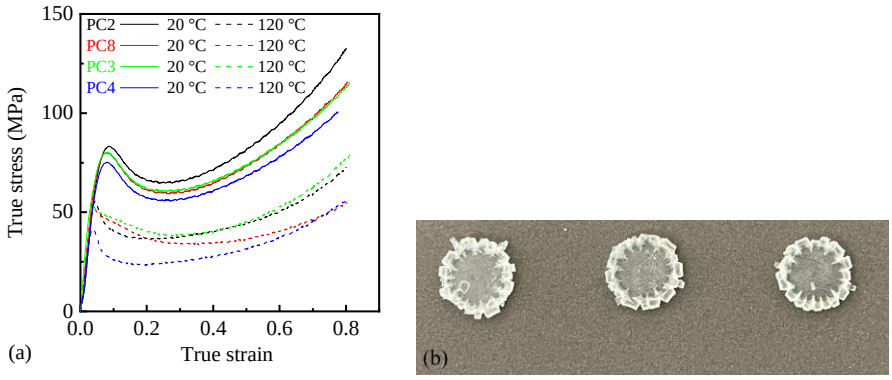

Figure 10. (a) Comparison of the four polycarbonates at 20 and 120 °C, showing the difference in post-yield softening of PCs 8 and 3 compared to 2 and 4. (b) Fracture in PC3 specimens tested in compression at 120 °C.

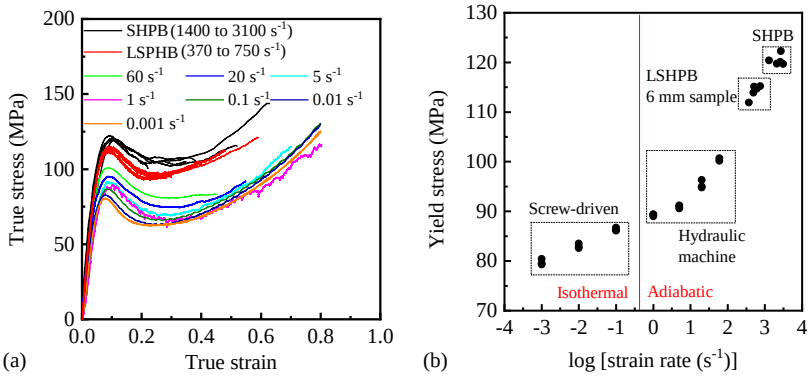

Figure 11. Data from experiments on PC2 at room temperature and different strain rates (a) true stress-true strain curves (b) yield stress vs log strain rate.

Discussion

The PCs exhibit the usual sensitivity to temperature and strain rate. In the DMA tests, the moduli decrease approximately linearly from -40 °C to 120 °C; slight differences exist because of the different melt flow rates. Frequency sweep experiments on PC2 in single cantilever and three-point bend configurations are compared in Fig. 12; the overall trends, and the transition temperatures are similar, but the absolute values of modulus are different. This is consistent with the temperature sweep data in Fig. 4. Master curves produced from these data also show the same trends, and the shift factors required to produce these curves are very consistent, except around the glass transition where it is known that the three-point bend configuration is unreliable. Equivalent DMA results from PC8, PC3 and PC4, which all show a similar trend, are presented in Appendix G.

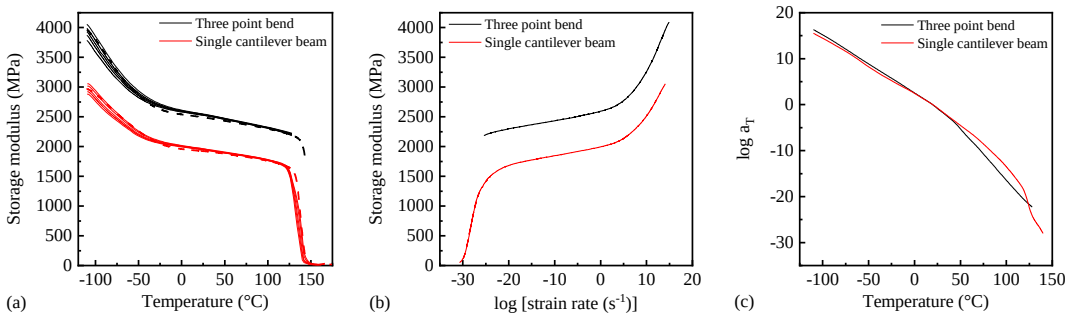

Figure 12. Comparing the three point bend and single cantilever beam mode frequency DMA results of PC2 (a) frequency sweep results (the dash line is obtained from temperature sweep (b) Time-temperature superposition curves (c) Shift factor versus temperature curves.

The temperature- and rate-dependent yield stresses are presented in Fig. 13(a) and Fig. 13(b), respectively. All yield stresses are consistent with the time-temperature equivalence principle: both decreasing the temperature and increasing the rate can increase the yield stress. The yield stresses of PC2 are higher than the other PCs, although the effects of MFR in this temperature and rate domain are not very large. For PC4, the yield stress drops at 120 °C, which is very close to its glass transition temperature.

The tension yield stresses are also plotted in Fig 13(b). These are converted directly from the engineering

stress-strain curves, using true strain rates of 0.00075 ± 5% and 0.0075 ± 5% for 5 and 50 mm/min loading speeds, respectively. Based on these data, the pressure-dependent coefficient as used in common polymer models (e.g. [42]) can be estimated using equation (7), where, σ_{cy} and σ_{ty} are compression and tension yield stresses; this gives a value of $a \sim 0.12$, which is consistent with other studies [26].

$$\frac{|\sigma_{cy}|}{\sigma_{ty}} = \frac{3+a}{3-a} \tag{4}$$

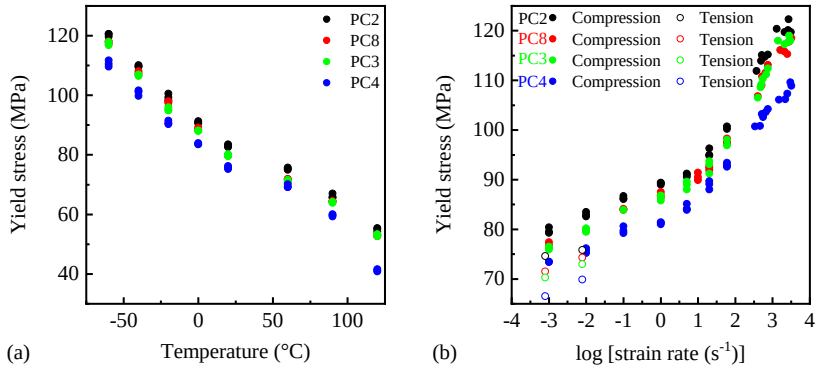

Figure 13. Comparison of (a) Temperature-dependence of yield stress in compression (b) Rate-dependence of yield stress in compression and tension

As the varying temperature compression tests are conducted at a constant strain rate (0.01 s^{-1}), the temperature-dependent yield stresses in Fig. 13(a) can be mapped onto the temperature-controlled varying rate tests in Fig. 13(b). The result of this is shown in Fig. 14(a) for PC2 (other PCs in Appendix H). It is well-established that the rate dependence and temperature dependence of the yield stresses are related, and this process gives the form of the relationship, which can be compared to the equivalence derived from the DMA data (Fig. 14(b)). It is observed that the DMA and yield stress shift factors are not consistent through the beta transition. It is important here to note the start conditions for tests at different strain rates and at different temperatures. The high strain rate experiments are performed at room temperature, and therefore the structure associated with the β- relaxations is in equilibrium at the start of loading. The low temperature experiments (for both DMA and quasi-static compression) start at temperatures below the onset of the β-transition: in these

experiments, this structure is not in equilibrium. Therefore there is a fundamental difference in the state of the material at the start of the experiments, which may then affect the TTS of the yield stress, in particular. It is noted that if the DMA shift data are applied to the yield stresses, Fig. 14(c), the shifted values appear to be linear in log(strain rate), this is common for all the materials.

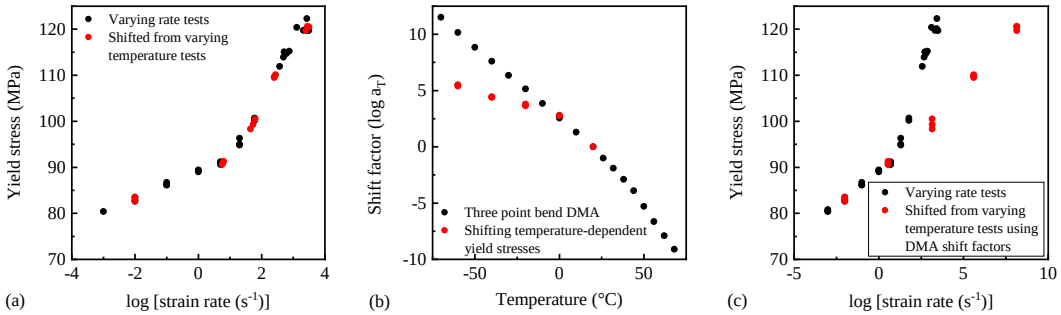

Figure 14. (a) Result of shifting temperature-dependent yield stress onto the yield stress-log rate curve, for PC2 (b) Comparison of shift factors obtained from three-point bend DMA data and from yield stress data (c) Result of shifting temperature-dependent yield stress onto rate-dependent yield stress using DMA shift factors.

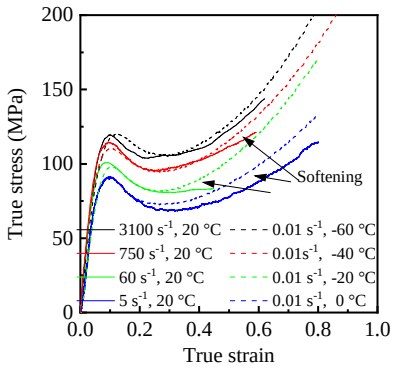

Figure 15. Comparison of stress-strain curves at low temperatures and high strain rates (PC2). The colours indicate which temperature/rate combinations are equivalent (e.g. 3100 s^{-1}, 20 °C and 0.01 s^{-1}, -60 °C).

Having shifted the yield stresses, it is now possible to compare the large strain behaviour for rate-dependent and temperature-dependent experiments that have the same yield. PC2 is shown as an example, Fig. 15, and the low-temperature and high-rate data comparisons for the other PCs are shown in Appendix I. These

agree well for strains lower than 0.3. However, at rates between 5 and 60 s^{-1} there is then more softening relative to the 'equivalent' quasi-static experiment at reduced temperature; this is not then observed at higher rates. It is likely that this behaviour is associated with heating during plastic deformation: temperature rises during high-rate tests on polycarbonate have been reported widely in the literature [35, 43-46]. This occurs because as the strain rate increases there is less time for heat to conduct out of the specimens, leading to a transition between isothermal (quasi-static) and adiabatic (high strain rate) conditions. The strain rate associated with this transition can be calculated from the thermal diffusivity [34]:

$$\alpha = \frac{k}{\rho C_p} \tag{5}$$

$$l_t = 2\sqrt{\alpha t} \Rightarrow t = \frac{1}{\alpha}\left(\frac{l_t}{2}\right)^2 \tag{6}$$

$$\dot{\varepsilon} = \frac{1}{t} \tag{7}$$

Here α is thermal diffusivity, k thermal conductivity (0.2 W m^{-1} K^{-1}), ρ density (1.2 g cm^{-3}), and C_P specific heat capacity (1.2 J g^{-1} K^{-1}) [47]. The timescale (t) of thermal diffusion can be estimated from these parameters and l_t, the length of the specimen. Using these equations, the transition from isothermal to adiabatic conditions starts at a rate around 0.06 s^{-1}, which is consistent with the larger strain softening seen in experiments at 0.1 s^{-1} and above compared to lower rates (e.g. 0.1, 1, 5, 20 and 60 in Figure 10; 5 and 60 s^{-1} in Fig. 15). This softening is usually attributed to temperature rises in the specimen under non-isothermal conditions. The increased softening is not, however, observed during the high-rate tests (e.g. 750 and 3100 s^{-1} in Figure 15). This implies that when the material is loaded on a timescale over which the β relaxations cannot occur, there is a change in the manner of the conversion of work to heat, or to the material's response to this heat generation. This is consistent with work by Kendall and Siviour [4] and more recently Trivedi *et al* [48], which show that the softening in high rate experiments can be replicated in low rate loading with only very small temperature rises, implying that conversion of work to heat has less effect than would be expected from

consideration of just low or intermediate strain rate data. Thus, further investigations are needed to understand both temperature rises and the rate-dependent softening and hardening behaviour at high rates, and at equivalent lower temperatures.

Conclusions

This paper presents results from DMA experiments, varying rate and temperature compressive experiments, and quasi-static tension tests, for polycarbonate materials with three different melt flow rates, and one co-polycarbonate. The results from the three point bend mode DMA show good consistency with the tension tests, however, the α-transition cannot be observed, so single cantilever beam experiments were instead used to calculate activation energies for both the β- and α-transitions. For the homo-polycarbonates, the low MFR PC has higher yield stresses than the other materials, whilst the co-polycarbonate has lower yield stress, but sees the effect of the beta transition at a lower strain rate. The temperature and strain rate dependence of the yield stresses can be shifted onto each other, but the shift factors obtained are not the same as those obtained from the DMA experiments, especially at low temperature (high rates), where the beta transition would be expected to affect the data. Indeed, if the DMA shift factors are used to shift the temperature-dependent yield stresses onto strain rate, the yield stresses are found to be linear in log(rate). This may be a result of the difference in starting condition, where the structural configuration associated with the beta relaxations is in equilibrium at the start of the high rate room temperature experiments, but not in equilibrium in the low temperature quasi-static experiments (or, indeed, the DMA). Further, DMA data only present the small strain modulus, so samples might also experience structural evolution before yielding.

For the large strain deformation, it is expected that the medium and high rate experiments are adiabatic, and that there is therefore an increase in temperature in the specimen during loading. This leads to softening of the material at large strains and medium strain rates, compared to the quasi-static results; however, this is not observed in the high rate tests. This means that the high rate behaviours of polycarbonates at small strains might be represented using low rate low temperature tests; however, the post-yield behaviours, and especially the apparent lack of thermal sensitivity of the large strain response at high strain rates needs to be further understood.

CRediT authorship contribution statement

Peihao Song: Conceptualization, Methodology, Software, Investigation, Formal analysis, Writing - original draft. **Akash R. Trivedi:** Formal analysis, Investigation review. **Clive R. Siviour:** Conceptualization, Project administration, Supervision, Writing – review & edit, Funding acquisition.

Declaration of competing Interest

The authors declare that they have no known competing financial interests or personal relationships that could have appeared to influence the work reported in this paper.

Acknowledgements

This research forms part of the research programme of DPI, project 827t19, *Impact Modelling of Polymers: high-Rate Experiments for Solid-state Simulations* and the materials were kindly supported by Saudi Basic Industries Corporation (SABIC). The authors thank our colleagues on this project, Dr Davide De Focatiis and Grace Owen at the University of Nottingham for helpful discussions. We also thank the technicians of the Solid Mechanics Group workshop, in particular Andy Bateman and Richard Duffin, for their help with the manufacture of specimens and fixtures for this project and Nicholas Hawkins for his help with the DMA tests. Finally, we thank Dr Georgina Gregory, from the Oxford University Chemistry Research Laboratory, for performing the GPC experiments.

For the purpose of Open Access, the authors have applied a CC BY public copyright license to any Author Accepted Manuscript (AAM) version arising from this submission.

Data Availability

All data supporting this study are openly available from the Oxford University Research Archive at DOI: 10.5287/bodleian:pr46jD5ar

Appendix A: Heat-cool-reheat DSC data

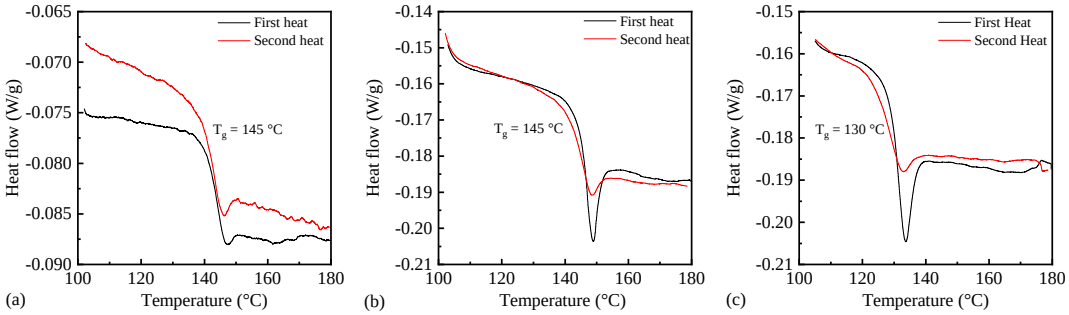

Figure A1. Heat-cool-reheat DSC data: (a) PC8 (b) PC3 (c) PC4

Appendix B: DIC setup

Table B1. Digital Image Correlation Setup

Loading speeds (mm/min)	50	5
Adopted Digital Image Correlation (DIC) Setup		
Camera (Point Grey)	GS3-U3-41C6M-C	GS3-U3-120S6M-C
Image resolution (pixel)	2048 x 2048, 10-bit	4240 x 2824, 14-bit
Frame rate (frame/s)	10	2
Lens	Nikon 60 mm Lens	
Field of view (pixels)	288 x 2048	380 x 2824
Pixel to mm conversion	0.01010	0.06135
Stand-off distance (mm)	960	
Speckle size (pixels)	≈ 7	≈ 10
DIC software	MatchID, version 2022.1.1	
Subset size (pixel)	21	25
Step size (pixel)	5	3
Progress history	Spatial and Update reference	
Subset shape function	Quadratic	

Appendix C: Single cantilever beam DMA results

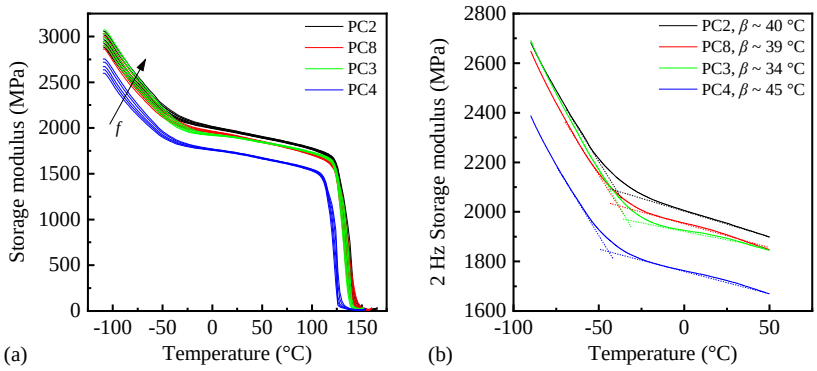

Figure C1. Results from DMA frequency sweep with single cantilever beam configuration.

Appendix D: Storage modulus versus log rate of PC2 using three-point bend configuration

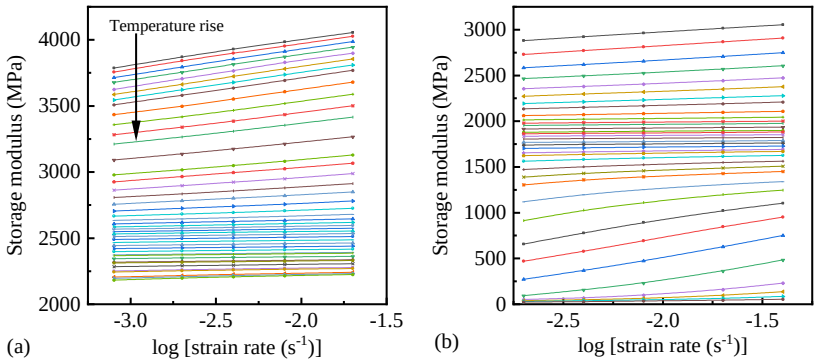

Figure D1. DMA Isotherms showing the dependence of modulus on frequency and temperature for PC2. For clarity, not all curves are shown (a) Three-point bend (b) Single cantilever beam. Other data available from the Oxford Research Archive.

Appendix E: Temperature-dependent compression data for PC8, PC3 and PC4

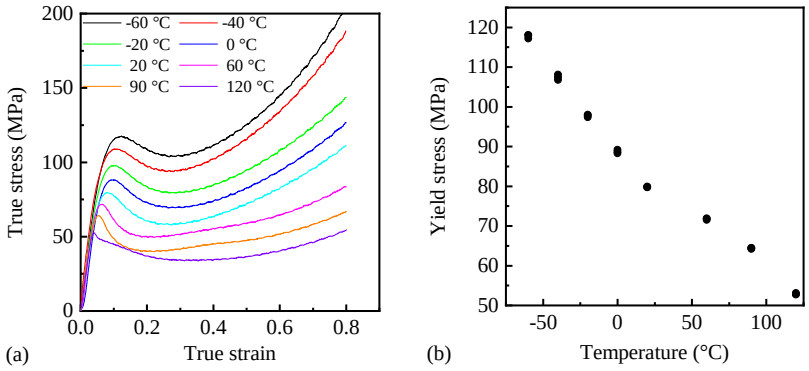

Figure E1. (a) Temperature-dependent true stress-strain curves (b) Yield stress-temperature curve for PC8.

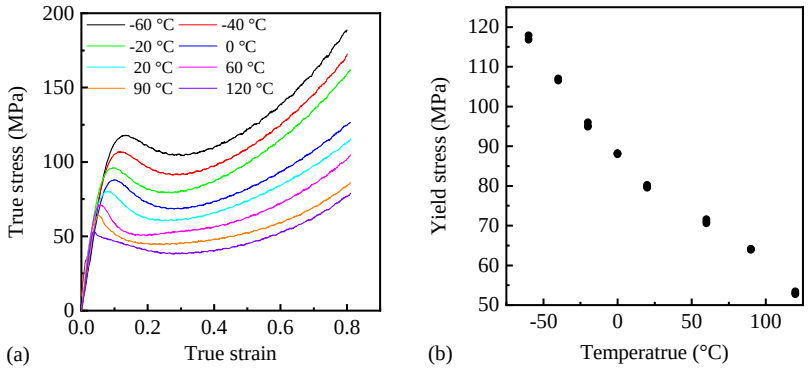

Figure E2. (a) Temperature-dependent true stress-strain curves (b) Yield stress-temperature curve for PC3.

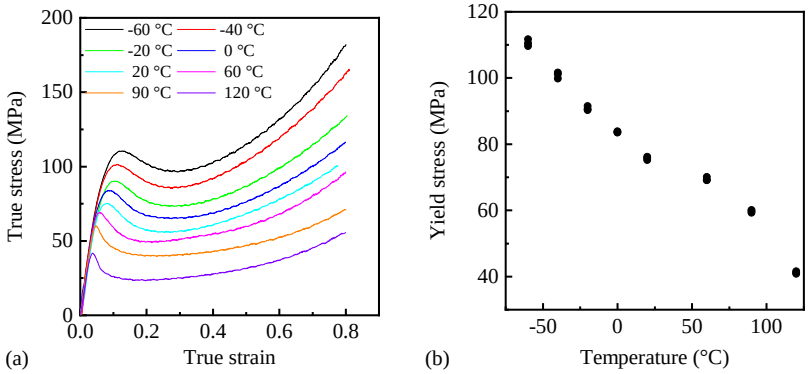

Figure E3. (a) Temperature-dependent true stress-strain curves (b) Yield stress-temperature curve for PC4.

Appendix F: Rate-dependent compression data for PC8, PC3 and PC4

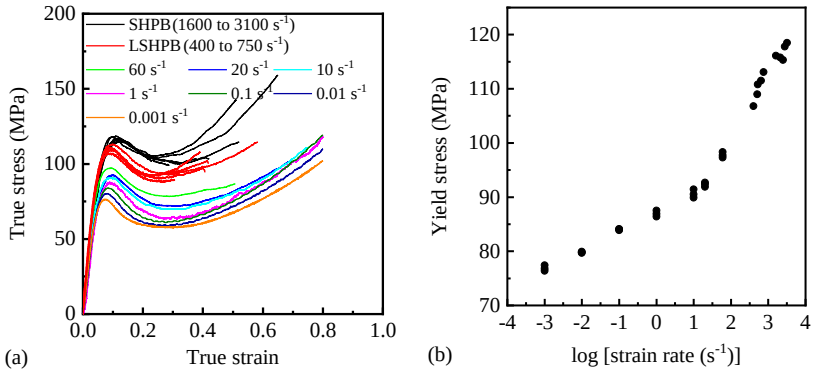

Figure F1. (a) Rate-dependent true stress-strain curve (b) Yield stress-log rate curve for PC8.

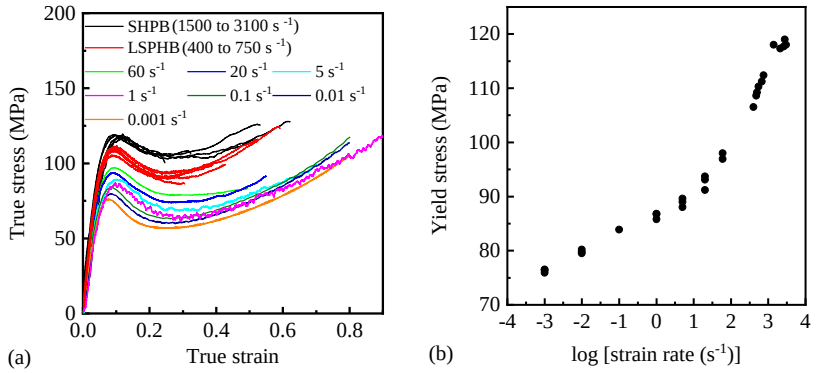

Figure F2. (a) Rate-dependent true stress-strain curve (b) Yield stress-log rate curve for PC3.

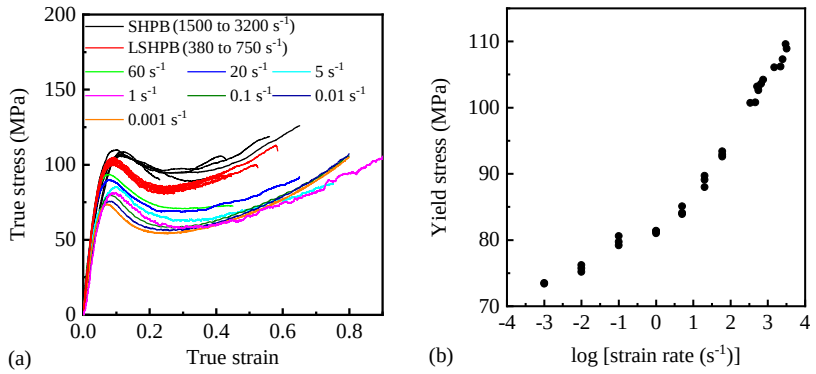

Figure F3. (a) Rate-dependent true stress-strain curve (b) Yield stress-log rate curve for PC4.

Appendix G: Frequency sweep DMA results for PC8, PC3 and PC4

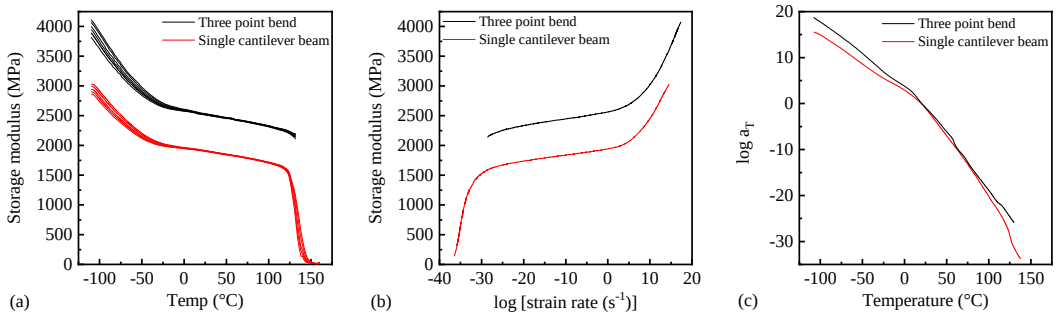

Figure G1. DMA results for PC8.

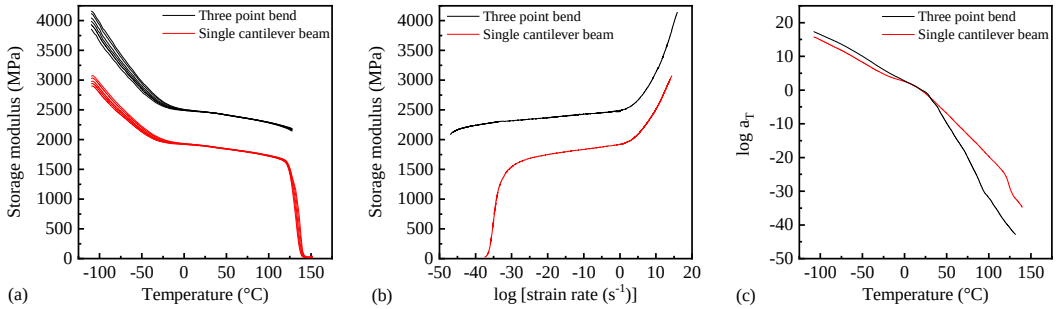

Figure G2. DMA results for PC3.

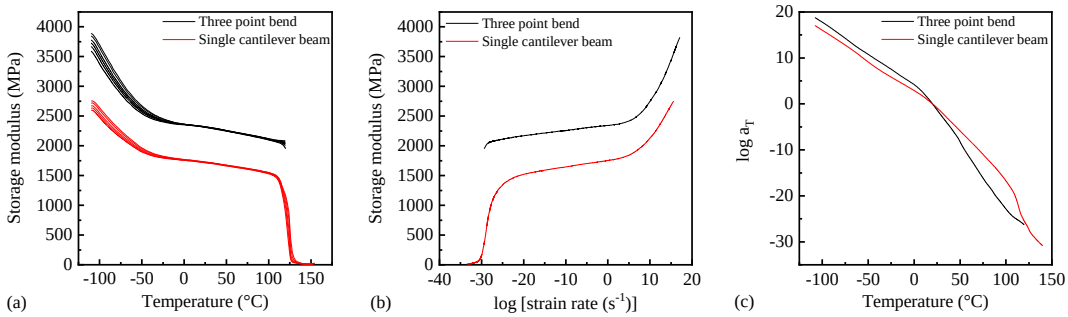

Figure G3. DMA results for PC4.

Appendix H: Shift of yield stresses from temperature-dependent to rate-dependent

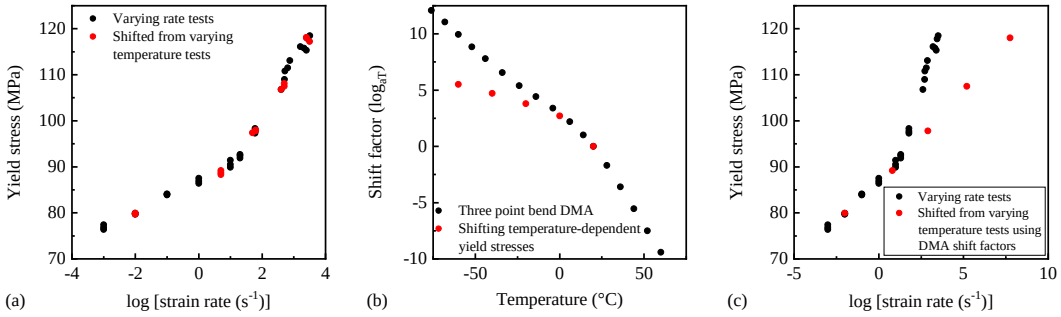

Figure H1. Shifting temperature-dependent yield stresses to rate-dependent yield stresses for PC8.

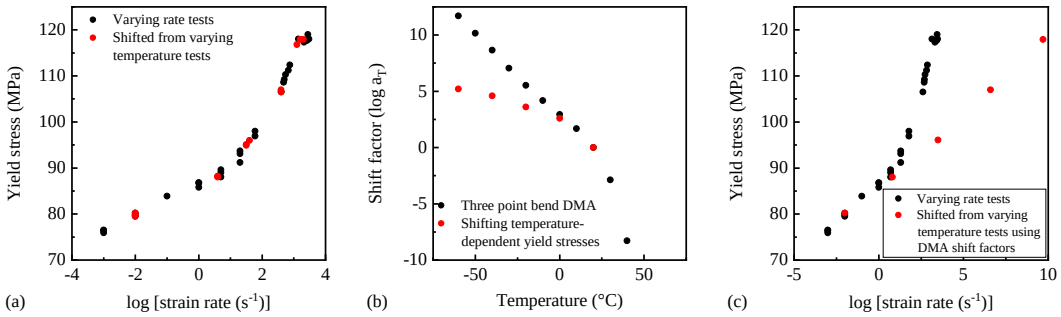

Figure H2. Shifting temperature-dependent yield stresses to rate-dependent yield stresses for PC3.

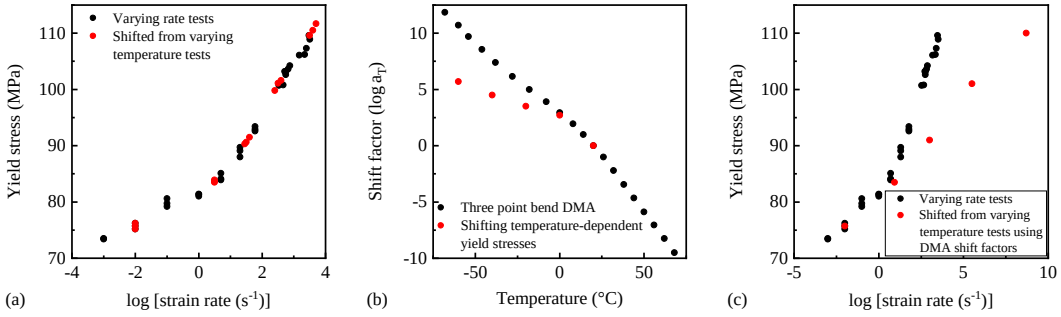

Figure H3. Shifting temperature-dependent yield stresses to rate-dependent yield stresses for PC4.

Appendix I: Low-temperature and high-rate compression data comparisons

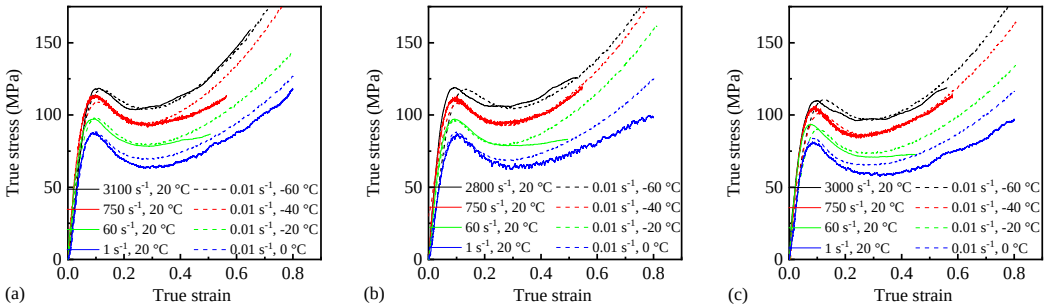

Figure I. Comparison of stress-strain curves at low temperatures and high strain rates: (a) PC8 (b) PC3 (c) PC4

References

1. Nishitsuji, S., et al., *Molecular weight dependence of the physical aging of polycarbonate.* Polymer, 2019. **178**: p. 121571.
2. Ohara, A. and H. Kodama, *Correlation between enthalpy relaxation and mechanical response on physical aging of polycarbonate in relation to the effect of molecular weight on ductile-brittle transition.* Polymer, 2019. **181**: p. 121720.
3. Micciche, F., V. Ramakrishnan, and T.L. Hoeks, *The effect of molecular structure on the secondary transitions and their influence on the decoloration kinetics of photochromic dyes in co-polycarbonates.* Journal of Polymer Science Part B: Polymer Physics, 2016. **54**(16): p. 1593-1601.
4. Kendall, M.J. and C.R. Siviour, *Experimentally simulating high-rate behaviour: rate and temperature effects in polycarbonate and PMMA.* Philos Trans A Math Phys Eng Sci, 2014. **372**(2015): p. 20130202.
5. Mulliken, A.D. and M.C. Boyce, *Mechanics of the rate-dependent elastic–plastic deformation of glassy polymers from low to high strain rates.* International Journal of Solids and Structures, 2006. **43**(5): p. 1331-1356.
6. Siviour, C.R., et al., *The high strain rate compressive behaviour of polycarbonate and polyvinylidene difluoride.* Polymer, 2005. **46**(26): p. 12546-12555.
7. Bauwens-Crowet, C., J.C. Bauwens, and G. Homes, *The temperature dependence of yield of polycarbonate in uniaxial compression and tensile tests.* Journal of Materials Science, 1972. **7**(2): p. 176-183.
8. Legrand, D.G., *Crazing, yielding, and fracture of polymers. I. Ductile brittle transition in polycarbonate.* Journal of Applied Polymer Science, 1969. **13**(10): p. 2129-2147.
9. Lee-Sullivan, P. and D. Dykeman, *Guidelines for performing storage modulus measurements using the TA Instruments DMA 2980 three-point bend mode: I. Amplitude effects.* Polymer testing, 2000. **19**(2): p. 155-164.
10. Shao, Q. and P. Lee-Sullivan, *Guidelines for performing storage modulus measurements using the TA Instruments DMA 2980 three-point bend mode II. Contact stresses and machine compliance.* Polymer testing, 2000. **19**(3): p. 239-250.
11. Menard, K.P. and N.R. Menard, *Dynamic mechanical analysis in the analysis of polymers and rubbers.* Encyclopedia of polymer science and technology (Fourth Edition), 2002: p. 1-33.
12. Deng, S., M. Hou, and L. Ye, *Temperature-dependent elastic moduli of epoxies measured by DMA and their correlations to mechanical testing data.* Polymer testing, 2007. **26**(6): p. 803-813.
13. Fleck, N.A., W.J. Stronge, and J.H. Liu, *High strain-rate shear response of polycarbonate and polymethyl methacrylate.* Proceedings of the Royal Society of London. A. Mathematical and Physical Sciences, 1990. **429**(1877): p. 459-479.
14. Parsons, E., M.C. Boyce, and D.M. Parks, *An experimental investigation of the large-strain tensile behavior of neat and rubber-toughened polycarbonate.* Polymer, 2004. **45**(8): p. 2665-2684.
15. Song, P., A. Trivedi, and C.R. Siviour, *Tensile testing of polymers: Integration of digital image correlation, infrared thermography and finite element modelling.* Journal of the Mechanics and Physics of Solids, 2023. **171**: p. 105161.
16. Sarva, S. and M. Boyce, *Mechanics of polycarbonate during high-rate tension.* Journal of Mechanics of Materials and Structures, 2007. **2**(10): p. 1853-1880.
17. Zhang, L., et al., *Temperature Dependent Dynamic Strain Localization and Failure of Ductile Polymeric Rods under Large Deformation.* International Journal of Mechanical Sciences, 2021: p.

106563.
18. Cao, K., et al., *Tensile behavior of polycarbonate over a wide range of strain rates.* Materials Science and Engineering: A, 2010. **527**(16): p. 4056-4061.
19. Cao, K., Y. Wang, and Y. Wang, *Experimental investigation and modeling of the tension behavior of polycarbonate with temperature effects from low to high strain rates.* International Journal of Solids and Structures, 2014. **51**(13): p. 2539-2548.
20. Bauwens, J.C., *Relation between the compression yield stress and the mechanical loss peak of bisphenol-A-polycarbonate in the β transition range.* Journal of Materials Science, 1972. **7**(5): p. 577-584.
21. Trivedi, A.R. and C.R. Siviour, *A novel methodology for predicting the high rate mechanical response of polymers from low rate data: application to (plasticised) poly (vinyl chloride).* Mechanics of Time-Dependent Materials, 2021. **25**: p. 383-409.
22. Jordan, J.L., et al., *Compressive properties of extruded polytetrafluoroethylene.* Polymer, 2007. **48**(14): p. 4184-4195.
23. Richeton, J., et al., *Influence of temperature and strain rate on the mechanical behavior of three amorphous polymers: Characterization and modeling of the compressive yield stress.* International Journal of Solids and Structures, 2006. **43**(7-8): p. 2318-2335.
24. Safari, K.H., et al., *The effect of heat developed during high strain rate deformation on the constitutive modeling of amorphous polymers.* Mechanics of Time-Dependent Materials, 2015. **20**(1): p. 45-64.
25. Safari, K.H., et al., *Constitutive modeling of polycarbonate during high strain rate deformation.* Polymer Engineering & Science, 2013. **53**(4): p. 752-761.
26. Siviour, C.R. and J.L. Jordan, *High Strain Rate Mechanics of Polymers: A Review.* Journal of Dynamic Behavior of Materials, 2016. **2**(1): p. 15-32.
27. Walley, S.M. and J.E. Field, *Strain rate sensitivity of polymers in compression from low to high rates.* DYMAT J, 1994. **1**(3): p. 211-227.
28. Cai, J., et al., *High-strain, high-strain-rate flow and failure in PTFE/Al/W granular composites.* Materials Science and Engineering: A, 2008. **472**(1-2): p. 308-315.
29. Lee, S.F. and G.M. Swallowe, *Direct measurement of high rate stress–strain curves using instrumented falling weight and high-speed photography.* The Imaging Science Journal, 2004. **52**(4): p. 193-201.
30. Trautmann, A., et al., *Lubrication of polycarbonate at cryogenic temperatures in the split Hopkinson pressure bar.* International Journal of Impact Engineering, 2005. **31**(5): p. 523-544.
31. Song, B., et al., *A long split Hopkinson pressure bar (LSHPB) for intermediate-rate characterization of soft materials.* Experimental Mechanics, 2008. **48**(6): p. 809-816.
32. Furmanski, J., C.M. Cady, and E.N. Brown, *Time–temperature equivalence and adiabatic heating at large strains in high density polyethylene and ultrahigh molecular weight polyethylene.* Polymer, 2013. **54**(1): p. 381-390.
33. Kendall, M.J., R.F. Froud, and C.R. Siviour, *Novel temperature measurement method & thermodynamic investigations of amorphous polymers during high rate deformation.* Polymer, 2014. **55**(10): p. 2514-2522.
34. Kendall, M.J. and C.R. Siviour, *Experimentally simulating adiabatic conditions: Approximating high rate polymer behavior using low rate experiments with temperature profiles.* Polymer, 2013. **54**(18): p. 5058-5063.
35. Rittel, D., *On the conversion of plastic work to heat during high strain rate deformation of glassy polymers.* Mechanics of Materials, 1999. **31**(2): p. 131-139.
36. Instruments, TA. *Dynamic Mechanical Analysis Basic Theory & Applications Training*. 2018; Available from: chrome-

extension://oemmndcbldboiebfnladdacbdfmadadm/http://docs.tainstruments.com/training/DMA_Training_2018-August.pdf.

37. Gray, G.T. and W.R. Blumenthal, *Split-Hopkinson Pressure Bar Testing of Soft Materials.* Materials Park, OH: ASM International, 2000., 2000: p. 488-496.
38. Chen, W.W. and B. Song, *Dynamic characterization of soft materials*, in *Dynamic Failure of Materials and Structures*. 2009, Springer. p. 1-28.
39. Laidler, K.J., *The development of the Arrhenius equation.* Journal of chemical Education, 1984. **61**(6): p. 494.
40. Yoon, S.-h., I. Giannakopoulos, and C.R. Siviour, *Application of the Virtual Fields Method to the uniaxial behavior of rubbers at medium strain rates.* International Journal of Solids and Structures, 2015. **69**: p. 553-568.
41. Qin, Q. and G.B. McKenna, *Correlation between dynamic fragility and glass transition temperature for different classes of glass forming liquids.* Journal of Non-Crystalline Solids, 2006. **352**(28-29): p. 2977-2985.
42. Van Loock, F. and N.A. Fleck, *Deformation and failure maps for PMMA in uniaxial tension.* Polymer, 2018. **148**: p. 259-268.
43. Regev, A. and D. Rittel, *Simultaneous transient temperature sensing of impacted polymers using infrared detectors and thermocouples.* Experimental Mechanics, 2008. **48**(5): p. 675-682.
44. Bjerke, T., Z. Li, and J. Lambros, *Role of plasticity in heat generation during high rate deformation and fracture of polycarbonate.* International Journal of Plasticity, 2002. **18**(4): p. 549-567.
45. Garg, M., A.D. Mulliken, and M.C. Boyce, *Temperature rise in polymeric materials during high rate deformation.* Trans. ASME: J. Appl. Mech, 2008. **75, 011009**.
46. Lerch, V., G. Gary, and P. Herve. *Thermomechanical properties of polycarbonate under dynamic loading*. 2003. J. Phys. IV France **110** 159-164
47. SABIC, *LEXAN™ Resin 103R Europe Technical Data Sheet*. 2021.
48. Trivedi, A.R., P. Song, and C.R. Siviour, *Experimentally simulating adiabatic behaviour: Capturing the high strain rate compressive response of polymers using low strain rate experiments with programmed temperature profiles.* Polymer Testing, 2022. **116**: p. 107773.

5 Thermomechanical Effects in Large Strain Compression

5.1 Introduction

Chapter 4 provided the extensive mechanical performances of polycarbonates, and examined the 'time-temperature equivalence' at small and large strain regions combining the temperature- and rate-dependent compression yield stresses. When comparing the tests having the same or similar yield stress at an adiabatic high strain rate and the isothermal low temperature, unexpectedly less softening in large strain region was observed in high rate test than other amorphous polymers. On the other hand, evident softening was observed in medium rate tests compared to the quasi-static low temperature tests. These observations were consistent with the literature, but fewer interpretations were available in existing research.

This chapter addresses the experimental observations in **Chapter 4** to understand the strain rate and temperature coupled effects at large strain regions in adiabatic experimental environments. A high-speed infrared camera was used to measure the temperature rise from 0.01 to 2600s^{-1} at ambient temperature by combining results from a number of experiments. The temperature-dependent temperature rise from -80 to 150 °C, spanning from secondary- to glass-molecular transition, at 0.5 s^{-1} was measured using an embedded thermocouple. In addition, a finite element model was created to understand the thermal boundary conditions to ensure the strain rate, 0.5 s^{-1}, used in these measurements was mostly adiabatic. Finally, the calculation results of the conversion ratio between heat and plastic work (Taylor Quinney coefficient) presented substantial temperature- and rate dependence.

5.2 Paper C: Understanding the temperature, strain rate and their coupled effects on the plastic deformation of polycarbonate. Part I: Experimental study[1]

Abstract

Polycarbonate is a widely used ductile glassy polymer that can undergo large strain deformation before failure. During the plastic deformation process, some mechanical energy is converted to heat, which, if the specimen is loaded at rates sufficient that the heat cannot conduct out of the material, can result in significant temperature rises that affect the mechanical response. Typically, this is expected to result in a reduction in stress, softening, compared to the behaviour under isothermal conditions; however, compared to other glassy polymers, it has been observed that less softening than expected is experienced in polycarbonate. The current paper describes a thorough investigation of temperature rises in polycarbonate. Compression experiments are performed using a screw-driven machine, a hydraulic machine, and a long split Hopkinson bar, all instrumented with a high-speed infrared camera to measure temperature rises at strain rates between 0.01 and 2600 s^{-1} at a starting temperature around 20 °C. Further, temperature rises in compression experiments at 0.5 s^{-1} and starting temperatures between -80 to 150 °C are measured using embedded thermocouples. These span the range of the secondary- to glass-transition of polycarbonate, allowing investigation of the effect of molecular evolution. These experiments are supported by finite element simulations that use a phenomenological viscoplastic model to understand the thermal boundary conditions. Temperature rises are observed in both temperature and rate-dependent tests: experiments at higher strain rates and lower temperatures experience a greater temperature rise because of the higher yield stress; however, there are differences in the conversion ratio between plastic work and heat (Taylor Quinney coefficient), which is both temperature and rate dependent, and strongly affected by both the secondary and glass transitions.

[1] Submitted to a scientific journal; Part II is a numerical study led by a modelling team at the University of Nottingham

Keywords: Polycarbonate; Temperature and rate-dependence constitutive behaviour; High-speed infrared thermography; Adiabatic heating; Taylor-Quinney coefficient.

Introduction

Polycarbonate (PC) is a widely used engineering polymer with good mechanical properties. These properties have been studied for many decades, along with their dependence on pressure [1-3], rate and temperature [4-6]. Several of these investigations have also considered coupled rate and temperature effects, especially at high rates.

It is well-known that the mechanical responses of polymers are highly dependent on the temperature and strain rate. Due to the challenges of conducting high-rate tests, Siviour *et al.* [5] proposed a mapping that was aimed at using low-temperature test data to simulate high-rate mechanical behaviours. The principle was that the yield stress of polymers typically increases with decreasing temperature or increasing strain rate [4-6]. The dependence is, in turn, affected by the glass (α)- and secondary (β)-transitions; in particular, the β-transition can affect the high-rate and low-temperature behaviours. A mapping can be derived by comparing yield stresses at different strain rates and temperatures, and this method has been used to understand the mechanical performance of epoxy [7, 8], polytetrafluoroethylene [7], polyethylene [9, 10]. However, a potential limitation of this mapping lies in the difficulty of predicting the large strain behaviours, which are affected by the elevated temperature rise under high-rate loading [9].

During large strain deformation, plastic work can be partly converted to heat; the conversion ratio from mechanical to thermal work is often called the Taylor-Quinney coefficient (TQC) [11]. As the strain rate increases, the experimental conditions change from isothermal to adiabatic, because the material cannot dissipate the heat into the environment on short timescales [12]. Thus, the heat generated from plastic work can lead to a significant temperature rise that can result in thermal softening at large strains. This has been

investigated in polymers such as PEEK [13], PMMA [14-16], PVC [17], plasticised PVC [18], polyamide 6 [19] and polypropylene [20]. In PVC and PMMA, the softening is consistent with the temperature rises observed or calculated; however, for PC, less softening is observed than expected [6, 14, 17, 21].

To explore this further and understand the motivation for the work in the current paper, Fig. 1(a), using data from a previous study [6], compares rate-dependent and temperature-dependent compression of PC. In particular, experiments at four adiabatic strain rates are compared directly to isothermal experiments at different temperatures, selected to match the yield stress at each of the strain rates. Whilst the experiments at 5 and 60 s^{-1} show significant softening compared to their isothermal 'equivalents', this is less apparent at the higher rates. Kendall and Siviour [14] used a method to reproduce (or experimentally 'simulate' the high-rate behaviour quasi-statically starting at a low temperature and then increasing the temperature of the environment as the test progressed. They found that for PVC, high rate behaviour was well replicated in low rate tests assuming a conversion of work to heat of approximately 100%, whilst for PC a value of 5% had to be used. Such a low TQC value is not consistent with measurements, such as those in Fig. 1(b), although it is also true that the measurements themselves are inconsistent. The work of Kendall and Siviour [14] was further confirmed by Trivedi *et al*. [22], Fig. 1(c), where it is again shown that increasing the temperature of the low rate experiments as though all work is converted to heat gives appropriate softening to replicate results at 20 s^{-1} but too much softening for 2600 s^{-1}.

A key assumption in all calculations of conversion of work to heat is the heat capacity, which is typically taken from Differential Scanning Calorimetry (DSC) measurements of a sample that is not under load. A small number of studies have tried to perform measurements during deformation. For the case of PC, a deformation calorimeter was used to understand the work, heat, and stored energy distribution in compression tests with a final true strain of about 0.4 [23, 24]; here, the heat was found to be around 70% of the mechanical work. However, these experiments were performed at room temperature and low rate, between 0.1 and 0.01 min^{-1}.

This means that the β-transition effects are much less evident than in experiments that span high strain rates or low temperatures.

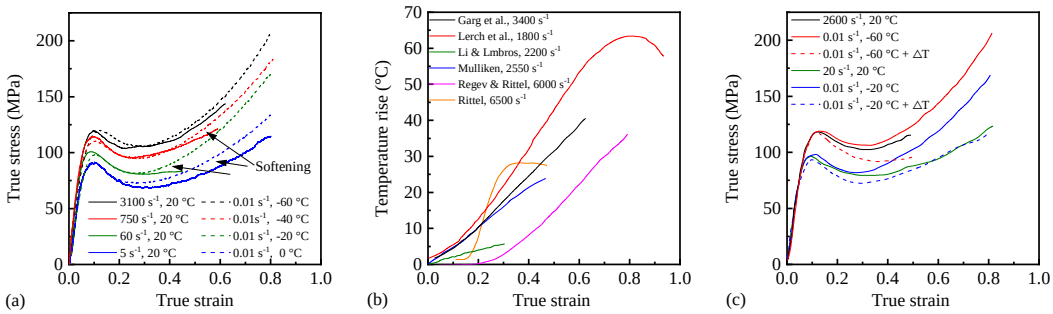

Figure 1. (a) Comparison of stress-strain curves at high strain rates and low temperatures. The colours indicate the equivalent temperature/rate combinations (e.g. 3100 s^{-1}, 20 °C and 0.01 s^{-1}, -60 °C), reproduced from [6], (b) Previously published results for temperature rise measurements in high rate deformation of PC [12, 17, 21, 25-27], (c) Comparison of stress-strain curves at 2600 s^{-1} and 20 s^{-1} with two equivalent quasi-static experiments (which have similar yield stresses) with and without temperature profiling, reproduced from [22].

Many efforts have been made to measure the temperature rise during high-rate experiments; results from the literature are shown in Fig. 1(b). IR detectors have been used [17, 21, 25, 26]; however, the movement of the incident bar can possibly block the cone of radiation [27], which means that this technique only allows a narrow measurement area, and hence small final strain. Thermocouple measurements have also been attempted, but it is very challenging to avoid thermal lag at high rates; for example, results [12, 27] in Fig. 1(b) show a later temperature rise compared with that obtained in the experiments using an IR detector. Moreover, neither method can produce visible thermal images, and to the current authors' understanding, no existing research has used full-field thermal imaging in high-rate experiments on PC. More information about using thermocouples and thermal imaging in high-rate (split Hopkinson bar) tests is given in the review by Walley *et al.* [28].

In the research presented in the current paper, we address these challenges through a comprehensive and careful evaluation of temperature rises across different strain rates and starting temperatures. For experiments starting at room temperature, and at rates from 0.01 to 2600 s^{-1}, a high-speed IR camera (Telops M3K) is used, with careful triggering allowing a higher data density than in previous studies. For the high rate experiments, a long split Hopkinson bar (LSHPB) was used to extends the final true strain to higher than 0.8. At the same time, compression experiments are performed from -80 to 150 °C at 0.5 s^{-1}, which is shown through a combination of experiment and modelling to be effectively adiabatic, with temperature rise measurements conducted using a thermocouple. Time-temperature equivalence is confirmed by comparing high-rate data with the 'equivalent' (similar yield stress) low-temperature data. Moreover, the Taylor-Quinney coefficient (TQC), the ratio of mechanical work to heat, is calculated using some different assumptions for estimating plastic strain. These calculations are enabled by careful DSC measurements of heat capacity over the full range of temperatures. This gives an understanding of the error introduced by the challenge of defining (and calculating) plastic work under high rate conditions. Finally, the rate- and temperature-dependence of these TQC values are used to evaluate the effect of the β- and α-transitions. Recognising that calculation of the TQC values involves a number of assumptions, stress-strain, DSC and temperature rise data will be made available in an online repository so that they can be directly compared to the output of future constitutive models.

Material information and sample preparation

Injection moulded high molecular weight polycarbonate, LEXAN^{TM} Resin 103R, is used in this study. The raw material was provided as a flat sheet, from which all compression samples were cut. Two sample sizes are used in this study, 5 mm diameter with 3 mm thickness (from a 3 mm thick sheet) and 12 mm diameter with 6 mm thickness (from a 6 mm thick sheet). To standardise the thermal history, and minimise residual stresses from moulding, before cutting samples, all sheets were annealed by heating to 10 °C above the glass-transition temperature (T_g = 145 °C) at 25 °C/hour, followed by a 6 hour hold before cooling to room temperature at 10 °C/hour. More information about materials and sample preparation can be found in previous papers [3, 6].

Experimental procedure

Modulated Differential Scanning Calorimetry (MDSC)

A commercial DSC device, TA Instruments Q2000, was used to perform MDSC to determine the specific heat capacity, C_p, as a function of temperature. The MDSC samples were 0.5 mm thick discs with a 5.6 mg mass, sealed in an aluminium alloy pan. The scanning was conducted using a 2 °C/min temperature ramp from -90 to 180 °C with ± 0.6 °C temperature oscillation over 60 seconds.

Dynamic Mechanical Analysis (DMA)

Isothermal frequency sweep DMA experiments were performed using the three-point bend configuration (50 mm span length), on samples of 10 mm width and 3 mm thickness; consistent with the ASTM standard D4065. The sweep frequencies were 0.2, 0.5, 1, 2, and 5 Hz, and the temperature range was from -110 to 170 °C with a 2 °C increment and a 5 min equilibrium time for each temperature step. For the case of PC, this configuration can generate more accurate temperature-dependent moduli than the single cantilever beam configuration. More experimental details can be found in Song *et al.* [6].

Compression experiments

Three mechanical test machines are employed in this study, screw-driven Instron 5980 universal tests machine, hydraulic machine and long split Hopkinson bar (LSHPB), which are sequentially used for quasi-static (QS), medium-rate and high-rate tests, Fig. 2. All low-rate tests, from 0.01 to 0.5 s^{-1}, are true rate controlled using an extensometer attached to the anvils near to the specimen, with temperature controlled using an environmental chamber from -80 to 150 °C. For the medium rate experiments, we used an in-house hydraulic testing system. Here, force is obtained from a strain gauge based load cell and displacement from the average of two linear variable differential transformers (LVDTs). Strain rates were 1 to 15 s^{-1}, and the machine operates at constant displacement rates, not constant true strain rates.

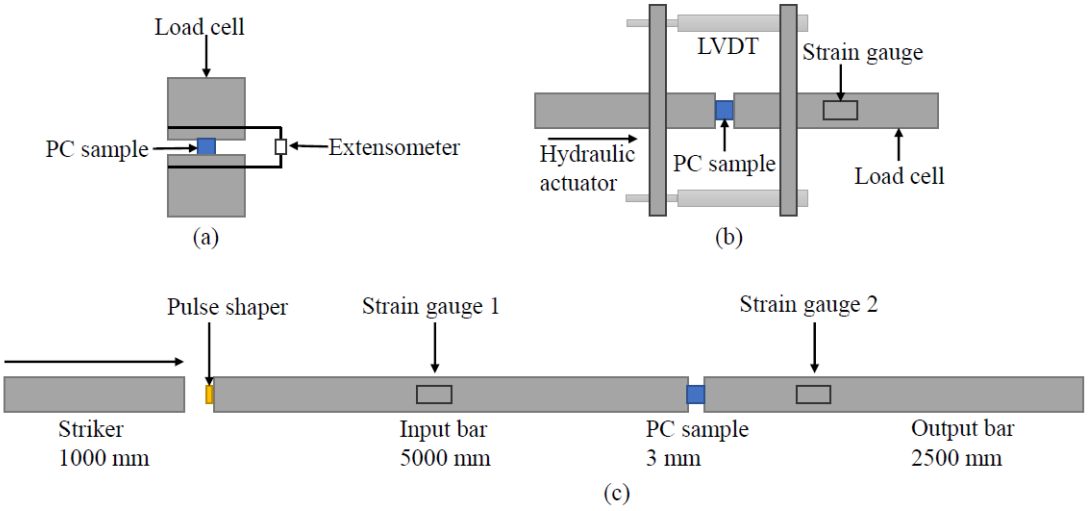

Figure 2. Mechanical test machines (a) Quasi-static compression, (b) Hydraulic compression, (c) Long Split Hopkinson pressure bar.

This study utilised a long split Hopkinson pressure bar (LSHPB), Fig. 2(c), to perform experiments at around 2600 s^{-1}, with a final true strain of about 0.85. PC specimens were sandwiched between the Ti-6AL-4V input and our bars, and the input, reflected and output signals from gauges mounted on the bars were used in standard calculations to derive the stress-strain behaviour in the specimen and to confirm static stress equilibrium during the tests. For a more detailed review of high rate testing of polymers and the advantages of the LSHPB system for polymers, readers can refer to [29-31] and [32], respectively.

At all rates, petroleum jelly was used as a lubricant between the specimen and anvils for experiments at and above room temperature [33] , whilst AEROSPEC® 210 graphited grease was used in the low-temperature tests.

Calibration of thermocouple, IR camera and emissivity of PC

For quasi-static experiments below room temperature, a K-type thermocouple with a 0.75 mm bead diameter was used to measure the temperature rise. A high-speed thermocouple amplifier with 5 K μs^{-1} response time is employed to capture the thermal data simultaneously with the load and displacement. The amplifier used had a voltage-temperature conversion ratio of 0.0113 V K^{-1}.

A high-speed infrared (IR) camera, TELOPS FAST-IR M3K IR camera, mounted with a 50mm lens and 0.75 inch (19 mm) extension ring, was used to measure the temperature rise in all experiments starting at room temperature. A sapphire window was used to protect the lens during LSHPB experiments. Before testing, the IR camera was carefully calibrated using a black body from 50 to 150 °C, with and without a sapphire window. The transmittance of the sapphire window was measured to be approximately 69% for the camera configuration used. The calibration process of the IR camera and IR camera settings for all experiments can be found in Appendix A.

In order to measure the emissivity of the specimen, a temperature-controlled black panel was used to elevate the temperature from 20 to 65 °C; calibrated black tapes and a PC sheet were attached to this black panel. By comparison to the panel and tape, the emissivity of PC was evaluated as 0.97 ± 0.1, which is very close to literature values: 0.92 to 0.96 [34], and 0.93 ± 0.2 from 40 to 100 °C [35]. The difference between using an emissivity of 0.97 and 0.92 at about 80 °C is about 1.4 °C; thus, in the current work, a mid-range value, 0.95, is used to post-process all thermal measurement data. The emissivity calibration setup and data are given in Appendix B.

Evaluation of thermal conditions

It is possible to estimate the strain rate above which the experiment becomes fully adiabatic using the following equations [29]:

$$\alpha = \frac{k}{\rho C_p} \tag{1}$$

$$l_t = 2\sqrt{\alpha t} \rightarrow t = \frac{1}{\alpha}\left(\frac{l_t}{2}\right)^2 \tag{2}$$

$$\dot{\varepsilon} = \frac{1}{t} \tag{3}$$

Here α is thermal diffusivity, k is thermal conductivity, C_p is the specific heat capacity, and l_t is the length of the specimen. This gives an approximate value with which to plan experimental programs; however, with the decrease in sample length during the compression, the timescale for heat diffusion also decreases, which means that a higher strain rate is required to ensure the experimental condition is adiabatic.

To better understand the evaluation of thermal conditions during experiments, an axisymmetric finite element model was created using a three-network viscoplastic constitutive model [36]. In the current work, this model is only used to replicate the experimental stress-strain curve phenomenologically and then to understand heat generation and dissipation during large strain deformation; we do not attempt a physical interpretation of the polymer behaviour. Detailed information, such as a schematic and information about parameter fitting, can be found in Appendix C. Thermal and displacement coupled axisymmetric elements, CAX4RT in Abaqus, are used for the PC samples (3 mm thickness and 5 mm diameter; 6 mm thickness and 12 mm diameter) and the steel anvils. Previous research on similar behaviour has simulated the interfaces between the sample and anvils as being in perfect contact, with the conductance across the interface defined as 1000 W m^{-2} K^{-1}, e.g. [37, 38]. However, thermal conductance is a pressure-dependent parameter, and values for polycarbonate/metal interfaces have been measured between 150 and 940 W m^{-2} K^{-1}, depending on interface pressure at pressures between 510 and 3000 kPa [39, 40] At the same time, the thermal conductivity of PC has

been found to be insensitive to the temperature and pressure [40], and 0.2 W m^{-1} K^{-1}[41] was used in this work.

Simulation results

Fig. 3(a) shows modelled temperature distributions in the specimen at 0.8 true strain, starting at an environmental temperature of 20 °C. To evaluate the temperature that would be measured by an embedded thermocouple, the temperature rise of the centre point (named as the 'output point' in Fig. 3(a)) is extracted for both 3 mm and 6 mm samples at rates of 0.1 and 0.5 s^{-1} and conductances of 0, 150 and 1000 W m^{-2} K^{-1} Firstly, the two extreme values are considered, Fig. 3(b). Here, the TQC is assumed to be 1, meaning all the plastic work is converted to heat. In these cases, the samples generate the maximum amount of heat, and dissipate the minimum and maximum amounts. When the strain rate is 0.1 s^{1}, the 3 mm sample reaches a lower temperature than the 6 mm sample, and the difference between no conductance and full conductance in the 6 mm sample at 0.8 true strain is of order 11 °C. For a strain rate of 0.5 s^{-1}, the temperature rise is almost the same for the models with high conduction and no conduction until 0.6 true strain, but at higher strains, the 3 mm model shows measurable thermal dissipation: the maximum temperature rise difference is 6.5 °C. It should, however, be noted that the conversion ratio between plastic work and heat cannot be 100%; at the same time, the interface between the sample and anvils is unlikely to have such a high conductance (e.g. lubricant decreases the heat transfer). Thus, the simulation was repeated using a more realistic TQC value from later experiments (0.55, in Fig. 15(c)) and a conductance of 150 W m^{-2} K^{-1}. In Fig. 3(c), the temperature rises obtained for the two sample lengths at 0.5 s^{-1} are consistent with the zero conductance model to a strain of 0.7, and at 0.8 the difference is less than 2 °C for the centre point. It is also noted that the temperature rise in this simulation is similar to the thermocouple measurement in Fig. 5(c); hence, it is concluded that experiments at 0.5 s^{-1} may be regarded as adiabatic for the purposes of this study.

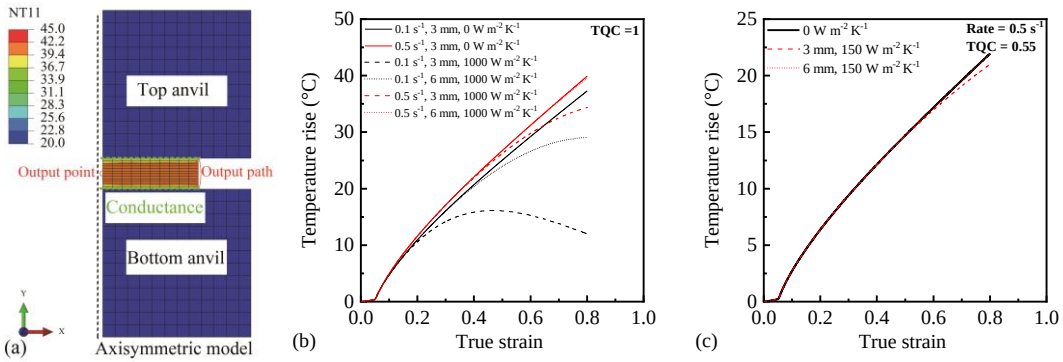

Figure 3. (a) Numerical model setup (here, true strain is 0.8) (b) Simulated temperature rise under different experimental conditions representing the extremes likely condition (c) Simulation of temperature rises using TQC = 0.55, and conductance 150 W m^{-2} K^{-1}.

In order to verify the thermal conditions used, it is instructive to look at the temperature distribution in the sample, and in particular the shape of this distribution, which is compared to data from one of the experiments described later in the paper. The surface temperature rises in the simulation and experiment, named 'output path' in Fig. 3(a) and Fig. 5(d), were extracted and are compared in Fig. 4. Here, the TQC is defined as 0.55 and three conductance values are used. The temperature rise values in the experiment are shifted (but not rescaled), using the right-hand y-axis, to make the maximum temperature rise overlap with the hottest point in the simulation; and enable comparison of the temperature distribution independent of the peak. At low strains, the experimental temperature rise is lower than the numerical value, which may be due to a larger fraction of energy being stored before strain hardening [42]; it will also be seen later that the TQC does not take a constant value, it shows an increasing trend before reaching a maximum value of 0.55 at a true strain of 0.6, and then decreases to the end of the test (Fig. 17). At larger strains, Fig. 4(b) to (d), the maximum temperature difference between the experiment and model is less than 1.5 °C. Near the boundary, the experimental value is between the numerical values at 150 and 1000 W m^{-2} K^{-1} and follows the shape of those curves. Together, these indicate that the model is a good representation of the experimental thermal conditions.

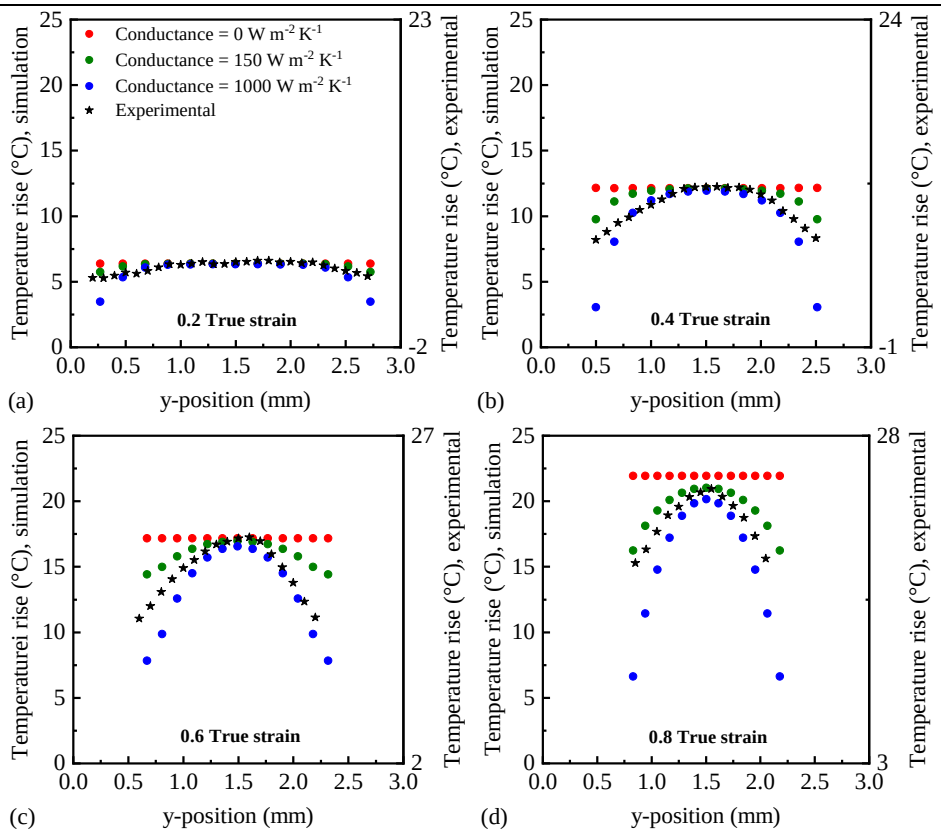

Figure 4. (a) Experimental (IR camera) and numerical temperature profiles along the length of the specimen at (a) 0.2 true strain (b) 0.4 true strain (c) 0.6 true strain (d) 0.8 true strain

Experimental validation

Results from validation experiments are shown in Fig. 5. The mechanical responses and the temperature rise obtained from different sample sizes and strain rates are compared in Fig. 5(a) and (b). All data in these figures are obtained from the pristine samples (no embedded thermocouple), and the temperature rise is the average value measured by the IR camera (see also Fig. 8(d)). The mechanical performances obtained from the different sample sizes at the same strain rate are very consistent, and trends in the temperature rise data with rate and sample size are consistent with the simulation results shown above: the difference in average temperature rise in the two sample sizes is much less at 0.5 s^{-1} than at 0.1 s^{-1}.

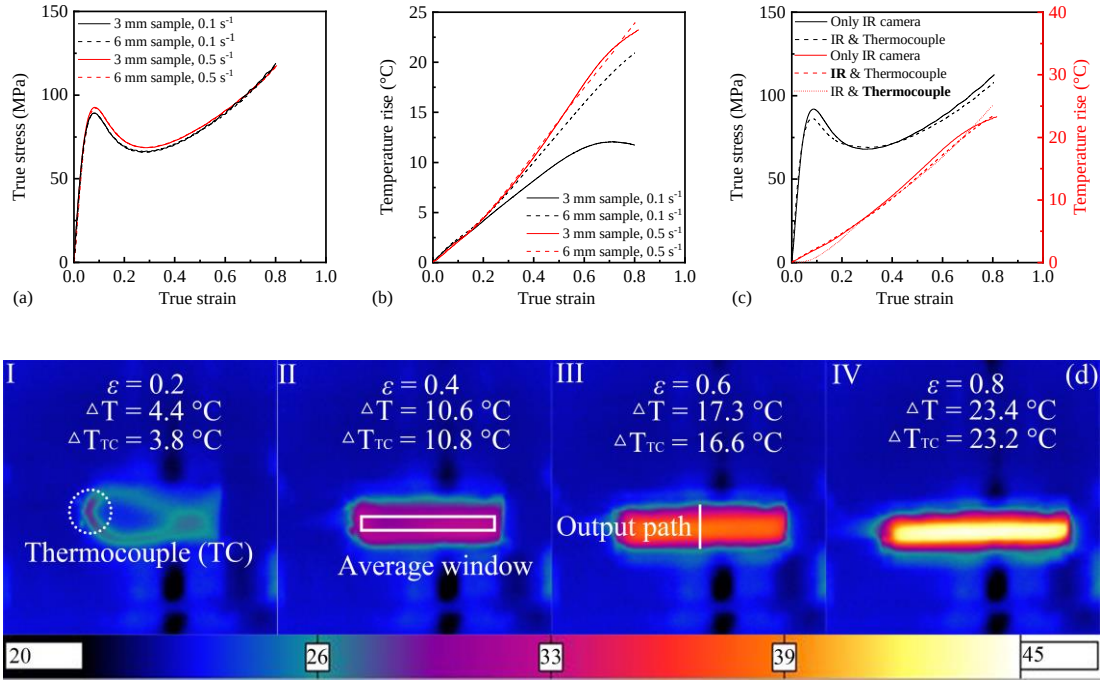

Figure 5. (a) True stress-true strain curve at 0.1 and 0.5 s^{-1} using two different sample sizes; (b) Temperature rise-true strain curve at 0.1 and 0.5 s^{-1} using two different sample sizes, measured using an IR camera only, averaged over the window indicated in (d); (c) Effects of thermocouple on true stress-true strain curve, and comparison of temperature rise measured by different methods at 0.5 s^{-1}; (d) IR temperature maps obtained on a sample embedded with a thermocouple at 0.5 s^{-1}.

The effects of the embedded thermocouple can be seen from the comparison of stress-strain curves and the temperature rise data in Fig. 5(c). The yield stress of the drilled sample (with the embedded thermocouple) is lower than the pristine sample at 0.5 s^{-1}. Notably, the large strain behaviour of drilled and pristine samples is very consistent. The temperature rise for the pristine sample and the drilled sample measured by the IR camera and the thermocouple together, are very similar from true strains of 0.2 to 0.7. The difference at low strains might be caused by the time taken for the sample to fully contact the thermocouple. It is noted that early in the experiment, there is some localisation visible around the thermocouple in the IR image, but that later, the distribution is homogeneous.

Experimental results

MDSC test

Fig. 6 shows the reversing specific heat capacity (Rev C_p) as a function of temperature. The dependence is linear below the glass-transition temperature. For later calculations, the piecewise fitting shown in the figure was used: -80 to 140 °C, 140 to 150 °C, and higher than 150 °C. It is worth mentioning that, in later calculations, comparisons are drawn between TQCs derived using C_p values that change with the changing temperature as the experiment progresses (simultaneous value) and those derived just using the C_p at the starting temperature (constant value); the former is in the main paper, and the latter in Appendix D.

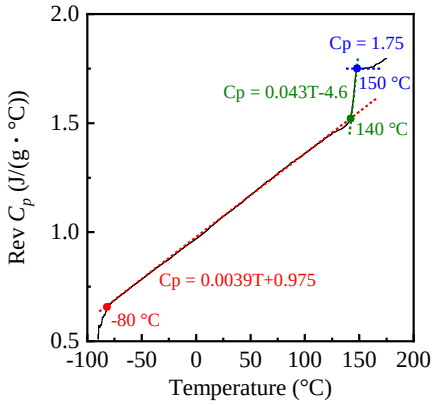

Figure 6. Temperature-dependent reverse specific heat capacity measured by MDSC.

DMA test

Curves of frequency-dependent storage modulus and Tan δ against temperature are presented in Fig. 7. The β-transition is observed at temperatures of -30 °C and below. Above that temperature, the moduli gradually decrease with the increased temperature until the glass transition temperature is reached. More detailed experiment results and analysis are presented in [6].

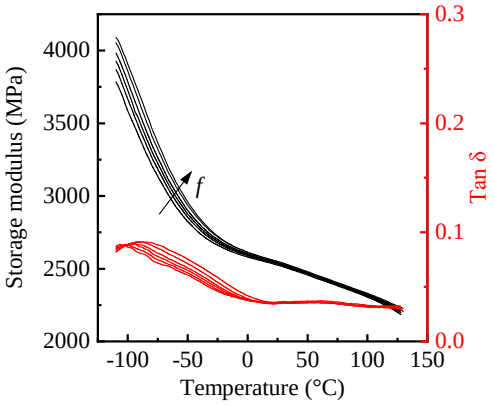

Figure 7. DMA data using three-point bend configuration, reproduced from [6]

Quasi-static tests

Quasi-static tests with IR camera at room temperature

Each test was repeated three times for all quasi-static and medium rate experiments. Fig. 8(a) shows the true stress-true strain curves obtained at 0.01, 0.1 and 0.5 s^{-1}. The initial yield stress increases with increasing strain rate. However, from around 0.5 true strain, the stresses at lower strain rates are higher, i.e. the higher rate data display less hardening. Fig. 8(b) shows the temperature rises (ΔT) captured using the IR camera. The maximum temperature rise at 0.01 s^{-1} is 1.8 °C, insignificant for the mechanical properties of PC; the temperature rises at 0.1 and 0.5 s^{-1} are much higher. Thus, the relative softening at large strain during deformation at higher strain rates is assumed to be a thermal effect. In Fig. 8(c), the total energy is obtained by the integration of the true stress-true strain curve; and the thermal energy is calculated using $\rho C_p \Delta T$. Here, ρ (1.2 g/cm^3) is the density provided by the material supplier [41], and the value of C_p is obtained from the DSC data. Fig. 8(d) presents selected thermal images from experiments at 0.1 and 0.5 s^{-1} (see footnote [1]).

[1] A large number of thermal images is captured in quasi-static tests, the full set will be made available in an online repository with DOI provided at the end of this paper.

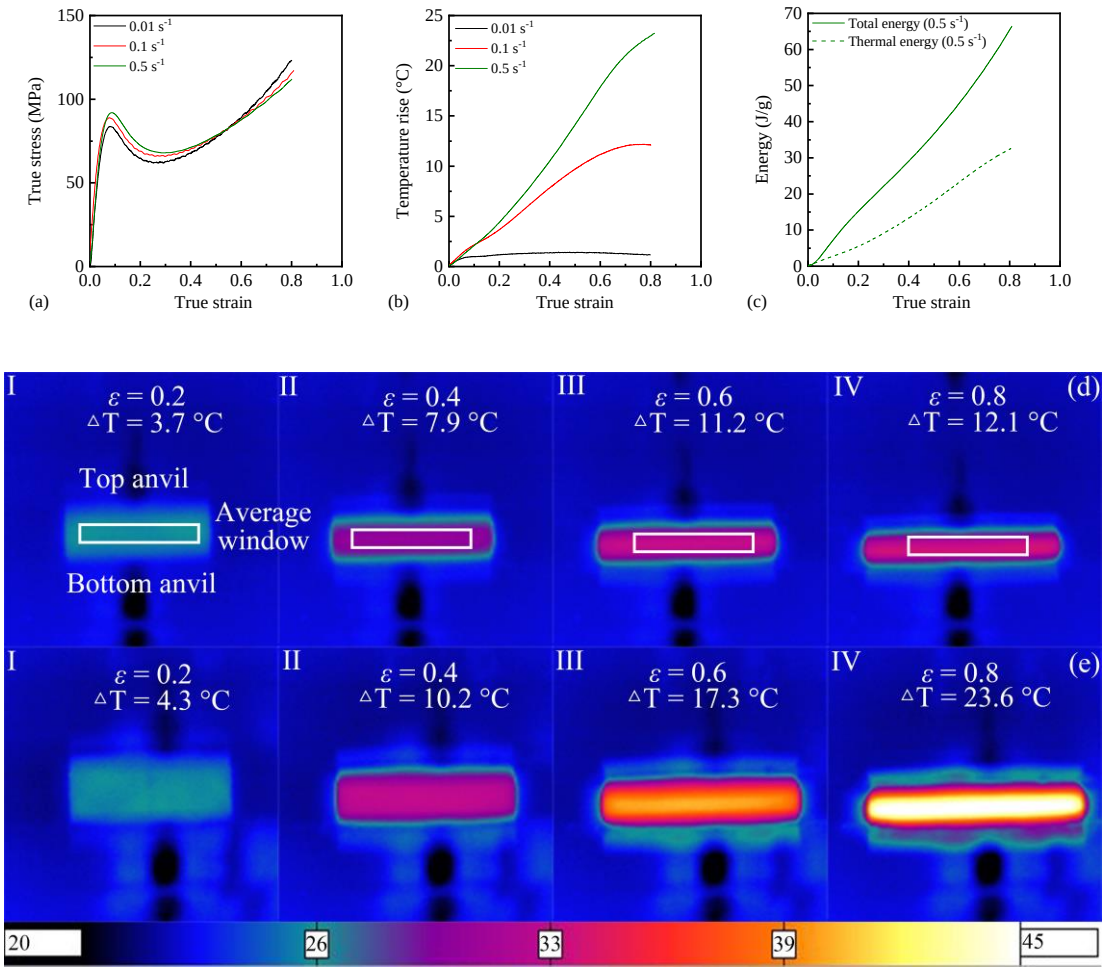

Figure 8. Data from quasi-static tests: (a) True stress - True strain curves; (b) Temperature rise - True strain curves obtained from IR camera using window shown in (d); (c) Total work and Heat work against true strain at 0.5 s^{-1}; (d) Thermal images from experiment at 0.1 s^{-1} (e) Thermal images from experiment at 0.5 s^{-1}.

Quasi-static tests at low temperatures

It is challenging to use an IR camera on experiments at non-ambient temperatures, hence, the temperature rise measurements are obtained from embedded thermocouples, noting the close agreement between IR and thermocouple data in Fig. 5(a). Fig. 9(a) compares the constitutive behaviour of the PC from -80 to 20 °C at 0.01 and 0.5 s^{-1}. Fig. 9(b) shows that the yield stresses are more rate-dependent when the temperatures are around the beta transition or lower, this observation is consistent with the DMA results in Fig. 7. As expected, the yield stresses are higher at the higher strain rate; however, at large strains, the stresses at 0.01 s^{-1} exceed those at 0.5 s^{-1}, this is attributed to the thermal effects.

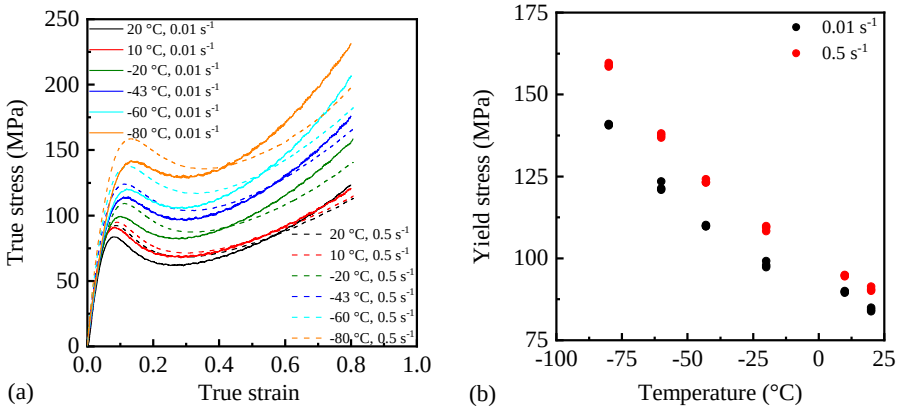

Figure 9. (a) Comparison of true stress - true strain between 0.1 and 0.5 s^{-1} at different temperature tests (all samples are pristine) (b) Comparison of yield stresses between 0.1 and 0.5 s^{-1} at different temperatures.

The temperature rises in low temperature tests were measured at 0.5 s^{-1} to quantify the thermal effects. Fig. 10(a) shows the effects of the embedded thermocouple on the constitutive behaviour from -80 to 20 °C. The pristine samples have higher yield stresses, but the stresses at large strain are only modestly affected. Fig. 10(b) plots the temperature rise as a function of true strain. The lower the temperature, the higher the temperature rises; this is expected because more plastic work is done at the lower temperatures. This results in more thermal softening, in the experiments at 0.5 s^{-1}, at -80 and -60 °C compared to 10 and 20 °C (Fig. 9(a)). The thermal energies (i.e., heat calculated from the temperature rise) at different temperatures are shown in Fig. 10(c).

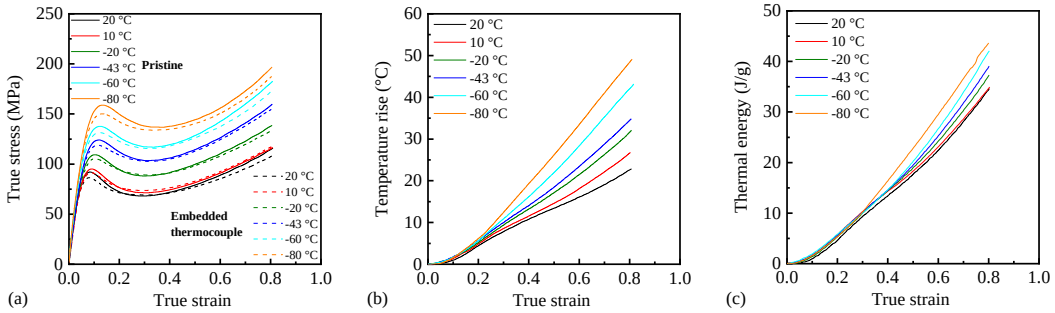

Figure 10. (a) True stress - True strain curves at low-temperature tests with and without embedded thermocouple (b) Temperature rise in low temperature experiments measured by an embedded thermocouple (c) Thermal energy (calculated using the simultaneous temperature-dependent C_p) versus true strain.

Medium rate tests

The temperature rises during the medium rate tests are measured using an IR camera. These experiments are not performed under closed loop control nor in true strain control, so regions of the experiment where the true strain has a linear relationship with time are selected, as shown in Fig. 11. Not surprisingly, the test at a higher strain rate has a higher yield stress and higher temperature rise, Fig. 11(a) and (b). Fig. 11(c) shows the total mechanical energy and thermal energy from these tests, calculated using the methods described above. Fig. 11(d) and (e) present the thermal images obtained at 1.5 and 13.5 s^{-1}. These are consistent with the stress-strain curves: the higher strain rate test has a higher temperature rise at the same strain. Again, each test was repeated three times.

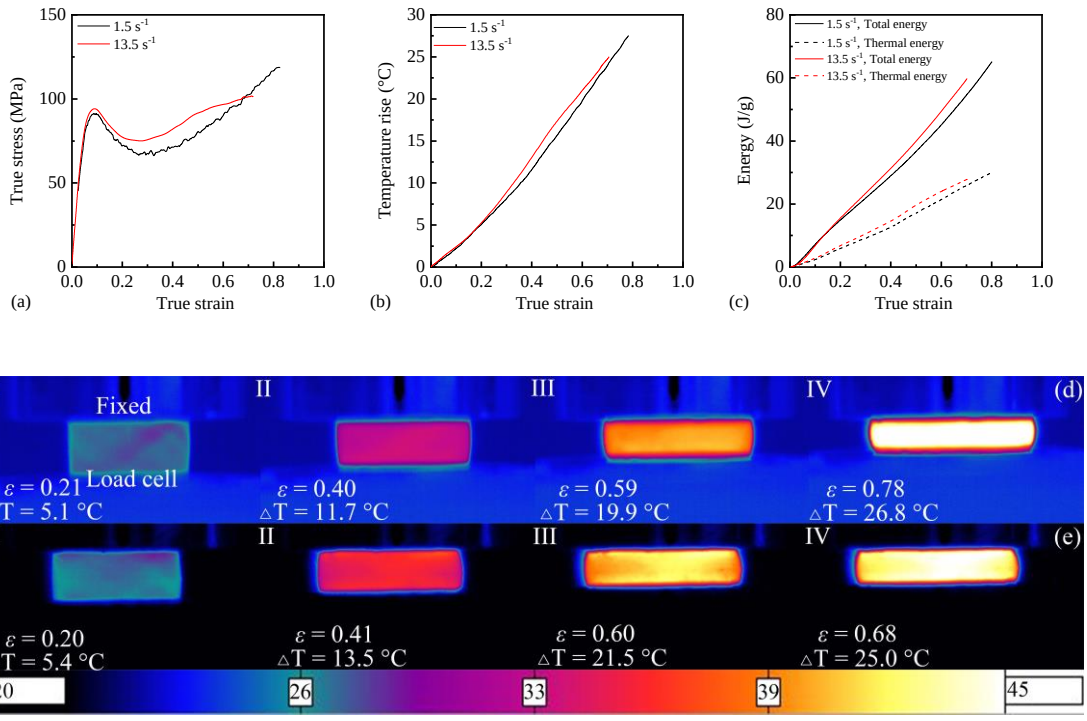

Figure 11. Data from medium rate tests (a) True stress-True strain curves (b) Temperature rise-true strain curves (c) Total mechanical energy and thermal energy (using the temperature-dependent simultaneous C_p)-true strain curves (d) Thermal images in experiment at 1.5 s^{-1} (e)Thermal images in experiment at 13.5 s^{-1}.

High rate experiments

Fig. 12(a) shows seven true stress-true strain curves obtained at a strain rate of about 2600 ± 150 s^{-1} using an LSHPB equipped with a high-speed IR camera. The mechanical response is repeatable between experiments, which provides an opportunity to combine thermal images from multiple experiments and construct a more complete set of temperature rise information. The IR camera was triggered at different times for each test, each time providing 3 to 5 thermal images during the loading period. The monitor signal from the camera, indicating exposure, can be synchronised with the signal collected from the output Hopkinson bar, as shown in Fig. 12(b). The average temperatures from all thermal images are stitched to produce a temperature rise curve as a function of true strain, Fig. 12(c). The good overlap between tests indicates the reliability of the results obtained. The maximum strain is 0.85, and the temperature rise at this strain is about 58 °C, however, the thermal softening at large strains is insignificant compared with that observed in the low and medium rate tests (Fig. 1(a)).

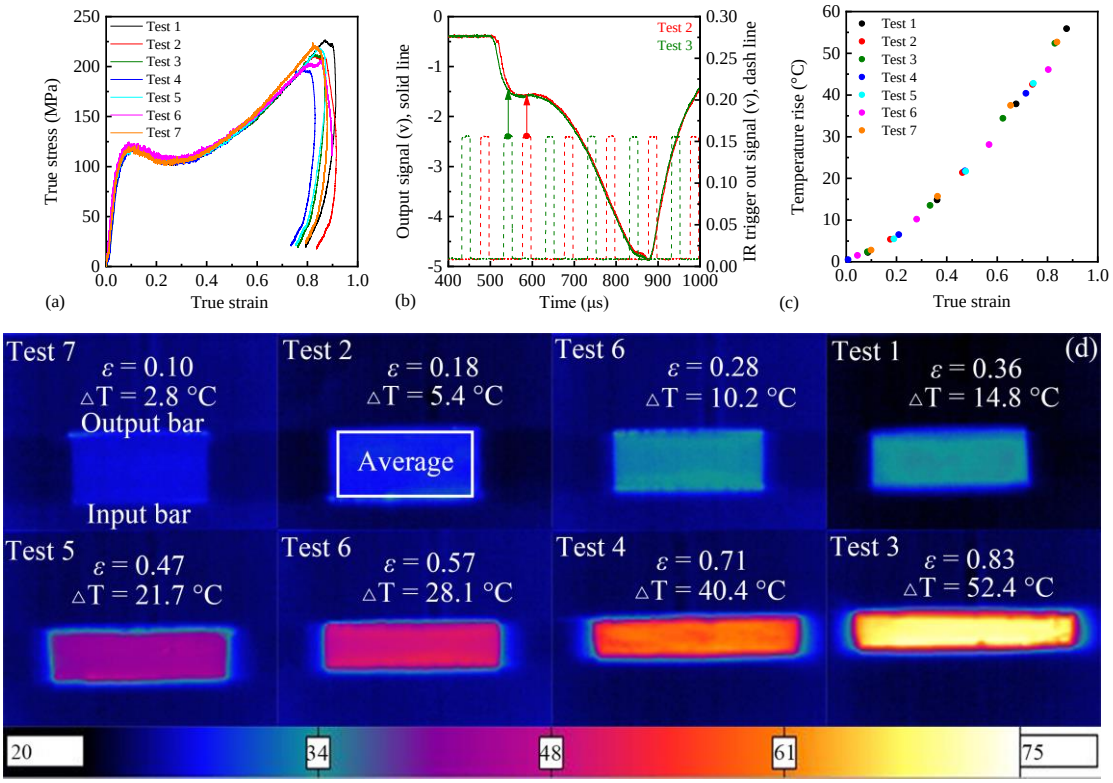

Figure 12. Data from high strain rate experiments: (a) True stress-true strain curves for seven Hopkinson bar tests; (b) Time-shifted output bar signal and IR monitor output from two tests; (c) Mean temperature rise-

true strain for all the images obtained (d) Selected thermal images from low to high strain, montage produced from seven tests.

Comparison between 'equivalent' rate and temperature tests

To further understand the thermomechanical deformation mechanisms during large strain deformation, rate and temperature 'equivalence' comparisons are performed, shown in Fig. 13. Here, the 'equivalence' refers to tests at different rates or temperatures with similar yield stress. Fig. 13(a) compares an isothermal (0.01 s^{-1}) test at -60 °C with one at 0.5 s^{-1} at -43 °C and one at 2600 s^{-1} at 20 °C. It is observed that the isothermal test overlaps with the high-rate test very well, even though the latter exhibits a temperature rise of about 55 °C. At the same time, evident thermal softening is seen in the low temperature 0.5 s^{-1} test (pristine sample), even though the temperature rise (measured using a thermocouple in a drilled sample) under these conditions is lower than in the high-rate experiment.

Fig. 13(b) compares further 'equivalent' experiments: 0.01 s^{-1}, -6 °C (isothermal); 0.5 s^{-1}, 10 °C; and 14.1 s^{-1}, 20 °C. The test at 0.5 s^{-1} (pristine sample) still shows more thermal softening than the isothermal test. Finally, 13(c) compares 0.01 s^{-1}, 10 °C and 1.4 s^{-1}, 20 °C; thermal softening can be observed at a higher rate in the strain hardening part.

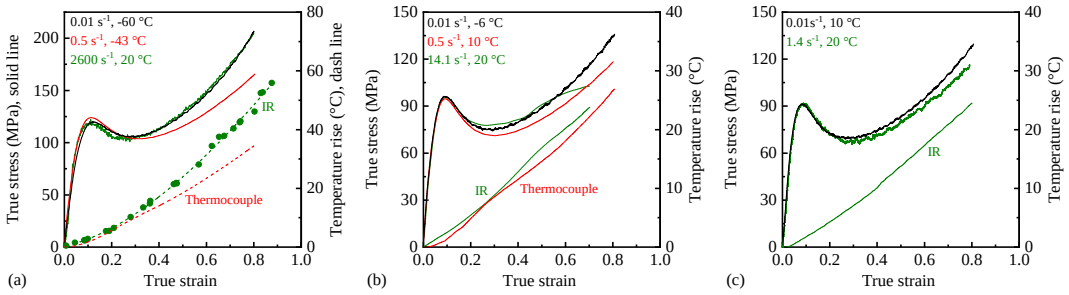

Figure 13. Comparison of true-stress-true strain curves at different test conditions (pristine samples) and corresponding temperature rise measurements.

These comparisons and thermal measurements at different loading conditions strengthen observations

made from literature data presented in the introduction, the temperature rises affect the medium (1 to 10 s^{-1}) and low rate (0.5 s^{-1}) tests as expected, but less thermal softening than expected is seen at high strain rates. The next section will discuss these data further.

Discussion

The ratio between plastic work to heat (TQC) can be calculated using the following equation:

$$\Delta T = \frac{TQC}{\rho C_p} \int \sigma \mathrm{d}\varepsilon_i \tag{4}$$

Here, $\int \sigma \mathrm{d}\varepsilon_i$ is the integral of the stress-strain curve. This is usually calculated using plastic strain, however, the apparent stiffness in compression experiments is typically less than the real material modulus, which makes accurate calculation of plastic strain difficult. This study uses three different methods (strains) to calculate the mechanical work, and the resulting values are compared. The first uses the total true strain. The second, called 'plastic strain' uses:

$$\text{Plastic strain} = \text{True strain} - \frac{\text{True stress}}{\text{Current modulus}} \tag{5}$$

Where the rate and temperature dependent modulus is obtained from a time-temperature mastercurve produced from DMA data, the third, 'shifted plastic strain', takes the same data and then shifts them to lower strain so that the yield point is at $\varepsilon = 0$. The three curves thus produced are shown in Fig. 14(a). Three different mechanical works can be calculated using the three strains, and at the same time two thermal energies are calculated using a simultaneous C_p and a constant C_p. All of these energies are shown in Fig. 14(b). Recall that the simultaneous C_p is obtained from the piecewise curve fitting to the MDSC test (Fig. 6), and the constant C_p uses the value at the experiment start temperature. Fig. 14(c) shows the three TQC values calculated using the different mechanical works and simultaneous C_p in high-rate experiments. In the remainder of this section, all thermal work-related calculations use the simultaneous C_p; the calculations based on constant C_p are shown in Appendix D.

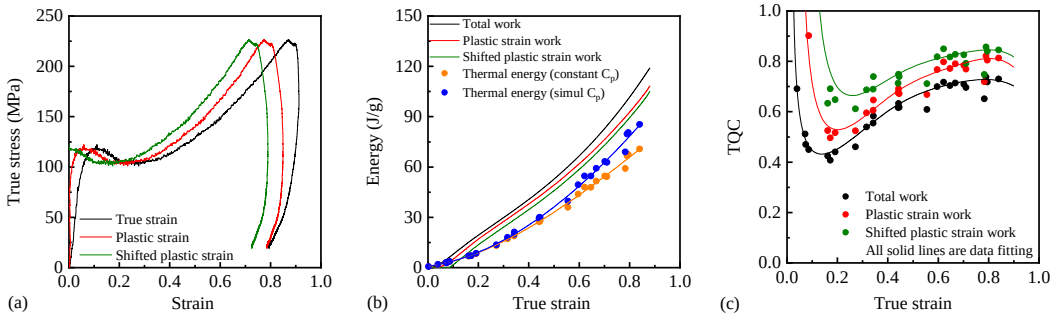

Figure 14. An example of TQC calculation (a) True stress against three different strains (b) Three mechanical work calculations obtained by integrating the curves in Fig. 14(a), with thermal energies calculated using simultaneous and constant C_p (c) TQC based on three different mechanical works, and simultaneous C_p.

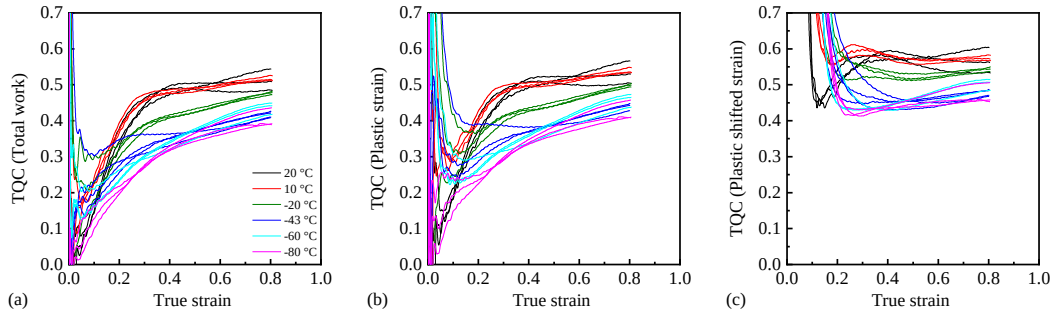

Figure 15. Temperature-dependent TQCs calculated based on three different mechanical works and the simultaneous C_p (here, all temperature rise data are obtained using a thermocouple).

Following the same method, Fig. 15 shows temperature-dependent TQCs calculated from quasi-static data. These curves present a decreasing trend with decreasing temperature. There is significant variation until about 0.3 true strain, followed by plateaus from 0.3 to 0.6. To investigate this further, room temperature calculations from thermocouple and IR data were compared. In Fig. 16(a), TQCs obtained from IR and thermocouple measurements made on drilled samples are consistent from strain 0.3 to 0.7, but vary at lower strains; there is also some evidence of an increase in the thermocouple value towards the end of the experiment. Fig. 16(b) shows a comparison of the temperature rises, showing that the temperature rise in the thermocouple is observed later in the thermocouple data than the IR data. This is because of poor contact between the specimen material

and thermocouple early in the experiment, which also therefore explains the poor TQC value at low strains.

Fig. 16(b) also shows a discrepancy between the average and maximum temperature rises from the IR camera, at small strains. This is attributed to localisation in the specimen around the thermocouple tip (also observed in Fig. 5(d). To confirm this, Fig 16(c) compares the average and maximum IR measurements from a pristine sample, the averaging region is indicated by the white window in Fig. 8(d). The two measurements agree until 0.7 strain, after which the effect of thermal conduction tends to reduce the average value.

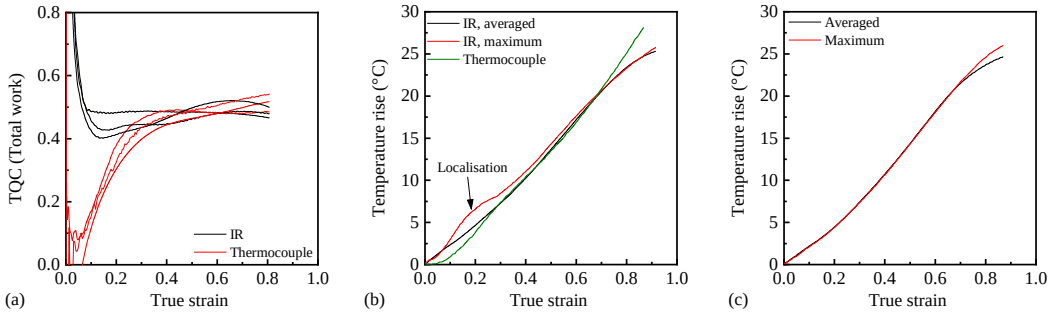

Figure 16. (a) Comparison of TQC calculated from the temperature rise measured using both an IR camera and a thermocouple at 0.5 s^{-1}; (b) Comparison of temperature rise measurements from IR and thermocouple; (c) Temperature rise measurements performed using an IR camera only on a pristine sample.

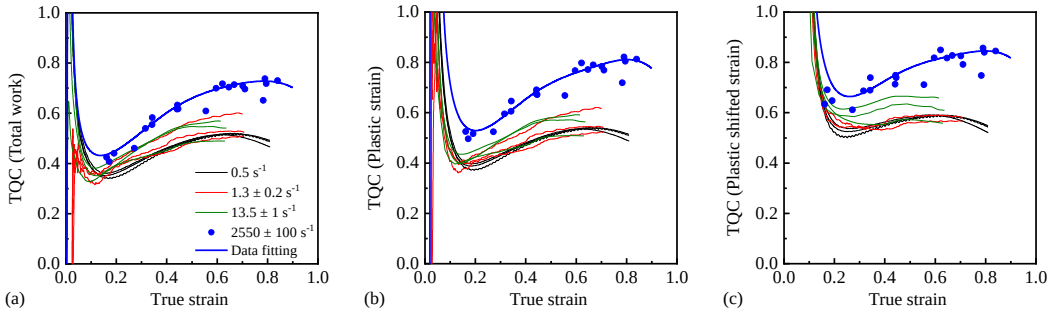

Figure 17. Rate-dependent TQCs calculated based on three different mechanical works calculated using a temperature-dependent specific heat capacity. All temperature rise data are measured using an IR camera. The blue circles indicate the stitched high strain rate data in different tests, and the solid blue line is generated using polynomial curve fitting.

The rate-dependent TQCs are plotted in Fig. 17. All three graphs indicate that the higher strain rate

experiments have a higher TQC, which means a higher fraction of energy is dissipated as heat in high-rate deformation than in quasi-static and medium-rate. Some variation can be found in medium-rate tests, which might be caused by the inaccurate controlled strain rate in these tests.

To better understand the effect of thermodynamic transitions, further experiments were conducted at different temperatures to include the β- and α-transitions. Stress-strain data can be found in Appendix D. In order to compare TQCs, mean values were obtained between 0.35 and 0.55 true strain at different temperatures; these are shown in Fig 18. The dependence of TQC on temperature below Tg is bilinear, with a higher gradient below the β- transition; TQC drops as the temperature moves through the α-transition.

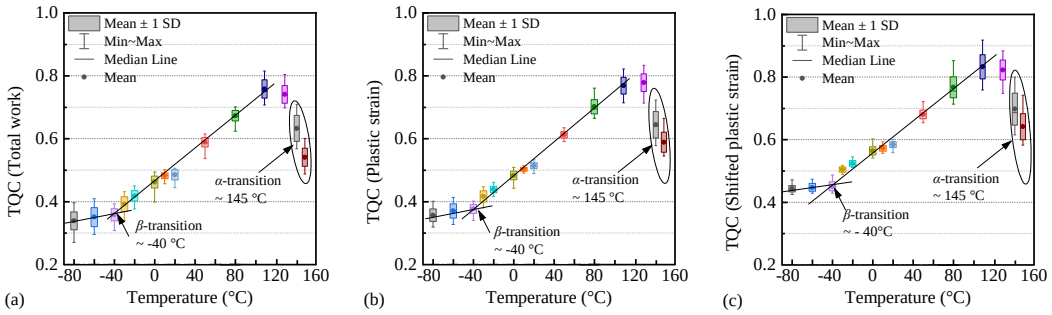

Figure 18. Temperature-dependent TQC calculated using (a) Total work (b) Plastic work (c) Shifted plastic work, and simultaneous specific capacities.

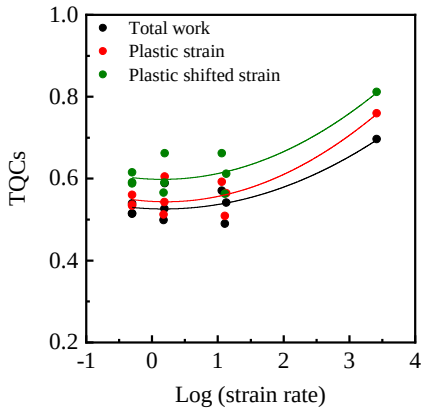

Figure 19. Temperature-dependent TQC calculated using total work, plastic work, shifted plastic work, and simultaneous C_p.

The rate dependent TQCs at 0.5 true strain are plotted as a function of the log strain rate in Fig. 19. It is

observed that the TQC is approximately constant from low to medium rates, but increases significantly at high rates.

There are a number of key observations, which will here be considered qualitatively. The TQC is the ratio of heat generated to total mechanical work. Heat can also be stored or used to drive the molecular level structural change in the material. In the linear region between the beta and alpha transitions, we conclude that the proportional change in mechanical work (because of the temperature dependence of the yield stress) is less than the proportional change in energy absorbed by structural evolution, hence as the temperature increases, a smaller fraction of the energy is needed to drive the structural change and the TQC increases. Above the alpha transition, the relative work converted to heat decreases again; this is unexpected because the amount of energy required for structural change should be less. However, we note that here, the calculation of plastic strain does not account for hyperelastic deformation: even though the calculated plastic true stress-true strain curve appears to extend to a strain of approximately 0.7 most of this is, in fact, recovered, and the final strains after unloading are approximately 13%, Fig. 20. This shows one of the challenges inherent in calculating plastic strains for these materials.

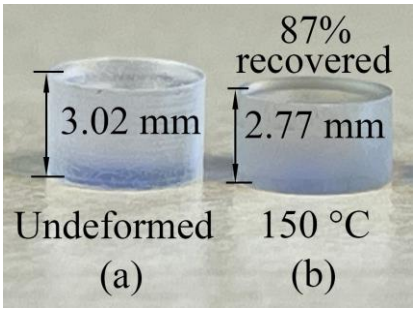

Figure 20. (a) Undeformed sample (b) Tested sample at 150 °C and 0.5 s^{-1} strain rate to 0.8 true strain.

At low temperatures, we find that the TQC is higher than we would expect from an extrapolation from the linear regime. Here, it is noted that as the temperature decreases below the beta transition, the yield stress increases more quickly with decreasing temperature, so the amount of work done is larger. However, non-reversing DSC data, Fig. 21, show no observable latent heat associated with this transition. This implies that

the total mechanical work increases without a corresponding increase in energy required for structural change and that there is more converted to heat. There is a corresponding effect at high strain rates: the yield stress increases more rapidly, which drives an increase in the TQC because the energy required for structural changes does not increase similarly. There is more energy available for conversion to heat.

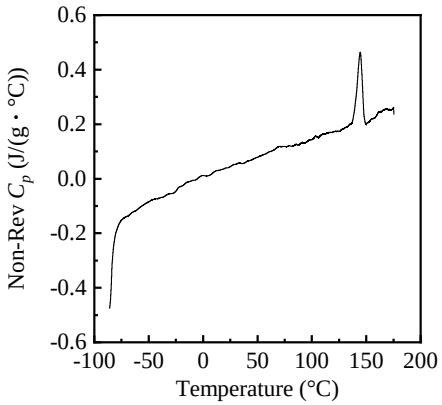

Figure 21. Non-reversed specific heat capacity against temperature.

Conclusions

Data have been presented from measurements of the temperature rise in PC specimens deformed under adiabatic conditions. Room temperature experiments were performed from 0.01 to 2600 s^{-1}, with adiabatic conditions above 0.5 s^{-1} in the specimens used. Quasi-static experiments were performed from -80 to 150 °C, to encompass β- and α-transition temperatures, at 0.5 s^{-1}. A high-speed IR camera and embedded thermocouple were used to measure the temperature rise in the rate- and temperature-dependent tests, respectively. Moreover, the Taylor-Quinney coefficient was calculated to reveal the energy distribution during the large strain deformation process.

For temperature-dependent experiments, the TQC was observed to increase linearly with temperature through the β-transition, and linearly again above this transition, but with a significantly higher gradient. At the glass transition, the calculated TQC decreases again, which may be associated with challenges in correctly identifying the plastic strain through the experiment.

For the rate-dependent tests, thermal softening was observed at low (0.5 s^{-1}) and medium (~ 1.5 and 14.5 s^{-1}) strain rates. However, much less softening can be observed in high-rate tests compared to the lower strain-rate tests, even though higher temperature rises were observed. These results are consistent with the previously published results. The high-rate experiments have a higher TQC, consistent with the low-temperature tests. In both cases this is likely to be because the transition affects the yield stress, and therefore the amount of mechanical work done more than it affects the energy required for structural evolution.

Comparing the 'equivalence' rate- and temperature-dependent tests, more heat is generated, but less softening is observed, in high-rate tests. The reduced softening may be because the molecular chain cannot relax on the short timescales. Further work will be required to consider the structural evolution and incorporate these observations into high-rate constitutive models.

CRediT authorship contribution statement

Peihao Song: Conceptualisation, Methodology, Investigation, Formal analysis, Writing - original draft. **David Chapman:** Methodology, Investigation, Review & edit. **Aaron Graham:** Investigation. **Akash Trivedi:** Investigation. **Clive Siviour:** Conceptualisation, Project administration, Supervision, Writing – review & edit, Funding acquisition.

Declaration of Competing Interest

The authors declare that they have no known competing financial interests or personal relationships that could have appeared to influence the work reported in this paper.

Acknowledgements

This research forms part of the research programme of DPI, project 827t19, *Impact Modelling of Polymers: high-Rate Experiments for Solid-state Simulations* and the materials were kindly supported by Saudi Basic Industries Corporation (SABIC). The authors thank our colleagues on this project, Dr Davide De Focatiis and Grace Owen at the University of Nottingham for helpful discussions. We are very grateful for the support of Nicholas Hawkins for DMA and DSC experiments, and to the technicians of the Solid Mechanics Group (especially Andy Bateman and Neil Warland) for specimen preparation. We thank the Hypersonics Research Group for using the high speed thermal imaging camera, and thank EPSRC for supporting thermomechanical characterisation as part of EP/V003321/1.

Data Availability

All data supporting this study are openly available from the Oxford University Research Archive at: DOI to be produced on acceptance.

Appendix A. Calibration of an infrared camera

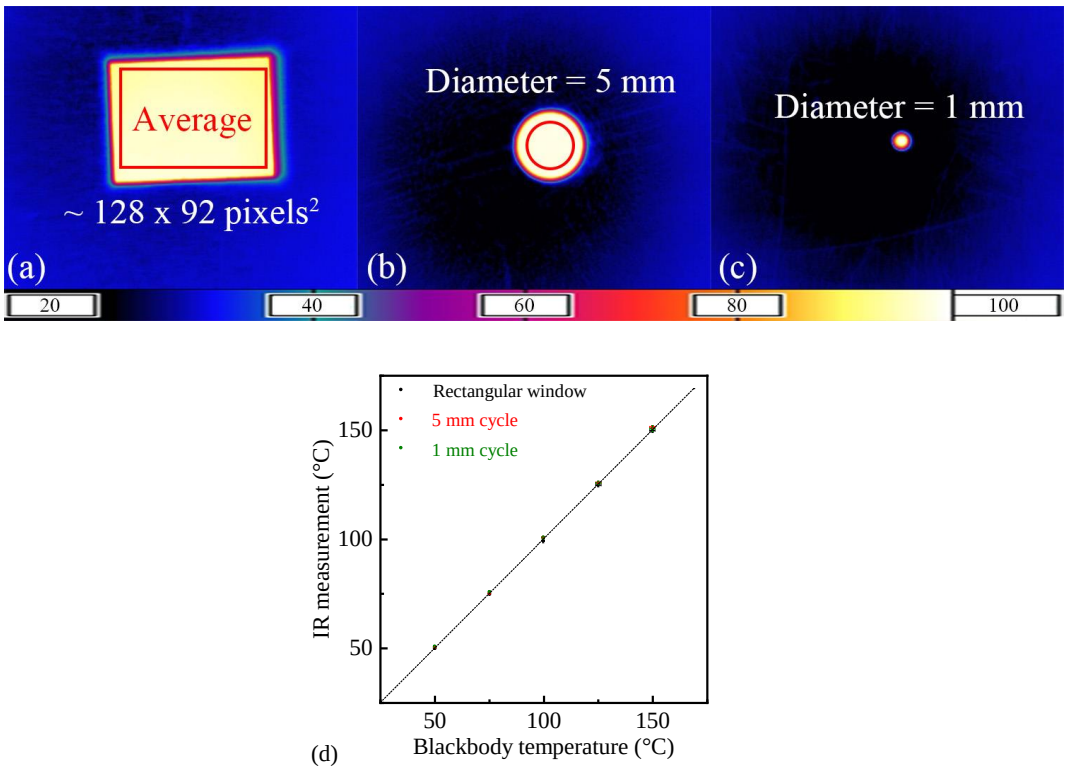

Figure A1. Calibration of an IR camera with different effective window sizes using blackbody.

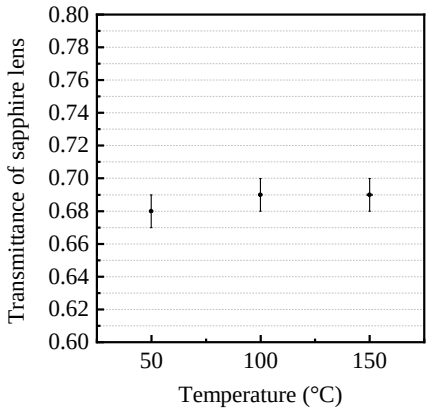

Figure A2. Calibration of an IR camera with a sapphire lens (used in high-rate tests).

Table A1 Details about the IR camera settings for all experiments

Strain rate (s^{-1})	Frame rate (Hz)	Exposure time (μs)	Window size ($pixel^2$)
0.01, 0.1, 0.5	100	100	128 × 128
1.5 ± 0.2, 13.5 ± 1.0	500	100	300 × 160
2350 ± 200	10000	20	128 × 92

Appendix B. Calibration of emissivity of PC and IR camera settings for all experiments

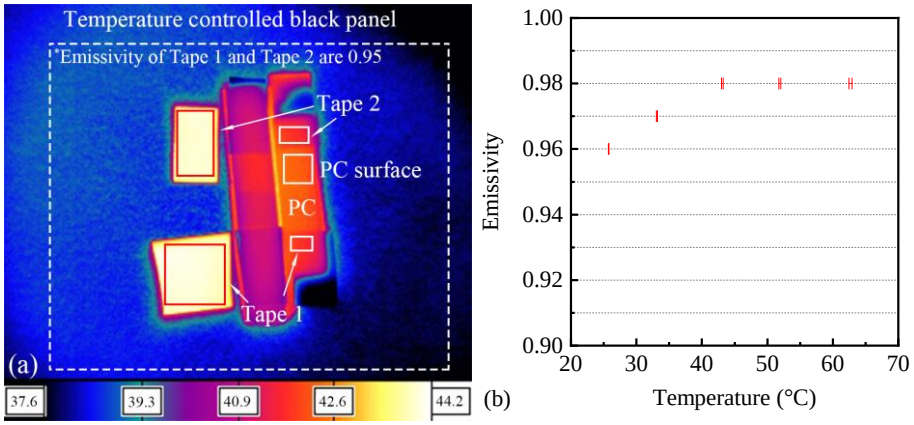

Figure B1. (a) Experimental setup of emissivity calibration (b) Emissivity versus temperature controlled black panel temperature

Appendix C. Three network viscoplastic (TNV) model

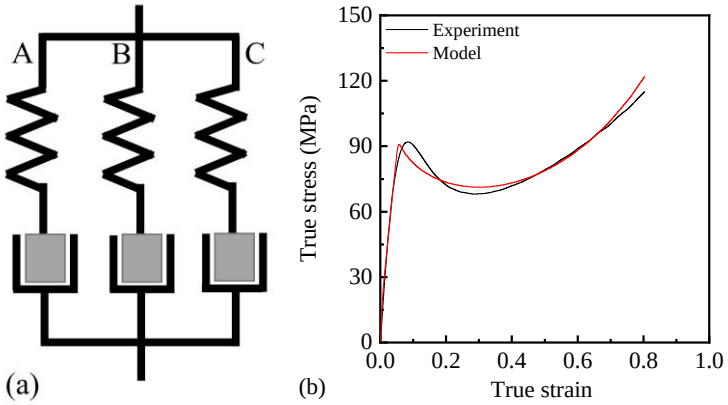

Figure C1. (a) Schematic of a three-network viscoplastic model (b) Comparison of experimental result and model simulation for true rate-controlled compression test at 0.5 s^{-1}.

In the present work, the Yeoh model [43] is applied to chain A without stress flow, and the same model is used for chain B and chain C with power-law stress flow as recommended in PolyUMod® [36]. More detailed information about this constitutive model can be found in [36, 44], and the parameters used in this study are listed in Table C1.

Table C1 Material parameters for the three-network viscoplastic model used in Abaqus/Explicit

Description	Value
Material parameters of PC	
Density, ρ	1.2 g/cm^3 [41]
Specific heat capacity, C_p	1.065 J/ (g °C), at 23 °C
Thermal conductivity, K	0.2 W/(m K) [41]
Inelastic heat fraction, TQC	0.55
Network A	
Yeoh parameter 1, C_{10}	6.0 (MPa)
Yeoh parameter 2, C_{20}	2.8 (MPa)
Yeoh parameter 3, C_{30}	0.28 (MPa)
Bulk modulus, κ_1	1750 (MPa)
Bulk modulus, κ_2	0 (MPa)
Bulk modulus, κ_3	0 (MPa)
Network B	
Yeoh parameter 1, C_{10}	300 (MPa)
Yeoh parameter 2, C_{20}	0 (MPa)
Yeoh parameter 3, C_{30}	0 (MPa)
Bulk modulus, κ_1	1760 (MPa)
Bulk modulus, κ_2	0
Bulk modulus, κ_3	0
Flow resistance of network, $\hat{\tau}$	10 (MPa)
Stress exponential of network, m	8.7

Volumetric flow coefficient, b	0
Pressure dependent of flow, p_0	0
Yield evolution of $\hat{\tau}$, f_f	0.93
Yield evolution of characteristic strain, ε_f	0.02
Flow damage strain, c_ε	0.25
Flow damage final state, f_s	0.5
Network C	
Yeoh parameter 1, C_{10}	263.2 (MPa)
Yeoh parameter 2, C_{20}	0 (MPa)
Yeoh parameter 3, C_{30}	0 (MPa)
Bulk modulus, κ_1	1760 (MPa)
Bulk modulus, κ_2	0
Bulk modulus, κ_3	0
Flow resistance of network, $\hat{\tau}$	65 (MPa)
Stress exponential of network, m	36
Volumetric flow coefficient, b	0
Pressure dependent of flow, p_0	0
Yield evolution of $\hat{\tau}$, f_f	0.49
Yield evolution of characteristic strain, ε_f	0.2
Flow damage strain, c_ε	0.1
Flow damage final state, f_s	1.5
Material parameters of loading anvils (Steel)	
Density, ρ	7.85 g/cm^3
Specific heat capacity, C_p	0.47 J/ (g °C)
Thermal conductivity, K	45 W/(m K) [41]
Young's modulus, E	210000 (MPa)
Poisson's ratio	0.3

To understand the temperature rise at -80 °C with the strain rate of 0.5 s^{-1}, the true stress-true strain curve in this experiment situation is duplicated using PolyUMod®. Here, the Specific heat capacity, C_p, is 0.65 J/ (g °C), obtained from the MDSC test; the inelastic heat fraction, TQC, is 0.4, obtained from the experiment. At the same time, the value of flow resistance of network B is changed to 75 MPa (only this parameter).

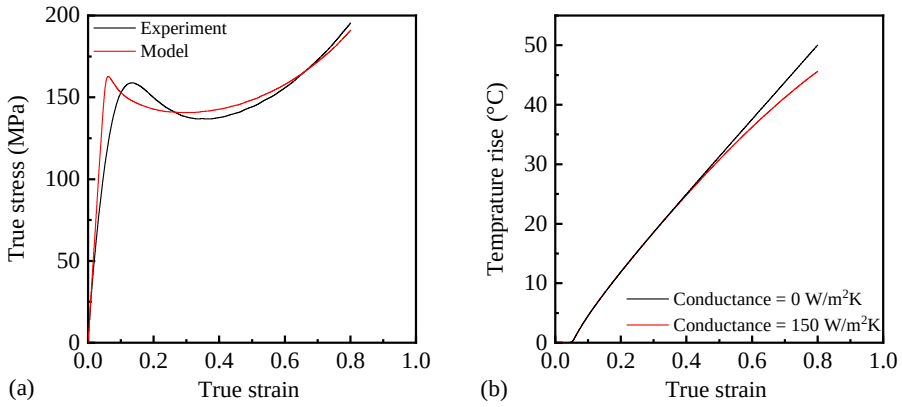

Figure C2. (a) Comparison of experimental and model true stress-true strain curve (b) Simulation temperature rise at -80 °C with the strain rate of 0.5 s^{-1} for 3 mm sample

Appendix D. Calculation of TQC using a constant C_p

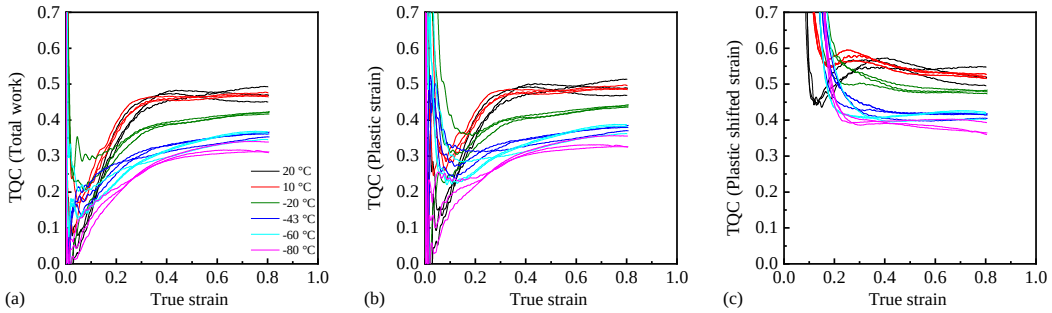

Figure D1. Temperature-dependent TQCs calculated based on three different mechanical works calculated using a constant specific heat capacity value at starting temperatures.

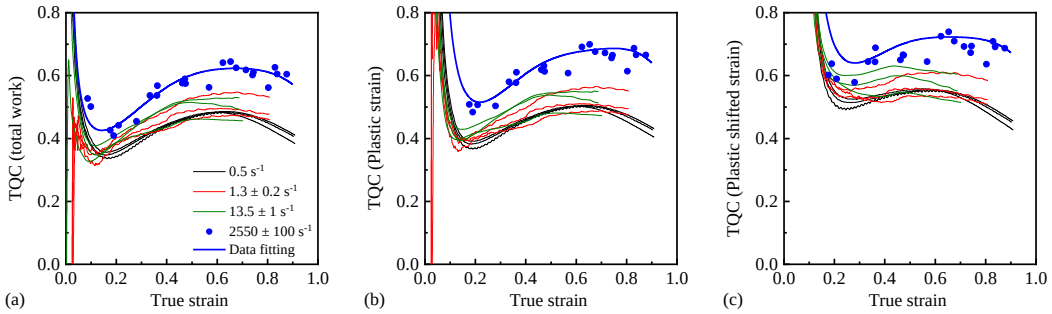

Figure D2. Rate-dependent TQCs are calculated based on three different mechanical works using a constant specific heat capacity at a starting temperature. (All data are measured using an IR camera. The blue squares indicate the stitched high strain rate data in different tests, and the solid blue line is generated using polynomial curve fitting).

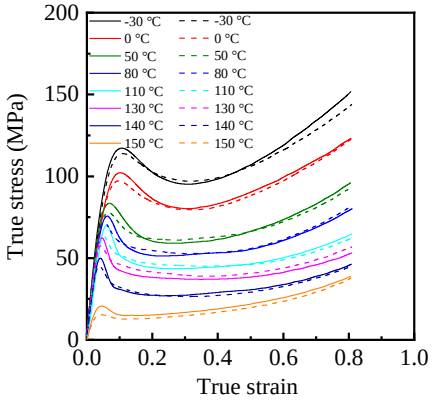

Figure D3. Additional true stress - true strain curves at various temperatures with (dash line) and without (solid line) embedded thermocouples at 0.5 s^{-1}.

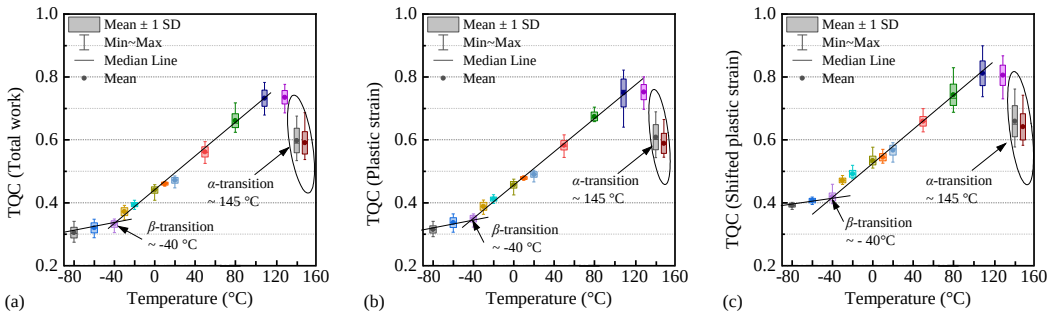

Figure D4. Temperature-dependent TQCs calculated using a constant C_p at starting temperature.

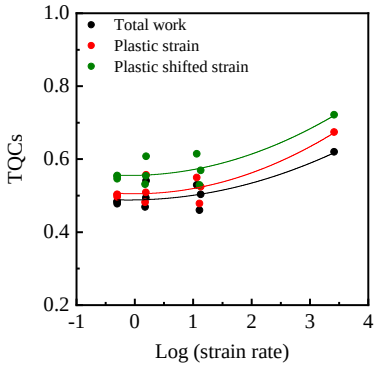

Figure D5. Rate-dependent TQCs calculated using a constant C_p at starting temperature.

References

1. Bauwens-Crowet, C., J.C. Bauwens, and G. Homes, *The temperature dependence of yield of polycarbonate in uniaxial compression and tensile tests.* Journal of Materials Science, 1972. **7**: p. 176-183.
2. Sarva, S. and M. Boyce, *Mechanics of polycarbonate during high-rate tension.* Journal of Mechanics of Materials and Structures, 2007. **2**(10): p. 1853-1880.
3. Song, P., A. Trivedi, and C.R. Siviour, *Tensile testing of polymers: Integration of digital image correlation, infrared thermography and finite element modelling.* Journal of the Mechanics and Physics of Solids, 2023. **171**: p. 105161.
4. Richeton, J., et al., *Influence of temperature and strain rate on the mechanical behavior of three amorphous polymers: Characterization and modeling of the compressive yield stress.* International Journal of Solids and Structures, 2006. **43**(7-8): p. 2318-2335.
5. Siviour, C.R., et al., *The high strain rate compressive behaviour of polycarbonate and polyvinylidene difluoride.* Polymer, 2005. **46**(26): p. 12546-12555.
6. Song, P., A.R. Trivedi, and C.R. Siviour, *Mechanical response of four polycarbonates at a wide range of strain rates and temperatures.* Polymer Testing, 2023. **121**: p. 107986.
7. Jordan, J.L., J.R. Foley, and C.R. Siviour, *Mechanical properties of Epon 826/DEA epoxy.* Mechanics of Time-Dependent Materials, 2008. **12**: p. 249-272.
8. Chen, H., et al., *Characterization and modelling of bisphenol-a type epoxy polymer over a wide range of rates and temperatures.* Polymer, 2022. **249**: p. 124860.
9. Furmanski, J., C.M. Cady, and E.N. Brown, *Time–temperature equivalence and adiabatic heating at large strains in high density polyethylene and ultrahigh molecular weight polyethylene.* Polymer, 2013. **54**(1): p. 381-390.
10. Jordan, J.L., et al., *Mechanical properties of low density polyethylene.* Journal of dynamic behavior of materials, 2016. **2**: p. 411-420.
11. Taylor, G.I. and H. Quinney, *The latent energy remaining in a metal after cold working.* Proceedings of the Royal Society of London. Series A, Containing Papers of a Mathematical and Physical Character, 1934. **143**(849): p. 307-326.
12. Rittel, D., *On the conversion of plastic work to heat during high strain rate deformation of glassy polymers.* Mechanics of Materials, 1999. **31**(2): p. 131-139.
13. Hao, P., et al., *Hydraulic-based testing and material modelling to investigate uniaxial compression of thermoset and thermoplastic polymers in quasistatic-to-dynamic regime.* Materials & Design, 2022. **224**: p. 111367.
14. Kendall, M.J. and C.R. Siviour, *Experimentally simulating high-rate behaviour: rate and temperature effects in polycarbonate and PMMA.* Philosophical Transactions of the Royal Society A: Mathematical, Physical and Engineering Sciences, 2014. **372**(2015): p. 20130202.
15. Mulliken, A.D. and M.C. Boyce, *Mechanics of the rate-dependent elastic–plastic deformation of glassy polymers from low to high strain rates.* International Journal of Solids and Structures, 2006. **43**(5): p. 1331-1356.
16. Arruda, E.M., M.C. Boyce, and R. Jayachandran, *Effects of strain rate, temperature and thermomechanical coupling on the finite strain deformation of glassy polymers.* Mechanics of Materials, 1995. **19**(2): p. 193-212.
17. Mulliken, A.D., *Mechanics of amorphous polymers and polymer nanocomposites during high rate deformation.* PhD Thesis, Massachusetts Institute of Technology, 2006.

18. Kendall, M.J. and C.R. Siviour, *Experimentally simulating adiabatic conditions: approximating high rate polymer behavior using low rate experiments with temperature profiles.* Polymer, 2013. **54**(18): p. 5058-5063.
19. Hao, P., et al., *A rate-dependent constitutive model predicting the double yield phenomenon, self-heating and thermal softening in semi-crystalline polymers.* International Journal of Plasticity, 2022. **153**: p. 103233.
20. Jordan, B., M.B. Gorji, and D. Mohr, *Neural network model describing the temperature- and rate-dependent stress-strain response of polypropylene.* International Journal of Plasticity, 2020. **135**: p. 102811.
21. Lerch, V., G. Gary, and P. Herve. *Thermomechanical properties of polycarbonate under dynamic loading*. in *Journal de Physique IV (Proceedings)*. 2003. **110** 159-164
22. Trivedi, A.R., P. Song, and C.R. Siviour, *Experimentally simulating adiabatic behaviour: Capturing the high strain rate compressive response of polymers using low strain rate experiments with programmed temperature profiles.* Polymer Testing, 2022. **116**: p. 107773.
23. Salamatina, O.B., et al., *Work, heat and stored energy in compressive plastic deformation of glassy polymers.* Thermochimica Acta, 1994. **247**(1): p. 1-18.
24. Rudnev, S., et al., *Plastic deformation kinetics for glassy polymers and blends.* Colloid and polymer science, 1991. **269**: p. 460-468.
25. Garg, M., A.D. Mulliken, and M.C. Boyce, *Temperature Rise in Polymeric Materials During High Rate Deformation.* Journal of Applied Mechanics, 2008. **75**(1).
26. Li, Z. and J. Lambros, *Strain rate effects on the thermomechanical behavior of polymers.* International Journal of Solids and Structures, 2001. **38**(20): p. 3549-3562.
27. Regev, A. and D. Rittel, *Simultaneous transient temperature sensing of impacted polymers using infrared detectors and thermocouples.* Experimental mechanics, 2008. **48**: p. 675-682.
28. Walley, S.M., et al., *Comparison of two methods of measuring the rapid temperature rises in split Hopkinson bar specimens.* Review of scientific instruments, 2000. **71**(4): p. 1766-1771.
29. Siviour, C.R. and J.L. Jordan, *High strain rate mechanics of polymers: a review.* Journal of Dynamic Behavior of Materials, 2016. **2**: p. 15-32.
30. Siviour, C.R., *High strain rate characterization of polymers.* AIP Conference Proceedings, 2017. **1793**, 060029.
31. Gray III, G.T., *Classic split-Hopkinson pressure bar testing.* ASM Handbook, Mechanical testing and evaluation, 2000. **8**: p. 462-476.
32. Song, B., et al., *A long split Hopkinson pressure bar (LSHPB) for intermediate-rate characterization of soft materials.* Experimental mechanics, 2008. **48**: p. 809-815.
33. Trautmann, A., et al., *Lubrication of polycarbonate at cryogenic temperatures in the split Hopkinson pressure bar.* International Journal of Impact Engineering, 2005. **31**(5): p. 523-544.
34. van der Tempel, L., *Thermography of semi-transparent materials by a FLIR ThermaCAM SC3000 infrared camera.* Philips Research, 2011.
35. Riou, O., et al., *Accurate methods for single-band apparent emissivity measurement of opaque materials.* Measurement, 2016. **89**: p. 239-251.
36. Bergstrom, J.S., *PolyUMod–A library of advanced user materials.* Veryst Engineering, LLC, Needham, Mass, USA, 2012.
37. Ames, N.M., *A thermo-mechanical finite deformation theory of plasticity for amorphous polymers: application to micro-hot-embossing of poly (methyl methacrylate).* PhD Thesis, Massachusetts Institute of Technology, 2007.
38. Lan, T., Y. Jiang, and P. Wu, *A thermodynamically-based constitutive theory for amorphous glassy*

polymers at finite deformations. International Journal of Plasticity, 2022. **158**: p. 103415.

39. Fuller, J.J. and E.E. Marotta, *Thermal contact conductance of metal/polymer joints: an analytical and experimental investigation.* Journal of thermophysics and heat transfer, 2001. **15**(2): p. 228-238.
40. Marotta, E.E. and L.S. Fletcher, *Thermal contact conductance of selected polymeric materials.* Journal of Thermophysics and Heat Transfer, 1996. **10**(2): p. 334-342.
41. SABIC, *LEXAN™ Resin 103R Europe Technical Data Sheet*. 2021.
42. Hasan, O.A. and M.C. Boyce, *Energy storage during inelastic deformation of glassy polymers.* Polymer, 1993. **34**(24): p. 5085-5092.
43. Yeoh, O.H., *Some forms of the strain energy function for rubber.* Rubber Chemistry and Technology, 1993. **66**(5): p. 754-771.
44. Bergstrom, J.S., *Mechanics of solid polymers: theory and computational modeling*. 2015, Amsterdam, The Netherlands: Elsevier.

6 Thermomechanical Properties of Short Glass Fibre Reinforced PC

6.1 Introduction

In **Chapter 3, 4 and 5**, the thermomechanical properties of polycarbonate (PC) have been extensively characterised, and the baseline characterisation framework has been built up and developed at a wide range of strain rates and temperatures. In this chapter, the experimental strategies used in previous chapters were extended to test the injection moulded 20 wt% short glass fibre reinforced polycarbonate composite; moreover, the in-situ micro-level damage characterisation (X-ray phase contrast imaging) under high rate tests was also conducted in the European Synchrotron Radiation Facility (ESRF).

The thermomechanical properties of the reinforced polymer were compared to its pure matrix PC resin; further, fibre flow orientation effects were also investigated utilizing Dynamic Mechanical Analysis, quasi-static tensile tests, and high rate compression tests in ESRF. The temperature and rate-dependent compression responses were addressed using the experimental methods described in **Chapter 4**. Like the PC matrix, the PC composite also presented rate- and temperature-dependent thermomechanical properties, and test results were consistent with the 'time-temperature equivalence' in the viscoelastic stage. In the large strain regimes, more pronounced temperature rises were observed compared with the PC matrix because the PC composite had a higher stress level at the same experimental conditions; additionally, apparent shear bands were captured in high-speed thermal images, and the maximum temperature exceeded the glass-transition temperature of the PC in high rate tests, which can cause significant softening. All these experimental data enable us to develop a more advanced numerical model from the micro- to macro-level and use these polymeric materials more efficiently in different engineering applications.

6.2 Paper D: Thermomechanical characterisation of thermoplastic polymer and its short glass fibre reinforced composite: Influence of fibre, fibre orientation, strain rates and temperatures[1]

Abstract

Polycarbonate and its composites are widely used in engineering products exposed to mechanical loads leading to large strain, high strain rate deformation at varying temperatures; however, their behaviour, especially for composites, is not well understood because of the complex structure and a lack of experimental data. This paper investigates the thermomechanical properties of injection flow moulded polycarbonate and 20 wt% glass fibre reinforced polycarbonate to provide experimental characterisation data and improved mechanistic understanding of the response to load. Frequency sweep Dynamic Mechanical Analysis and time-temperature superposition are performed to investigate temperature and frequency dependence at small strains. For large strains, compressive behaviour is characterised from 0.001 to 5000 s^{-1} at room temperature and from -60 to 120 °C at 0.01 s^{-1}; some of these experiments are instrumented with a thermal imaging camera to obtain temperature rise data during adiabatic deformation. Quasi-static tensile experiments were also performed in which, for the composite, specimens were cut in different orientations relative to the injection flow direction. Finally, high-rate compression experiments are performed with ultra-fast in-situ X-ray phase contrast imaging, allowing internal localisation behaviour to be studied using digital image correlation. As well as providing information about rate dependence of yield stresses and softening behaviour in the two materials, these data are drawn together to show how adiabatic shear band formation can lead to very high temperature rises and lead to significant softening in the composite material. These data will enhance the use of these polymers in different applications and facilitate the development of advanced thermo-mechanical models accounting for

[1] Submitted to a scientific journal

microstructural material characteristics.

Keywords: Polycarbonate; Fibre Reinforced Polycarbonate; High strain rate; Plastic deformation; Adiabatic heating; Thermography; High rate in-situ characterisation

Introduction

Polycarbonate (PC) is a widely used glassy thermoplastic polymer with good mechanical, thermal, and electrical properties [1]. However, the pure polymer does not have high enough strength and stiffness for some structural applications [2]. Adding short fibres into thermoplastics is a common way to significantly improve their mechanical response [3]. Short fibre reinforced composites (SFRCs) are becoming increasingly popular owing to fast, inexpensive manufacturing compared to laminated composites [3]. This fast-growing demand for SFRC leads to a requirement for reliable material characterisation methods and data to understand and model mechanical behaviour [4].

The mechanical properties of SFRCs are highly dependent on fibre content, fibre orientation, interfacial adhesion strength, and polymer matrix properties [3, 4]; typical fibre lengths are of order 0.2 to 0.4 mm [4, 5]. Anisotropic stiffness and strength are an unavoidable result of SFRC manufacture, e.g. through injection flow-induced fibre orientation, and mechanical properties can also vary between different parts of a manufactured product because of changes in flow conditions [6, 7]. Furthermore, manufacturing history, e.g. processing temperature and cooling rate, can result in variations in the thermomechanical responses of the matrix polymer [8, 9].

Polycarbonate composite components used in automotive, aeronautics, and sports engineering applications are likely to be exposed to mechanical loading at various strain rates and temperatures. Some aspects of the subsequent response under quasi-static loading conditions have been characterised, such as the effect of fibre flow orientation [10, 11] or fibre weight fraction [4], fatigue behaviour [6], influence of fibre

type and interfaces [12], impact of manufacturing process [4, 13], and tribological properties [14]. However, unlike pure polycarbonate, fewer studies have investigated the time and temperature-dependent properties of short fibre reinforced PC (SFPC), particularly high strain rate behaviours.

The split Hopkinson pressure bar (SHPB) allows the characterisation of polymers in uniaxial compression at strain rates from about 10^2 to 10^4 s^{-1} [15-17]. For polycarbonate, Siviour *et al.* [18] and Mulliken and Boyce [19] reported that the yield stress increases with strain rate, with a more significant dependence at rates above ~1000 s^{-1}; this observation was attributed to the secondary (β)-transition [18, 20]. An equivalent effect is, of course, observed by lowering the temperature at a single strain rate, providing the chance to replicate the high rate behaviour using quasi-static low temperature data [21, 22]. In recent years, the SHPB system has also been used to investigate the dynamic compression properties of thermoplastic polymer composites such as polyamide 66 composite [23] and polyester composite [24]. Nevertheless, to our knowledge, no research has yet been published on dynamic compression response of PC-based composites.

One of the key features of large plastic deformation is the temperature rise that occurs from the conversion of plastic work to heat. At high strain rates, in which the experiment is adiabatic, this temperature rise can have a significant effect on the mechanical responses of polymeric materials [15]. Thus, quantifying the temperature rises under different loading conditions is essential to fully understand the constitutive behaviour. These measurements have been made for PC using Infra-Red (IR) detectors [25-31], IR cameras [28, 32] and embedded thermocouples [27, 33]. For composites, embedded thermocouples can aggravate the anisotropic behaviour and accelerate the failure process; in addition, as a point-measurement, the full-field thermal gradient information induced by strain localisation during large strain deformation would be missed. This can be important, for example, in recent studies [24, 34], high rate compression behaviours of glass fibre reinforced polymer laminate were measured using an SHPB with an IR camera; all the samples showed nonuniform thermal distribution as a result of the strain localisation. Hence, even though the fastest thermal cameras can

only give a small number of full-field images (say 3-5) with a useful spatial resolution, thermal imaging is the most appropriate approach to measuring temperature rises in composite materials.

In the study reported here, the rate and temperature dependent compression behaviour of PC and injection moulded 20 wt% glass fibre reinforced PC composite was characterised at rates from 0.001 to 5000 s^{-1} at room temperature, and temperatures from -60 to 120 °C at 0.01 s^{-1}. The room temperature experiments were instrumented with a thermal camera to measure temperature rise in the specimens. To support these experiments, frequency sweep DMA tests were performed to understand the time-temperature dependent viscoelastic behaviour of both materials, as well as fibre and fibre flow orientation effects. Tensile tests with different loading speeds were also performed to characterise dependence on injection direction and loading rate effects. Together, these provide a complete dataset for evaluating and developing constitutive models. To better understand the mechanics of damage formation at high strain rates, and support model development, further dynamic compression experiments were performed using an SHPB at beamline ID-19 of the European Synchrotron Radiation Facility (ESRF), with samples cut in different orientations relative to the injection moulding flow direction. These experiments aimed to explore the capability of single-bunch X-ray phase contrast imaging (XPCI) to investigate the incipient stages of internal damage formation, fibre delamination, and fibre breakage during high-rate deformation of the polycarbonate composite. Radiographs from these experiments were analysed using digital image correlation (DIC), exploiting the microstructural heterogeneity of the composite to understand the strain distribution (localisation) during tests, this was compared to temperature rises measured using the IR camera in other experiments. Here it is noted that some of the stress-strain data from the PC matrix have been published in [20]; however, all the composite data and temperature rise data are unique to the current paper.

Material information and sample preparation

The polycarbonate matrix (LEXAN™ 500R resin) and a composite made by combining this resin with 20wt% short glass fibre were provided by SABIC® as 175 × 175 × 3 mm sheets manufactured by injection flow moulding; the fibre length was from 0.2 to 0.4 mm, and the fibre diameter was between 0.01 to 0.02 mm. Both materials were annealed by heating at 25 °C/hour to 155 °C, which is 10 °C above the glass (α)-transition temperature, holding at this temperature for six hours and cooling at 10 °C/hour to room temperature. T_g was measured using the second heat cycle in heat-cool-reheat differential scanning calorimetry (DSC) tests [20]. The annealing process minimises residual stresses from manufacturing and ensures that the materials have the same thermal history, so that the effects of fibre can be investigated more explicitly.

Samples for all experiments were cut from the centre of the annealed sheets, as indicated in Fig. 1(a). For the composites, tensile samples were cut in three directions, 0° (injection flow direction), 45° and 90°; the sample dimensions were chosen according to ISO 527 type 1BA, Fig. 1(b). Three-point bend DMA samples, with a length of 60 mm, width of 10 mm and thickness of 3 mm, were also cut in these three directions. For the pure PC matrix, it was assumed that there are no orientation effects and specimens were cut in one direction only. For mechanical characterisation experiments, compression samples for both materials were obtained by cutting specimens through-thickness (TT) with a 5 mm diameter and 3 mm thickness. For the in-situ X-ray experiments on the composite, two different types of compression specimens were made: all were 2 × 2 mm cylinders with the subsequent loading direction through-thickness or in the injection flow direction as indicated in Fig. 1(a). Moreover, the micro-CT image for the through-thickness 2 x 2 mm cylinder sample has been shown in Fig. 2-2 in Chapter 2.

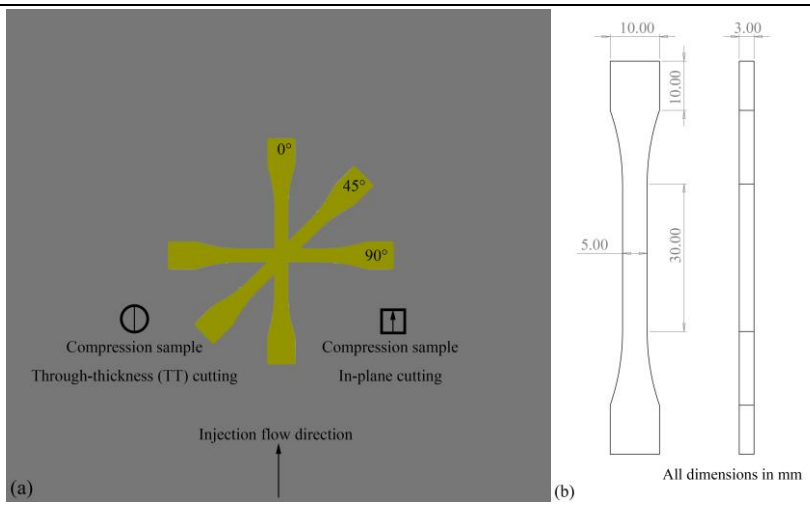

Figure 1. (a) Schematic of sample cutting, (b) Dimensions of tension sample.

Experimental procedures

Dynamic Mechanical Analysis (DMA)

Experiments were performed on a TA Instruments Q800 DMA. Previous research [20, 35] has shown that the storage modulus obtained from DMA experiments in three point bend are consistent with results from tensile experiments. Therefore, in the current study experiments were conducted in three point bend on specimens with a span of 50 mm, width of 10 mm and thickness of 3 mm, consistent with ASTM standard D4065 and our previous study [20]. Careful calibration of apparatus and fixtures was conducted prior to the experiments according to the manufacturer's instructions. Isothermal frequency sweep experiments were performed at frequencies of 0.2, 0.5, 1, 2, 5 and 10 Hz, over a temperature range from -110 to 180 °C at 2 °C/min temperature increments with a five-minute isothermal equilibrium time before gathering data at each temperature.

Tensile tests

A screw-driven Instron 5980 universal test machine mounted with a 100 kN load cell was used to perform tension tests at room temperature. The samples were tested under displacement control at 10, 1 and 0.1 mm/min. Engineering stress-strain curves were calculated using force data from the load cell and the cross-head displacement.

Compression experiments

The true rate controlled quasi-static (QS) experiments from 0.001 to 0.5 s^{-1} were conducted using the same test machine as the tensile tests; however, strain was measured using an extensometer mounted to the anvils close to the specimen, shown in Fig. 2(a). The temperature dependent compression experiments were performed at 0.01 s^{-1} from -60 to 120 °C using the same machine with an environmental chamber. Here, a digital thermometer was attached to the load anvil to monitor the chamber temperature before and during testing. Petroleum jelly lubricant was used in room and high temperature tests, and AEROSPEC® 210 graphited

grease at low temperatures.

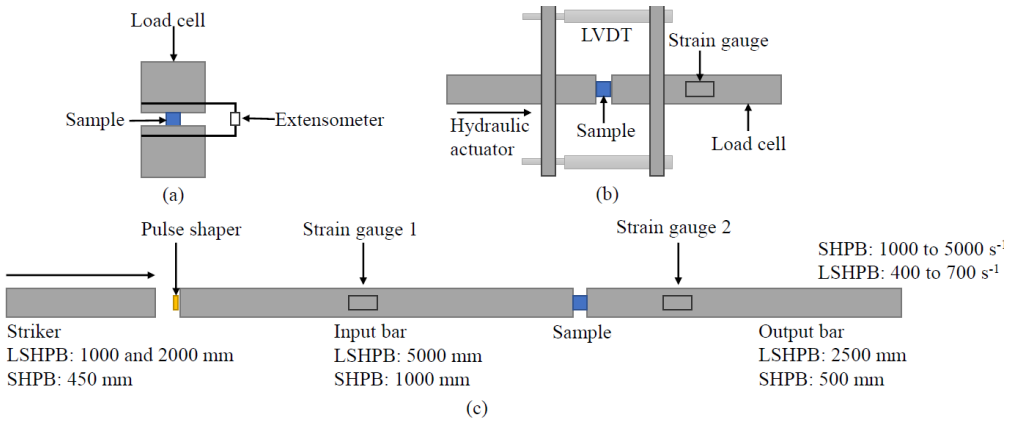

Figure 2. (a) Screw-driven tests, (b) Hydraulic machine, (c) Split Hopkinson pressure bar.

Medium rate measurements from 1 to 60 s^{-1} were conducted using a hydraulic machine; the displacement was measured by the averaged value obtained from a pair of linear variable differential transformers (LVDTs), and force was obtained by a strain-gauge based load cell (Fig. 2(b)). A long split-Hopkinson pressure bar (LSHPB) with a 2000 mm striker was employed for experiments from 400 to 750 s^{-1}, and SHPB from 1000 to 5000 s^{-1}, Fig. 2(c). To achieve both a high rate and large strain, an LSHPB with a shorter striker (1000 mm) was utilised to characterise the material properties at around 2500 s^{-1}. In all high-rate tests, cylindrical specimens were sandwiched between Ti-6AL-4V input and output bars. The input reflected and output waves were measured using gauges attached to bars. Readers are referred to the literature for a more detailed review of the SHPB system [36]. Following the suggestions in [37], a thin brass film was attached to the input bar to form a pulse shaper, as shown in Fig. 2(c), to reduce the oscillations in the input bar induced by wave dispersion. Petroleum jelly was used to lubricate the interface between bars and specimen for all medium and high rate experiments.

Thermal measurements

A TELOPS FAST-IR M3K IR camera with a 50 mm lens and 0.75 inches extension ring was used to measure the temperature rise during deformation at room temperature. Before testing, the factory camera

calibration was carefully verified using a calibrated black body source from 50 to 150 °C. The transmissivity of the sapphire window (used in high rate tests) was also confirmed using the black body source over the same temperature range. Finally, the emissivity of the two PC materials was measured as 0.97 using a calibrated emissivity surface and a temperature-controlled black panel. This value is very close to the value from 0.92 to 0.96 in the literature [38]. The temperature error introduced by changing the calibration in this range is approximately 1.5 °C for a measurement of 130 °C and consequently, all data were reduced using a constant mid-range emissivity of 0.95. For QS and medium rate tests, a complete sequence of images can be taken using this IR camera, rates of 100 and 500 frames per second were used. However, the speed of the IR camera was insufficient to adequately resolve the thermal evolution during the high-rate Hopkinson bar tests. Here, the IR camera was used with a 10 000 Hz frame rate and 20 μs exposure time, and was triggered when the striker impacted the input bar. A monitor signal from the camera was recorded alongside the strain gauge signals to allow alignment of the IR images and the strain gauge data (appropriately time-shifted). In this case, a single experiment of 400 to 500 μs duration can provide four or five images. In order to increase the utility of images from different experiments, the trigger delay of the camera was then altered in 20 μs steps. In this way, and having checked that the data between experiments are consistent, a series of images can be constructed by stitching a number of single tests together. Table 1 gives further details about the IR camera settings for all sets of experiments.

Table 1 IR camera settings for all experiments

Strain rate (s^{-1})	Frame rate (Hz)	Exposure time (μs)	Window size ($pixel^2$)
0.01, 0.1, 0.5	100	100	128 × 128
1.5 ± 0.2, 12.5 ± 2.5	500	100	300 × 160
2500 ± 200	10000	20	128 × 92

In-situ X-ray experiments

In-situ dynamic measurements on PC composites were performed at the ID-19 beamline at the European Synchrotron Radiation Facility (ESRF) [39]. The SHPB system includes a 1300 mm input bar, an 1100 mm

output bar and a 400 mm striker with 12.7 mm diameter, and all components were aluminium alloy (7075 T6); more detailed information, such as schematics of an experimental setup can be found in [40], and details of synchronisation and similar imaging system in [41, 42]. The cylindrical composite samples were sandwiched between 1 mm thick aluminium anvils to protect the end of the aluminium bars. This study used the 16-bunch filling mode (75 mA storage current), with the X-ray pulse width of ~60 ps measured in [43], separated in time by ~176 ns, and the white beam from the two axially aligned U32 undulators, filtered with 3.2 mm of diamond, and 0.7 mm of aluminium to reduce the heat load of the sample and the imaging system. The white beam was gated during the experiment using a fast-shutter which remained open for approximately 15 ms. These experiments aimed to visualise the internal failure process and deformation localisation occurring during the high-rate compression of the filled polycarbonate specimens. Consequently, these experiments employed a 10x magnification coupled to an indirect X-ray detector assembly, providing an approximately 1.28 × 0.8 mm field of view and a pixel size of 3.2 μm. To improve the signal to noise ratio in the resulting radiographs, 16 Be-based compound refractive lenses were used to compress the X-ray beam into the magnified field of view. In order to enhance the visualisation of the fibres and the presence of cracks, the imaging system was located within the near-field diffraction regime, facilitating edge enhancement by propagation based X-ray phase contrast [41, 44]. The X-ray beam having transmitted through the specimen, and propagated over approximately 1.2 m, was converted to visible light by a LYSO:Ce single crystal (150 micrometre thickness), and captured by a Shimadzu HPV-X2 camera, employing a 200 ns exposure time and 880 ns interframe time. Consequently, radiographs were formed from every fifth X-ray bunch (with minimal ghosting) in the 16 bunch filling mode, recording 128 frames over a total duration of nearly 120 μs. The strong image contrast produced by the edge enhancement of the XPCI technique was exploited to perform DIC analysis to track the deformation of the specimen.

Experimental results

DMA results

DMA data for the PC matrix materials and specimens of the composite cut in three orientations are shown in Fig. 3(a). In all tests, the modulus shows the effect of the secondary (β)-transition below -40 °C, followed by a slowly decreasing modulus with increasing temperature. A very rapid decrease is observed at about 130 °C, but the three point bend configuration does not allow measurements above this temperature because of the low specimen stiffness. All the filled materials have a higher modulus than the PC matrix; as expected, this depends on the specimen orientation. Time-temperature superposition (TTS) was used to construct master curves, Fig 3(b), to estimate the rate dependent storage modulus and aid later interpretation of the compressive data. Fig. 3(c) plots the relationship between the TTS shift factor and temperature; the PC matrix shows the most considerable variation from low to high temperature, followed by 90° and 45° samples. The temperature sensitivity of the 0° PC composite is lower than the other specimens, consistent with this behaviour being dominated by the temperature insensitive fibres.

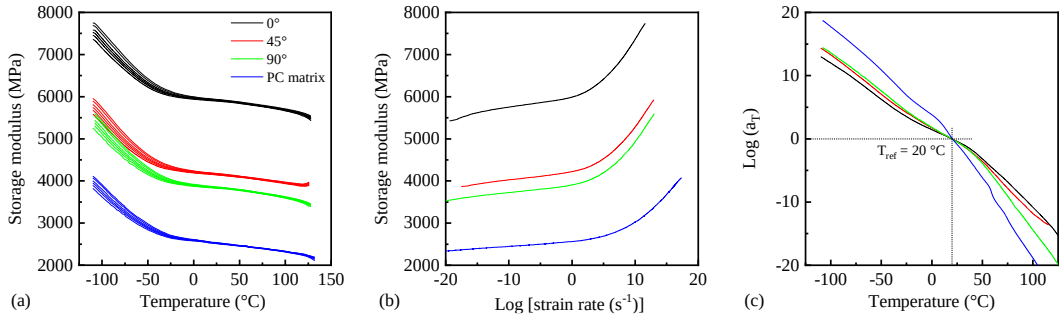

Figure 3. (a) Storage modulus against temperature, (b) Time-temperature superposition master curves at 20 °C, (c) Shift factor versus temperature.

Tensile test results

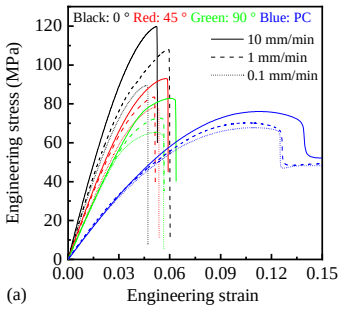

Figure 4. Engineering stress-strain curves at three different loading rates for the composite cut in three orientations relative to the injection flow direction and PC matrix (representative specimens shown here, raw data provided online for all specimens tested).

All materials show rate-dependent behaviour, Fig. 4: an increase in loading speed increases the failure stress for PC composites and the yield stress for PC matrix. All PC specimens were tested to a final engineering strain larger than 120%, whilst the PC composite failed at strains around 5%. The stiffnesses derived from these data were quantitatively consistent with the DMA test results: further, a higher loading speed increases the stiffness, and specimens cut from the fibre direction are stiffer than in other directions at the same speed. It is also noted that the failure stress of the specimen cut from the transverse direction (90°) is very close to the yield stress of the pure matrix material.

Compression test results

Fig. 5(a) and 5(b) present the compressive response of the PC matrix and PC composite at a constant true strain rate of 0.01 s^{-1} at temperatures from -60 to 120 °C. Three tests were performed at each temperature; here, one true-stress strain curve and all three yield stresses are plotted. In all these experiments, the specimen is assumed to deform at a constant volume when calculating the true stress. In this section, all PC composite specimens are made by through-thickness (TT) cut, which means the specimens were loaded perpendicular to the fibre flow orientation.

The PC matrix shows a very obvious yield, followed by softening and hardening during deformation at

all temperatures, and the yield stress increases from 55 to 120 MPa with decreasing temperature. The temperature dependent yield stress of PC composite has the same trend; the yield stress increases with decreasing temperature, from 65 to 174 MPa. However, the softening was less than observed in the matrix material, and not observed at all at high temperatures, such as 90 and 120 °C. Research in the literature [45-47] has reported that the glass transition temperature (T_g) of the interface region of polymer based composite materials is much lower than the pure matrix material. This means that in these higher temperature experiments, for PC composite, part of the matrix might already be above its T_g, removing the softening process after yield, which is only seen in polymers below the glass transition.

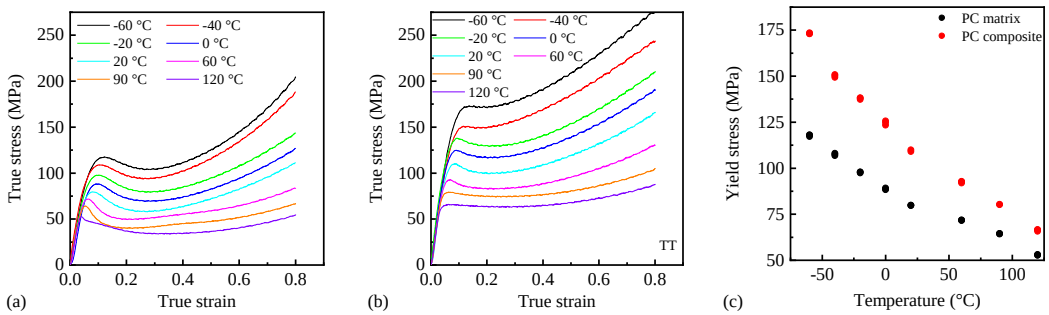

Figure 5. (a) Temperature dependent stress-strain curves for PC matrix, (b) Temperature dependent stress-strain curves for PC composite (TT), (c) Yield stress versus temperature for PC matrix and composite

The rate dependent compression responses are shown in Fig. 6(a) and 6(b) for the PC matrix and PC composite, respectively. The yield stress for both materials shows a bilinear increase with an increased log strain rate over seven decades, as shown in Fig. 6(c); this is caused by the secondary (β) transition [18, 20].

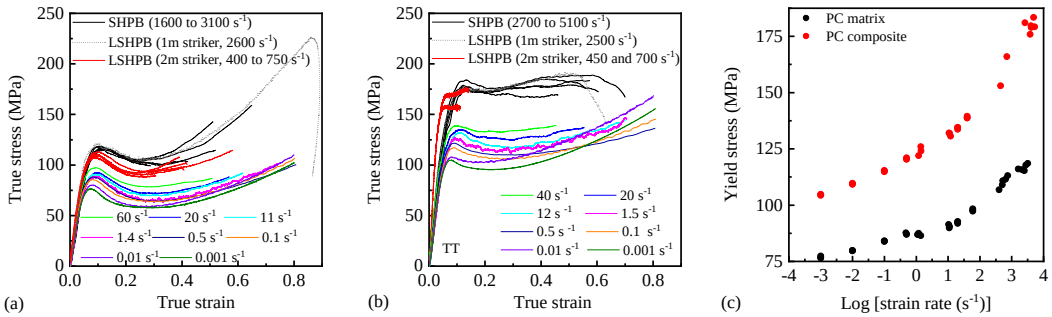

Figure 6. (a) Rate dependent stress-strain curves for PC matrix, (b) Rate dependent stress-strain curves for PC composite (TT), (c) Yield stress versus logarithm strain rate for PC matrix and composite.

By comparing Fig 5(c) and Fig 6(c), it is observed that both PC matrix and PC composite show time-temperature equivalence: decreasing temperature and increasing strain rates both increase yield stress. To explore this further, low temperature and high-rate stress-strain data are compared for both materials in Fig 7. These agree well for strains lower than 0.3. Above this strain, for the PC matrix, more softening is found at rates of 1 and 60 s^{-1} relative to the 'equivalent' QS experiment at low temperatures, but this is not observed in high rate tests (i.e. 530 and 3100 s^{-1}), for which the stress-strain curves are almost identical. For the PC composite, obvious softening can be seen, relative to the 'equivalent' low temperature results, in both medium (12 and 40 s^{-1}) and high rate (4300 s^{-1}) experiments. All rate dependent experiments in Fig.7 experience adiabatic heating of the specimen; thus, to further understand the observed behaviour, temperature rise data are presented in the next section.

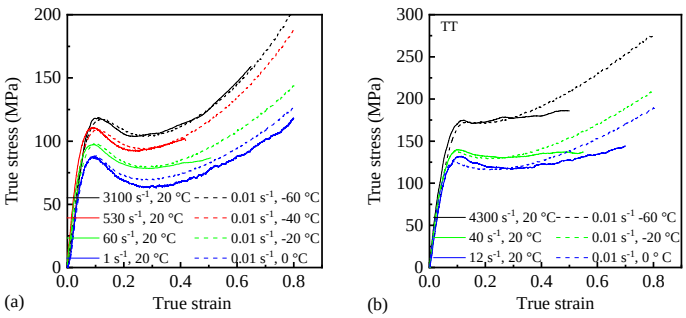

Figure 7. Comparison of stress-strain curves at low temperatures and high strain rates; the colours indicate which temperature and rate combinations are equivalent. (a) PC matrix, (b) PC composite (TT).

Temperature rise measurements for PC matrix

Temperature rise measurements were performed in QS (0.01, 0.1 and 0.5 s^{-1}), medium rate (1.1 and 11 s^{-1}) and high rate (~ 2600 s^{-1}) experiments. Of interest are temperature rises in higher rate experiments in which heat does not have time to conduct out of the specimen on the timescale of the experiment. It is possible to estimate the strain rate above which this happens using the following equations [20, 21]:

$$\alpha = \frac{k}{\rho C_p} \qquad (1)$$

$$l_t = 2\sqrt{\alpha t} \rightarrow t = \frac{1}{\alpha}\left(\frac{l_t}{2}\right)^2 \quad (2)$$

$$\dot{\varepsilon} = \frac{1}{t} \quad (3)$$

Here α is thermal diffusivity, k thermal conductivity (0.2 W m^{-1} K^{-1}), ρ density (1.2 g cm^{-3}), and C_P specific heat capacity (1.2 J g^{-1} K^{-1}). The timescale (t) of thermal diffusion can be estimated using Equation (3), where, l_t is the length of the specimen. Using this 1-D approximation, the transition from isothermal to adiabatic condition starts at a rate of around 0.06 s^{-1} for a full length (3 mm) sample. This is consistent with experimental observations: the temperature rise at a rate of 0.01 s^{-1} is only 2 °C (for 0.8 strain), which has a small effect on the mechanical properties; the equivalent rise at 0.1 s^{-1} is about 9 °C, and 20 °C at 0.5 s^{-1}.

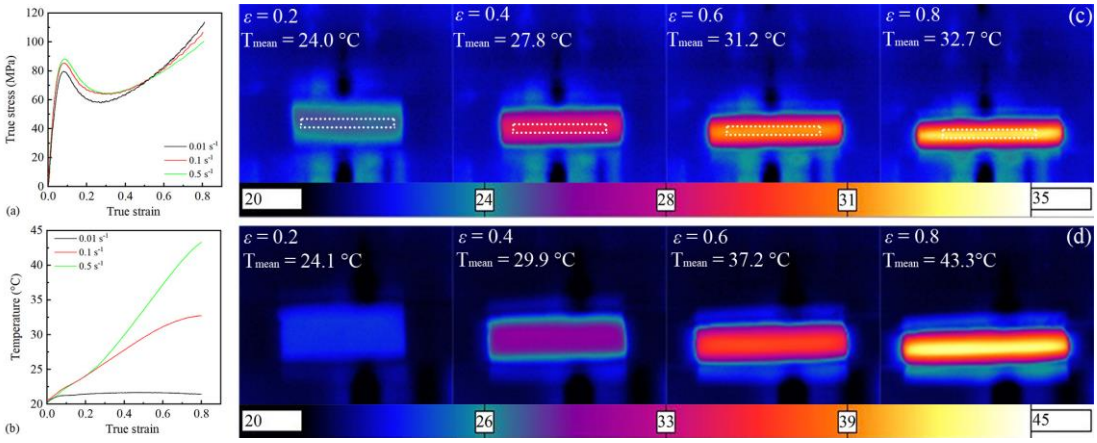

Figure 8. (a) stress-strain data for three quasi-static experiments on PC; (b) mean temperature rise data obtained from thermal images of these experiments; (c) selected thermal images from experiment at 0.1s^{-1}, (d) selected thermal images from experiment at 0.5 s^{-1}.

Fig. 8 shows selected thermal images and mean temperature data from two quasi-static compression experiments. In the thermal images, the mean temperature within the white dotted box is recorded and shown as T_{mean}. Here, we see the larger temperature rises at the higher strain rate of 0.5 s^{-1}, which we expect to be close to adiabatic; hence, the data obtained are consistent with increased thermal losses at the lower rate due to the increased importance of conduction.

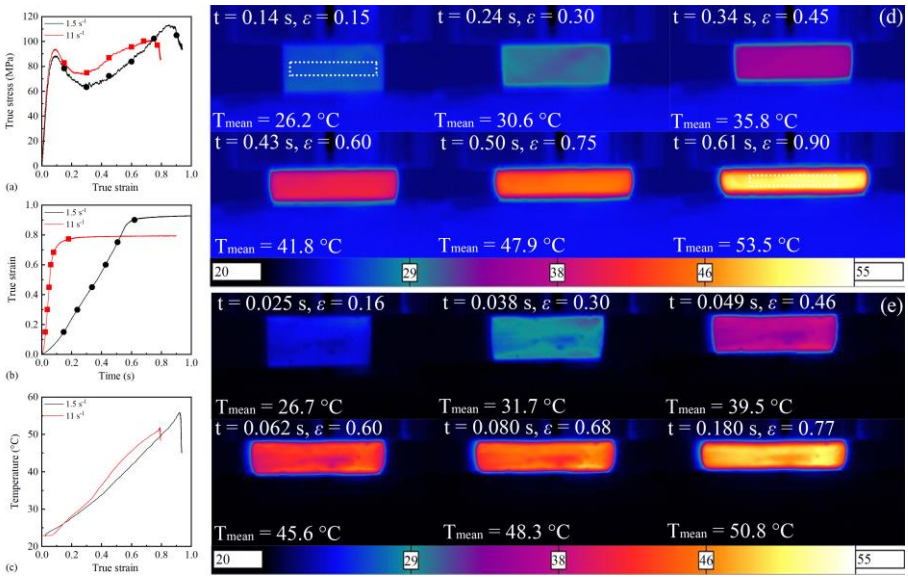

Figure 9. (a) True stress versus true strain curves in two medium rate tests on PC; (b) true strain versus time data for the same experiments; (c) mean temperature-true strain; (d) selected thermal images from experiment at 1.5 s^{-1}, (e) selected thermal images from experiment at 11 s^{-1}. Markers on the stress-strain and strain-time curves indicate when the thermal images were taken.

Temperature rises were measured in medium rate experiments at 1.5 and 11 s^{-1}, Fig. 9. The strain rate control in these experiments is not as good as in the quasi-static tests, and when interpreting these data, the departure from a constant strain rate at large strain apparent in Fig 9(b) must be considered. The stress at 11 s^{-1} is higher than in the lower rate test until a strain of around 0.7, after which the loading ends in the higher rate test. This is consistent with the thermal images: the higher rate tests show higher temperature rises for strains lower than 0.7, whilst the temperature for the 1.5 s^{-1} test is higher at the end of the deformation because the strain is larger.

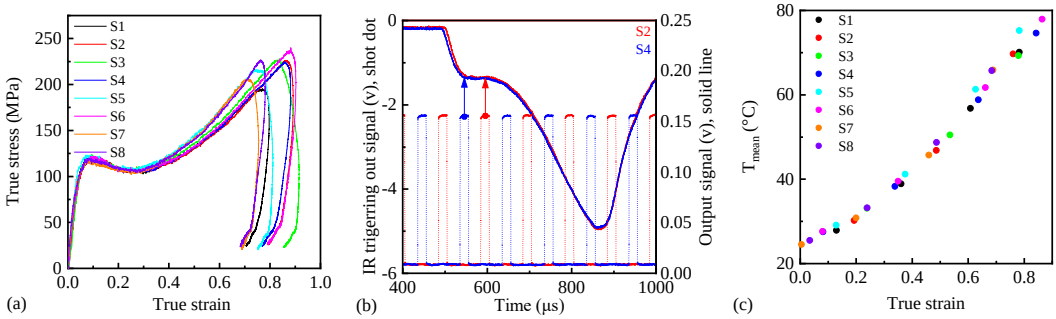

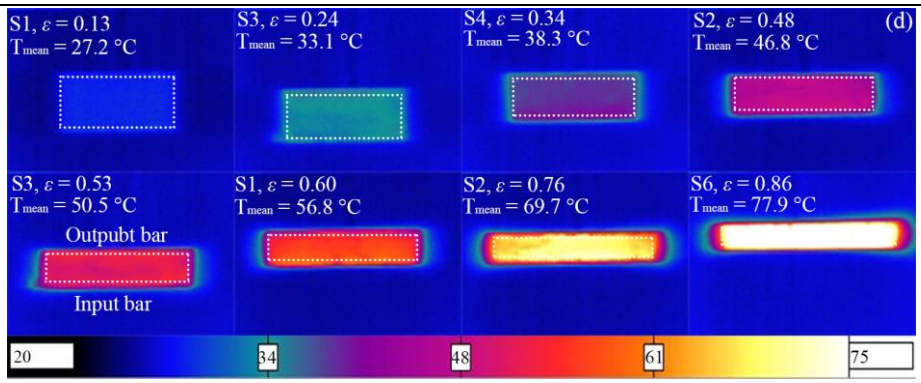

Figure 10. (a) True stress versus true strain curves for eight Hopkinson bar experiments on PC; (b) Time-shifted IR monitor out signal and LSHPB output bar signal from two experiments; (c) Mean temperature rise versus true strain for all the images obtained, the numbers S1-S8 indicate the eight different specimens tested; (d) Selected thermal images from low to high strain, montage produced from a number of experiments, again the numbers S1-S6 indicate from which specimen the image was obtained.

Eight experiments were conducted at a strain rate of 2500 ± 200 s^{-1} using the long split Hopkinson bar and instrumented with the high speed IR camera, which can provide 3 to 5 thermal images during the loading period. The IR camera was triggered at a different time for each experiment, and as shown in Fig. 10(b), this changes the timing of the exposure relative to the stress pulse in the specimen. The mean temperatures obtained from each thermal image were then combined to form the temperature versus strain curve in Fig. 10(c). The maximum temperature is ~ 80 °C at 0.86 strain; however, as discussed above there is less softening in the stress-strain curve compared to equivalent isothermal (low rate) experiments performed at low temperature. This observation is consistent with previous work on PC [21, 22, 30]. Further investigations are required to understand the relationship between temperature rise and the mechanism of softening and hardening in high rate experiments for the PC matrix.

Temperature rise measurements for PC composite

The same methodology is used to measure the temperature rise for PC composites. According to the thermal parameters of a similar product (LEXAN™ FR RESINS 3412R, 20wt% glass fibre reinforced

polycarbonate) [48], the 3 mm specimen experiences adiabatic conditions at strain rates above 0.07 s^{-1}; similarly to the pure PC specimens, with the decrease in sample length, this rate will be changed. Fig. 11 shows the temperature rises obtained in the quasi-static experiments. Here, both mean and maximum temperature rises are shown, because in later experiments at medium and high strain rates localisation is observed, leading to very high temperature rises in regions of the specimen. Here, the maximum and mean temperatures are very close to each other for both strain rates, indicating that strain localisation is not apparent in these quasi-static tests. Similar to the matrix material, the temperature rise at 0.5 s^{-1} is higher than at 0.1 s^{-1}, indeed the temperature in the low-rate experiment is observed to decrease at higher strains as the heat dissipates into the anvils. For the PC composite, the strain at which the stress in the 0.01 s^{-1} exceeds 0.1 and 0.5 s^{-1} is lower than for the PC matrix. This might be because more heat is generated in the PC composite than in the pure matrix material at the same rate (Fig. 8 and Fig. 11).

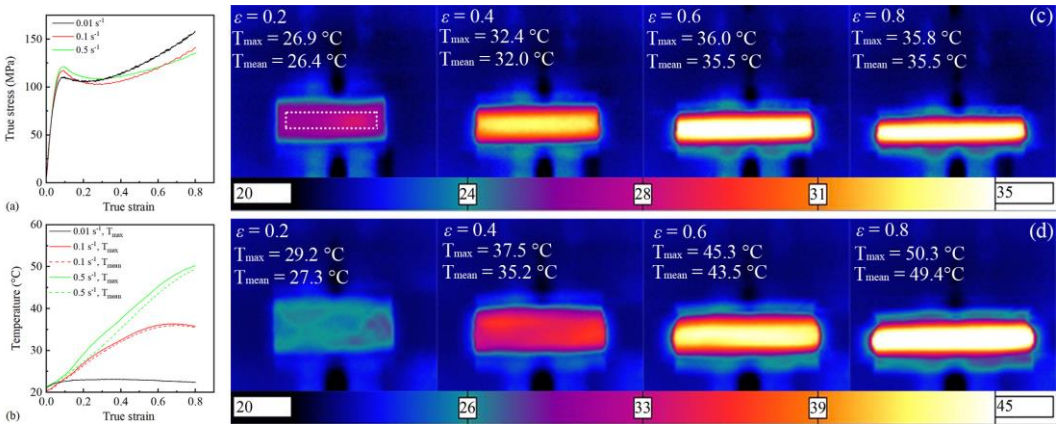

Figure 11. (a) stress-strain data for three quasi-static experiments on PC composite; (b) maximum and mean temperature rise data obtained from thermal images of these experiments; Temperature against true strain at different rates; (c) selected thermal images from experiment 0.1 s^{-1}; (d) selected thermal images from experiment at 0.5 s^{-1}.

Fig. 12 presents measurements made at medium rates, 1.4 and 11.4 s^{-1}. The initial yield stress at the higher rate is larger; however, later in the experiments, the stress at 1.4 s^{-1} exceeds that at 11.4 s^{-1} when the strain is

over 0.45. This might be caused by greater thermal softening at 11.4 s^{-1}. Unlike the experiments reported above, an uneven thermal distribution is observed in Fig. 12(c) and (d), e.g. the difference between the maximum and mean temperatures is 5.5 °C and 7.9 °C at strain around 0.3 for the compression tests at 1.4 s^{-1} and 11.4 s^{-1} respectively. After that, the difference between the maximum and mean temperatures decreases. The temperature patterns in these images indicate that strain localisation occurs in the medium rate experiments but is somewhat homogenised during the deformation process.

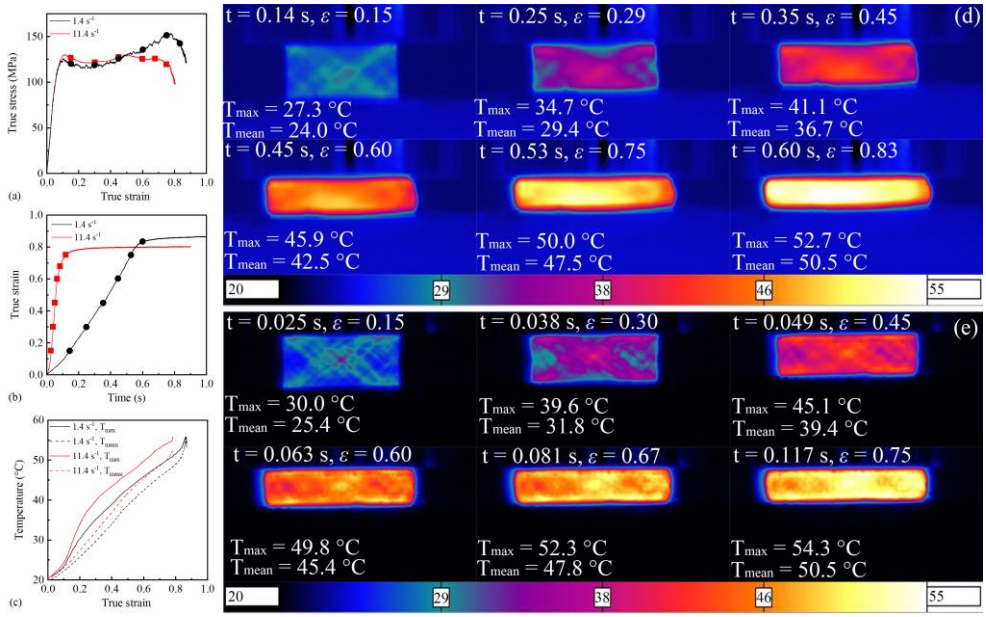

Figure 12. (a) True stress versus true strain curves in two medium rate tests on PC composite; (b) true strain versus time data for the same experiments; (c) maximum and mean temperature vs true strain; (d) selected thermal images from experiment at 1.4 s^{-1}, (e) selected thermal images from experiment at 11.4 s^{-1}. Markers on the stress-strain and strain-time curves indicate when the thermal images were taken.

For the high rate experiments, samples (TT cut) were tested in two directions relative to the flow orientation: with the flow direction parallel to the camera and with the flow direction toward the camera, Fig. 13(a) and 13(b). In order to obtain a full sequence of images, the same stepped trigger timing over multiple experiments as described in Fig. 10(b). The strain rates are 2500 ± 200 s^{-1}, and the stress-strain curves agree well for different experiments. In fact, it was found that the maximum and mean temperature values measured

in the two directions overlap very well, the orientation has no significant effects.

These temperature rise data help us to interpret the differences between high rate experiments and the 'equivalent' low temperature quasi-static test with the same yield stress, e.g. Fig. 7(b). The stress-strain curves begin to diverge at a true strain of about 0.3, at which the maximum temperature is around 50 °C, indicating that thermal softening is important in these experiments on composite materials. As the high rate experiment progresses, the local maximum temperature approaches 80 °C at a strain of around 0.6, which may approach the T_g of the interface material as discussed above. Following this, an apparent stress drop is observed (Fig. 13(a) and 13(b)) and very large temperature rises are seen in the thermal images (Fig. 13(d) and 13(e)), indicating the formation of an adiabatic shear band. At this point, temperatures in the specimen exceed the softening temperature indicated by DMA (Fig. 3(a)). This is accompanied by a rapid increase in overall strain rate as the material softens (Fig. 13(b)). The divergence between experiments at these larger strains is probably due to small differences in microstructure (e.g. fibre alignment, fibre distribution, interface behaviour) and the effect this has on the formation of the adiabatic shear bands.

The softening of high rate tests after yield but before the stress drop might be caused by localised heating in the specimen or micro-failure during the loading process, this is explored further below, whilst the significant stress drop after strain over 0.6 is due to the adiabatic shear band. It appears that in medium rate experiments localisation starts, but there is sufficient time for the higher temperature regions to lose heat to surrounding material before they become hot enough to form shear bands.

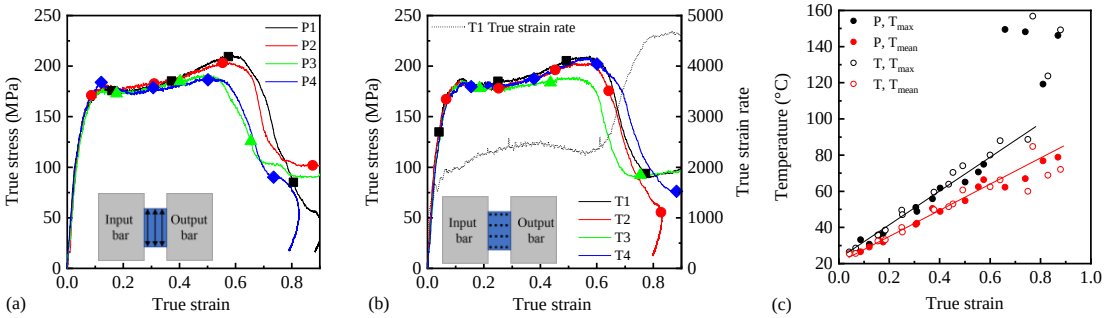

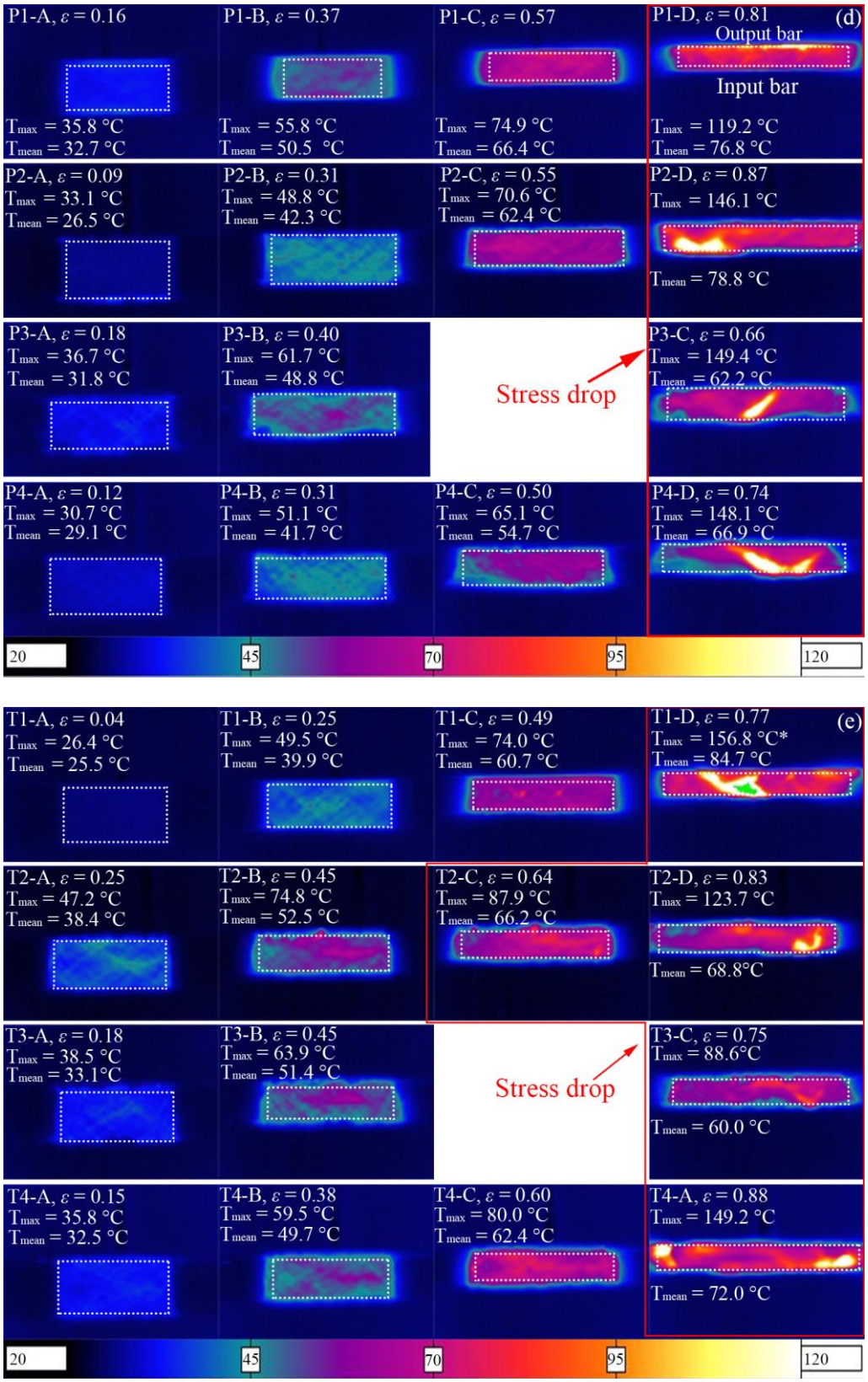

Figure 13. Temperature rise measurements in high rate experiments on PC composite (a) True stress-true strain curves for fibre flow parallel to the IR camera (P), markers indicate when the IR images were taken; (b) True stress-true strain curves for fibre flow towards the IR camera (T), note that the stress-strain

behaviour for P and T is the same, but the data are shown separately for easier comparison to the thermal images; (c) Temperature rise measurements for the eight experiments; (d) Thermal images for fibre flow parallel to the IR camera, (e) Thermal images for fibre flow towards the IR camera (note that green colour indicates that the temperature has exceeded 150 °C.

Dynamic in-situ measurements in ESRF

In-situ experiments were conducted in the European synchrotron radiation facility (ESRF) to examine microstructure evolution during the high rate tests. For these experiments, smaller specimens were used (2 mm long and 2 mm diameter), and these could be cut in a number of orientations: through-thickness specimens were equivalent to the specimens used in all the experiments above, although smaller, and could again be loaded with the injection flow direction parallel to the imaging plane (i.e. P) or perpendicular to the imaging plane (i.e. T). In plane specimens were loaded along the injection flow direction (see Fig. 14). Here, it is noted that the macroscopic response is the same as obtained in earlier experiments, showing that there is no significant effect from the X-rays.

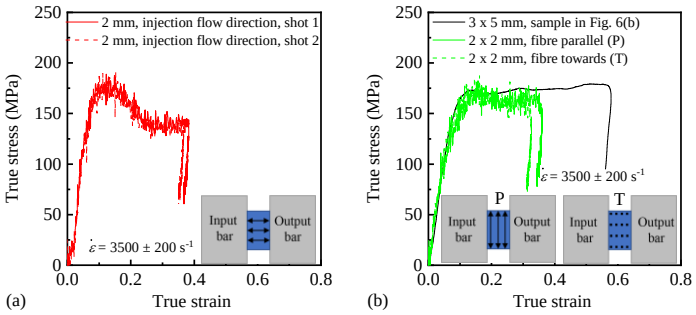

Figure 14. True stress versus true strain curves: (a) In-plane specimens (2 × 2 mm), loaded in the injection flow direction (b) Through thickness specimens (2 × 2 mm) with the injection flow direction parallel (P) and perpendicular (T) to the image plane.

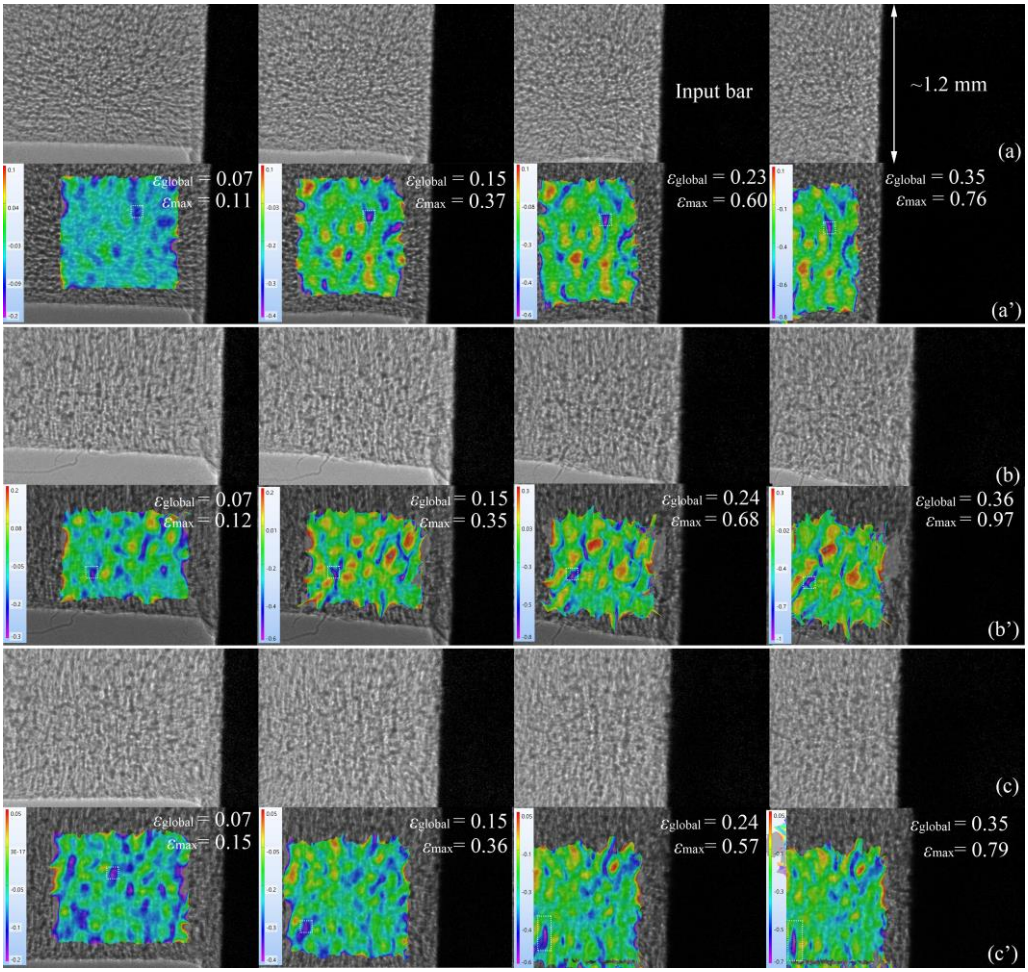

Figure 15. X-ray images and DIC mapping for 2 × 2 mm samples: (a) and (a') loaded in the injection flow direction, (b) and (b') injection flow direction parallel to the image plane (P), (c) and (c') injection flow direction perpendicular to the image plane (T). Zoomable images will be made available online.

Firstly, the mechanical data are compared to those obtained in the other Hopkinson bar experiments, see Fig. 14(a) and (b). Here, the yield and flow stresses are consistent for the specimens loaded through thickness, Fig 14(b); for the specimen loaded along the fibre flow direction, the yield stress is the same (a), but there is significant post-yield softening. X-ray images were obtained at a rate of 1.6 MHz, Fig. 15(a), (b), (c) show four images spaced through the duration of loading, no microcracking was observed in these images. In order to further explore the deformation, Fig.15(a'), (b') and (c') show full-field strain maps produced using DIC on the X-ray images obtained at global strains (determined from the timing of the image relative to the strain history from the SHPB) of 0.07, 0.15, 0.25 and 0.35 for three 2 × 2 mm samples in different orientations;

further information about the DIC processing is given in the Appendix. In performing this analysis, it is acknowledged the speckle contrast used in the DIC analysis is formed from the projection through the entire specimen rather than from a single plane within the specimen, and consequently, the resulting strain maps produced are interpreted cautiously, particularly as strain increases. To address this, a future study will seek to employ high density particles located on a known specimen plane to form the speckle contrast. Nonetheless, all strain maps indicate strain localisation, consistent with the thermal images in Fig. 13(d) and (e).

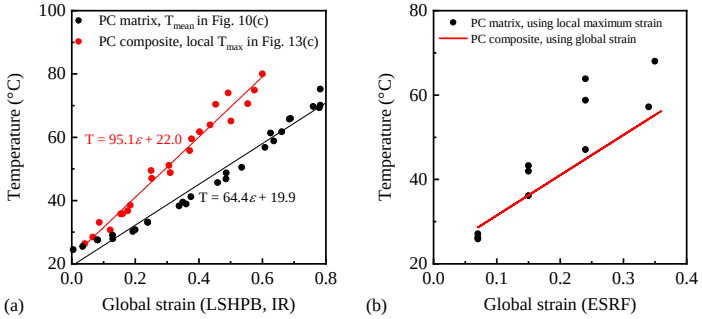

Figure 16 (a) Temperature vs strain for PC matrix and maximum temperature vs strain for PC composite, (b) Temperature change inferred using global strain in ESRF data compared to temperature change inferred using local maximum strain in ESRF data.

In order to link global and local behaviours of this inhomogeneous material, the temperature rise is used as a 'bridge'. We start by considering the strain dependence of the mean temperature rise in the (homogeneously deforming) PC and the local maximum temperature rise in the (inhomogeneous) PC composite, obtained from the results in the preceding sections, Fig. 16(a). Then, the local temperature rises in the composite can be inferred from the DIC strain measurements and our knowledge of the expected temperature rises in the PC matrix at those strains, assuming that the matrix sees most of the strain and, on these timescales, most of the heating. The result obtained is shown in Fig. 16(b); here, for each X-ray image, the global strain is measured, and the expected maximum temperature is then found using a line fit to the composite data in Fig. 16(a), this produces a series of points on a straight line (the red line labelled PC composite using global strain). Then the maximum local (true) strain in each X-ray image is found, and this is

combined with the fit to the matrix data in Fig. 16(a) to infer the local temperature rise corresponding to this maximum strain, which is a series of somewhat scattered points. If the maximum local strains observed in the ESRF X-ray data are consistent with the peak temperatures observed in the IR experiments, the points should lie around the line, which is indeed observed at low global strains. The increasing disagreement with increasing global strain may be attributed to the inability of the DIC analysis to accurately capture the strain localisation at large strains due to the use of the projection through the whole specimen or uncertainty in the thermal measurements owing to the localisation.

Summary of temperature rises in the rate-dependent compression experiments

Fig. 17 shows the temperature rise for the two materials at four adiabatic strain rates between 0.5 to 2500s^{-1}. As expected, the higher strain rate experiments have higher temperature rises and a more significant difference, in the composite, between the peak and mean temperatures. High strain rates can enhance localisation behaviour, and the stiffness is reduced rapidly because of the significant temperature rise in the adiabatic shear bands. Combined with the X-ray data, the implication is that adiabatic strain localisation plays a more significant role than microcracking in softening of these materials.

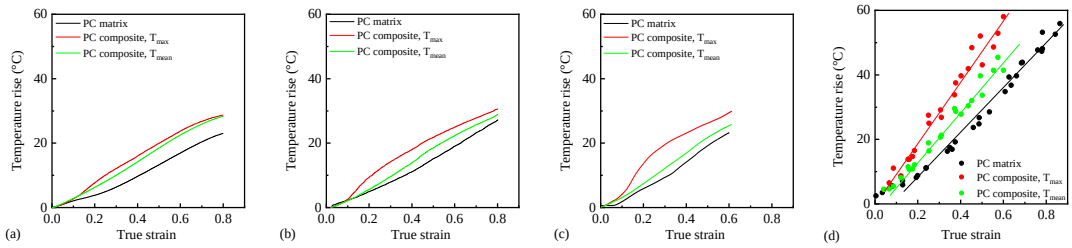

Figure 17. Temperature rise comparison for PC and its composite at different strain rates: (a) 0.5 s^{-1}, (b) ~1.5 s^{-1}, (c) ~12 s^{-1}, (d) ~2500 s^{-1}.

Conclusions

Thermomechanical characterisation of a polycarbonate composite with 20 wt% glass fibre reinforcement has been performed alongside the matrix polycarbonate materials. Frequency sweep dynamic mechanical analysis (DMA) tests were performed on the composite material cut at 0°, 45° and 90° to the fibre flow direction, as well as the matrix and used to construct time-temperature superposition master curves. Tensile samples were obtained in different orientations and loaded at different speeds; all samples displayed rate dependent failure (composite) or yield (PC matrix) stresses. Temperature dependent compression experiments were performed from -60 to 120 °C, and rate dependent compression experiments from 0.001 s^{-1} to above 5000 s^{-1}. The results for both materials display time-temperature equivalence: a decrease in temperature has the same effect as an increase in strain rate. The yield stress shows a bilinear increase with the increased logarithm of rate for both matrix and composite material due to the secondary (β)-transition. For large strains the equivalence is less, in particular, increased softening is observed in the high-rate experiments compared to their equivalent quasi-static low temperature tests. Two possible reasons for the softening are assumed: thermal softening and microcracking. Using an IR camera, temperature rises during deformation are measured for strain rates between 0.01 to 2500 s^{-1}. In all cases, the PC matrix deforms homogeneously, with a larger temperature rise at the higher strain rates. However, thermal localisation is observed in high rate tests on the PC composites, with a divergence between the maximum local and mean temperature, which increases with increasing strain until it reaches around 80 °C at 0.6 true strain. Here, a rapid stress drop is observed, accompanied by adiabatic shear bands in which the temperature can reach the glass transition temperature of the matrix material. At medium rates, some localisation is observed, but this does not lead to shear band formation. To further investigate localisation, in-situ split Hopkinson pressure bar (SHPB) tests were performed in ESRF using ultra-fast X-ray imaging, which was combined with DIC analysis to produce strain maps in the specimen. The X-ray images did not reveal failures, such as debonding and cracks, but did show

strain localisations that were consistent with the temperature rises observed in the IR images. These temperature rises were used to link global and local behaviours in the composite, which further reinforces the conclusion that softening in these materials at high strain rates is a result of adiabatic shear band formation.

CrediT authorship contribution statement

Peihao Song: Conceptualisation, Methodology, Investigation, Formal analysis, Writing - original draft. **David J Champman:** Methodology, Investigation, Writing – review & edit. **Aaron M Graham:** Investigation, Writing – review & edit. **Bratislav Lukić**: Methodology, Data acquisition, Writing – review & edit. **Alexander Rack:** Methodology, Data acquisition. **Clive R. Siviour:** Conceptualisation, Project administration, Supervision, Writing – review & edit, Funding acquisition.

Declaration of competing interesting

The authors declare that they have no known competing financial interests or personal relationships that could have appeared to influence the work reported in this paper.

Acknowledgements

This research forms part of the research programme of DPI, project 827t19, *Impact Modelling of Polymers: high-Rate Experiments for Solid-state Simulations* and the polycarbonates were kindly supported by Saudi Basic Industries Corporation (SABIC). The authors thank our colleagues on this project, Dr Davide De Focatiis and Grace Owen at the University of Nottingham for helpful discussions. We also thank the technicians of the Solid Mechanics Group workshop, in particular, Andy Bateman for his help with the manufacture of specimens and fixtures for this project and Nicholas Hawkins for his help with the DMA tests. We thank the Hypersonics Research Group for the use of the high speed thermal imaging camera, and thank EPSRC for support of thermomechanical characterisation as part of EP/V003321/1. X-ray imaging was performed at ESRF under proposal beamtime MI-1397, under the Shock BAG supported by the European Union's Horizon 2020 research and innovation program under Grant Agreement No. 870313, Streamline). For the purpose of Open Access, the authors have applied a CC BY public copyright license to any Author Accepted Manuscript (AAM) version arising from this submission.

Data Availability

All data supporting this study are openly available from the Oxford University Research Archive at [DOI will be made available on paper acceptance].

Appendix

Table A1 Adopted Digital Image Correlation (DIC) setup

DIC software	MatchID, version 2023.1.1
Image filtering	Gaussian, 5 x 5 pixel^2 kernel
Subset size (pixel)	21
Step size (pixel)	2
Subset shape function	Quadratic
Matching criterion	Zero-normalised sum of square differences (ZNSSD)
Interpolant	Local Bicubic Spline Interpolation
Strain tensor	Hencky (True) strain tensor
Estimates progress history	Spatial and updated reference
Strain window size	13 x 13 pixels^2, Quadratic Quadrilateral

References

1. Hsissou, R., et al., *Polymer composite materials: A comprehensive review.* Composite Structures, 2021. **262**: p. 113640.
2. Chen, C., et al., *Effect of fiber reinforcement and fabrication process on the dynamic compressive behavior of PEEK composites.* International Journal of Mechanical Sciences, 2019. **155**: p. 170-177.
3. Fu, S.-Y., B. Lauke, and Y.W. Mai, *Science and engineering of short fibre-reinforced polymer composites*. 2019: Woodhead Publishing.
4. Pastukhov, L.V. and L.E. Govaert, *Plasticity-controlled failure of fibre-reinforced thermoplastics.* Composites Part B: Engineering, 2021. **209**: p. 108635.
5. Bernasconi, A. and F. Cosmi, *Analysis of the dependence of the tensile behaviour of a short fibre reinforced polyamide upon fibre volume fraction, length and orientation.* Procedia engineering, 2011. **10**: p. 2129-2134.
6. Pastukhov, L.V. and L.E. Govaert, *Crack-growth controlled failure of short fibre reinforced thermoplastics: Influence of fibre orientation.* International Journal of Fatigue, 2021. **143**: p. 105982.
7. De Monte, M., E. Moosbrugger, and M. Quaresimin, *Influence of temperature and thickness on the off-axis behaviour of short glass fibre reinforced polyamide 6.6–cyclic loading.* Composites Part A: Applied Science and Manufacturing, 2010. **41**(10): p. 1368-1379.
8. Engels, T.A.P., et al., *Predicting the Long-Term Mechanical Performance of Polycarbonate from Thermal History during Injection Molding.* Macromolecular Materials and Engineering, 2009. **294**(12): p. 829-838.
9. Janssen, R.P.M., et al., *Fatigue life predictions for glassy polymers: a constitutive approach.* Macromolecules, 2008. **41**(7): p. 2520-2530.
10. Amiri-Rad, A., et al., *An anisotropic viscoelastic-viscoplastic model for short-fiber composites.* Mechanics of Materials, 2019. **137**: p. 103141.
11. Amiri-Rad, A., et al., *Improved associated flow rule for anisotropic viscoplasticity in thermoplastic polymer systems.* Mechanics of Materials, 2021. **163**: p. 104087.
12. Ozkan, C., et al., *Short carbon fiber reinforced polycarbonate composites: Effects of different sizing materials.* Composites Part B: Engineering, 2014. **62**: p. 230-235.
13. Amiri-Rad, A., et al., *Constitutive modeling of injection-molded short-fiber composites: Characterization and model application.* Journal of Applied Polymer Science, 2020. **137**(41): p. 49248.
14. Ho, K.-C. and M.-C. Jeng, *Tribological characteristics of short glass fibre reinforced polycarbonate composites.* Wear, 1997. **206**(1-2): p. 60-68.
15. Siviour, C.R. and J.L. Jordan, *High strain rate mechanics of polymers: a review.* Journal of Dynamic Behavior of Materials, 2016. **2**: p. 15-32.
16. Perry, J.I. and S.M. Walley, *Measuring the effect of strain rate on deformation and damage in fibre-reinforced composites: A review.* Journal of Dynamic Behavior of Materials, 2022. **8**(2): p. 178-213.
17. Chen, W.W. and B. Song, *Split Hopkinson (Kolsky) bar: design, testing and applications*. 2010: Springer Science & Business Media.
18. Siviour, C.R., et al., *The high strain rate compressive behaviour of polycarbonate and polyvinylidene difluoride.* Polymer, 2005. **46**(26): p. 12546-12555.
19. Mulliken, A.D. and M.C. Boyce, *Mechanics of the rate-dependent elastic–plastic deformation of glassy polymers from low to high strain rates.* International Journal of Solids and Structures, 2006. **43**(5): p. 1331-1356.
20. Song, P., A.R. Trivedi, and C.R. Siviour, *Mechanical response of four polycarbonates at a wide range*

of strain rates and temperatures. Polymer Testing, 2023: p. 107986.

21. Kendall, M.J. and C.R. Siviour, *Experimentally simulating high-rate behaviour: rate and temperature effects in polycarbonate and PMMA.* Philosophical Transactions of the Royal Society A: Mathematical, Physical and Engineering Sciences, 2014. **372**(2015): p. 20130202.
22. Trivedi, A.R., P. Song, and C.R. Siviour, *Experimentally simulating adiabatic behaviour: Capturing the high strain rate compressive response of polymers using low strain rate experiments with programmed temperature profiles.* Polymer Testing, 2022. **116**: p. 107773.
23. Zhang, L., et al., *Temperature dependent dynamic compressive response of PA66-GF30 composite under constant strain rate multiaxial loading.* Composites Part B: Engineering, 2022. **234**: p. 109738.
24. Pournoori, N., et al., *Adiabatic heating and damage onset in a pultruded glass fiber reinforced composite under compressive loading at different strain rates.* International Journal of Impact Engineering, 2021. **147**: p. 103728.
25. Li, Z. and J. Lambros, *Strain rate effects on the thermomechanical behavior of polymers.* International Journal of Solids and Structures, 2001. **38**(20): p. 3549-3562.
26. Arruda, E.M., M.C. Boyce, and R. Jayachandran, *Effects of strain rate, temperature and thermomechanical coupling on the finite strain deformation of glassy polymers.* Mechanics of Materials, 1995. **19**(2-3): p. 193-212.
27. Regev, A. and D. Rittel, *Simultaneous transient temperature sensing of impacted polymers using infrared detectors and thermocouples.* Experimental mechanics, 2008. **48**: p. 675-682.
28. Goviazin, G.G., A. Shirizly, and D. Rittel, *A Comparative Study of the Performance of IR Detectors vs. High-Speed Cameras Under Dynamic Loading Conditions.* Experimental Mechanics, 2022: p. 1-10.
29. Bjerke, T., Z. Li, and J. Lambros, *Role of plasticity in heat generation during high rate deformation and fracture of polycarbonate.* International Journal of Plasticity, 2002. **18**(4): p. 549-567.
30. Lerch, V., G. Gary, and P. Hervé, *Thermomechanical properties of polycarbonate under dynamic loading.* J. Phys. IV France, 2003. **110**: p. 159-164.
31. Garg, M., A.D. Mulliken, and M.C. Boyce, *Temperature Rise in Polymeric Materials During High Rate Deformation.* Journal of Applied Mechanics, 2008. **75**(1).
32. Lin, P., S. Cheng, and S.-Q. Wang, *Strain hardening during uniaxial compression of polymer glasses.* ACS Macro Letters, 2014. **3**(8): p. 784-787.
33. Rittel, D., *On the conversion of plastic work to heat during high strain rate deformation of glassy polymers.* Mechanics of Materials, 1999. **31**(2): p. 131-139.
34. Tarfaoui, M., A. El Moumen, and H.B. Yahia, *Damage detection versus heat dissipation in E-glass/Epoxy laminated composites under dynamic compression at high strain rate.* Composite Structures, 2018. **186**: p. 50-61.
35. Deng, S., M. Hou, and L. Ye, *Temperature-dependent elastic moduli of epoxies measured by DMA and their correlations to mechanical testing data.* Polymer testing, 2007. **26**(6): p. 803-813.
36. Gray III, G.T. and W.R. Blumenthal, *Split-Hopkinson pressure bar testing of soft materials.* ASM handbook, 2000. **8**: p. 488-496.
37. Chen, W.W. and B. Song, *Dynamic characterization of soft materials.* Dynamic Failure of Materials and Structures, 2010: p. 1-28.
38. van der Tempel, L., *Thermography of semi-transparent materials by a FLIR ThermaCAM SC3000 infrared camera.* Philips Research, 2011.
39. Weitkamp, T., et al. *Status and evolution of the ESRF beamline ID19*. American Institute of Physics.
40. Cohen, A., et al., *In-situ radiography of a split-Hopkinson bar dynamically loaded materials.* Journal of Instrumentation, 2019. **14**(06): p. T06008.

41. Escauriza, E.M., et al., *Ultra-high-speed indirect x-ray imaging system with versatile spatiotemporal sampling capabilities.* Applied Optics, 2018. **57**(18): p. 5004-5010.
42. Lukić, B., et al., *Single Bunch X-Ray Phase-Contrast Imaging of Dynamic Tensile Failure in Geomaterials.* Journal of Dynamic Behavior of Materials, 2022: p. 1-13.
43. Plass, C.T., et al., *Spatially Resolved Dynamics of Cobalt Color Centers in ZnO Nanowires.* Advanced Science, 2023. **10**(1): p. 2205304.
44. Wilkins, S.W., et al., *Phase-contrast imaging using polychromatic hard X-rays.* Nature, 1996. **384**(6607): p. 335-338.
45. Palmese, G.R., R.L. McCullough, and N.R. Sottos, *Relationship between interphase composition, material properties, and residual thermal stresses in composite materials.* The Journal of Adhesion, 1995. **52**(1-4): p. 101-113.
46. Sottos, N.R., R.L. McCullough, and W.R. Scott, *The influence of interphase regions on local thermal displacements in composites.* Composites Science and Technology, 1992. **44**(4): p. 319-332.
47. Skourlis, T.P. and R.L. McCullough, *The effect of temperature on the behavior of the interphase in polymeric composites.* Composites science and technology, 1993. **49**(4): p. 363-368.
48. SABIC, *LEXAN^{TM} FR RESINS 3412R Data Sheet*. 2023.

7 Conclusions

7.1 Thesis objectives

The primary objective of this thesis was to characterise the thermomechanical responses of three homo-polycarbonates (PCs) with different molecular weights, a co-polymer, and a short glass fibre-reinforced PC, and to develop experimental approaches to interpret the constitutive behaviours of PCs under different loading conditions. The thesis, therefore, provides an extensive dataset for assembling and calibrating continuum constitutive models and novel experimental methodologies.

This research started by combining traditional tensile test methods with advanced optical measurements to provide a fundamental mechanistic understanding of large-strain tensile deformation, **Chapter 3**. Following that, a comprehensive thermomechanical characterisation of three different molecular weight PCs and one co-monomer PC was performed, **Chapter 4**. These baseline thermomechanical characterisations included, but were not limited to, Differential Scanning Calorimetry (DSC), Dynamic Mechanical Analysis (DMA), quasi-static tensile tests at different loading speeds, wide temperature and strain rate range compression tests. Hence, this study provided a fundamental dataset for model development for our collaborators at the University of Nottingham. These investigations enhanced the time-temperature equivalence at the viscoelastic region and also proposed a research question: why is less softening observed for PC at large strains in high-rate tests compared to medium-rate tests and to other amorphous polymers (PVC, PMMA)?

To address the question above, experimentally measuring the temperature rises at different loading conditions was necessary. In **Chapter 5**, the temperature rises at different strain rates and at varying temperatures with an adiabatic loading rate were measured using a high-speed infrared (IR) camera and thermocouple, respectively. These experimental results provided an extensive dataset for modelling, and measured the Taylor Quinney Coefficient (TQC, the ratio between heat and plastic work) across two molecular

relaxations of PC.

All experimental methodologies developed and employed above were utilized to characterise the injection moulded 20 wt% glass fibre reinforced PC in **Chapter 6**. The influence of fibre, fibre orientation, strain rates and temperatures was studied. Moreover, the *in-situ* characterisations during split Hopkinson pressure bar (SHPB) tests were performed in the European Synchrotron Radiation Facility (ESRF), which helped to understand the internal damage mechanism during the high-rate tests.

In general, these experimental insights not only created a comprehensive dataset of polycarbonates, but also provided a thermomechanical characterisation process of polymer from small to large deformation, from simple isotropic (PC resin materials) material to complex anisotropic (PC composite). Some advanced experimental methods were developed and used to achieve the objectives of this research, and the detailed contributions are summarized below.

7.2 Summary of accomplishments

7.2.1 Calibration of constitutive behaviours of ductile polymer using traditional tensile test

The tensile test is the most often used strategy to characterise materials and their constitutive model calibration, however, only relying on the global force-displacement curve to validate the model parameters is insufficient because of the strain localisations (neck) always being observed during the large strain tensile deformation process for ductile polymers. **Chapter 3** used a digital image correlation (DIC) system to track the full-field displacement and the local strain-time response during tensile experiments on polycarbonate specimens. At the same time, an infrared (IR) camera was used to measure the full-field temperature rise during tests. These were combined with uniaxial compression test data (**Chapter 4**) from the same material to calibrate a visco-plastic constitutive model, which was shown to agree well with the experimental results describing local (true strain-time curve) and global behaviours. The main contributions here are to show that constitutive models can be appropriately calibrated using a combination of techniques, including the full-field measurements, but that simply using force-displacement information, as is often done, is insufficient.

7.2.2 Generation of a comprehensive dataset of four polycarbonates

Chapter 4 extensively characterised three homo-polycarbonates with different melt flow rates (MFRs) and one co-polycarbonate, with consistent thermal histories. Dynamic Mechanical Analysis (DMA) was performed using two configurations, and the experimental results presented that the moduli obtained from the three point bend mode were consistent with the mechanical test results (tensile tests in **Chapter 3**), whilst single cantilever beam mode lowers the moduli because of the clamp effects. However, as an amorphous polymer, PC will lose its stiffness very rapidly at temperatures above the glass transition; thus, a single cantilever beam mode can be used to obtain the loss modulus and Tan delta peak, as well as the activation energies for glass transition can be approached using the Arrhenius plot. Compression responses were measured at temperatures from -60 to 120 °C at a rate of 0.01 s^{-1} and strain rate from 0.001 to 3000 s^{-1} at room

temperature. This research fills the blanks of stress-strain data at rates between 1 and 700 s^{-1} using an LSHPB, and it gives more complete data on the trend in the yield stress versus log-strain rate. Moreover, the time-temperature equivalence theory was used for all PCs to understand their yield stress dependences better.

7.2.3 Measurements of temperature rise under different loading conditions

In **Chapter 4**, a comprehensive dataset was generated, and the small strain behaviour was consistent with the 'time-temperature equivalence', both increasing in strain rate and decreasing in temperature can enhance the yield stress of PC. However, for the large strain region, the stresses showed less softening than medium rate tests and other amorphous polymers under high rate loading in the literature. The temperature rise measurements were performed under different loading conditions in **Chapter 5** to address the experimental observations in **Chapter 4**.

From the aspect of experimental technique development, it is worth mentioning that the frame rate for the most advanced IR camera cannot provide a series of high spatial resolution thermal images within the 400 μs duration of the split Hopkinson Bar experiment. Thus, a new method was developed to construct 'continuous' thermal images by stitching images from a series of tests; in this way, the thermal data at each strain overlapped with their neighbour very well, and the comprehensive full-field thermal data were obtained. At the same time, the LSHPB was triggered using the same or similar pressure to ensure the constitutive behaviour was highly duplicatable between each test.

Besides, the ratio between plastic work and heat, the Taylor Quinney Coefficient (TQC), under different loading conditions were addressed; the temperature-dependent tests were carried out at adiabatic rate from -80 to 150 °C which covered the secondary- to glass-transition temperature region, and the rate-dependent tests were performed from 0.01 to 2500 s^{-1} at 20 °C. Tests with higher stress levels can generate higher temperature rise, however, the TQCs are different in different adiabatic loading conditions. The changes in TQC in these tests are similar to yield stresses at a small strain regime: elevating the strain rate while lowering the

temperature can increase this conversion ratio. These experimental results indicate that microstructural evolution (molecular relaxation) might significantly affect energy conversions.

7.2.4 Characterisation of short glass fibre reinforced PC

All experiments described above for PCs were also applied for this injection moulded 20 wt% glass fibre reinforced PC in **Chapter 6**: DSC, DMA, tensile tests using different loading speeds for specimens cut from different fibre flow orientations, varying rate and temperature compression tests. The sample preparation and experimental methodologies were kept the same as those used for the pure matrix polycarbonate, thus, it is possible to understand the effects of fibre and fibre flow orientation on the thermomechanical properties. Compared to the PC matrix: (1) the yield stress or strength of reinforced material is dramatically increased; (2) less hardening was observed for PC composite at high rate tests, and no evident damages can be observed.

To understand the softening mechanism of PC composite, again, the high-speed IR camera was utilized from 0.1 to 2600 s^{-1} to measure the temperature rises. The higher stress level can generate more heat for PC composites than pure PC matrix in the tests with the same strain rate. In medium rate tests, pronounced shear bands appeared at the beginning, and the localised thermal distribution was homogenized at large strain. The same 'stitching' method was used for PC composite in high rate tests; the very obvious shear bands were observed with the maximum temperature rise beyond the glass transition of the PC matrix, which led to a significant stress drop in high-rate tests.

In addition, the PC composite specimens were tested in ESRF with a synchronized high-density X-ray in SHPB tests. The results presented a similar constitutive behaviour as experiments performed in Oxford, and no damage was observed in these transmission X-ray images. Moreover, the DIC was adopted to understand the strain localisation during the tests, and the ESRF data and data obtained in Oxford were linked using the thermal measurement data.

7.3 Limitations and recommendations for future work

In **Chapter 3**, 2-D DIC cannot experimentally approach the current cross-section area in tension tests, thus, some assumptions, (1) the stretch ratio in unloading directions is the same, (2) the material is incompressible, had to be made to calculate the true stress. Moreover, the frame rate of a CCD camera is not adequate to capture the whole process of the shear band formation. In the future, firstly, 3-D DIC is recommended to capture the deformation information of the side surface for obtaining more accurate true stress. Secondly, the high-speed camera might be able to be added to record the shear band formation process so that more detailed information on strain localisation can be addressed. Thirdly, the Virtual Fields Method (VFM), which is an ineverse identification method, can be utilized to approach the material constitutive parameters without many fitting trials.

The different melt flow rate (molecular weight) PCs (PC2, PC3, PC8) did not present evident differences in constitutive behaviours in **Chapter 4**. This might be due to the differences in molecular weight for the available materials in this project is not big enough, or the molecular weight differences for PCs can only significantly affect the ductile/brittle transition. In the future, a large gap in molecular weight for PCs is suggested for further characterising to approach its potential effects on the deformation process.

To address the TQC, the specific heat (C_p) is a necessary physical parameter. In **Chapter 5**, the value of C_p is obtained from the MDSC measurement for the undeformed samples. However, no mature techniques exist to determine the *in-situ* C_p, especially in extreme experimental conditions, such as very high or very low temperatures or high rate tests. Moreover, the calibration of the emissivity of a material is also very challenging, particularly for a deformed sample, like C_p, there is no mature approach to calibrate the *in-situ* emissivity of materials during the deformation process. This research has carried out the tests at the adiabatic strain rate (0.5 s^{-1}) through the secondary- to glass-transition temperature region; in the future, the strain rate could be increased to above 1000 s^{-1} using the SHPB system with this temperature region to further understand the

molecular relaxation effects on the energy conservation.

Due to the limitations of the supplied PC composite, only 20 wt% short glass fibre reinforced PC is characterised in **Chapter 6**. Thus, it might be worth having a PC with various fibre content in the future to understand the fibre content effects. The DIC is only conducted on the transmission X-ray images, however, the high-speed IR imaging was used to measure the temperature rise at the surface. Next, the synchronized high-speed camera and high-speed IR cameras can simultaneously measure the full-field deformation and temperature rise, and then the results of displacement and temperature field might be better correlated.

7.4 Closing remarks

The achievements of this project are summarised as follows: new data, new understanding and new techniques. Together, these will form the fundamental foundations required for model development and the development of high-performance composites with properties optimised for impact applications. New understanding will come from rate and temperature dependence in polymers and composites, and the new techniques can characterise the localisation formation, damage formation and microstructural evolution in various loading conditions. In the future, it will allow us to produce high-performance, recyclable polymeric materials optimised to work efficiently in different impact applications.